Polymer network dynamics during electrospinning and its effect on the fibers nanostructure

Modeling, simulation and experiments

Israel Greenfeld

Polymer network dynamics during electrospinning and its effect on the fibers nanostructure

Modeling, simulation and experiments

Research Thesis

Submitted in Partial Fulfillment of the Requirements
for the Degree of Doctor of Philosophy

Israel Greenfeld

Submitted to the Senate of the
Technion – Israel Institute of Technology

Tishrei 5774, Haifa, September 2013

To my family

Acknowledgments, publications and presentations

The research thesis was performed under the supervision of Prof. Eyal Zussman in the Department of Mechanical Engineering, with Dr. Arkadii Arinstein as advisor.

I am grateful to Prof. Zussman for his confidence in me and his friendship, for his professional and dedicated guidance, and for opening his world, the world of tiny things, to me. I thank Dr. Arinstein for the long enjoyable hours I spent with him learning the secrets of polymer physics, and for our joint work in developing the model and simulations.

The generous financial help of the Technion, the United States-Israel Binational Science Foundation, the RBNI–Russell Berrie Nanotechnology Institute, and the Israel Science Foundation is gratefully acknowledged.

The research was carried out in collaboration with Prof. Miriam H. Rafailovich from the Stony Brook University (USA), Dr. Kamel Fezzaa from Argonne National Laboratory (USA), Prof. Dario Pisignano and Dr. Andrea Camposeo from the Università del Salento (Italy), and Dr. Ulrike Wangenheim and Prof. Robert H. Schuster from the Deutsches Institut für Kautschuktechnologie (Germany). I am indebted to them for supporting my research and for their productive cooperation.

The research was summarized in five papers, and presented by the author in several lectures at the Technion and Stony Brook University (USA), and in three Annual American Physical Society March Meetings (USA). Refer to lists of publications and presentations in the next pages.

Publications

[1] Greenfeld, I., A. Arinstein, K. Fezzaa, M.H. Rafailovich, and E. Zussman, *Polymer dynamics in semidilute solution during electrospinning: A simple model and experimental observations.* Physical Review E, 2011. **84**(4): p. 041806.[1]

[2] Greenfeld, I., K. Fezzaa, M.H. Rafailovich, and E. Zussman, *Fast X-ray phase-contrast imaging of electrospinning polymer jets: Measurements of radius, velocity, and concentration.* Macromolecules, 2012. **45**(8): p. 3616-3626.[2]

[3] Camposeo, A.,* I. Greenfeld,* F. Tantussi, S. Pagliara, M. Moffa, F. Fuso, M. Allegrini, E. Zussman, and D. Pisignano, *Local mechanical properties of electrospun fibers correlate to their internal nanostructure.* Nano Letters, 2013. **13**(11): p. 5056−5062.[3]

* These authors contributed equally to this work.

[4] Camposeo, A.,* I. Greenfeld,* F. Tantussi, M. Moffa, F. Fuso, M. Allegrini, E. Zussman, and D. Pisignano, *Mechanistic insight and nanoscale control of the orientational and polarization properties of active polymer fibers.* Submitted for publication, 2013.[4]

* These authors contributed equally to this work.

[5] Greenfeld, I. and E. Zussman, *Polymer entanglement loss in extensional flow: evidence from electrospun short nanofibers.* Journal of Polymer Science Part B-Polymer Physics, 2013. **51**(18): p. 1377–1391.[5]

Presentations

[1] Greenfeld, I. *Polymer stretching during electrospinning - random walk simulations.* Lecture in the nano colloquium, Dep. of Mechanical Engineering, Technion, Haifa, Israel, 2010.

[2] Greenfeld, I., A. Arinstein, K. Fezzaa, M.H. Rafailovich, and E. Zussman. *Polymer network stretching during electrospinning.* Proc. of the Annual American Physical Society March Meeting, Dallas, TX, 2011.

[3] Greenfeld, I., K. Fezzaa, M.H. Rafailovich, and E. Zussman. *X-ray imaging of electrospinning polymer solutions.* Poster in the American Physical Society March Meeting, Boston, MA, 2012.

[4] Greenfeld, I. *Effect of electrospinning on the polymer matrix in nanofibers - modeling and experiments.* Lecture in the Dep. of Materials Science and Engineering, State University of New York, Stony Brook, NY, 2013.

[5] Greenfeld, I., Camposeo, A., F. Tantussi, S. Pagliara, F. Fuso, M. Allegrini, D. Pisignano, and E. Zussman. *Axial and radial nanostructures in electrospun polymer fibers.* Proc. of the Annual American Physical Society March Meeting, Baltimore, MD, 2013.

[6] Greenfeld, I. *Polymer network in a strong extensional flow - a study of the electrospinning jet.* Faculty seminar, Dep. of Mechanical Engineering, Technion, Haifa, Israel, 2013.

Table of Contents

List of Figures

List of Figures (cont.)

List of Figures (cont.)

List of Figures (cont.)

List of Tables

Abstract

The high strain rate extensional flow of a semi-dilute polymer solution can cause substantial stretching and disentanglement of the polymer network. The research presented in this thesis encompasses a theoretical and experimental investigation of the effects of electrospinning, a flow governed by high strain rate and rapid evaporation, on the dissolved polymer network, and on the nanostructure and mechanical properties of the resulting nanofibers.

Electrospun polymeric nanofibers, typically 50 to 1000 nanometers in diameter, exhibit unique mechanical properties. Specifically, below a certain crossover diameter, dependent on the polymer molar mass, the nanofiber elastic moduli begin to rise sharply. Understanding the mechanisms behind these phenomena is of interest for improving the mechanical, electrical and optical properties of nanofibers, and can lead to novel applications in engineering and life sciences.

In this study, modeling of the dynamic evolution of the entangled polymer network in an electrospinning jet predicted substantial longitudinal stretching and radial contraction of the network, a transformation from an equilibrium state to an almost fully-stretched state. This prediction was verified by fast X-ray phase-contrast imaging of electrospinning jets, which revealed a noticeable increase in polymer concentration at the jet center, within a short distance from the jet start. The model was expanded to semi-flexible conjugated polymer chains, and scanning near field optical microscopy of electrospun nanofibers of such electrically and optically active polymers revealed that the network conformation effectively remains after jet solidification.

Hence, at high flow strain rates, the resulting fiber nanostructure is that of a dense core with axially aligned macromolecules, surrounded by an amorphous boundary. Such molecular and supramolecular structures can account for the increase of the elastic moduli at small fiber diameters. Furthermore, polymer entanglement loss in consequence of network stretching under very high strain rates, evidenced in jet fragmentation and appearance of short nanofibers, reduces the fiber diameter and enhances the homogeneity and alignment of the nanostructure, potentially improving the elastic properties even more.

This thesis reviews and discusses the relevant literature in the fields of polymer physics, polymer mechanical properties, electrospinning, and nanofibers. A description of the methods used in the research, combining theoretical, simulation, and experimental work, is provided. The results are presented in five publications, which summarize the research in a streamlined fashion, and then discussed.

List of symbols and abbreviations

Symbols

A	estimated cross-section of a fully extended chain [m^2], p. 145
$A_{x,i}$	force function constants in a random walk [dimensionless], p. 34
a	Kuhn length, size of a rigid chain element or monomer [m], p. 25
a	jet radius [m], p. 69
a	confining tube diameter in a polymer network [m], p. 114
$\hat{a}$	normalized jet radius [dimensionless], p. 70
a_0	internal radius of a jet orifice [m], p. 70
a_{def}	confining tube diameter in an undeformed polymer network [m], p. 118
a_{eff}	effective subchain size [m], p. 58
a_p	polymer network radius [m], p. 80
a_s	jet radius where the polymer network reaches full extension [m], p. 94
$a_{z=0}$	jet initial radius [m], p. 71
B	criterion for determining the flow type [dimensionless], p. 71
Bo_E	electric Bond number [dimensionless], p. 71
b	Kuhn length, size of a rigid chain element or monomer [m], p. 91
C_∞	Flory's characteristic ratio for long chains [dimensionless], p. 132
Ca	capillary number [dimensionless], p. 71
c	polymer concentration in a solution [$kg\,m^{-3}$], p. 19
c	initial concentration of a polymer in a solution [$kg\,m^{-3}$], p. 70
c^*	crossover concentration of a polymer in a solution [$kg\,m^{-3}$], p. 19
c_e	entanglement concentration of a polymer in a solution [$kg\,m^{-3}$], p. 107
c_{net}	sound velocity in a polymer network [$m\,s^{-1}$], p. 58
c_p	polymer concentration in a solution [$kg\,m^{-3}$], p. 52
Δc_p	concentration change of a polymer in a solution [$kg\,m^{-3}$], p. 52
c_s	solvent concentration in a solution [$kg\,m^{-3}$], p. 52
D	fiber diameter [m], p. 19
D	fiber fragment diameter [m], p. 111
$Đ$	molar mass dispersity of polymer chains [dimensionless], p. 107
D_c	condensed diameter of a polymer network [m], p. 116
$Đ_D$	diameter dispersity of a fiber fragment [dimensionless], p. 112
D_{FIT}	power fitted diameter of a fiber fragment [m], p. 112
$Đ_L$	length dispersity of a fiber fragment [dimensionless], p. 112
D_H	hydraulic diameter [m], p. 68
D_n	number-average (mean) diameter of a fiber fragment [m], p. 111
D_s	solvent diffusion coefficient (through the fiber skin) [$m^2\,s^{-1}$], p. 23
D_w	weight-average diameter of a fiber fragment [m], p. 111
d	travel distance of an X-ray beam through the jet [m], p. 52
d	particle size in a suspension fluid [m], p. 68
d	diameter of a spherical bead in a rigid chain segment [m], p. 91
d	electrodes gap distance [m], p. 113

d	size of an ordered region in a nanofiber [m], p. 152
d_w	skin thickness of a core-shell nanofiber [m], p. 23
E	electric field intensity [$V\,m^{-1}$], p. 22
E	Young's modulus [Pa], p. 24
ΔE	energy barrier between trans and gauche states [J], p. 131
E_0	Young's modulus of a bulk material [Pa], p. 24
E_{app}	apparent Young's modulus [Pa], p. 151
E_{fiber}	Young's modulus of a fiber [Pa], p. 79
E_{max}	maximal Young's modulus of a fiber [Pa], p. 79
E_t	Young's modulus of an AFM cantilever [Pa], p. 85
F	force on a monomer [N], p. 32
F	Helmholtz free energy [J], p. 142
F	bending force on a suspended nanofiber [N], p. 147
ΔF	increase in the force on a monomer [N], p. 60
F_0	effective force on a subchain in a network at rest [N], p. 43
F_{end}	force at chain (or subchain) ends [N], p. 32
F_{field}	hydrodynamic force on a monomer [N], p. 32
F_{load}	AFM tip force [N], p. 80
F_n	tension force acting on a subchain n [N], p. 43
δF_n	additional tension force on subchain n due to hydrodynamics [N], p. 60
F_{tot}	total free energy of a chain [J], p. 40, 138
F_x	force on a monomer in direction x [N], p. 33
f	normalized force on a monomer [dimensionless], p. 33
f	extension force [N], p. 142
f, f'	modulation frequency [s^{-1}], p. 90
f_0	normalized effective force on a subchain in a network at rest [dimensionless], p. 43
f_N	normalized extension force in a Langevin function [dimensionless], p. 142
f_x	normalized force on a monomer in direction x [dimensionless], p. 33
G	shear modulus [Pa], p. 143
G_0	shear modulus of a bulk material [Pa], p. 147
G_{ibbs}	Gibbs free energy [J], p. 142
g	X-ray scattering form factor [dimensionless], p. 62
g_{exp}	X-ray scattering form factor [dimensionless], p. 62
g_{sim}	simulated X-ray scattering form factor [dimensionless], p. 62
h	local nanofiber thickness [m], p. 82
H	small dimension of the flow [m], p. 68
I_E	electric current carried by the jet [A], p. 19
I	number of chains in a random walk simulation [dimensionless], p. 36
$I_{\parallel}$, $I_{PL\parallel}$	photoluminescence intensity parallel to fiber axis [grey level], p. 94
$I_{\perp}$, $I_{PL\perp}$	photoluminescence intensity perpendicular to fiber axis [grey level], p. 94
I_{back}	background intensity (background image) [grey level], p. 51
I_{dark}	reference intensity (dark image) [grey level], p. 51

I_{laser} intensity of laser incident light [grey level], p. 90
I_s intensity of the light transmitted through the fiber [grey level], p. 80
I_{sub} intensity of the light transmitted through the substrate [grey level], p. 80
I_{trans} X-ray transmitted intensity [grey level], p. 51
i index [dimensionless]
i chain index in a sample of random walks [dimensionless], p. 36
j index [dimensionless]
j probability band index [dimensionless], p. 36
j Cartesian axis or position [m], p. 60
K constant prefactor [dimensionless], p. 113
k velocity increase parameter [dimensionless], p. 22, 71
k_0 velocity increase modified parameter [dimensionless], p. 115
k_1 velocity increase modified parameter [dimensionless], p. 116
k_B Boltzmann constant [$= 1.38 \cdot 10^{-23}\ \mathrm{J\,K^{-1}}$], p. 32
k_{cap} velocity parameter for a capillary dominated flow [dimensionless], p. 71
k_G geometry constant of an object in a flow [dimensionless], p. 39
k_l tensile force constant of a covalent bond [$\mathrm{N\,m^{-1}}$], p. 144
k_{vis} velocity parameter for a viscosity dominated flow [dimensionless], p. 71
k_θ angular force constant of a covalent bond [$\mathrm{N\,m\,rad^{-1}}$], p. 144
L fiber fragment length [m], p. 111
L_{cor} correlation length in the amorphous region of a solid polymer [m], p. 25
L_{cryst} thickness of a polymer crystallite [m], p. 25
LD linear optical dichroism [arb. un.], p. 99
LD_{PL} photoluminescence linear optical dichroism [arb. un.], p. 99
L_{FIT} power fitted length of a fiber fragment [m], p. 112
L_n number-average (mean) length of a fiber fragment [m], p. 111
L_w weight-average length of a fiber fragment [m], p. 111
L_f fiber length [m], p. 150
ΔL_f change in fiber length due to surface tension [m], p. 150
L_s length of an extended chain segment [m], p. 145
δL_s longitudinal deflection of an extended chain segment [m], p. 145
l length variable [m], p. 58
l distance between two entanglements along a chain [m], p. 114
l covalent bond length [m], p. 131
l_0 initial distance between two entanglements along a chain [m], p. 114
l_k Kuhn segment length (or Kuhn length) [m], p. 132
l_p persistence length [m], p. 131
l_s distance between chain ends where the jet breaks [m], p. 114
M_{sc} molar mass (molecular weight) of a subchain [$\mathrm{kg\,mol^{-1}}$], p. 143
M_n number-average (mean) molar mass (molecular weight) [$\mathrm{kg\,mol^{-1}}$], p. 107
M_w weight-average molar mass (molecular weight) [$\mathrm{kg\,mol^{-1}}$], p. 19
m effective subchain mass [kg], p. 58

m slope of the external profile of a jet [dimensionless], p. 71

m scaling exponent [dimensionless], p. 137

N number of monomers or rigid chain elements in a polymer chain (degree of polymerization of a linear chain) [dimensionless], p. 30

N_{beads} number of spherical beads in a rigid chain segment [dimensionless], p. 91

N_e number of monomers in an entanglement strand [dimensionless], p. 98

$N_e(1)$, N_{e1} number of monomers in an entanglement strand in a melt [dimensionless], p. 98, 114

N_k number of monomers (Kuhn segments) in a chain [dimensionless], p. 132

N_{net} number of subchains in a network [dimensionless], p. 46

N_s number of monomers in a subchain [dimensionless], p. 43

N_{sT} number of rigid chain segments in a thermal blob [dimensionless], p. 98

N_{sc} number of subchains per unit volume [m^{-3}], p. 143

n monomer index in a chain [dimensionless], p. 36

n subchain index in a network [dimensionless], 43

n aspect ratio of a rigid chain segment [dimensionless], p. 91

n number of backbone bonds in a polymer chain [dimensionless], p. 132

n_e number of entanglements along a chain [dimensionless], p. 110

n_k number of backbone bonds in a Kuhn segment [dimensionless], 152

O orientation parameter [dimensionless], p. 38

P, P_1 derivative substitutions [dimensionless], p. 58

P probability, probability distribution, probability density [dimensionless]

Pe Péclet number [dimensionless], p. 71

P_e number of chains in a single strand volume in a melt [dimensionless], p. 98

$P_x^{\pm}$ stepping probability in any of the 6 Cartesian directions in a random walk [dimensionless], p. 33

$P(x)$, $P(r)$ Gaussian distribution of the end-to-end distance of a polymer chain [dimensionless], p. 136

$P(\vec{R}, N)$ probability distribution of the end-to-end vector of a polymer chain [dimensionless], p. 134

$P(R, N)$ probability distribution of the end-to-end distance of a polymer chain [dimensionless], p. 134

$P(R/R_0)$ probability density of the relative end-to-end distance of a polymer chain [dimensionless], p. 36

$P(z,\rho,\varphi)$ Mathcad function for stepping probability in a random walk simulation [dimensionless], p. 33

p parameter in a hyperbolic fit of the jet velocity [dimensionless], p. 71

Q partition function [dimensionless], p. 32

Q, Q_F volumetric flow rate of a jet [$m^3\ s^{-1}$], p. 19, 68

R end-to-end distance (radius, length) of a polymer chain [m] or [step], p. 32

R AFM tip radius [m], p. 85

$\vec{R}$ end-to-end vector of a polymer chain [m] or [step], p. 37

R_0 root-mean-square end-to-end distance of an ideal chain [m] or [step], p. 25

R_{cap} core radius of a core-shell nanofiber [m], p. 23

Re Reynolds number [dimensionless], p. 68

R_F root-mean-square end-to-end distance of a real chain [m], p. 135

R_g radius of gyration of a polymer chain [m], p. 25

R_{gas} gas constant [= 8.31 J mol^{-1} K^{-1}], p. 143

$R(I,N)$ Mathcad function for random walking in a random walk simulation [dimensionless], p. 36

R_{max} fully extended length of a polymer chain [m] or [step], p. 37

R_n radial position in a jet at subchain n of the polymer network [m], p. 57

R_P radius of a polymer network in a jet [m], p. 59

R_x end-to-end distance of a polymer chain in direction x [m] or [step], p. 37

r jet radius [m] or [step], p. 22

r end-to-end distance of a polymer chain [m], p. 43

r radial position with respect to a jet central axis [m], p. 52

r_0 initial radius of a jet [m] or [step], p. 22

r_J jet radius [m] or [step], p. 44

r_P radius of a polymer network in a jet [m] or [step], p. 48

r_{pol} optical polarization ratio of a fiber [dimensionless], p. 93

S entropy [J K^{-1}], p. 142

S_f surface area of a fiber [m^2], p. 150

ΔS_f change in the surface area of a fiber due to surface tension [m^2], p. 150

s surface density of an electric charge [C m^{-2}], p. 22, 107

s velocity gradient (strain rate) of a flow [s^{-1}], p. 40

s_c critical velocity gradient (strain rate) of a flow [s^{-1}], p. 138

T temperature [K]

T optical transmission (transmittance) [dimensionless], p. 62

T single modulation period in SNOM [s], 100

T_{exp} measured X-ray transmission of a jet [dimensionless], p. 51

T_{sim} simulated X-ray transmission of a jet [dimensionless], p. 51

T_g glass transition temperature [K]

T_m melting temperature [K]

t time [s]

Δt time interval between X-ray exposures [s], p. 69

U effective potential [J], p. 32

U internal energy of a polymer chain [J], p. 142

U, $U(r)$ field potential, potential at position r [J], p. 134

U_{st} energy density due to surface tension [N m^{-2}], p. 150

U_x potential at position x [J], p. 33

U_ε strain energy density of a polymer network [J m^{-3}], p. 143

V_f fiber volume [m^3], p. 150

ΔV_f change in fiber volume due to surface tension [m^3], p. 150

v excluded volume parameter [m^3], p. 97

v_0 volume of a rigid chain segment [m^3], p. 98

v jet velocity [m s^{-1}] or [step s^{-1}], p. 21

$\vec{v}$	velocity vector field [m s^{-1}], p. 73
v_0	initial velocity of a jet [m s^{-1}] or [step s^{-1}], p. 21
v_c	jet velocity estimated by volume conservation assumption [m s^{-1}], p. 72
v_n	jet velocity at subchain n in the polymer network [m s^{-1}] or [step s^{-1}], p. 43
v_{n0}	jet velocity at the origin of the first subchain [m s^{-1}] or [step s^{-1}], p. 43
v_p	jet velocity measured by particle tracing [m s^{-1}], p. 72
v_s	jet velocity where the jet breaks [m s^{-1}], p. 114
v_x	jet velocity in direction x [m s^{-1}] or [step s^{-1}], p. 44
v_{x0}	initial jet velocity in direction x [m s^{-1}] or [step s^{-1}], p. 44
$\hat{v}_z$	normalized jet velocity [m s^{-1}], p. 58
x	scaling exponent [dimensionless], p. 24, 114
x	Cartesian axes system or position z,ρ,φ [m] or [step], p. 33
x	horizontal position of an image pixel [pixel], p. 51
x	distance from the free end of a jet fragment [m], p. 107
x	relative end-to-end distance of a polymer chain [m], p. 136
y	vertical position of an image pixel [pixel], p. 51
z	Cartesian axis or position [m] or [step], p. 33
z	position along a jet [m], p. 22
z_0	parameter determining the scale of velocity increase [m], p. 57
$\bar{z}$	relative position along a jet [dimensionless], p. 40
$\hat{z}$	normalized position along a jet [dimensionless], p. 58
z_n	position along a jet at subchain n in the polymer network [m], p. 57
z_s	position along a jet where the jet breaks [m], p. 113
$z_{stretch}$, z_s	position along a jet where the polymer network approaches full extension [m], p. 58, 91
α	parameter used in the theoretical modeling [dimensionless], p. 49
α	X-ray absorption coefficient of a jet [m^{-1}], p. 52
α	optical absorption coefficient of a fiber [m^{-1}], p. 80
α	scaling exponent of the degree of polymerization [dimensionless], p. 110
$\Delta\alpha$	change in the X-ray absorption coefficient of a jet [m^{-1}], p. 52
α_0	initial X-ray absorption coefficient of a jet [m^{-1}], p. 52
α_{abs}	absorption term in an apparent X-ray absorption coefficient [m^{-1}], p. 69
α_{app}	apparent X-ray absorption coefficient of a jet [m^{-1}], p. 52
$\Delta\alpha_{app}$	change in the apparent X-ray absorption coefficient of a jet [m^{-1}], p. 52
α_{max}	maximal optical absorption coefficient of a fiber [m^{-1}], p. 80
α_{rel}	relative optical absorption coefficient of a fiber [dimensionless], p. 80
α_{scat}	scattering term in an apparent X-ray absorption coefficient [m^{-1}], p. 52
α_{sim}	simulated X-ray absorption coefficient of a jet [m^{-1}], p. 52
β	scaling exponent of the jet position [dimensionless], p. 22, 70
β	parameter used in the random walk simulation [dimensionless], p. 61
γ	surface tension [N m^{-1}], p. 19
γ	optical dichroic ratio [dimensionless], p. 90
γ_{max}	maximal optical dichroic ratio [dimensionless], p. 90

γ_{rel} relative optical dichroic ratio [dimensionless], p. 90

δ distance of an X-ray diffraction peak from the jet boundary [m], p. 69

δ AFM tip deflection [m], p. 80

δ bending deflection of a suspended nanofiber [m], p. 147

ε strain [dimensionless], p. 63

$\dot{\varepsilon}$ strain rate [s^{-1}], p. 63

$\bar{\varepsilon}$ dielectric permittivity of the medium around a jet [$F\,m^{-1}$], p. 19

$\Delta\varepsilon$ energy difference between trans and gauche states [J], p. 131

ε_m relative permeability of the medium around a jet [dimensionless], p. 22, 71

ε_{max} maximal elastic strain [dimensionless], p. 151

ε_p mass absorption coefficient of a polymer [$m^2\,kg^{-1}$], p. 52

ε_s mass absorption coefficient of a solvent [$m^2\,kg^{-1}$], p. 52

η viscosity of a polymer solution [Pa s], p. 22

$[\eta]$ intrinsic viscosity of a polymer solution [$m^3\,kg^{-1}$], p. 117

η_0 zero shear rate viscosity of a polymer solution [Pa s], p. 20

η_s solvent viscosity [Pa s], p. 39

η_{sp} specific viscosity of a polymer solution [dimensionless], p. 98

θ covalent bond tetrahedral angle [rad], p. 131

θ angle between a chain segment end-to-end vector and the z axis [rad], p. 38

θ_{cr} coil stretch transition criterion [dimensionless], p. 63

κ curvature of the external profile of a jet [m^{-1}], p. 71

κ quality of a solvent blend [dimensionless], p. 112

κ_0 parameter used in the theoretical modeling [dimensionless], p. 59

$\kappa(z)$ function used in the theoretical modeling [dimensionless], p. 59

λ, λ_{exc} wavelength of optical excitation [m], p. 82

λ deformation factor of a subchain (strand) [dimensionless], p. 118

μ zero shear rate viscosity of a polymer solution [Pa s], p. 68

ν Flory scaling exponent [dimensionless], p. 58

ν Poisson ratio [dimensionless], p. 151

ν_{fiber} Poisson ratio of a fiber [dimensionless], p. 85

ν_t Poisson ratio of an AFM cantilever [dimensionless], p. 85

ξ average mesh size (subchain length) of a polymer network in a semi-dilute solution [m] or [step], p. 42

ξ_0 initial subchain length [m] or [step], p. 43

$\xi_{\parallel}$ elongation of a subchain in the longitudinal direction [m], p. 58

$\xi_{\perp}$ elongation (i.e., contraction) of a subchain in the radial direction [m], p. 59

ξ_n elongation of subchain n in a polymer network [m] or [step], p. 43

ξ_{max} fully extended length of a subchain [m] or [step], p. 49

ξ_x elongation of a subchain in direction x [m] or [step], p. 47

ρ material density [$kg\,m^{-3}$]

ρ Cartesian axis or position [m] or [step], p. 33

ρ normalized radial position [dimensionless], p. 59

ρ_0 normalized initial radial position [dimensionless], p. 59

ρ_p polymer density [kg m^{-3}], p. 63
ρ_p particle density [kg m^{-3}], p. 68
ρ_s solvent density [kg m^{-3}], p. 63
ς self-simulated variable in the theoretical modeling [dimensionless], p. 58
σ electric conductivity of a polymer solution [S m^{-1}], p. 22
σ absorption cross-section at the incident laser light [m], p. 82
σ stress or force per unit area [Pa], p. 145
τ, τ_{relax} single chain relaxation time in a polymer solution [s], p. 63, 137
τ_0 monomer relaxation time in a polymer solution [s], p. 40
τ_e solvent evaporation time [s], p. 23
τ_t electric shear stress [N m^{-2}], p. 22
ϑ relative free volume between chains [dimensionless], p. 152
φ Cartesian axis or position [m] or [step], p. 33
φ scaling exponent of the relative jet radius [dimensionless], p. 74
φ covalent bond torsion (rotation) angle [rad], p. 131
ϕ , φ polymer volume fraction in a solution [dimensionless], p. 80
ϕ *, φ* crossover volume fraction in a solution [dimensionless], p. 107
ϕ_e , φ_e entanglement volume fraction in a solution [dimensionless], p. 107
χ ratio of the initial jet length to the nozzle diameter [dimensionless], p. 19
χ Flory's interaction parameter [dimensionless], p. 91
Ω number of possible coil configurations for a given extension [dimensionless], p. 142

Abbreviations

1D one-dimensional
3D three-dimensional
AFAM atomic force acoustic microscopy, p. 149
AFM atomic force microscopy, p. 17
APS advanced photon source, p. 50
B bead, p. 109
CF continuous fiber, p. 109
CFB continuous fiber with beads-on-string, p. 109
$CHCl_3$ chloroform, p. 62
ClPP chlorinated polypropylene, p. 146
CNT carbon nano tube, p. 24
DCM dichloromethane, p. 57
DMF dimethyl formamide, p. 18

DMSO	dimethyl sulfoxide, p. 91
DMTA	dynamic mechanical thermal analysis, p. 17
FEI	field emission system, p. 85
FFT	fast Fourier transform, p. 69
LDPE	low-density polyethylene, p. 94
MEH-PPV	poly[2-methoxy-5-(2-ethylhexyl-oxy)-1,4-phenylene-vinylene], p. 15
PCL	polycaprolactone, p. 57
PE	polyethylene, p. 130
PEM	photoelastic modulator, p. 90
PEO	poly(ethylene oxide), p. 15
PET-*co*-PEI	poly(ethylene terephthalate-co-ethylene isophthalate), p. 20
PEVA	poly(ethylene-co-vinyl acetate), p. 149
PL	photoluminescence, p. 79
PM	polarization modulation, p. 100
PMMA	poly(methyl metacrylate), p. 15
PMT	photomultiplier, p. 90
PP	polypropylene, p. 130
PS	polystyrene, p. 24
PVA	poly(vinyl alcohol), p. 146
RW	random walk, p. 30
SAED	small-area electron diffraction, p. 79
SANS	small angle neutron scattering, p. 17
SAW	self-avoiding (random) walk, p. 135
SAXS	small angle X-ray scattering, p. 17
SEM	scanning electron microscope, p. 17
SF	short fiber, p. 109
SFB	short fiber with beads-on-string, p. 109
SMFM	shear modulation force microscopy, p. 147
SNOM	scanning near-field optical microscopy, p. 15, 79
TEM	transmission electron microscope, p. 17
THF	tetrahydrofuran, p. 18
WAXS	wide angle X-ray scattering, p. 17

1. Introduction

Structures of nanoscale size, one millionth of a millimeter (10^{-9} m, or 1 nm), reveal unique size-dependent mechanical, electrical and optical properties, since their size is of the same order of magnitude as the size of the atoms and molecules composing them.[6-15] Polymers exhibit such behavior even on higher scales due to their large molecular size and flexible conformation.

Polymers are very long molecules (macromolecules or chains), whose backbone is constructed from many successive carbon-carbon chemical bonds. When the chains are extended and aligned with respect to each other, the polymer can theoretically achieve strength and rigidity two orders of magnitude higher than those found in ordinary commercial plastic materials,[16-19] thereby indicating the ultimate potential of polymers as engineering materials. However, due to flexibility in bond rotation, these macromolecules tend to coil in random conformations and create entangled networks when dissolved in solvent,[20-22] with a resultant reduction in their strength and rigidity after solidification.

One of the more accessible techniques used to create nanostructures is electrospinning, which has attracted considerable interest over the past fifteen years, both within the academic community and among those engaged in commercial exploitation. Electrospinning found many new and prospective applications in the fields of life sciences, tissue engineering, filter media, cosmetics, clothing, nanosensors and more.[23, 24]

An electrospinning jet is created when a polymer solution is drawn from a capillary and stretched by the force of a strong electric field, producing very thin fibers – nanofibers – of diameters typically ranging from 50 nm to 1000 nm (1 μm).[23-26] The high extension rate of the polymer network during electrospinning,[27-33] and the extremely rapid evaporation of the solvent from the jet,[34-37] are the two dominant factors that affect the morphology and nanostructure of electrospun fibers.

Recent experiments found that the strength and elastic properties of electrospun nanofibers are highly dependent on their diameter and chain size (i.e. the polymer molar mass).[6-10, 14, 15] The smaller the nanofiber diameter (especially below a certain crossover radius), and the larger the polymer chain size, the more rigid and strong the nanofiber becomes.

It has been common knowledge for many years that polymer fibers of microscale size (10^{-6} m) have improved strength and elasticity when post-processed by mechanical drawing or rolling.[38] The phenomenon is similar – in both the nano- and micro-process the random coils of the polymer macromolecules are stretched along the fiber's longitudinal axis, attaining a higher degree of alignment, thereby approaching their ultimate mechanical properties. However, in nanofibers the nanostructure is created as part of the process and not by post-processing, and additional factors are involved due to supramolecular structures that are of the same order of magnitude as the fiber's diameter.[10, 39, 40]

Hence, the motivation for this research is better understanding of the reasons for the unique properties of electrospun polymeric nanofibers, a valuable knowledge for future designs and applications. Two interrelated research questions were posed, of which the first is in the focus of this thesis: what is the effect of electrospinning on the polymer matrix nanoscale structure? and, what is the mechanism by which this nanostructure impacts the mechanical properties?

The first question involves the research fields of polymer physics and electrospinning. Polymer physics studies macromolecule and network conformations and properties, in both the solution and solid states, extensively applying scaling concepts and statistical methods. Electrospinning is emerging as a research and engineering field in its own right, involving basic study of the complex static and dynamic phenomena, and development of measurement and fabrication techniques.

The second question involves the research field of mechanical properties of polymers, specifically electrospun polymeric nanofibers, which extends from nanoscale physics to the macroscale investigation of bulk properties. The relevant literature on electrospinning and nanofibers is reviewed in Chapter 2. Background on the physics of polymer conformations and elasticity is provided in Appendix A, and a review of recent experimental and theoretical observations of nanofiber size-dependent elasticity is presented in Appendix B.

In view of the broadness of the fields of research, the presented thesis focuses on the first research question, specifically the dynamic behavior of the polymer network in an electrospinning jet, and the resulting solid nanostructures. The thesis research methods and findings are generally applicable to strong extensional flows, of which electrospinning is a representative test bed. Although the effects of the nanostructure on fiber elasticity (the second research question) are not within the scope of this thesis, their possible influence on elasticity is discussed.

The research goals and outline are presented in Chapter 3, and the theoretical and experimental methods specifically developed for the research are described in Chapter 4. The detailed description of the research and its results are presented in five publications in Chapter 5, and are discussed and concluded in Chapter 6. The research outline and main findings are depicted in Figure 1-1.

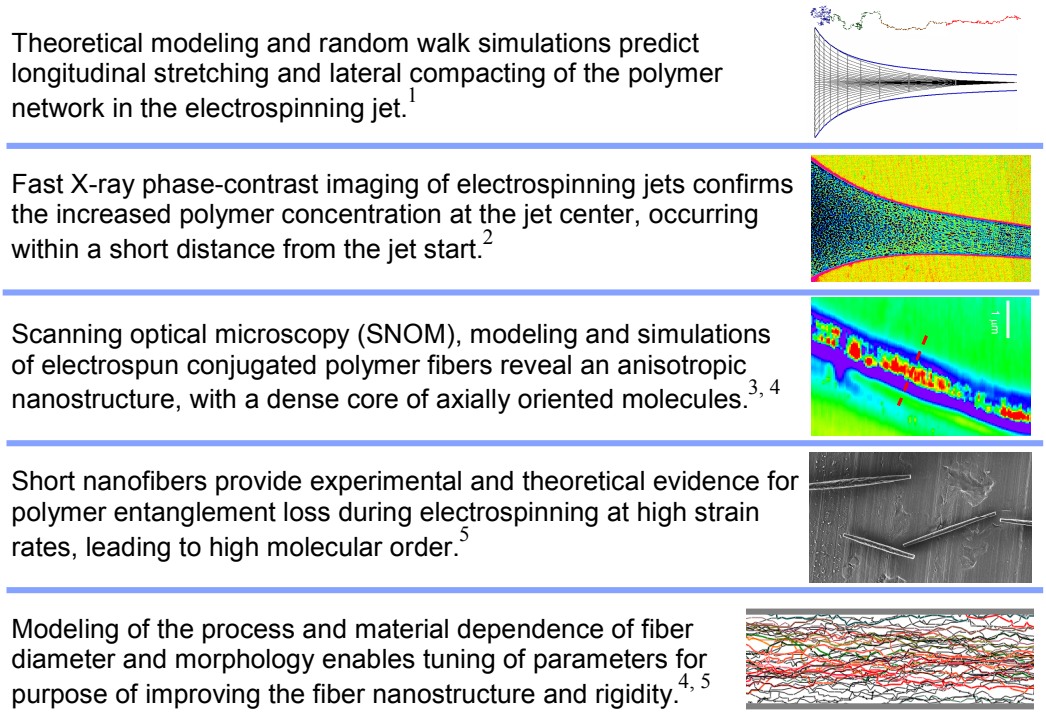

Figure 1-1. Research outline and main findings. The pictures are (top to bottom): random walk simulation of network stretching and compacting in an electrospinning jet; X-ray 2-pulsed image of a PEO-water solution jet containing silica microbeads; optical polarization modulation map of an MEH-PPV electrospun fiber (red indicates molecular alignment along the fiber axis); electrospun short PMMA nanofibers; illustration of the solid nanostructure created by high strain rate electrospinning.

2. Bibliography review

This chapter reviews the literature relevant to this research, focusing on the electrospinning method for fabricating nanofibers, dynamics of a polymer solution jet, and nanostructure and elasticity of nanofibers.

The basic relevant concepts of the science of polymer physics are described in Appendix A (Sections A.1 through A.3), including single chain conformation, polymer networks and dynamics, and the coil stretch transition phenomenon. The scientific foundation for the mechanical properties of solid polymers is described in Section A.4.

A detailed review on the size-dependent elasticity of polymeric nanofibers, including experimental evidence and suggested physical mechanisms, is provided in Appendix B.

2.1 Electrospinning process and nanofibers

Electrospinning, or electrostatic spinning, is a convenient and industrially-scalable technique for fabricating polymer nanofibers, at diameters ranging typically from 50 to 1000 nm. Due to their nanoscale size and unique mechanical, electrical and optical properties, nanofibers are applied in diverse fields such as life science, tissue engineering, filter media, cosmetics, clothing, and nanosensors (Figure 2-1).[23, 24]

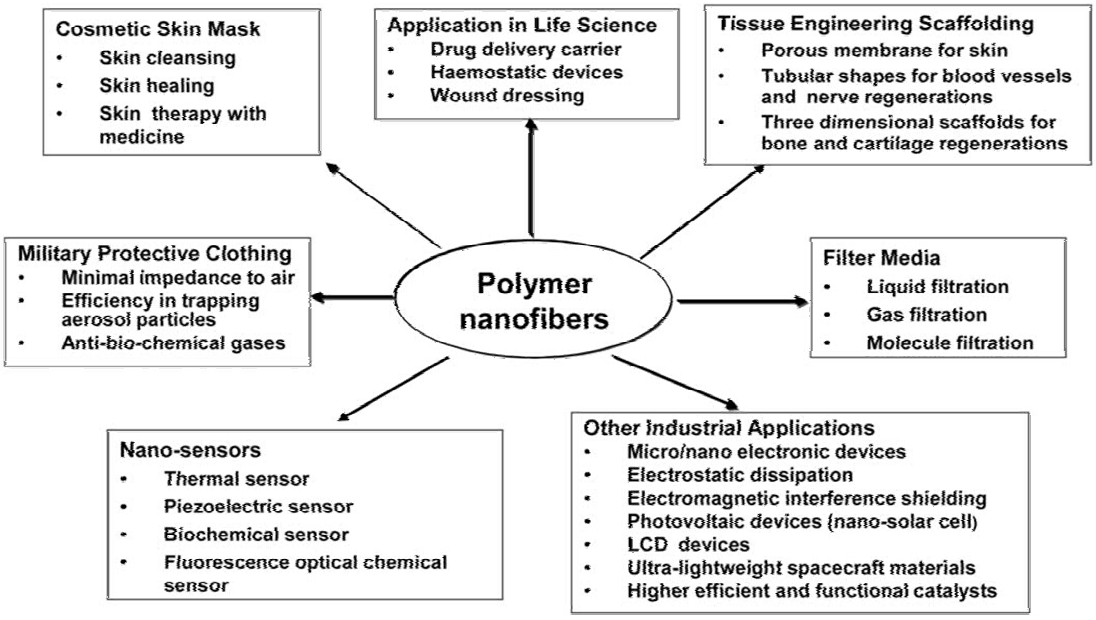

Figure 2-1. Actual and potential applications of electrospun polymer nanofibers, spanning life sciences and engineering.[23]

Though discovered and patented by J. F. Cooley and W. J Morton a long time ago [US patent # 692631, 1902], and further researched and developed by G. Taylor[41] and others during the 20th century, the process gained considerable focus in the last 10-15 years due to the nanotechnology revolution, generating a surge of publications and patents on the subject. Several text books and articles by Andrady[24], Stanger[25], Huang[23], and Gogotsi[26] provide good overview of the process, the science behind it, the control of its parameters, and its applications.

The **process** consists of (Figure 2-2) a viscous polymer solution, pumped into a syringe and drawn into a capillary needle, subjected to an electric field, typically of 1-2 kV/cm, that draws the solution out of the needle into a cone-shaped drop (Taylor cone), and sprays it as a jet towards a ground plate (collector). The distance between the electrodes is typically 10-20 cm. The solvent evaporates rapidly and the nanofiber is almost dry when reaching the ground plate, where it is collected by various techniques, creating a mat with ordered or arbitrarily-oriented nanofibers. Examples of typical materials and process parameters are shown in Table 2-1.

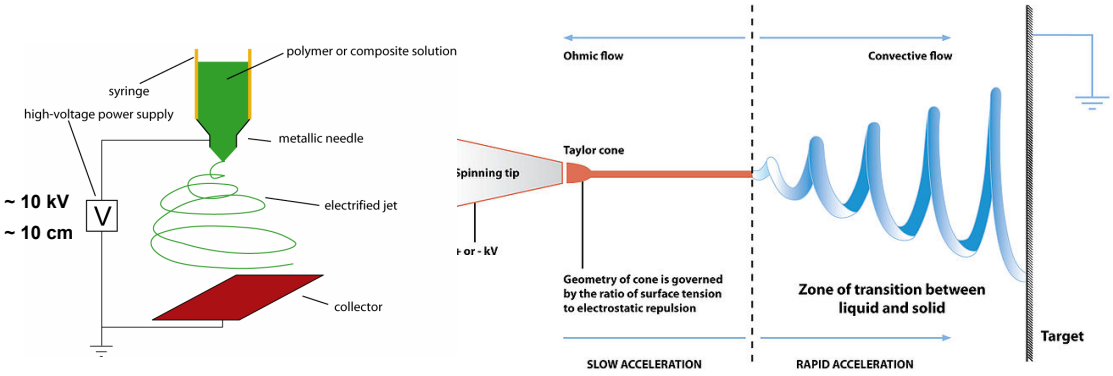

Figure 2-2. A schematic of the electrospinning process, showing the basic equipment and the creation of the jet.[42, 43]

Some of the experimental tools and methods used for characterization of polymers in general (see, for example, the books by Campbell[44] and Roe[45]) and electrospun nanofibers in particular[24] are: in-process imaging of the jet (optical, laser or X-rays) to measure its shape and velocity; scanning electron microscope (SEM) and transmission electron microscope (TEM) electron microscopy imaging to measure the nanofiber morphology; scattering techniques, such as wide angle X-ray scattering (WAXS), small angle X-ray scattering (SAXS), and small angle neutron scattering (SANS), to measure the degree of crystallinity and molecular orientation; atomic force microscopy (AFM) to measure shape, size and elastic moduli and to perform tensile and bending tests; and dynamic mechanical thermal analysis (DMTA) tensile

testing equipment to measure the elastic moduli, ultimate strength, viscoelastic properties, and glass transition temperature. Tests can be performed on single nanofibers, a difficult task requiring micro-manipulation, or on dense mats of collected nanofibers.

Table 2-1. Typical materials and process parameters used in electrospinning. Based on ref[25].

Parameter	Polyethylene oxide (PEO)	Polystyrene (PS)	Polypropylene (PP)
Solvents	Water, Acetone Chloroform, Ethanol, N,N-Dimethyl-formamide Acetic acid Water, Methanol Water, Ethanol	DMF, Toluene Carbon Disulfide (CS2) Chloroform, THF, Methylethylketone Acetic acid	Melt at 285°C
Concentration, %	10	20	-
Molar mass, g/mol	400,000	200,000 – 300,000	200,000
Voltage, kV	10 – 20	30	20
Distance, cm	15	15	4
Electric field, kV/cm	0.5 – 1	1	5

The quality of the electrospun nanofiber strongly depends on the rheological and electrical properties of the polymer solution and on the process parameters (electrostatic field, flow rate, ambient conditions). Demir et al.[46] investigated the effects of electric field, temperature, conductivity and viscosity of the solution on polyurethane electrospinning process, and the morphology and properties of the nanofibers obtained, and concluded that the solution viscosity, i.e. its concentration and temperature, is the dominant factor. Hsu[47] provides examples of morphologies that can be obtained by electrospinning (Figure 2-3), demonstrating how beads, and fibers with uneven diameter, can be formed at low polymer molar masses and low solution concentrations.

The structural morphology of nanofibers depends on the balance between the strong stretching, caused by the flow's high strain rate, and the rapid evaporation of the solvent. Rapid evaporation can adversely affect the polymer matrix macrostructure, by inducing a heterogeneous and porous fiber structure.[34, 35]

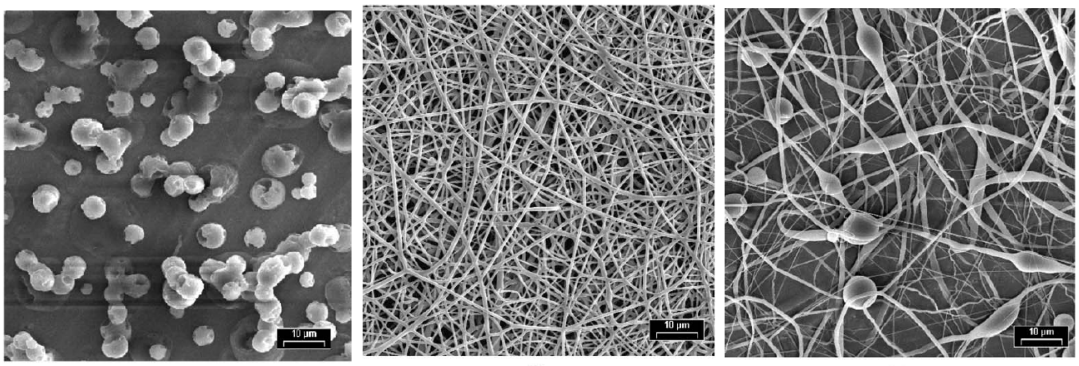

(a) (b) (c)

Figure 2-3. Range of structures that can be produced by electrospinning of poly(ε-caprolactone): (a) beads, (b) fibers, and (c) beads on string.[47]

A key objective in fabricating nanofibers is to achieve a desired fiber **diameter** by proper adjustment of the process parameters. Fridrikh et al.[48] developed an equation governing the nanofiber diameter D

$$D = \left[\gamma \bar{\varepsilon} \frac{Q_F^2}{I_E^2} \frac{2}{\pi(2\ln\chi - 3)} \right]^{1/3}, \tag{2.1}$$

where γ is the surface tension, $\bar{\varepsilon}$ is the dielectric permittivity of the outside medium, Q_F is the volumetric flow rate, I_E is the electric current carried by the fiber, and χ is the ratio of the initial jet length to the nozzle diameter. However, since I_E and χ are in themselves dependent on the electrospinning parameters, this equation is not useful for predicting the outcome of the process.

Colby et al.[49] observed that the dependence of the polymer solution viscosity on the solution concentration exhibits three distinct concentration regions: dilute, semidilute unentangled, and semidilute entangled, expanding the definitions of Figure A-7. Gupta et al.[28] measured the dependence of PMMA solution viscosity on the relative concentration c/c^* [c^* is the overlap concentration, defined in Equation (A.12)], and found the following regions: dilute ($c/c^* < 1$), semidilute unentangled ($1 < c/c^* < 3$), and semidilute entangled ($c/c^* > 3$) (Figure 2-4). A semidilute entangled solution contains entangled polymer chains, ensuring the elastic behavior of the jet and continuous nanofibers. Conversely, in a semidilute unentangled solution, the polymer chains are not sufficiently entangled, resulting in beads rather than continuous nanofibers. Additionally, Gupta observed the dependence of the fiber diameter on concentration (Figure 2-5).

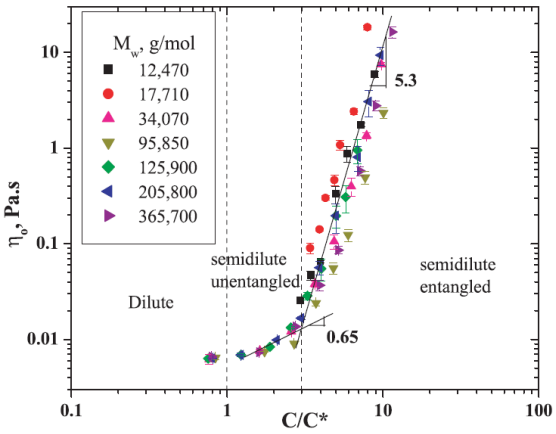

Figure 2-4. Zero shear rate viscosity η_0 versus relative concentration c/c^*, for different molar masses M_w of poly(methyl methacrylate) (PMMA).[28]

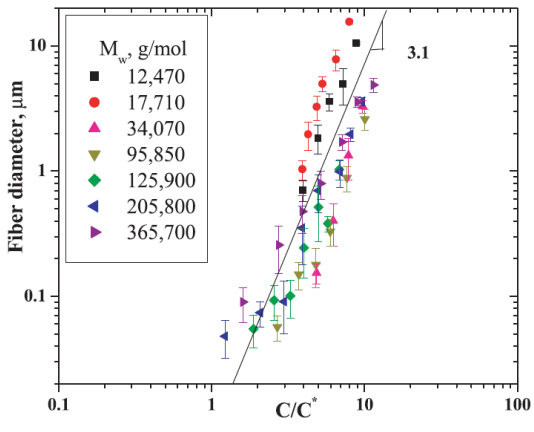

Figure 2-5. Variation of fiber diameter versus relative concentration c/c^*, for different molar masses M_w of poly(methyl methacrylate) (PMMA).[28]

Based on these experiments, Gupta derived the following scaling relationships for the dependencies of the fiber diameter D on the relative concentration c/c^* and on the zero shear rate viscosity (viscosity at very low strain rate) η_0

$$D \sim \left(\frac{c}{c^*}\right)^{3.1} \quad \text{and} \quad D \sim (\eta_0)^{0.72}, \tag{2.2}$$

in agreement with Demir et al.[46] who measured $D \sim c^3$ using polyurethane, and Mckee et al.[50] who measured $D \sim c^{3.1}$ using linear and branched PET-*co*-PEI copolymers. These results suggest a useful universal scaling law, but do not provide a quantitative physical explanation for this dependence. Other experimental observations showed that the fiber diameter is smaller at higher electric field intensities[51, 52], lower flow rates[53], and larger gap distances between the electrodes[54].

2.2 Jet dynamics and solvent evaporation

The jet undergoes substantial **stretching** during the electrospinning process. The jet velocity and diameter were measured as a function of the distance x along the jet by Han et al.[27] (Figure 2-6) and by Bellan et al.[31] (Figure 2-7), using in-process optical microscopy. The observed region started at the Taylor cone, and extended up to 5mm (Han) and 1.2 mm (Bellan), as shown on the attached photographs. The maximal measured jet velocity v within the observed region was 0.8 m/s (Han) and 0.35 m/s (Bellan), while the maximal jet strain rate (velocity gradient, dv/dx) can be estimated from the graphs as 300 s^{-1} (Han) and 500 s^{-1} (Bellan), demonstrating a non-constant gradient. Han also evaluated the viscoelastic relaxation time [see definition

in Equation (A.14)] to be in the range of 3 - 8 ms. The jet travel time between the electrodes, estimated by integrating $t = \int dx / v$, is 170 ms (Han) and 80 ms (Bellan).

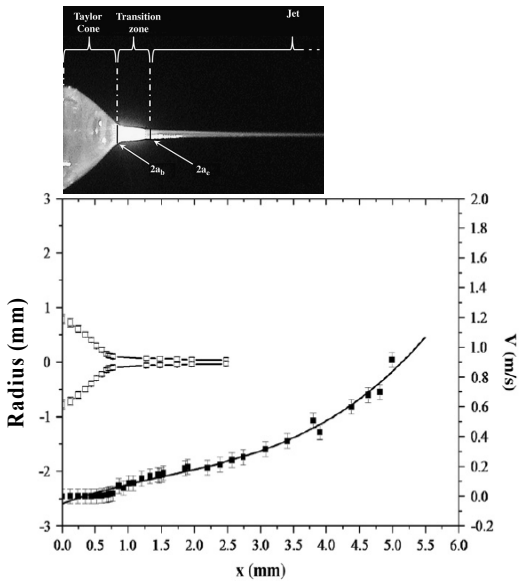

Figure 2-6. Optical microscopy measurement of the jet profile and velocity, versus the *x* position along the jet: poly(ethylene oxide) (PEO), M_W = 400,000 g/mol, 6 wt% solution in water.[27]

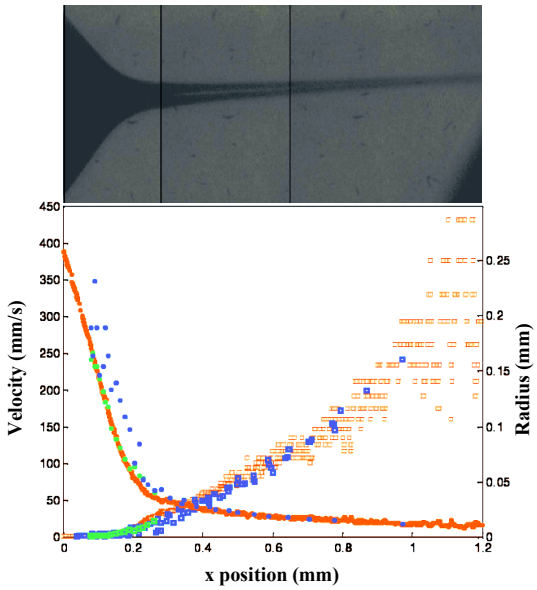

Figure 2-7. Optical microscopy measurement of the jet profile and velocity , versus the *x* position along the jet: poly(ethylene oxide), M_W = 100,000 g/mol, 20 wt% solution in water.[31]

Reneker et al.[29, 30] investigated also the region beyond the initial straight jet, using a poly(ethylene oxide) aqueous solution, and found that electrical bending (whipping) instability (similar to Figure 2-2) causes the jet to form a sequence of smoothly curved loops, generating a considerable elongation of the fiber, with an average strain rate of 10^3 s^{-1}. The theoretical value of the strain rate was estimated as 10^5 s^{-1}; however, the measured value was much lower due to evaporation and solidification. With relaxation time for this polymer solution equaling 10^{-2} s, the scaling expression $s\tau$ from Equation (A.15) was estimated as 10^1-10^3, much greater than 0.5, indicating that the polymer macromolecules were stretched significantly.

Analysis of electrically driven fluid jets has shown that the jet reaches an asymptotic regime sufficiently far from its exit. In this region, the jet diameter can be expressed by a power law of the form $r \sim z^{-\beta}$, where z is the distance from the exit and β is a positive exponent.[55-59] The exponent β was found to vary between 0.25 and 1. For example, running the model developed by Reneker et al.[30], we observed a good asymptotic fit to a power law, with $\beta \cong 0.25$ over a wide range of the dimensionless parameters (voltage, elastic modulus and electric charge).

The jet hydrodynamic equations were solved by Reznik et al.[59, 60] for Newtonian flow. The asymptotic local radius r and longitudinal velocity v of the jet were calculated:

$$\frac{r}{r_0} \cong \frac{1}{k}\left(\frac{z}{r_0}\right)^{-\beta}, \quad \text{and} \quad \frac{v}{v_0} \cong k^2\left(\frac{z}{r_0}\right)^{2\beta}, \tag{2.3}$$

where r_0 and v_0 are the jet's initial radius and velocity, respectively, $\beta = 1$ (hyperbolic shape), and k is a dimensionless parameter, of order 10^{-1} - 10^{1}, that determines the scale of velocity increase. The theoretical derivation yielded $k \cong \varepsilon_m^{1/6} r_0^{2/3} \sigma^{1/4} \eta^{-5/12} v_0^{-2/3} E^{5/6}$ (in CGS electrostatic units), where $\varepsilon_m \cong 1$ is the permeability of the medium (air), σ is the solution electric conductivity, η is the viscosity, and E is the electric field intensity.[58, 59]

We can obtain a rough approximation of k by using a simple scaling approach: the velocity gradient scales as $\nabla v \sim v_0 k^2 / r_0^2$ [Equation (2.3) with $\beta = 1$]; the upper bound for the electric charge surface density scales as $s \sim \varepsilon_m \sigma E$, assuming static conditions; the electric shear stress is therefore $\tau_t \approx sE \sim \varepsilon_m \sigma E^2$, producing a velocity gradient of $\nabla v \approx \tau_t / \eta \sim \varepsilon_m \sigma E^2 \eta^{-1}$; hence, $k \sim \nabla v^{1/2} v_0^{-1/2} r_0 \sim \varepsilon_m^{1/2} r_0^1 \sigma^{1/2} \eta^{-1/2} v_0^{-1/2} E^1$.

Closer to the jet start, Equations (2.3) take the form shown in Equations (5.1-1) and (5.1-2)[1], including also a radial velocity component. It should be noted that this model is an approximation since it assumes a Newtonian flow, in which the viscosity is constant, whereas the polymer solutions used in electrospinning are viscoelastic (i.e., non-Newtonian), exhibiting shear-thinning and shear-thickening phenomena (reduced and increased viscosity, respectively).

Reznik's model exhibits a non-constant velocity gradient, in agreement with the experiments by Han and Bellan described above. It is clear that the longitudinal velocity cannot go to infinity and is therefore expected to saturate at some point. Similarly, the jet radius cannot converge to zero and should saturate as well. Saturation can obviously occur during the process of solidification.

The substantial stretching of the polymer during electrospinning is subject to complex effects of solvent **evaporation**. Evaporation may cause early solidification of the outer part of the fiber, lessening the stretching effect, followed by partial relaxation of polymer chains in the inner part of the fiber that is still in solution state. The dynamics of this process is dependent upon the respective characteristic times of

evaporation and relaxation in a particular polymer solution, and on the opposite restraining effect of the polymer network caused by the high strain rate. Since Equations (2.3) do not account for evaporation, their validity is limited to the initial jet phase. Yarin et al.[30, 61] added the mechanism of solvent evaporation to their model, describing the jet dynamics throughout both the straight and bending-instability regions, and showed that evaporation has a major effect on the jet radius at the bending-instability region, while only a minor effect at the straight region.

Guenthner et al.[36] analyzed and simulated the solvent evaporation process in nanofibers, and found (Figure 2-8) that above a critical evaporation rate solid skin layers are formed, while the fiber core is still in solution state, and the process is governed by the competition between the solvent evaporation rate and its diffusion rate through the skin. Below a critical rate, evaporation is fairly uniform across the fiber cross-section. The process is accompanied by fiber shrinkage, and often, as a result of possible cavity in the core, by fiber buckling.

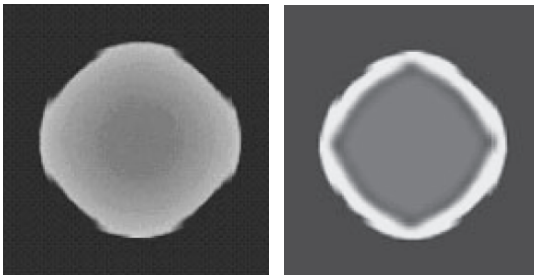

Figure 2-8. Simulation of solvent evaporation in nanofibers: (left) diffuse skin layer formation in relatively slow solvent loss, after 2.4 ms, and (right) sharp skin layer formation in rapid solvent loss, after 0.24 ms.[36]

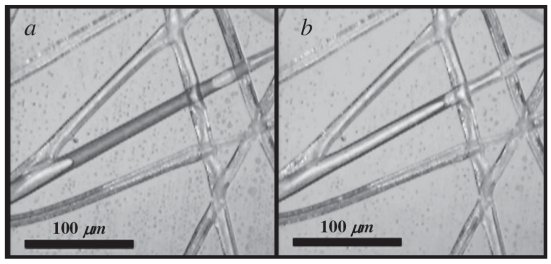

Figure 2-9. Electrospun tubular core-shell nanofibers: (a) entrapped slug bounded by two menisci, and (b) disappearance of this slug as a result of solvent evaporation.[62]

Arinstein et al.[62] provide experimental and analytical assessments of the evaporation process and time, for tubular core-shell[63] electrospun nanofibers, and argue, based on Guenthner's observations, that it is similar to the process of solid-core nanofibers (Figure 2-9). An estimate for the evaporation time τ_e is given by

$$\tau_e = \frac{R_{cap} d_w}{2D_s} \approx \frac{10^{-5}\,\mathrm{m} \cdot 0.5 \times 10^{-6}\,\mathrm{m}}{2 \cdot 5 \times 10^{-13}\,\mathrm{m^2/s}} \approx 5\,\mathrm{s}, \qquad (2.4)$$

where R_{cap} is the internal core radius, d_w the skin thickness, and D_s the solvent diffusion coefficient (through the skin). This value is deemed to be a lower bound for the actual evaporation time in a solid-core fiber, but is much higher than Guenthner's estimate.

In summary, the conformal behavior of polymer chains throughout the electro-spinning process is a non-equilibrium state that depends upon the combined dynamic effects of stretching, evaporation and relaxation.

2.3 Fiber nanostructure and elasticity

The experimental data presented in Section B.1 provides evidence for the dependence of the elastic modulus, a supposedly invariant intrinsic material property, on the fiber diameter.[6-10, 14, 15] Figure 2-10 summarizes the data from 6 different tests, in the form of fitted power curves, $(E/E_0 - 1) \sim D^{-x}$, where E is the elastic modulus, E_0 is the bulk elastic modulus, D is the fiber diameter, and x is a scaling exponent. The tensile modulus and the shear modulus behave similarly with respect to their diameter dependence. The scaling exponent was estimated from the data and vary from -1.3 to -2.1. Addition of CNT filler (in PS) and higher crystallinity (in Nylon 66) increase the diameter dependence (higher magnitude of the exponent).

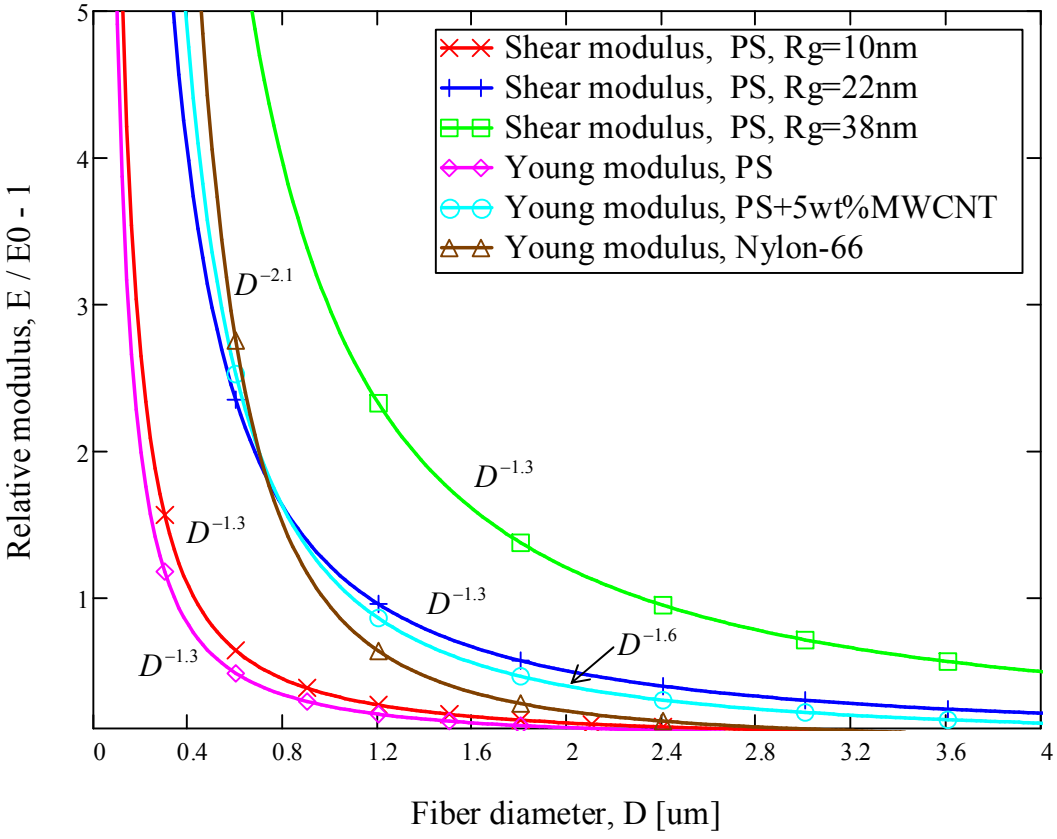

Figure 2-10. Scaling of relative moduli E/E_0-1 to fiber diameter D: fitted power curves of the experimental data from Figure B-4, Figure B-6 and Figure B-8. The fitting exponent of each test is indicated. Power fit error ±15%.

The modulus dependence on both the fiber diameter and the polymer chain length (expressed by the radius of gyration R_g), fitted from the data of Figure B-6, is:

$$\frac{E}{E_0} - 1 \sim \left(\frac{D}{R_g} \right)^{-1.2} . \qquad (2.5)$$

This evidence implies the existence of a universal law linking the elastic modulus to the fiber radius and the polymer chain length. Three possible physical mechanisms were suggested as explanation for this size-dependence phenomenon: surface tension[11, 13, 64-66], molecular orientation at the fiber boundary[8], and confinement of supramolecular structures[10, 39, 40]. The surface tension mechanism was shown to be negligible by both analysis and experiment[6, 10, 39, 40], while the molecular orientation mechanism is not expected to be a dominant factor in view of its mild dependence on the diameter (Figure B-9)[10]. Rigid supramolecular structures, created by correlation between neighboring polymer segments, can be of the same size scale as the fiber diameter, and therefore can cause confinement and consequently an increase in the effective elastic modulus.[40]

The dependence of polymer elastic moduli on nanostructure has been long known (Section A.4). For example, the tensile modulus of mechanically drawn polyethylene (Figure A-13)[38] increases sharply due to formation of crystalline fibrils that act as reinforcement. However, in nanofibers, the size of such nanostructures may have the same order of magnitude as the fiber diameter, and therefore can affect the modulus by mechanisms like confinement. Size **scales** relevant for such mechanisms are the chain radius of gyration R_g, the correlation length L_{cor}, and the effective Kuhn length, as illustrated in Figure 2-11.

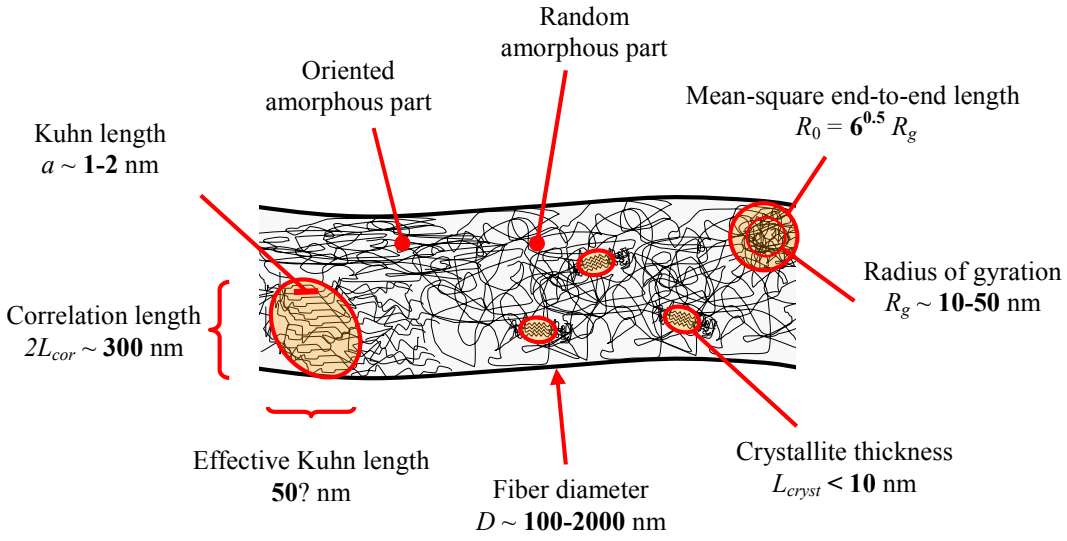

Figure 2-11. Size scales in nanofibers. The terms are defined and described in Appendix A and Appendix B.

3. Research goals and outline

3.1 Research approach and goals

Substantial research has been performed on the macro-mechanical properties of nanofibers, including the effects of material, size, and reinforcement, but the explanations for their unique properties are mostly descriptive and qualitative, leaving several open questions. The size-dependence of the elastic properties was characterized by experiments (Section B.1), yet the underlying physical mechanisms are conjectured with diverse explanations such as surface tension, confinement and stretching (Section B.2), which are currently supported by preliminary calculations and lack detailed theoretical and experimental justification.

While the influence of nanostructure on the mechanical properties of bulk polymers was broadly investigated (Section A.4), its application to electrospinning and nanofibers has not been carried out. More importantly, the effects of the small size of nano-objects have not been accounted for. These effects can be assigned to two different but interrelated categories:

- The effect of electrospinning on the polymer matrix nanoscale structure.
- The mechanism by which this nanostructure impacts the nanofiber mechanical properties.

The analysis of these effects involves diverse fields of research, including rheology of electrified jets, electrospinning process and nanofibers, polymer conformation and elasticity, polymer network dynamics (in solution), polymer structure, and mechanical properties of polymers.

In view of the broadness of these fields, the thesis focuses on the dynamic behavior of the polymer network in an electrospinning jet (the first category), and the resulting solid nanostructures. Although the effects of nanostructure on fiber elasticity (the second category) are not within the scope of the thesis, their possible influence on elasticity is discussed.

This research seeks to provide a deeper insight into the conformation of nanostructures created by electrospinning, to explain the mechanisms that lead to these structures, to develop respective quantitative models and simulation, and to validate the theoretical prediction by experiments.

Table 3-1 summarizes the research questions, and the goals to resolve them.

Table 3-1. Research questions and goals.

Research questions	Research goals
What is the conformation of the polymer network during electrospinning? Can a dynamic structure with a high degree of order be identified? Does the polymer network undergo a stretch transition? During which stage of the jet does it occur? Does the polymer network separate from the solvent? Are there boundary effects on polymer conformation? What are the mechanisms that govern the dynamic conformation of the polymer?	Study the dynamics of the polymer network during electrospinning
What is the influence of strain rate, evaporation, and relaxation on the polymer network? What is the influence of the material and process variables, such as molar mass, solution properties, flow rate, and electric field intensity, on the polymer network conformation? Can universal scaling laws be formulated to describe the parametric dependences of the conformation?	Study the effects of material and process parameters on the polymer network conformation in the jet
Does the polymer network conformation during the liquid state remain in the solid state (i.e., in the fibers) after solidification? Are there ordered structures in the nanofiber? Where are these structures located? Does the nanofiber have an anisotropic structure, with varying polymer densities and preferred orientations? Can chain orientation be controlled by tuning process variables?	Study the nanofiber nanostructure, and its correlation to the conformation of the polymer network in the jet
What is the effect of entanglement loss on the polymer network during electrospinning? Does entanglement loss affect the solid nanostructure? How is the nanofiber diameter affected by entanglement loss? Can the revealed nanostructure explain the size-dependent elasticity? Can universal scaling laws be formulated to describe the diameter dependence of the elasticity?	Study the entanglement loss in the jet and its effect on the solid nanostructure

3.2 Research outline

The research main topics and methods, and the publications prepared as part of the research, are shown in Figure 3-1, followed by a detailed list of topics.

The polymer conformation in the jet was investigated by theoretical modeling and random walk simulation. The predicted conformation was then verified by X-ray imaging of electrospinning jets. The model and simulation were generalized for semi-flexible polymers, and the predicted conformation was verified by scanning optical microscopy of fibers. Finally, the effects of polymer entanglement loss during electrospinning were investigated by experiment and modeling.

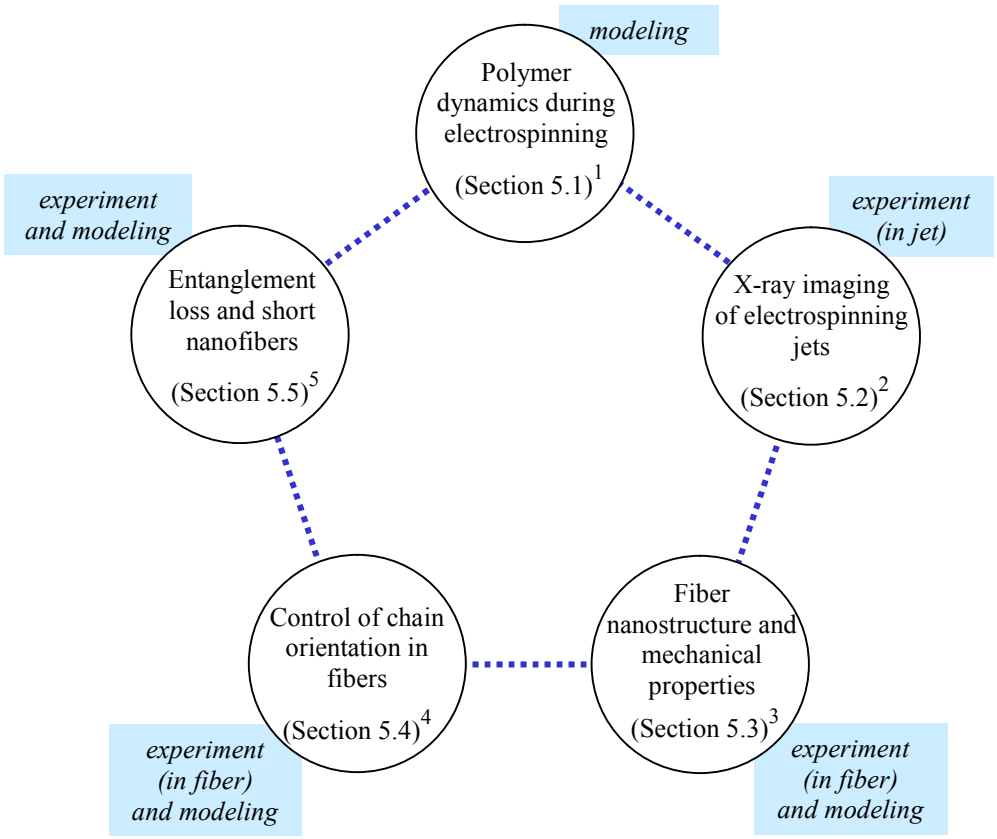

Figure 3-1. Diagram of the research main topics, indicating the methods applied and the publications included in the thesis.

List of research topics

Polymer dynamics during electrospinning (Section 5.1)[1]

Definition of the jet rheology

Definition of the entangled polymer network structure

Theoretical modeling of the network stretching during electrospinning

Derivation of a scaling law for full network extension

Theoretical modeling of the network lateral contraction

Random walk simulation of the network conformation in the jet

Validation by X-ray absorption measurements of electrospinning jets

X-ray imaging of electrospinning jets (Section 5.2)[2]

X-ray imaging of electrospinning jets

Development of algorithms and tools for the analysis of X-ray images

Measurement of jet radius, and validation of the used rheological model

Measurement of the jet flow field and velocity by particle tracing

Measurement of the X-ray absorption of the jet

Calculation of the polymer concentration variations along & across the jet

Observation and assessment of the evaporation rate and effect

Fiber nanostructure and mechanical properties (Section 5.3)[3]

Scanning optical microscopy of nanofibers

Measurement of the optical absorption of fibers, and density mapping

Mapping of the compression modulus, by atomic force microscopy

Random walk simulation of the conjugated polymer network conformation

Control of chain orientation in fibers (Section 5.4)[4]

Scanning optical microscopy of nanofibers

Measurement of optical polarization, and molecular orientation mapping

Theoretical generalization of network structure for semi-flexible polymers

Random walk simulation of the conjugated polymer network conformation

Derivation of a scaling law for full extension of semi-flexible polymers

Validation by measuring the concentration dependence of orientation

Entanglement loss and short nanofibers (Section 5.5)[5]

Electrospinning of short nanofibers

Proposed macroscopic and microscopic mechanisms for short fibers

Mapping of the conditions for occurrence of short nanofibers and beads

Measurement of lengths and diameters under various conditions

Derivation of scaling laws for short nanofiber lengths and diameters

Theoretical description by means of the entanglement loss mechanism

Validation of the scaling laws by theoretical derivation

Theoretical derivation of the diameter of continuous fibers, and validation

4. Research methods

Three unique methods were developed and applied in this research:

- Random walk simulation of the polymer network: The simulation was developed specifically for this research, and allowed, for the first time, visualization of the polymer network and individual chains in various stages of the electrospinning jet. Described in Section 5.1.[1]
- Fast X-ray phase-contrast imaging of electrospinning jets: The first experiment to image a live electrospinning jet using fast X-ray. The experiment was planned and executed specifically for this research, and allowed, for the first time, mapping of the polymer concentration variations in the jet. Described in Section 5.2.[2]
- Scanning near-field optical microscopy (SNOM) of nanofibers (developed and executed by our Italian colleagues, and interpreted jointly): The first optical probing of nanofibers at nano resolution (below diffraction limit). This experiment unveiled, for the first time, the internal spatial variation of the molecular order in nanofibers. Described in Sections 5.3 and 5.4.[3, 4]

Further description of the first two methods follows.

4.1 Random walk simulation

4.1.1 Introduction

A flexible polymer chain in equilibrium state, having a degree of polymerization N, can be described by N steps of fixed length a, where a step represents a single monomer (or Kuhn segment). Refer to the definitions of N and a in Section A.1. Each step is independent and has the same probability to move in any of the six Cartesian directions. Random walk on a Cartesian lattice can describe each possible chain conformation of a freely jointed long chain. The end-to-end distance of such a free ideal chain has a Gaussian distribution [see Section A.1 and Equation (A.6)]. Examples of free chain simulations are shown in Figure 4-1 and Figure 4-2.

A RW (random walk) simulation consists of generating a large enough sample of individual walks, each constructed from N successive unit-steps, and then generating a distribution of a chosen parameter (end-to-end distance, segmental orientation, etc.) from the complete sample, and finding the statistical moments and other characteristic features of the distribution.

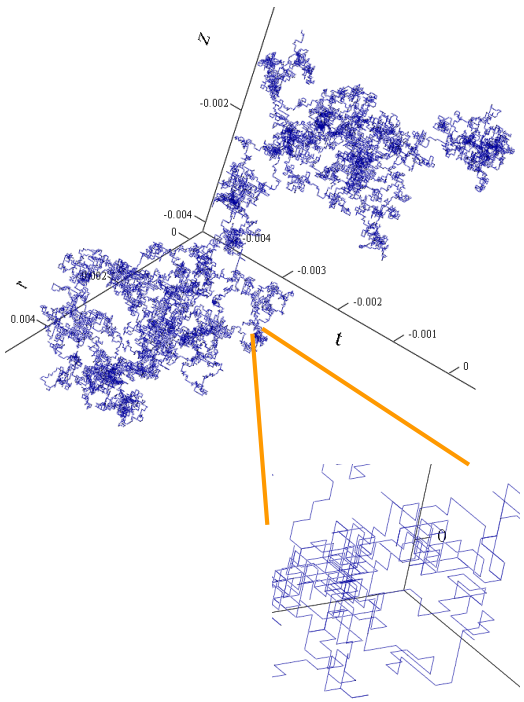

Figure 4-1. Example of random walk simulation of a single free flexible chain on a Cartesian lattice, with N = 2000 monomers (rigid chain elements).

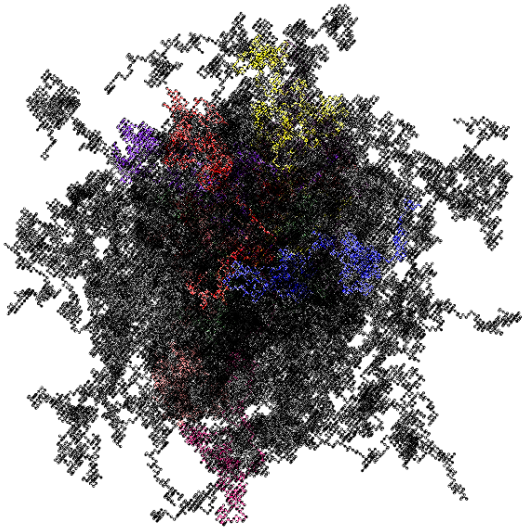

Figure 4-2. Example of random walk simulation of 100 free flexible chains on a Cartesian lattice. All of the chains start from the same point, and each chain contains N = 2000 monomers.

Random walk simulation of a polymer chain or a network in a solution can be an effective tool for describing the polymer conformation, especially when the theoretical solution is too complex, when visualization of the behavior of an individual chain is desired, or when applying complex boundary constraints and potential fields (e.g., a non-uniform flow). Under the effects of boundary or strong extensional flow, the statistical conformation of polymer chains is not Gaussian. The RW simulation tool, developed as part of this research, was used extensively to investigate the conformation of the polymer chains and network during electrospinning, under varying process variables such as molar mass, flow strain rate, and solution viscosity.

Although RW is efficient in providing the complete conformational statistics of a chain, the applicability of the method to this research requires some simplifying assumptions on chain type, walk type, and monomers connectivity. The RW model used in this work is non self-avoiding, meaning that monomers in the chain are allowed to overlap (i.e., occupy the same lattice position). The simulated chains are therefore ideal and not real (in the sense defined in Section A.1), resulting in tighter chain conformations. However, this difference is of second order compared to the effects of external forces on the conformation. Moreover, for the concentrated

solutions used in electrospinning, an ideal chain model is a good estimate, since in dense systems the repulsive forces between distant monomers in a chain are screened by repulsive forces from neighboring monomers of other chains[20, 21].

An important concern is whether random walk adequately represents the monomers connectivity in a chain under tension.[67] Each random walk step is completely independent of the preceding and succeeding steps, and therefore can be described as a Brownian motion of a single particle. However, under external forces, free Brownian motion is not applicable, since monomers apply tension forces on their linked neighbors, and therefore their motion is not independent. The approach used in this research is to define an effective potential field that represents the external forces, similar to the potential arising from hydrodynamic friction suggested by Kramers[68], and to calculate the RW stepping probabilities from the potential gradient. This approach is shown to be valid in Figure 4-11.

4.1.2 Theoretical basis and simulation tool

A monomer in a linear chain or chain section, in the presence of an effective potential field U, experiences a force $F = -\nabla U$, where ∇U is the potential gradient. This effective potential may arise from an external force acting at the chain ends, which propagates evenly along the chain, or from a local force acting directly on monomers such as a hydrodynamic force, or from a combination of both force types (Figure 4-3).

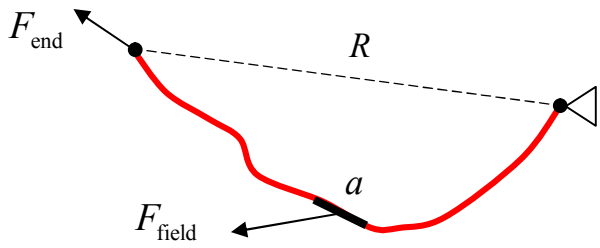

Figure 4-3. The general case of forces acting on a chain or a chain section. An external force F_{end} acts at the chain end, and, in addition, a potential field applies a force F_{field} on each monomer a.

From statistical mechanics it is known that, if a system in equilibrium can be in any one of several states, the probability that the system will be in a state having a potential U is $e^{-U/(k_B T)}/Q$, where T is the temperature and k_B is the Boltzmann constant.[69] The partition function Q is determined so that the sum of the probabilities of all the possible states equals 1. In terms of a RW on a Cartesian lattice, the probability $P_x^{\pm}$, that the system will make a step a in any of the 6 possible directions,

is defined as $P_x^{\pm} \equiv P_x^{\pm}(x \to x \pm a)$, where $x = z, \rho, \varphi$ are the three Cartesian axes. Therefore

$$P_x^{\pm} = \frac{1}{Q}\exp\left(-\frac{U_{x\pm a} - U_x}{k_B T}\right) = \frac{1}{Q}\exp\left(\mp\frac{\nabla U_x a}{k_B T}\right), \tag{4.1}$$

where ∇U_x is the potential gradient in the direction *x*. In correspondence to an electrospinning jet, *z* is coincident with the jet main axis, while ρ and φ are two radial mutually perpendicular axes. The sum of the probabilities of the 6 possible states of the system should be a unity

$$\sum_x P_x^{\pm} = \sum_x \left(P_x^{+} + P_x^{-}\right) = \frac{2}{Q}\sum_x \cosh\left(\frac{\nabla U_x a}{k_B T}\right) = 1, \tag{4.2}$$

from which *Q* can be derived. Defining a normalized force (using $F = -\nabla U$)

$$f = \frac{Fa}{k_B T} = -\frac{\nabla U a}{k_B T}, \tag{4.3}$$

and substituting into Equation (4.1), we obtain the probabilities for a random walk step under a force f

$$P_x^{\pm}(z,\rho,\varphi) = \frac{\exp\left[\pm f_x(z,\rho,\varphi)\right]}{2\sum_x \cosh\left[f_x(z,\rho,\varphi)\right]}, \quad x = z,\rho,\varphi. \tag{4.4}$$

Since the potential is a function of the three dimensional position (z,ρ,φ), the force acting on a monomer, and its related stepping probabilities, are written as functions of the position.

The algorithm developed for this research was implemented in a set of programs written in Mathcad. The 3D simulation uses the uniform randomization function of Mathcad, and is dimensionless. Unit steps are used to represent monomers, but since for a given polymer the monomer size *a* is constant (of order 1 nm), the real dimensions of the chain can be restored without loosing generality. Similarly, the force is dimensionless, as defined for Equations (4.3) and (4.4). The core engine of the program consists of a stepping probability function (Figure 4-4), and a stepping function (Figure 4-7).

The RW stepping probability function, $P(z,\rho,\varphi)$, defines the force functions, and the stepping probabilities associated with them, in accordance with Equation

(4.4). The three force functions, (f_z, f_ρ, f_φ), can be any functions of the 3D position of the current monomer, (z, ρ, φ). For example, using quadratic functions of the position, the force functions could be

$$\begin{aligned} f_z(z) &= A_{z,0} + A_{z,1} z + A_{z,2} z^2 \\ f_\rho(\rho, z) &= A_{\rho,0} + A_{\rho,1} \rho + A_{\rho,2} \rho z \\ f_\varphi(\varphi, z) &= A_{\varphi,0} + A_{\varphi,1} \varphi + A_{\varphi,2} \varphi z, \end{aligned} \tag{4.5}$$

where $A_{x,i}$ are constants. These functions are suitable (with adjustments) for describing the cases of interest for this research, particularly the force field of the electrospinning jet (Section 4.1.5), in which the corresponding constants of the functions f_ρ and f_φ are equal. The constants $A_{x,0}$ represent forces acting at the chain ends, whereas the other terms represent a force field which varies as a function of the monomer position. The field force in the positive direction of z grows quadratically with z, while the radial field forces, which are acting toward the jet center, grow linearly with z and diminish toward the jet center Consequently, all the constants should be positive, except for the prefactors of ρ and φ which should be negative.

$$\mathrm{P}(z,\rho,\varphi) = \left|\begin{array}{ll} \mathrm{f} \leftarrow \begin{pmatrix} Az_0 + Az_1 \cdot z + Az_2 \cdot z^2 \\ A\rho_0 + A\rho_1 \cdot \rho + A\rho_2 \cdot \rho \cdot z \\ A\varphi_0 + A\varphi_1 \cdot \varphi + A\varphi_2 \cdot \varphi \cdot z \end{pmatrix} & \text{Force functions (quadratic example)} \\ \mathrm{f} \leftarrow \mathrm{f} - 10^{10} \cdot \begin{pmatrix} 0 \\ \mathrm{sign}(\rho) \\ \mathrm{sign}(\varphi) \end{pmatrix} \text{ if } \left(\rho^2 + \varphi^2\right) > \frac{r_0}{1 + k \cdot z} & \text{Forces on boundary (hyperbolic example)} \\ \mathrm{Q} \leftarrow 2 \cdot \sum_{x=0}^{2} \cosh(\mathrm{f_x}) & \text{Partition function} \\ \mathrm{P} \leftarrow \frac{1}{\mathrm{Q}} \cdot \exp\left[\begin{pmatrix} \mathrm{f_0} & -\mathrm{f_0} & \mathrm{f_1} & -\mathrm{f_1} & \mathrm{f_2} & -\mathrm{f_2} \end{pmatrix}^{\mathrm{T}}\right] & \text{Stepping probabilities in 6 directions} \\ \text{return P} & \end{array}\right.$$

Figure 4-4: Random walk stepping probability function in Mathcad. The function sets the force functions acting on each monomer at the given 3D position of the monomer [Equation (4.5)], and calculates the corresponding stepping probability for each of the 6 possible directions [Equation (4.4)]. The coordinates dimensions are in unit step. Also included is a hyperbolic boundary function that sets bouncing forces on the boundary in order to keep the random walk within a confined volume.

The program in Figure 4-4 also incorporates an example of a conditional hyperbolic boundary, similar to the shape of an electrospinning jet [see Equation (5.1-

2)]. When the random walk hits the boundary, a strong force is applied on the monomer in the direction opposite to the direction of the last step.

The trends of the stepping probabilities are demonstrated in Figure 4-5 for the simple case of an end force in the z direction [the term $A_{z,0}$ in Equation (4.5)], with all other forces null: when the force rises, the probability to step toward $+z$ increases, while the other probabilities decrease correspondingly. The probabilities in the presence of a boundary are demonstrated in the example of Figure 4-6, in which when a boundary is hit while stepping in the $+\rho$ direction, the probability to step toward $-\rho$ jumps to 1, while the other probabilities drop to 0.

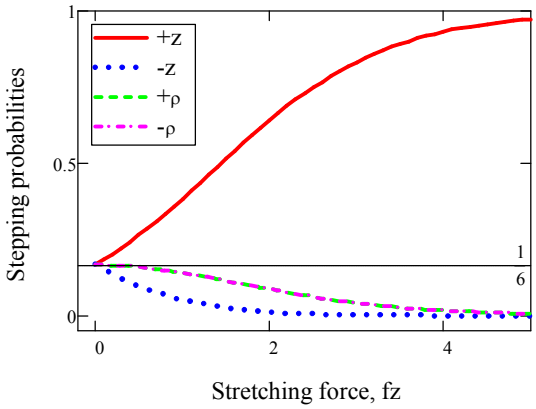

Figure 4-5. Stepping probabilities along the z axis, as a function of a stretching end force f_z.

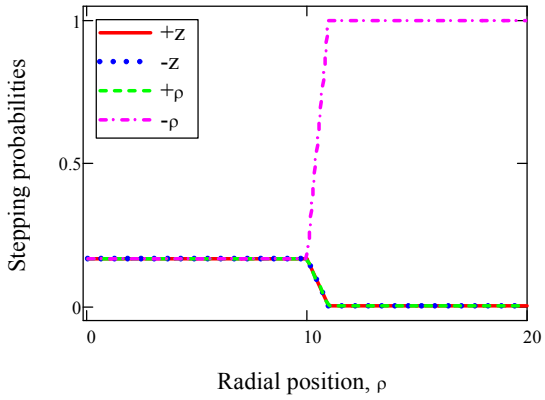

Figure 4-6. Stepping probabilities without forces, versus the radial position ρ, in the presence of a boundary parallel to z and located at ρ=10.

The random walk stepping function, $R(I,N)$, executes random walks for a sample of I chains, each with N steps (i.e., monomers). The function uses the stepping probabilities, calculated by the function $P(z,\rho,\varphi)$ for the next step, to partition the range 0-1 into divisions whose sizes are proportional to the probabilities. A random number, uniformly distributed between 0 and 1, is generated, and the division on which it falls is selected as the stepping direction.

The function $R(I,N)$ returns the full stepping history of all the chains in the sample. This data is used by other utilities (not presented in the thesis), to draw the 3D conformation of the stretched chains, to calculate the statistical distribution of the end-to-end distance R and the corresponding statistical moments, to calculate the orientational preference of chain segments, to calculate the free energy of chains, and more. Examples of chain conformations under stretching are shown in Figure 4-8, without and with a cylindrical boundary (similar to the outer surface of a jet).

Boundary causes widening of chains, though not significantly, in parallel to its surface (also observed in the 1D theoretical analysis in the preliminary study[70]).

```
R(I,N) =  for i ∈ 0..I                                          Sample loop, I times
            (z0)   (0)
            (ρ0) ← (0)                                          Coordinates initialization
            (φ0)   (0)
            for n ∈ 1..N                                        Chain loop, N times
              p0 ← 0
              rndNum ← rnd(1)                                   Random number generation
              for j ∈ 0..5
                pj+1 ← P(zn–1, ρn–1, φn–1)j + pj                Probability bands
                qj ← [(rndNum ≥ pj) ∧ (rndNum < pj+1)]          Stepping decision
              (zn)   (zn–1 + q0 − q1)
              (ρn) ← (ρn–1 + q2 − q3)                           Stepping
              (φn)   (φn–1 + q4 − q5)
            Ri ← (z ρ φ)^T                                      Chain i conformation
          return R                                              All chains in sample
```

Figure 4-7. Random walk stepping function in Mathcad. The function runs random walks for a sample of I chains, each of N monomers, using the stepping probabilities calculated by the function P (Figure 4-4). The function returns the full position vectors of each chain and monomer in the sample. A random number between 0 and 1 is generated for each step, so that a direction with a higher probability will have a higher chance to be selected for stepping.

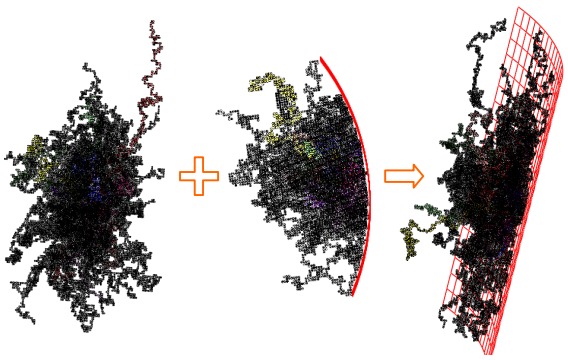

Figure 4-8. Example of random walk simulations of 100 freely-jointed chains, each with N=1,000 monomers. From left: chains under a field force f_z=0.004·z, free chains in the presence of a cylindrical boundary, and superposition of both.

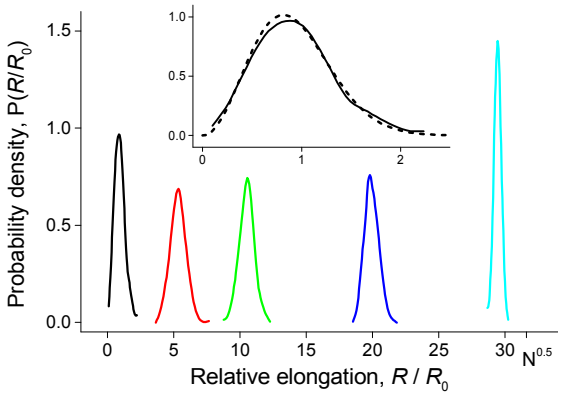

Figure 4-9. Probability density of relative end-to-end distances of 1000 simulated chains, each with N=1,000 monomers. A stretching end force f_z is applied, equal to (from left): 0, 0.5, 1, 2, and 4. A comparison to theory (dashed line, Equation (A.7)) is shown in the inset (f_z =0).

The probability density of the end-to-end distance, $R = |\vec{R}|$ (Figure 4-9), shows that in the case of a tensile force at chain ends, the distribution width remains

essentially unchanged, except under very high forces where the distance is bound by the fully extended length of the chain.

4.1.3 Single chain under tension

The modeling of this case is strongly related to the dynamics of the polymer network during electrospinning, since, as explained in Section 4.1.5, the dominant force acting on a subchain entangled in a network is the extension force exerted at its ends by the linked subchains.

A longitudinal (normalized) force f_z, acting at the chain ends, propagates from one monomer to another, so that force on each monomer is equal to f_z. Since the transversal forces f_ρ and f_φ are zero, the probability that the monomer will step in the longitudinal positive and negative directions is [Equation (4.4)]

$$P_z^{\pm} = \frac{\exp(\pm f_z)}{2[\cosh f_z + 2]}. \tag{4.6}$$

Similarly, the probability to step in one of the transversal positive and negative directions is

$$P_\rho^{\pm} = P_\varphi^{\pm} = \frac{1}{2[\cosh f_z + 2]}. \tag{4.7}$$

Since in this case the stepping probabilities are the same for all the *N* monomers in the chain, it is possible to derive an analytical solution for the chain mean end-to-end distance, *R*, that results from the end force

$$R_x = R_{\max}\left(P_x^{+} - P_x^{-}\right), \quad x = z, \rho, \varphi, \tag{4.8}$$

where $R_{\max} = aN$. Substituting the stepping probabilities from Equations (4.6) and (4.7), the mean longitudinal distance is

$$\frac{R_z}{R_{\max}} = \frac{\sinh(f_z)}{\cosh(f_z) + 2}, \tag{4.9}$$

while the transversal distances are $R_\rho = R_\varphi = 0$.

An example of a RW simulation of the extension of a freely-jointed chain under several values of the end force is shown in Figure 4-10. The force-elongation relationship of a freely-jointed chain, obtained by the RW simulation, is shown in Figure 4-11, and is compared with the Gaussian, Langevin, and analytic solutions.

The Gaussian solution represents Hooke's law, and is valid only for small elongations, whereas the Langevin and RW solutions both saturate at elongations approaching the extension limit of the chain.

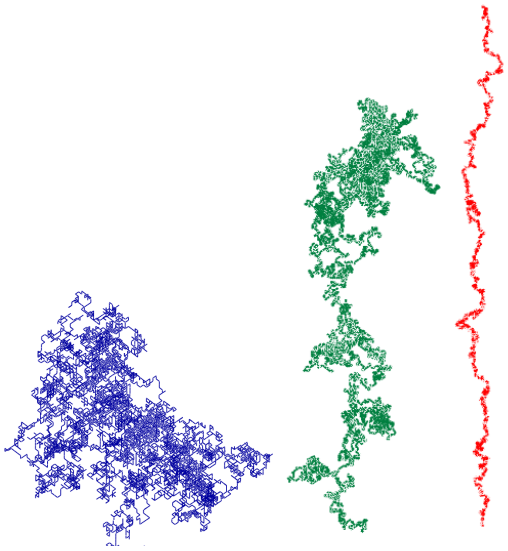

Figure 4-10. Random walk simulation of a freely-jointed chain with N=10,000 monomers. The stretching end force, f_z, is (from left) 0 (free state), 0.05, and 0.3.

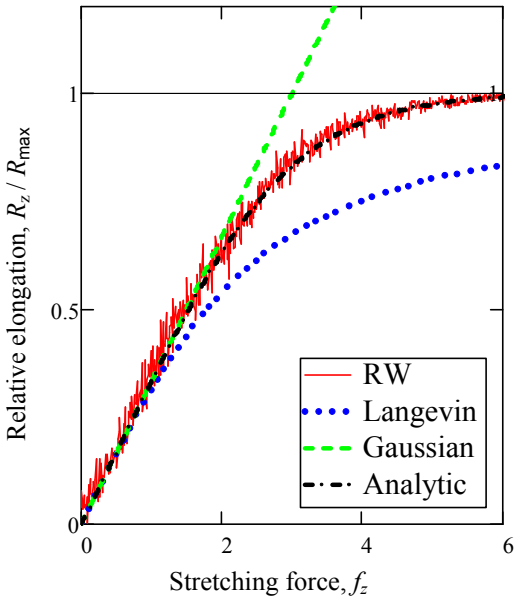

Figure 4-11. Force-elongation relationship of a freely-jointed chain. Comparison of the mean elongation of random walk (RW) simulation of 10 chains, each with N=30, to Langevin [Eq. (A.18)], Gaussian [Eq. (A.17)], and Analytic [Eq. (4.9)].

The redistribution of stepping probabilities during application of a longitudinal extension (Figure 4-5), results in lateral contraction of the chain, as seen in the narrowing of the distribution of the chain mean-square end-to-end radial distance in Figure 4-12 when the tension force is increased. The mean-square radial distance is calculated from the simulated distribution [the function $R(I,N)$], and is normalized by the mean-square end-to-end distance of a free chain [Equation (A.2)].

$$\frac{R_\rho}{R_0} = \frac{\left|R_\rho\right|}{N^{1/2}}. \tag{4.10}$$

Also, as a result of stretching, the alignment of chain segments with respect to the z axis increases. The orientation parameter O is averaged over the complete contour length of the chain

$$O = \frac{3}{2}\left\langle \cos^2\theta \right\rangle - \frac{1}{2}, \quad \left\langle \cos^2\theta \right\rangle = \frac{1}{N-2m+1}\sum_{n=m}^{N-m}\left[\frac{\left|z_{n+m}-z_{n-m}\right|}{\left|\vec{R}_{n+m}-\vec{R}_{n-m}\right|}\right]^2, \tag{4.11}$$

where θ is the angle between the segment's end-to-end direction and the z axis, and $2m+1$ is the number of monomers in the segment. The result is then averaged over a sample of chains to reduce noise. As expected, the orientation increases when the force is higher (Figure 4-13). Obviously, the orientation depends on the size of the selected segment: when too short, the Cartesian lattice can introduce an error, whereas when too long, the orientation gradually drops to 0.

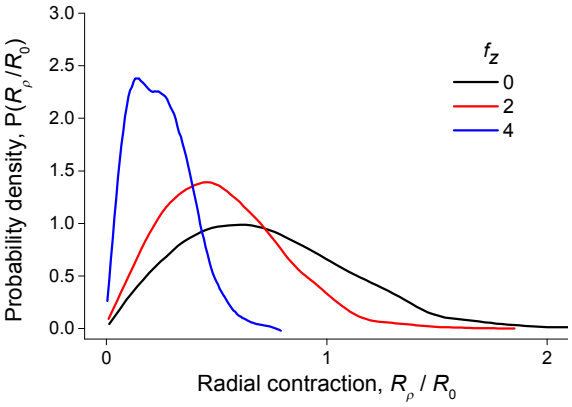

Figure 4-12. Probability density of the radial mean-square end-to-end distances, for three values of the stretching end force f_z (from left): 4, 2, and 0. I=1,000 simulated chains, each with N=500 monomers.

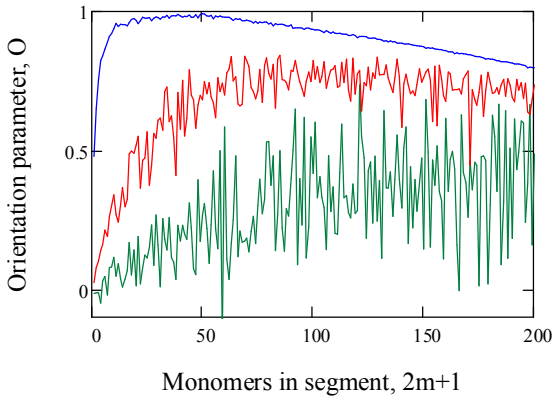

Figure 4-13. Segmental orientation as a function of the number of monomers in a segment, for three values of the stretching end force f_z (from top): 2, 0.5, and 0.2. The number of monomers in a chain is N=1,000.

4.1.4 Single chain in a flow field

A single chain in a flow field is not representative of the dynamic behavior of a polymer network during electrospinning. However, this problem was investigated analytically by de Gennes and others (reviewed in Section A.3), and therefore it is interesting to study it with a different tool. Moreover, the extension of the chain in this case is not uniform, unlike the case of a chain under tension at its ends (described in the previous section), but varies along its contour, somewhat analogous to the conformation of a polymer network along an electrospinning jet.

A single chain in an extensional flow field experiences field forces acting directly on its monomers. The force on a single monomer of size a can be estimated by Stokes law

$$F = k_G a \eta_s v, \tag{4.12}$$

where η_s is the solvent viscosity, v is the velocity difference between the monomer and the solvent, and k_G is a dimensionless geometrical factor or order 1 that depends on the monomer's shape. Assuming that the center of the sum of forces is moving at

the velocity of the jet, the origin of a Cartesian coordinate system $x=(z,\rho,\varphi)$ can be attached to the force center, with *z* pointing toward the direction of the flow. Within the small scale of a single chain, the velocity gradient can be considered constant, and therefore the force center is located approximately at the chain center; however, this condition is not necessary, so long as the location of the force center on the chain is known. The velocity *v* is then the jet velocity with respect to the moving force center. Writing the velocity in units of step/s instead of nm/s (in common polymers 1 step has the scale of 1 nm), and normalizing the force as in Equation (4.3)

$$f=\frac{Fa}{k_BT}\cong\frac{k_Ga^3\eta_s}{k_BT}v\cong\tau_0 v, \tag{4.13}$$

where $\tau_0\approx\eta_s a^3/(k_BT)$ is the monomer's relaxation time from Equation (A.14).

In the case of a constant velocity gradient *s* in the *z* direction (remembering that *z* is referenced to the force center), and no gradient in the perpendicular directions

$$f_z\cong s\tau_0 z. \tag{4.14}$$

The dimensionless parameter $s\tau_0$ is the force field coefficient $A_{z,1}$, used in the force functions of Equation (4.5). Due to symmetry with respect to the chain center, which coincides in this case with the force center, the random walk is run for half the chain. Note that the force can be rewritten in the form $f_z\approx s\tau\bar{z}/N$, where $\tau\approx\tau_0N^{3/2}$ is the chain relaxation time from Equation (A.14), and $\bar{z}=(z/N^{1/2})$ is the relative position. This form incorporates the familiar $s\tau$ term, used by de Gennes to express the condition for coil stretch transition (see Section A.3).

The results of the corresponding RW simulation provide a striking resemblance to the analytic solution by de Gennes. The distribution $P(R/R_0)$ of the chain's end-to-end distance $R=|\vec{R}|$ in Figure 4-14 shows that, when gradually increasing $s\tau_0$, the end-to-end distance of the chain transitions from small elongation to very large elongation, with an intermediate widely-spread bimodal distribution (inset). The total free energy (elastic + friction) of the chain is derived in the same way as in Equation (A.16)

$$\frac{F_{tot}}{k_BT}=const-\ln\left[\frac{P(R/R_0)}{4\pi(R/R_0)^2}\right], \tag{4.15}$$

where the term $4\pi(R/R_0)^2$ is inserted in order to convert the distribution from the 1D form of Equation (A.7) to the 3D form of Equation (A.6). The energy is depicted in Figure 4-15, in excellent agreement with de Gennes' Figure A-9. Below a critical gradient s_c, the elongation is Gaussian, while above it the curve corresponds to large elongation and has two energy minima, eventually converging to very large elongation.

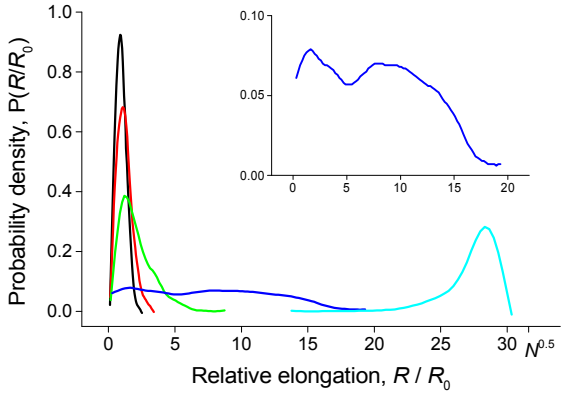

Figure 4-14. Probability density of relative end-to-end distances R/R_0 of a polymer coil in an extensional flow with a constant gradient. I=1000 simulated chains, each with N=1,000 monomers. The field force is $s\tau_0 z$, where $s\tau_0$ is (from left): 0, 0.003, 0.006, 0.012, and 0.063. The inset ($s\tau_0$=0.012) shows a transitional bimodal density.

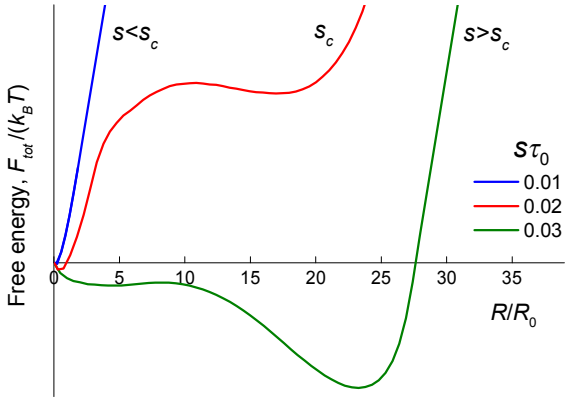

Figure 4-15. Free energy versus the relative elongation of chains under a field force $s\tau_0 z$ in an extensional flow with a constant gradient. Calculated for three values of $s\tau_0$ (from left): 0.01, 0.02, and 0.03. N=1,000 monomers.

The value of the critical gradient s_c, where coil stretch transition occurs, is seen in Figure 4-16 for three values of the degree of polymerization N. This plot was achieved by calculating the elongation distribution for each value of $s\tau_0$, and detecting the peaks of the probability density, from which the statistical mode (most frequent value) of the elongation is inferred.

Below the transition point, the dependence of the elongation on s is low (Gaussian), whereas above it the dependence is initially steep and then, at very high gradients, it tapers off. Around the transition point, within a very small $s\tau_0$ range (e.g., 0.013 - 0.014 for the case N=1,000), the elongation fluctuates between small and large values (inset). Additionally, when the chain is longer (higher N), the hydrodynamic friction becomes dominant over the elastic force, and the transition point occurs at a lower s, as shown by de Gennes. For N=5,000 monomers, the transition occurs at a very low gradient.

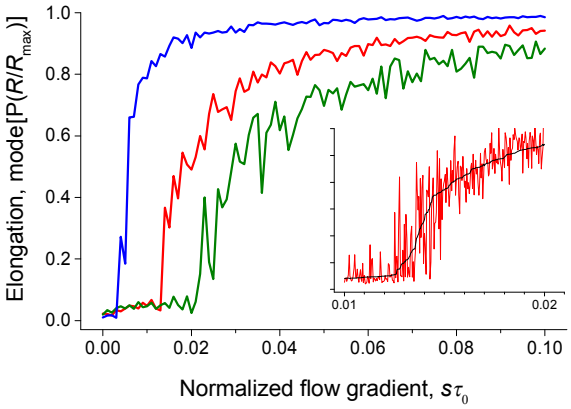

Figure 4-16. The distribution mode of the relative elongation R/R_{max} of a single polymer coil in an extensional flow with a constant gradient, versus the normalized flow gradient $s\tau_0$. The field force is $s\tau_0 z$. The value of N is (from left): 5,000, 1,000, and 500 monomers. The inset magnifies the transitional zone of the case N=1,000.

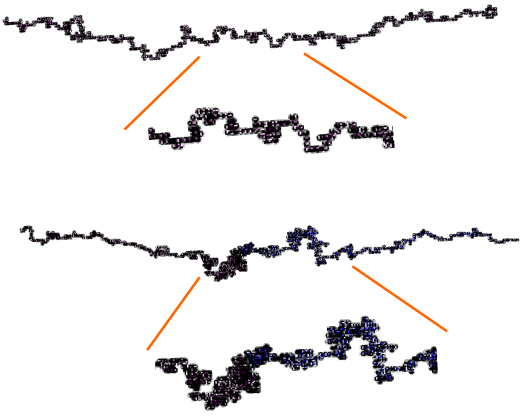

Figure 4-17. Examples of extended chains with N=1,000. The top view is a chain under tension at its ends. The bottom view is a chain under a force field, such as a flow with a constant strain rate in the direction of the chain's elongation.

The conformation of a chain extended by such a force field is different from a chain under tension at its ends, described in the previous section. While a chain under tension has a uniform density along its contour (top view of Figure 4-17), a chain in a force field is denser around its center, where the force is low, and more extended farther from the center, where the force is high (bottom view).

4.1.5 Network in a flow field

Polymer in a semi-dilute solution forms an entangled network (Sections 2.1 and A.2). In such a network, each chain segment between two adjacent topological links (i.e., topological constraints), can be practically regarded as a subchain, with an end-to-end distance ξ, equivalent to the network mesh size (see illustration in Figure 5.1-2). Each subchain experiences an extensional force at its ends, exerted by the other subchains connected to the same topological links, and a local hydrodynamic force acting on each of the subchain's monomers by the solvent. Since the scale of a single subchain (~10 nm) is several orders of magnitude smaller than the scale of the electrospinning jet (~1 mm), the tension gradually builds up from subchain to subchain due to network connectivity, and becomes dominant over the hydrodynamic force. The subchain can therefore be treated as a single chain under tension, as in Section 4.1.3.

Subchains in a network at rest have an end-to-end distance ξ_0, caused by an effective stretching force [normalized as in Equation (4.3)] of scale

$$f_0 \approx \frac{F_0 a}{k_B T} \approx \frac{3ar}{R_0^2} \approx \frac{3a}{\xi_0} \approx \frac{3}{\sqrt{N_s}}, \tag{4.16}$$

obtained by Equation (A.17) with $R_0 = r = \xi_0 = aN_s^{1/2}$, where N_s is the number of monomers in the subchain. For a given polymer solution, ξ_0 and N_s can be calculated by Equation (A.13).

The force on a monomer in a flow field is $F = k_G a \eta v$ [Equation (4.12)], where η ($\eta > \eta_s$) is the effective viscosity of the dilute solution (Sections 2.1 and A.2) surrounding the monomer. In this we assume that, although the solution as a whole is semi-dilute entangled, locally the fluid around the monomer has a higher viscosity than that of the solvent, as a result of dissolved unentangled chains. Given a velocity gradient in the vicinity of a subchain n, ∇v_n, and the subchain end-to-end distance ξ_n, the average velocity increase along that subchain is $\xi_n \nabla v_n$. Consequently, the hydrodynamic force grows with respect to the previous subchain, and the force on a monomer in that subchain is increased by

$$\delta F_n \cong k_G a \eta \xi_n \nabla v_n. \tag{4.17}$$

This force is on average the same for all the monomers in the subchain, and is therefore equivalent to a tension force of the same scale applied at the subchain ends, as reasoned in Section 4.1.3. Writing the mesh size in unit steps instead of nm (1 step is ~1 nm), and normalizing the force

$$\delta f_n = \frac{\delta F_n a}{k_B T} \cong \frac{k_G a^3 \eta}{k_B T} \xi_n \nabla v_n \cong \tau_0 \xi_n \nabla v_n, \tag{4.18}$$

where $\tau_0 \approx \eta a^3 / (k_B T)$ is the monomer's relaxation time [Equation (A.14)], which corresponds to the dilute viscosity η. Summing the friction forces over all the subchains in a desired direction, we obtain the total tension force acting on subchain n

$$f_n = \sum_{i=1}^{n} \delta f_i \cong \tau_0 \sum_{i=1}^{n} (\xi_i \nabla v_i) \cong \tau_0 (v_n - v_{n0}), \tag{4.19}$$

where v_n is the flow velocity around subchain n, and v_{n0} is the flow velocity at the origin of the first subchain, both in units of step/s. In view of the huge difference in scale between a subchain and the network, f_n and v_n can be written as continuous

functions of the global position $x=(z,\rho,\varphi)$, or $f(z,\rho,\varphi)$ and $v(z,\rho,\varphi)$, in which the position corresponds to the subchain sequential number. Thus,

$$f_x \approx \tau_0 (v_x - v_{x0}), \tag{4.20}$$

where v_x and v_{x0} are the velocity and the initial velocity in the direction *x*, respectively. Adding the initial force of the network at rest from Equation (4.16), we obtain the total force on a monomer

$$f_x \approx f_0 + \tau_0 (v_x - v_{x0}). \tag{4.21}$$

The flow of the electrospinning jet has axial and radial velocity components. For the quadratic velocity profile shown in Equations (5.1-1) and (5.1-2), we use the form

$$\begin{aligned} v_z &= v_0 (1+kz)^2 \\ v_\rho &= -v_0 (1+kz) k\rho, \end{aligned} \tag{4.22}$$

where v_0 is the jet initial velocity, *k* is a dimensionless parameter that determines the velocity gradient [same as *k* in Equation (2.3) but multiplied by $a/r_0 \sim 10^{-5}$], and the units of length and velocity are step and step/s, respectively. The corresponding jet radius (assuming volume conservation) is $r_J = r_0 (1+kz)^{-1}$, where r_0 is the jet initial radius. The initial velocity in the axial direction is taken at the jet start ($z=0$), whereas the initial velocity in the radial direction is taken on the free surface of the jet ($\rho = r_J$), and therefore

$$\begin{aligned} v_{z0} &= v_0 \\ v_{\rho 0} &= -v_0 k r_0. \end{aligned} \tag{4.23}$$

Inserting the velocity expressions into Equation (4.21), we can now summarize the force functions for the random walk simulation (in unit steps) of an entangled subchain in a flow field, in a form similar to Equation (4.5):

$$\begin{aligned} f_z &= f_0 + \tau_0 v_0 k (2+kz) z \\ f_\rho &= f_0 - \tau_0 v_0 k [r_0 - (1+kz)\rho] \\ &= f_0 - \tau_0 v_0 k r_0 (1 - \rho / r_J). \end{aligned} \tag{4.24}$$

The forces in Equation (4.24) are specific to the quadratic velocity profile of Equation (4.22), but Equation (4.21) can be adapted to any velocity profile by the same logic. In view of the rotational symmetry in the radial direction, the same value of the force f_ρ is used for the force f_φ, an approximation that reduces the complexity of the simulation. Note that in the radial direction, the sign of the velocity was reversed since the network starts at the jet boundary and not at the center, and consequently, since $\rho < r_J$, the force due to the radial flow is negative (a compressive force). Also, the overall radial force should always be $f_\rho \geq 0$, since a negative value would mean stretching.

In the axial direction, the stretching force due to the flow rises quadratically with z and becomes much larger than f_0, and therefore $f_z \cong \tau_0 v_0 k^2 z^2$. In the radial direction, the compression force due to the flow decreases proportionally to the ratio between the local radius and the jet radius, and reaches a maximum magnitude of $\tau_0 v_0 k r_0$ at the jet center, independently of the position z. Typically, the order of magnitude of this compressive force is much lower than $f_0 \sim 10^{-1}$, and therefore it does not cause a significant compression with respect to the initial mesh size of the network. Hence, the dominant effect on the radial contraction of the network is that induced by the axial stretching force, which is many orders of magnitude higher than the radial compressive force (their ratio is of order $z/r_J >> 1$). These effects are demonstrated in the simulation example shown in Figure 4-18. In fact, the influence of the radial compressive force is even lower, since the network radius becomes smaller than the jet radius as a result of stretching, and therefore the jet radius r_J in Equation (4.24) should be replaced by the smaller network radius r_P.

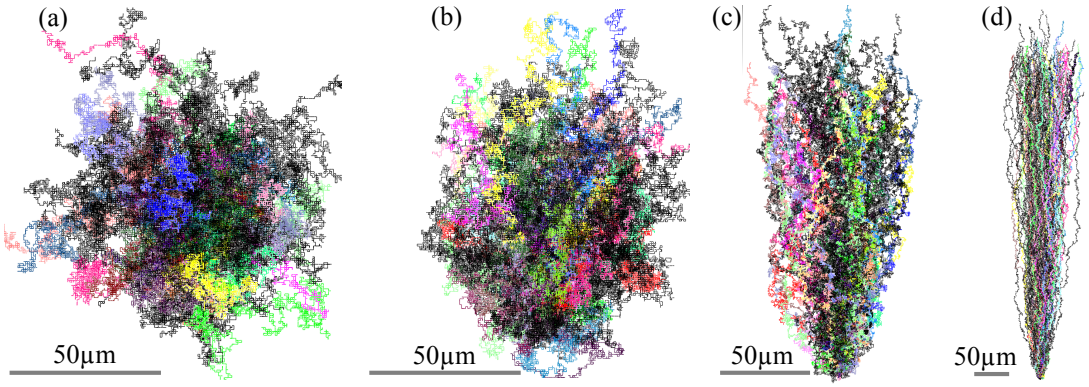

Figure 4-18. Example of subchains conformation generated by random walk, demonstrating the dominant effect of stretching over radial contraction. Each image consists of a sample of 100 subchains, starting from the same node. $N_s = 4{,}000$. (a) Network at rest, f_x=f_0. (b) Maximal radial compression, f_ρ=f_φ=0. (c) Axial stretching, f_z=4f_0. (d) Axial stretching, f_z=11f_0.

The simulation starts at an initial subchain, and proceeds from subchain to subchain in accordance with the procedure described in Figure 4-19 (additional details are provided in Section 5.1). The force at a given position is calculated by Equation (4.21), or, alternatively, by adding the force increment from Equation (4.18) to the force in the previous subchain. The mesh size is then obtained by running a RW for the current subchain. In the axial direction, the simulation typically runs a sequence of $\sim 10^6$ subchains. In the radial direction, the number of subchains is fixed, given by $r_0 / \xi_0 \sim 10^4$, and the simulation starts at the network radius, given at each position z by $r_P = r_J \xi_\rho / \xi_0$ [Equation (5.1-22)], and proceeds toward the jet center.

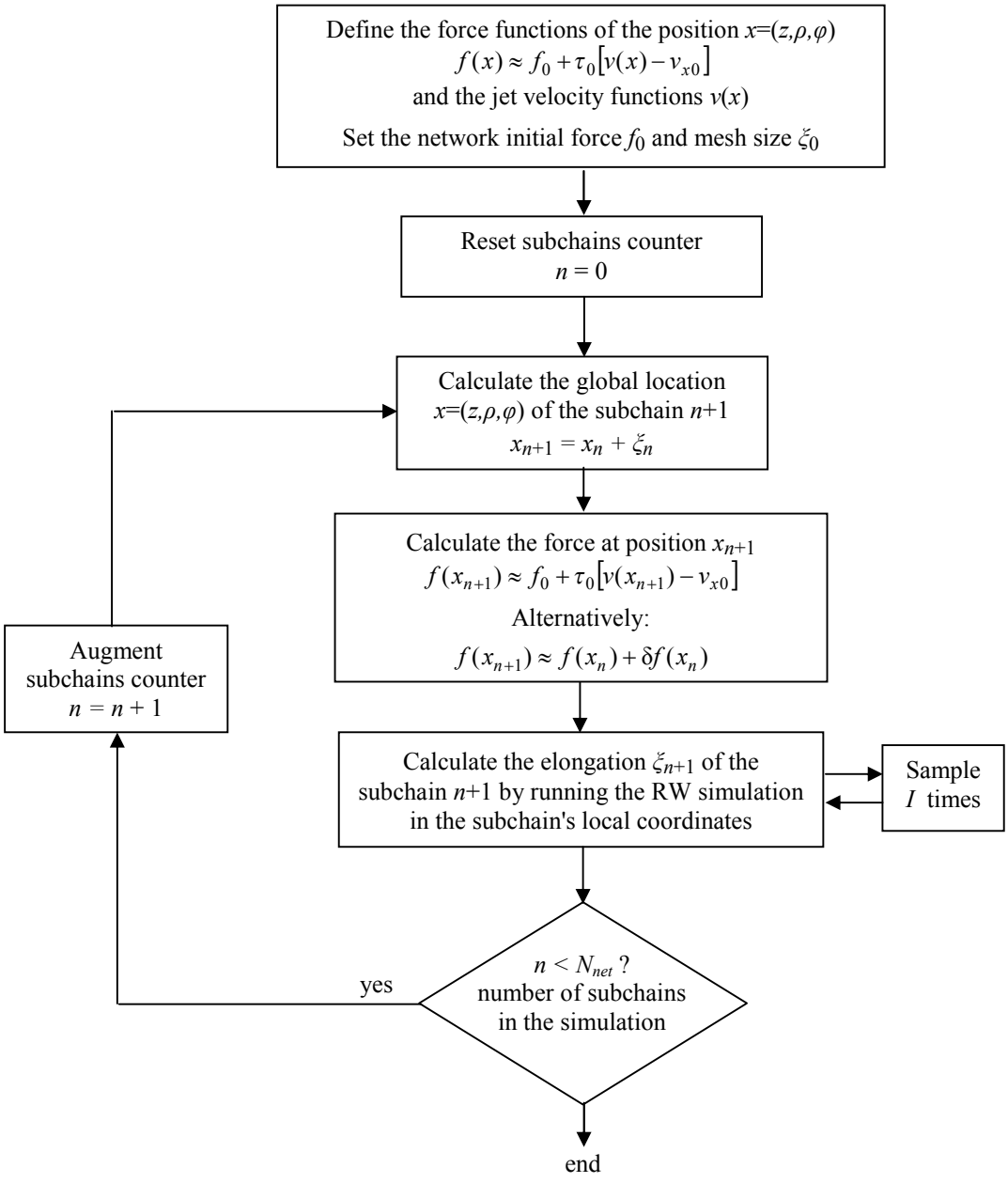

Figure 4-19. Procedure for RW simulation of a polymer network in an extensional flow.

Typical results of a simulation run of a sequence of ~9,000 subchains in the axial direction are depicted in Figure 4-20, showing the evolution of the axial force and the axial and radial mesh sizes, as functions of the distance from the jet start. In this run, the radial compression force was ignored ($f_\rho = f_0$), allowing observation of the net effect of stretching on the radial mesh size, which indeed converges to zero around 10^6 steps from the jet start (~1 mm). At that position, the axial mesh size converges to the fully extended length of the subchain, and the axial force rises to ~70f_0. The parameter τ_0 was tuned so that at small elongations the axial mesh size will conform to that obtained by the affine stretching result of the theoretical modeling [Equation 5.1-12].

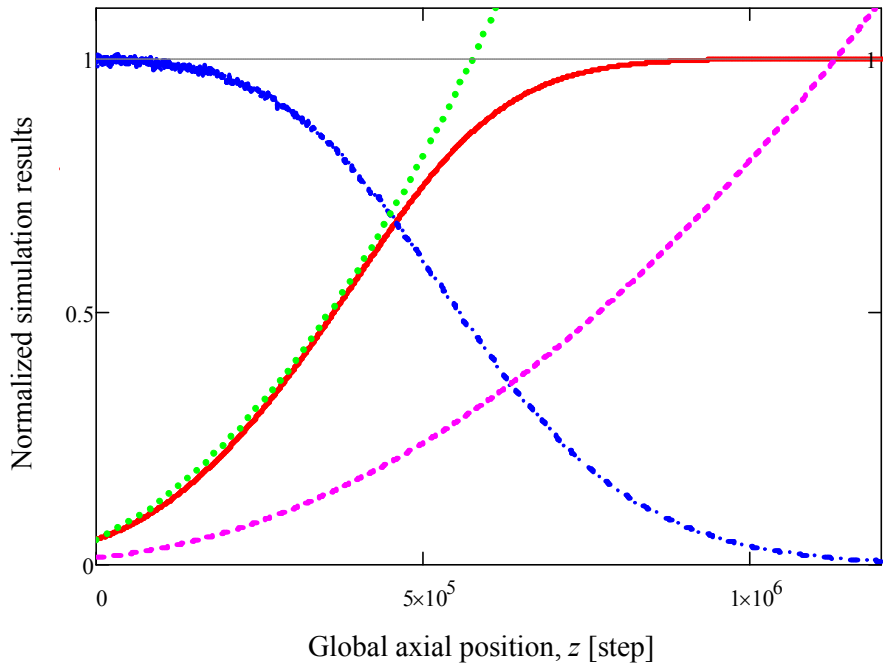

Figure 4-20. Simulation of a polymer network in an electrospinning jet, for a sequence of 8855 chains in the axial direction, using the force functions of Equation (4.24) with f_ρ=f_φ=f_0. The plots are: ξ_z/N_s (solid), $\xi_\rho/(N_s/3)^{1/2}$ (dash-dot), $v_z/v_0/N_s^{1/2}$ (dot), and $f_z/f_0/70$ (dash). The simulation parameters are: N_s=400 step (monomers), ξ_0=20 step, f_0=0.15, v_0=2.6·10^6 step/s, k=6·10^{-6}, and τ_0= 5.8·10^{-8} s.

The overall simulated network is depicted in Figure 4-21(a), demonstrating the longitudinal extension and the simultaneous lateral contraction, resulting in a network radius smaller than the jet radius. The conformation of a sequence of subchains is presented in Figure 4-21(a) and (b). Obviously, it is not likely that the network would have such a sharp boundary as depicted, but nevertheless the general phenomenon of network compacting should be expected. In this run, the radial compression force was included, and its effect can be noticed in the gradual growth of the radial density toward the jet center.

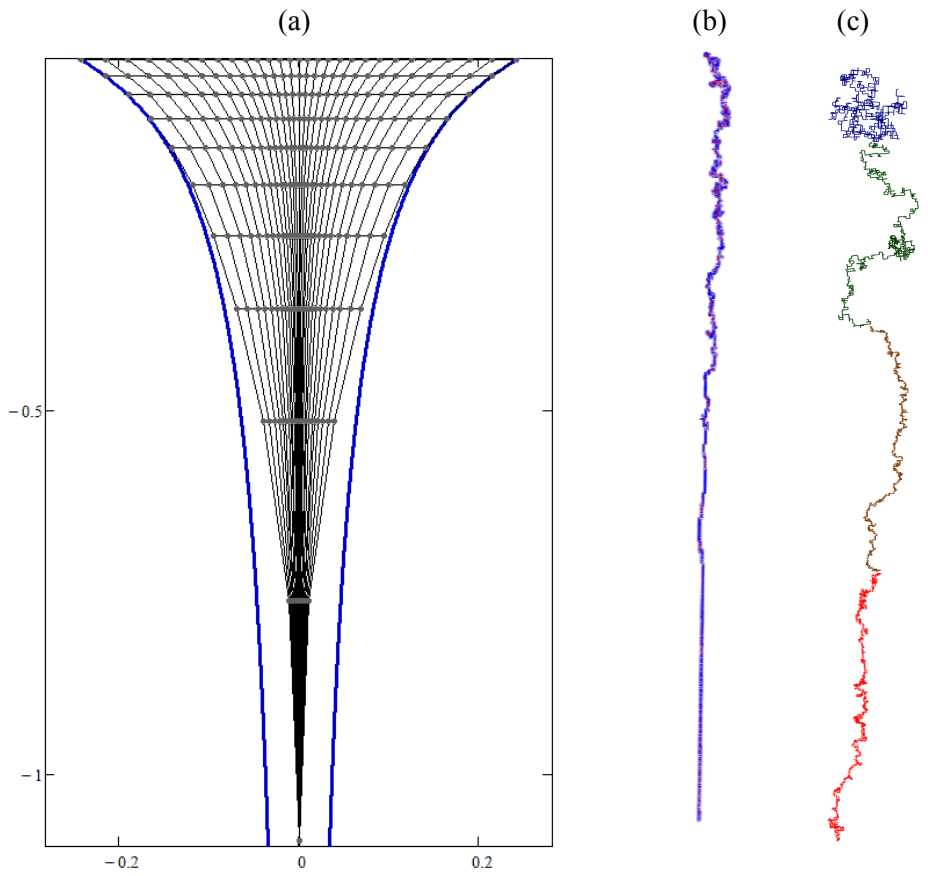

Figure 4-21. Conformation of the polymer network during electrospinning, simulated using the force functions of Equation (4.24) including radial compression. The conditions are as in Figure 4-20, with r_0=2.5·10^5 step. (a) Network map of a jet section ~1 mm long: line segments represent subchains and line crossings topological entanglements. Viewed density is diluted x800 in each direction. The jet profile is depicted by the external (blue) lines. (b) A single vertical sequence of linked subchains along the z axis. (c) Same as (b), but with enlarged subchains (not to scale).

As already implied in the analysis of a single chain in a flow field (Section 4.1.4), the network simulation can be achieved by running a single "very long" chain of ~10^7 monomers, which represents a sequence of subchains in the axial direction. Shortly after the jet start, f_0 and v_0 in Equation (4.21) can be neglected, and the force function becomes analogous to that of a single chain in a flow field [Equation (4.13)], $f \cong \tau_0 v$. The force center is chosen at the jet start, where the relative velocity between the network and the solvent is zero, so that half of the chain extends in the direction $+z$, and the opposite half is imaginary. v is the jet velocity, and τ_0 is the monomer's relaxation time in the dilute fluid of viscosity η. Such a "long" chain is depicted in Figure 4-21(b). This analogy also implies a network stretch transition, and the existence of two distinct energy equilibrium states and corresponding network stretching lengths; however, as pointed out in the single chain analysis, for a very long chain this transition occurs at a very low velocity gradient (see for example the left

curve in Figure 4-16), and is therefore not expected during electrospinning.

Using the same approach as for a single chain under tension (Section 4.1.3), the subchain mean end-to-end distance (mesh size), ξ, that results from the force functions (ignoring radial compression), is

$$\begin{aligned}\frac{\xi_z}{\xi_{\max}} &= \frac{\sinh\left[f_0+\tau_0\left(v_z-v_0\right)\right]}{\cosh\left[f_0+\tau_0\left(v_z-v_0\right)\right]+2\cosh\left[f_0\right]},\\ \frac{\xi_\rho}{\xi_{\max}} &= \frac{\sinh\left(f_0\right)}{\cosh\left[f_0+\tau_0\left(v_z-v_0\right)\right]+2\cosh\left(f_0\right)}.\end{aligned} \tag{4.25}$$

These equations are depicted in Figure 5.1-3. Shortly after the jet start, but before the network approaches full stretching ($f<1$), the relative longitudinal elongation of a subchain can be approximated by

$$\frac{\xi_z}{\xi_0} \approx \frac{\xi_0\tau_0 v_0}{3}\left(\frac{v_z}{v_0}\right). \tag{4.26}$$

The dimensionless prefactor $\frac{1}{3}\xi_0\tau_0 v_0$ (length in unit steps), or $\frac{1}{3}\xi_0 v_0 a\eta/\left(k_B T\right)$ (length in nm), determines the elongation of the network with respect to that of the jet, and is of order $10^1 10_s^{-8} 10_{s^{-1}}^7 \sim 1$. Note the similarity between this prefactor and the dimensionless parameter α used in the theoretical modeling of the network in Equation 5.1-12 (they are the same if z_0 is substituted by a, and the inertia m is neglected), both of which determine the extent of affinity. In case $\frac{1}{3}\xi_0\tau_0 v_0 = 1$, the network elongation is affine, as found by the theoretical modeling [Equation (5.1-12)]. In case $\frac{1}{3}\xi_0\tau_0 v_0 < 1$, the network elongation is slower that the jet, and vice versa. Conversely, if affinity is assumed, the value of the monomer's relaxation time should be $\tau_0 = 3a^2/\left(\xi_0 v_0\right)$ (length in nm), and the corresponding effective viscosity should be $\eta \approx 3k_B T/\left(a\xi_0 v_0\right)$.

In the case of a constant gradient $s = v_0 k$ in the z direction, the force in that direction is $f_z \approx s\tau_0 z \approx s\tau\bar{z}/N_s$ (ignoring f_0), where $\tau \approx \tau_0 N_s^{3/2}$ is the subchain relaxation time, and $\bar{z} = z/N_s^{1/2}$ is the relative position. This force is analogous to the force in the case of a single chain [Equation (4.14)]. The subchain end-to-end distance is $\xi_z \approx \frac{1}{3}N_s\tau_0 v_z \approx \frac{1}{3}s\tau\bar{z}$ (in unit steps).

4.2 Fast X-ray phase-contrast imaging

In-line fast X-ray phase-contrast imaging[71, 72] was used for measuring the geometry, velocity and radiation absorption of the straight section of electrospinning jets. The experiments were carried out at 32-ID Beamline, Advanced Photon Source [APS, Figure 4-22(a)], Argonne National Lab in Chicago, using a partially coherent undulator X-ray white beam. The experimental setup [Figure 4-22(b)], located inside a sealed room for protection against exposure to X-ray radiation, was remotely controlled during the measurements.

Velocity was measured by tracing silica microbeads mixed in the solution at low volume fraction (<1%), using two-pulse images. Polymer concentration variations caused by polymer network stretching [see example in Figure 4-22(c)] were derived from X-ray absorption measurements,. More details are presented in Figure 5.2-1, Figure 5.2-2, and the related text.

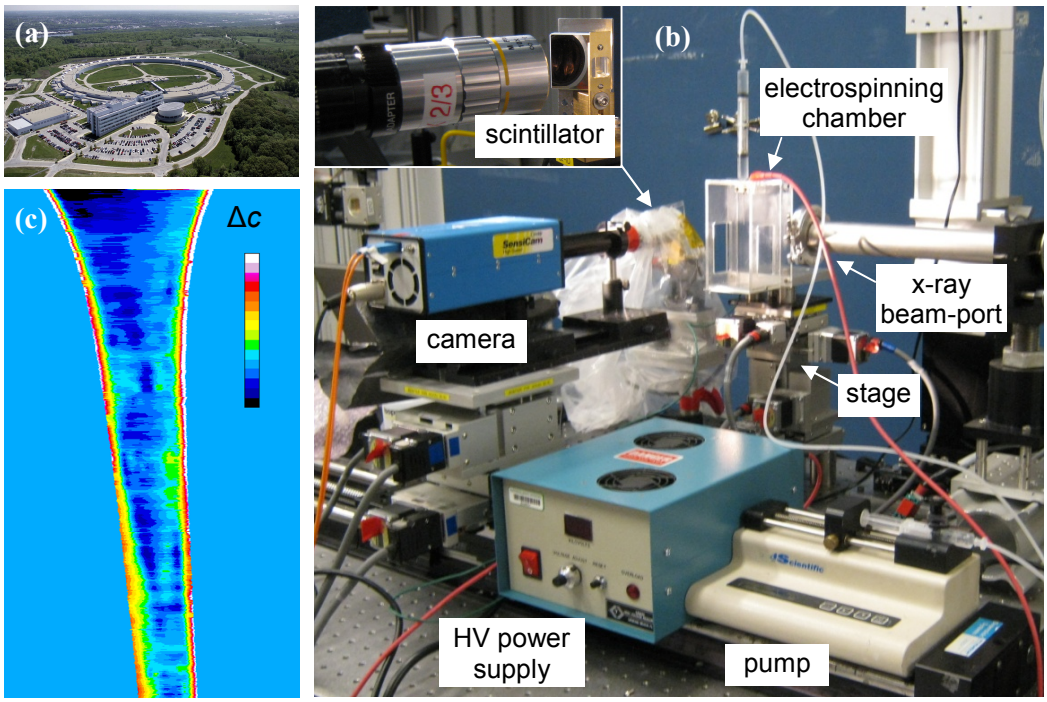

Figure 4-22. Fast X-ray phase-contrast imaging. (a) Advanced Photon Source in Argonne National Laboratory. (b) Experimental setup of X-ray imaging during electrospinning. The X-ray beam passed through the electrospinning chamber, was imaged by the scintillator and recorded by the camera. The motorized stage allowed remote control of the chamber position. (c) Example of polymer concentration change map, derived from the absorption measurements.

The method offers several unique advantages, among them an extremely short exposure time (< 0.5 μs), high spatial resolution (0.67 μm/pixel), high penetrability, enhanced phase boundary contrast, and an essentially monochromatic beam.

Two concerns are associated with the application of the technique to the study of electrospinning jets. Prolonged exposure of the jet to X-ray radiation may degrade the polymer or affect the solvent, as well as disrupt the flow of the jet. To avoid these problems, only the jet section that was currently imaged was exposed to the beam, and the setup was tuned to capture the transmission image of the first issued X-ray pulse. The second concern is the significant scattering of X-rays penetrating a small object,[73] seen in the peculiar transmission profile at a cross section of the jet (Figure 5.2-5), dominated by edge diffraction. In particular, the scattering effects are high when the distance between the jet and the imaging target (the scintillator) is relatively large (10 cm in our experiment), and when the jet diameter becomes small.

The rest of the section presents the acquisition and analysis technique, including the introduction of a correction factor for neutralizing the scattering effect. The block diagram in Figure 4-23 summarizes the process of X-ray image acquisition, processing, and analysis.

Each recorded image of the transmitted X-ray intensity (raw image), I_{trans}, was processed using imageJ (see example in Figure 5.2-6), by removing the recorded reference intensity (dark image), I_{dark}, and normalizing by the recorded background intensity (background image), I_{back}, in order to remove spatial nonuniformity and normalize the background transmission to 1. The resulting transmission of each pixel (x,y) in the image, $T_{exp}(x,y)$, is given by:

$$T_{exp}(x,y)=\frac{I_{trans}(x,y)-I_{dark}(x,y)}{I_{back}(x,y)-I_{dark}(x,y)}, \tag{4.27}$$

Due to pixel noise remaining after background removal, data smoothing was done by running the Mathcad supsmooth function, which uses a local linear least-squares fitting with an adaptive bandwidth.

The polymer concentration mapping of the jet makes use of the different X-ray mass absorption coefficients of the polymer and solvent, ε_p and ε_s, respectively. Specifically, at the testing beam energy, the PEO [poly(ethylene oxide)] polymer and the solvent (water) had absorption coefficients of $\varepsilon_p = 1.51$ cm^2/gr and $\varepsilon_s = 2.29$ cm^2/gr, respectively.[74] The absorption coefficient of the polymer solution is then given by[75]

$$\alpha(r,z)=\varepsilon_p c_p(r,z)+\varepsilon_s c_s(r,z), \tag{4.28}$$

where c_p and c_s denote the mass concentrations of the polymer and solvent, respectively, and the coordinates (r,z) are the radial and axial position in the jet, respectively. Using the volume fraction relationship $c_s/\rho_s = 1 - c_p/\rho_p$ (ρ denotes density), the change in the local polymer concentration, $\Delta c_p(r,z)$, is linearly dependent on the change in the local absorption coefficient $\Delta\alpha(r,z)$:

$$\Delta c_p(r,z)=\frac{\Delta\alpha(r,z)\rho_p}{\varepsilon_p\rho_p-\varepsilon_s\rho_s}, \tag{4.29}$$

where $\Delta\alpha(r,z)=\alpha(r,z)-\alpha_0$ is the change in the local absorption coefficient, with respect to the solution's initial absorption coefficient α_0 obtained from Equation (4.28).

We can obtain the change in the apparent absorption coefficient, $\Delta\alpha_{app}(r,z)$, by subtracting the simulated absorption coefficient α_{sim} of a homogenous jet, from the measured absorption coefficient α_{exp} (Figure 5.2-5):

$$\Delta\alpha_{app}(r,z)=\alpha_{exp}(r,z)-\alpha_{sim}(r,z)=-\frac{1}{d(r,z)}\ln\frac{T_{exp}(r,z)}{T_{sim}(r,z)}, \tag{4.30}$$

where $d(r,z)$ is the beam travel distance through the jet at a position (r,z) on the jet, calculated by Equation (5.2-1), and T_{sim} is the simulated transmission of a homogenous jet. The absorption coefficients were calculated by the Beer–Lambert absorption law, $\alpha_{exp}(r,z)=-\ln T_{exp}(r,z)/d(r,z)$ and $\alpha_{sim}(r,z)=-\ln T_{sim}(r,z)/d(r,z)$.

The local jet diameter was measured by an algorithm that detects the edge diffraction white peaks, and adjusts for the diffraction width. The algorithm also sets the pixel position of the jet center, and converts the data from image space (x,y) to jet space (r,z). The variable T_{sim} was calculated by a wave propagation simulation (performed by the APS team), that accounts for all the optical effects when penetrating a homogenous polymer solution cylinder of a given diameter, at the X-ray beam energy used in the experiment.

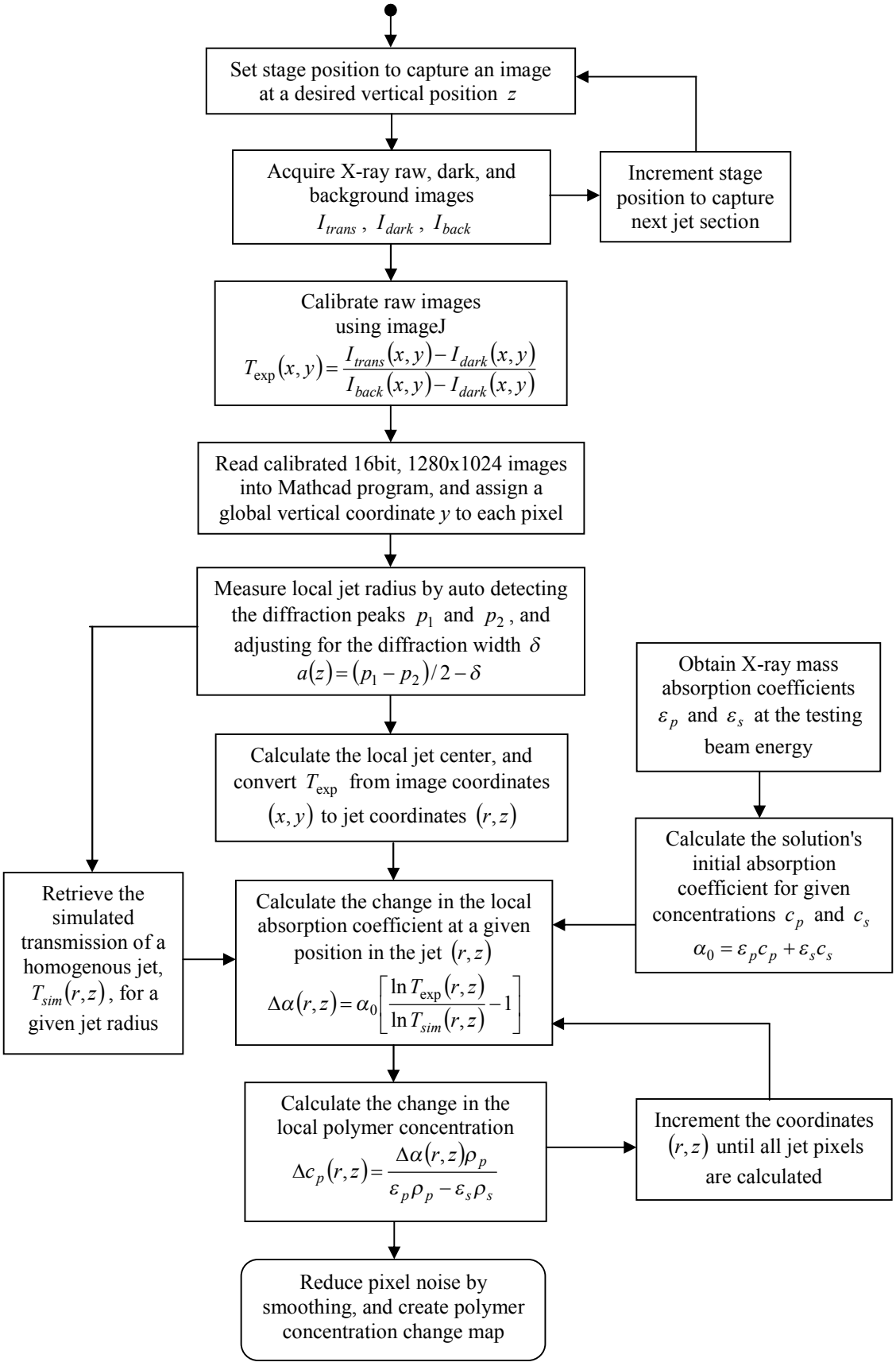

Figure 4-23. Process used for X-ray image acquisition, processing, and analysis.

The apparent absorption coefficient of Equation (4.30), α_{app}, consists of an absorption term α and a scattering term α_{scat}, such that $\alpha_{app} = \alpha + \alpha_{scat}$.[75] However, for the purpose of calculating the polymer concentration changes by Equation (4.29), the effect of the scattering term must be removed. This is achieved by introducing a correction factor, $\alpha_0 / \alpha_{sim}(r,z)$, where α_0 and $\alpha_{sim}(r,z)$ are the absorption and apparent absorption coefficients of a homogenous jet, respectively.

Since α_0 reflects only absorption, whereas α_{sim} incorporates both absorption and scattering, this correction factor filters out the effects of scattering in a homogenous jet, and can be used as an approximation for the non-homogenous electrospinning jet. The corrected local change in the absorption coefficient is:

$$\Delta\alpha(r,z) = \Delta\alpha_{app}(r,z)\frac{\alpha_0}{\alpha_{sim}(r,z)} = \alpha_0\left[\frac{\alpha_{exp}(r,z)}{\alpha_{sim}(r,z)} - 1\right] = \alpha_0\left[\frac{\ln T_{\exp}(r,z)}{\ln T_{sim}(r,z)} - 1\right]. \quad (4.31)$$

Notice that the corrected absorption coefficient is invariant with respect to the beam travel distance through the jet, $d(r,z)$.

5. Research description and results - publications

5.1 Polymer dynamics during electrospinning

Greenfeld, I., A. Arinstein, K. Fezzaa, M.H. Rafailovich, and E. Zussman, *Polymer dynamics in semidilute solution during electrospinning: A simple model and experimental observations.* Physical Review E, 2011. **84**(4): p. 041806.[1]

Polymer dynamics in semidilute solution during electrospinning: A simple model and experimental observations

Israel Greenfeld,[1] Arkadii Arinstein,[1] Kamel Fezzaa,[2] Miriam H. Rafailovich,[3] and Eyal Zussman[1]
[1]*Department of Mechanical Engineering, Technion, Israel Institute of Technology, Haifa 32000, Israel*
[2]*Advanced Photon Source, Argonne National Laboratory, Argonne, Illinois 60439, USA*
[3]*Department of Materials Science and Engineering, State University of New York, Stony Brook, New York 11794-2275, USA*
(Received 25 July 2011; published 14 October 2011)

Electrospun polymer nanofibers demonstrate outstanding mechanical and thermodynamic properties as compared to macroscopic-scale structures. Our previous work has demonstrated that these features are attributed to nanofiber microstructure [Nat. Nanotechnol. **2**, 59 (2007)]. It is clear that this microstructure is formed during the electrospinning process, characterized by a high stretching rate and rapid evaporation. Thus, when studying microstructure formation, its fast evolution must be taken into account. This study focuses on the dynamics of a highly entangled semidilute polymer solution under extreme longitudinal acceleration. The theoretical modeling predicts substantial longitudinal stretching and transversal contraction of the polymer network caused by the jet hydrodynamic forces, transforming the network to an almost fully stretched state. This prediction was verified by x-ray phase-contrast imaging of electrospinning jets of poly(ethylene oxide) and poly(methyl methacrylate) semidilute solutions, which revealed a noticeable increase in polymer concentration at the jet center, within less than 1 mm from the jet start. Thus, the proposed mechanism is applicable to the initial stage of the microstructure formation.

DOI: 10.1103/PhysRevE.84.041806 PACS number(s): 83.80.Rs, 47.85.md, 83.50.Jf, 47.61.−k

I. INTRODUCTION

The size-dependent behavior of nano-objects is a generally accepted phenomenon, observed in polymer nanofibers [1,2], metallic nanowires [3], and thin polymer films [4]. Experimental studies have demonstrated the effect of size on the mechanical, thermomechanical, and thermodynamic properties of nano-objects. For example, the elastic modulus of nanowires [3], polypyrrole nanotubes [5], and electrospun polystyrene and nylon-66 nanofibers [1,2] sharply increases when their diameter becomes sufficiently small. Also, a shift in the glass transition and melting temperatures is observed in polymer nano-objects [6]. All proposed mechanisms attributing this behavior to surface tension [5] or near-surface layers [7,8] do not satisfactorily explain the above phenomena. Moreover, our recent work has demonstrated that the contribution of surface energy to size-dependent elasticity of nano-objects is negligible [9]. Overall, the physical mechanisms governing the size-dependent behavior of nano-objects are largely unclear.

Further progress in understanding of the features of electrospun polymer nanofibers influencing their behavior requires examination of their internal structure, more specifically, the supermolecular structures in the amorphous regions of the polymer matrix, as well as crystallite ordering. At the initial stages of such analyses, the impact of fabrication conditions upon the final state of the polymer matrix of as-spun nanofibers must be determined. In doing so, the high strain rate (on the order 10^3 s^{-1}) acting during electrospinning [10–16], must be considered. This dominant factor is believed to cause stretching and orientation of polymer chains, as indicated by in-process measurements of jets, using birefringence [17] and Raman [18] techniques.

In parallel, extremely rapid evaporation of solvents adversely affects the polymer matrix macrostructure of as-spun nanofibers**.** Rapid evaporation first leads to formation of a solid skin, followed by further evaporation from the liquid core, leaving voids previously occupied by solvents and allowing partial relaxation of the matrix. This frequently induces generation of a heterogeneous and porous fiber structure [19,20]. Theoretical analyses [21,22], confirmed by experimental observations [19] and computerized simulations [23], demonstrated that a sharp increase in polymer density at the fiber-vapor interface is induced upon rapid solvent evaporation, consequently increasing heterogeneity and porosity. Thus, heterogeneous, high-porosity fiber structures can be formed under certain electrospinning conditions [see Fig. 1(a)].

At the same time, skin formation prevents further stretching and orientation of polymer chains within the semiliquid fiber core. Relaxation of the nonequilibrium state of the stretched macromolecules consequentially occurs, with no detectable influence of the fabrication conditions on the final state of the polymer matrix of as-spun nanofibers. On the other hand, spinning conditions resulting in homogeneous as-spun fiber structures can be selected [see Fig. 1(b)]. In such cases, relaxation of stretched polymer chains is suppressed, and the effect of fabrication conditions on the final state of the nanofiber polymer matrix should be noticeable.

While the physical mechanism underlying formation of the porous structure of as-spun nanofibers is well understood [19,21,22], the physical principles governing generation of the homogeneous fiber structure demand clarification. Significant insight is expected to emerge from examination of the evolution of the polymer system within the semidilute solution jet during electrospinning. The mechanism required to form an homogeneous fiber structure can be proposed based on the assumption that the polymer system, which is an interconnected network of subchains, undergoes substantial stretching during electrospinning.

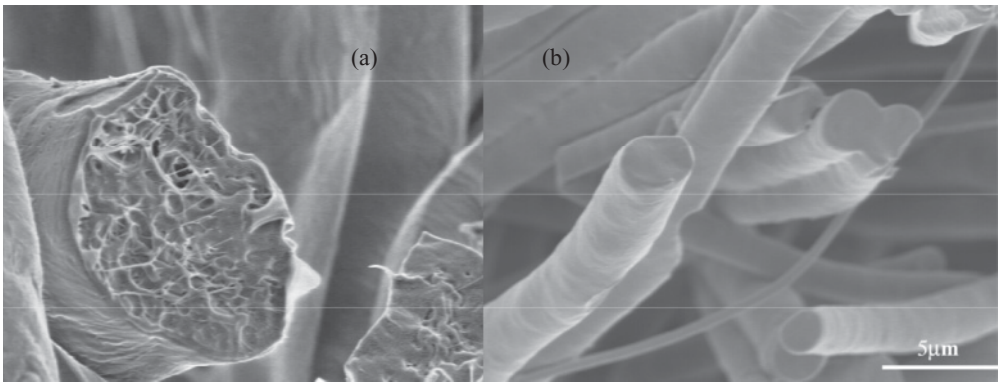

FIG. 1. SEM images of electrospun nanofibers fabricated from 10 wt% PCL (Mw 80 kDa) in DCM/DMF (75:25 wt%), in an electric field of 0.63 kV/cm [24]. (a) Heterogeneous fibers fabricated at a flow rate of 20 ml/h and (b) homogeneous fibers fabricated at a flow rate of 3 ml/h.

In order to confirm the stretching hypothesis, a theoretical model describing the polymer system as an entangled network and its evolution in the initial stage of electrospinning is presented. The conformational state of individual subchains is clarified by a three-dimensional (3D) random-walk simulation. The theoretical analysis and simulations show that the initial equilibrium state of the polymer network transforms to an almost fully stretched state along the jet. This stretching is accompanied by network contraction across the jet. These theoretical results were experimentally confirmed by x-ray phase-contrast imaging of electrospinning jets of PEO (polyethylene oxide) and PMMA (polymethyl methacrylate) semidilute solutions, which revealed a noticeable polymer concentration increase at the jet center, within less than 1 mm from the jet start.

II. THEORETICAL MODELING

A. Velocity and radius of an electrospinning jet

Under an electric field, the moving solution jet accelerates, so that its local velocity contains both longitudinal and radial components. Hydrodynamic analysis demonstrates that in the jet beginning the longitudinal velocity can be approximated by a parabolic profile, whereas the radial velocity component increases linearly along the jet [25]:

$$v_z \approx v_0\left(1+\frac{z}{z_0}\right)^2, \quad v_r = -\frac{r}{2}\frac{\partial v_z}{\partial z} \approx -v_0\left(1+\frac{z}{z_0}\right)\frac{r}{z_0}, \tag{1}$$

and, therefore, the jet has the hyperpolic form:

$$r_J(z) = \frac{r_0}{1+z/z_0}, \tag{2}$$

where v_0 is the jet initial velocity and r_0 is the jet initial radius. The characteristic length z_0 determines the scale of velocity increase and depends on the solution's flow rate, viscosity, electric field, and electric conductivity. Typical values of these parameters, measured by optical microscopy of the jet [15,16], and substantiated by our experimental observations are $v_0 \sim (1\text{–}5) \times 10^{-2}$ m/s and $z_0 \sim (0.5\text{–}1) \times 10^{-3}$ m. Such hydrodynamic flux with increasing longitudinal velocity influences on the polymer macromolecules results in their nonequilibrium conformation state and heterogeneous distribution inside the jet.

The velocity increase of the liquid jet is clearly limited, due to viscosity increase as a result of solvent evaporation and final solidification of the jet. Since this work focuses only on the initial stage of jet spinning, the above saturation effect lies beyond the scope of this paper.

B. Polymer system structure

It is well known that viscoelasticity is a prerequisite for polymer solution spinnability, meaning that spinnable solutions are semidilute, highly entangled. Therefore, the polymer system is assumed to be a network, whose connectivity is provided by topological knots [11] [see Fig. 2(a)]. The sections of macromolecules between two adjacent topological knots are called subchains, which feature a conformation at equilibrium that corresponds to their nonzero end-to-end distance, even in the absence of external force. This end-to-end distance is equal to the distance between two topological knots or to an average

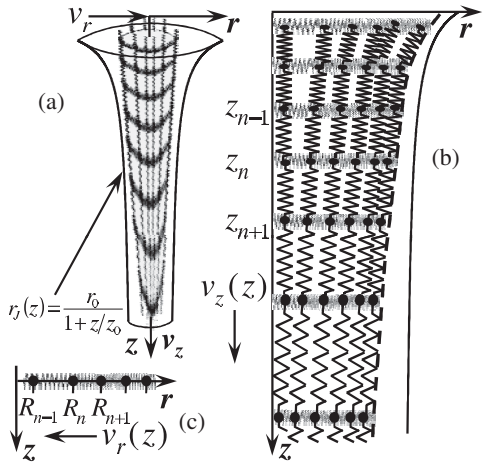

FIG. 2. (a) Illustration of polymer network stretching in an electrospinning jet. (b) Definition of an effective 1D system describing polymer network stretching in the axial direction. (c) Definition of an effective 1D system describing polymer network contraction in the radial direction.

mesh size ξ_0 of the network in a semidilute solution

$$\xi_0 \propto R_g (c/c^*)^{\nu/(1-3\nu)}, \tag{3}$$

where $R_g \propto aN^{\nu}$ is the end-to-end distance of a polymer coil, c is the mass concentration of the polymer solution, c^* is the crossover concentration of macromolecules overlap, N is the number of monomers in a polymer chain, and a is the monomer scale. Solvents usually used in such systems vary between good and moderately poor solvents; so the conformation of a polymer chain should be a Gaussian or swelled coil ($1/2 < \nu < 3/5$). On the other hand, the polymer concentration in spinnable solutions is relatively high [$(5-10)\times c^*$], and this prevents a coil swelling. Therefore, for simplicity, we can assume that $\nu = 1/2$. Assuming Gaussian statistics of subchains, one can estimate the number of monomers in a subchain as follows:

$$N_s = (\xi_0/a)^2 = N(c/c^*)^{-2}. \tag{4}$$

Thus, the elements of the system which undergo noticeable stretching are the above-defined subchains. The evolution of subchain conformation under stretching of the polymer network will now be examined.

C. Axial stretching of an entangled polymer network during electrospinning

The polymer network in question can be approximated by a lattice model of "beads" and linear "springs," similar to the Rouse model. Each bead represents a topological knot and is connected to six adjacent beads by springs, or polymer subchains, demonstrating Gaussian statistics, leading to a linear force-elongation relationship. The averaging of the system over the jet cross section results in a one-dimensional chain of springs that interconnects the beads, each having an effective subchain mass, m. The beads are influenced by an effective hydrodynamic force proportional to the effective subchain size, $a_{\text{eff}} \propto \xi_0$, as well as entropic elastic forces from its two neighbors [see Fig. 2(b)]. The dynamics of this chain of springs can be described by the following difference-differential equation:

$$m\frac{d^2 z_n}{dt^2} = a_{\text{eff}}\eta\left[v_z(z_n) - \frac{dz_n}{dt}\right] + \frac{T}{\xi_0^2}\{[z_{n+1} - z_n - \xi_0] - [z_n - z_{n-1} - \xi_0]\}, \tag{5}$$

where η is the effective viscosity of the dilute solution surrounding the polymer network, v_z is the jet axial velocity from Eq. (1), and T/ξ_0^2 is the entropic elasticity of polymer subchains, where T is the temperature in units of the Boltzmann constant k_B.

The difference equation (5) can be approximated by the following differential equation:

$$\frac{d^2 z(l,t)}{dt^2} = \frac{a_{\text{eff}}\eta}{m}\left[v_z(z) - \frac{dz(l,t)}{dt}\right] + c_{\text{net}}^2\frac{d^2 z(l,t)}{dl^2}, \tag{6}$$

where $c_{\text{net}} = \sqrt{T/m} \sim 0.3$ m/s is the "sound" velocity in the polymer network and $l = \xi_0 n$. As the polymer network demonstrates only entropic elasticity of a semidilute solution, it is much lower than the sound velocity in solid polymer systems. The polymer is at equilibrium at the cross section $z = -z_0$, while free boundary conditions are assumed at $z = +\infty$.

The partial differential equation (6) allows one to find a self-similar solution. Indeed, upon introduction of the dimensionless, self-simulated variable $\varsigma = (l + v_0 t)/z_0$ and the function $\hat{z}(\varsigma) = z(l,t)/z_0$, Eq. (6) can be rewritten as an ordinary differential equation:

$$\frac{d^2\hat{z}(\varsigma)}{d\varsigma^2} = -\alpha\left[\hat{v}_z(\hat{z}) - \frac{d\hat{z}(\varsigma)}{d\varsigma}\right]; \tag{7}$$

here $\alpha = z_0 v_0 a_{\text{eff}}\eta/[m(c_{\text{net}}^2 - v_0^2)] \sim 10^3$–$10^4 \gg 1$ is a dimensionless parameter and $\hat{v}_z(\hat{z}) = v_z(z)/v_0$.

Using the substitution $d\hat{z}(\varsigma)/d\varsigma = P(\hat{z})$, the second-order differential equation (7) can be reduced to a first-order equation:

$$\frac{dP(\hat{z})}{d\hat{z}} = -\alpha\left[\frac{\hat{v}_z(\hat{z})}{P(\hat{z})} - 1\right]. \tag{8}$$

The solution of Eq. (8) can be obtained, using a $(1/\alpha)$ approximation. Assuming that

$$\frac{\hat{v}_z(\hat{z})}{P(\hat{z})} - 1 = \frac{1}{\alpha}P_1(\hat{z}) + \cdots, \tag{9}$$

we obtain $P_1(\hat{z}) = -d\hat{v}_z(\hat{z})/d\hat{z}$, so within accuracy of $(1/\alpha)^2$ the function $P(\hat{z})$ is

$$P(\hat{z}) = \frac{d\hat{z}(\varsigma)}{d\varsigma} = \frac{dz(l,t)}{dl} \approx \frac{\hat{v}_z(\hat{z})}{1 - \frac{1}{\alpha}d\hat{v}_z(\hat{z})/d\hat{z}}, \tag{10}$$

and the function $\hat{z}(\varsigma)$ can be obtained as an inverse function:

$$\varsigma(\hat{z}) = \int_0^{\hat{z}}\frac{dx}{\hat{v}_z(x)} - \frac{1}{\alpha}\ln[\hat{v}_z(\hat{z})]. \tag{11}$$

The stretching of the polymer network is characterized by Eq. (10), which allows one to determine the stretched mesh size $\xi_{\parallel}$ along the jet

$$\xi_{\parallel} = \xi_0\frac{dz(l,t)}{dl} \approx \frac{\xi_0\hat{v}_z(\hat{z})}{1 - \frac{1}{\alpha}d\hat{v}_z(\hat{z})/d\hat{z}}. \tag{12}$$

The obtained dependence $\xi_{\parallel}/aN_s$ is shown in Fig. 3 with respect to the position z along the jet, for longitudinal velocity v_z from Eq. (1). Note that the stretching of the polymer subchains exceeds the maximal possible elongation corresponding to fully stretched subchains.

The region where the stretched subchains are approaching full extension, i.e., $\xi_{\parallel} \simeq aN_s$, can be estimated using Eq. (12) for $\alpha \gg 1$ resulting in $\hat{v}_z(\hat{z}) \simeq N_s^{1/2}$. Using typical values for electrospinning solution jets of the experimental system (PEO 3 wt% in water; see Sec. III), we may predict that the stretching occurs at $z_{\text{stretch}}/z_0 \simeq 3.5$.

A term providing the unlimited increase in an effective modulus of an almost fully stretched subchain can be introduced into Eq. (5) by replacing the linear elasticity of polymer subchains, T/ξ_0^2, with the nonlinear $T/\{\xi_0^2[1 - (z_{n+1} - z_n)/aN_s]\}$. However, such a modification does not account well for the system behavior and the additional processes associated with high levels of polymer subchain stretching. More specifically, almost fully stretched subchains begin to disentangle, thereby raising the subchain length ξ_0. In addition, the highly stretched polymer network begins to

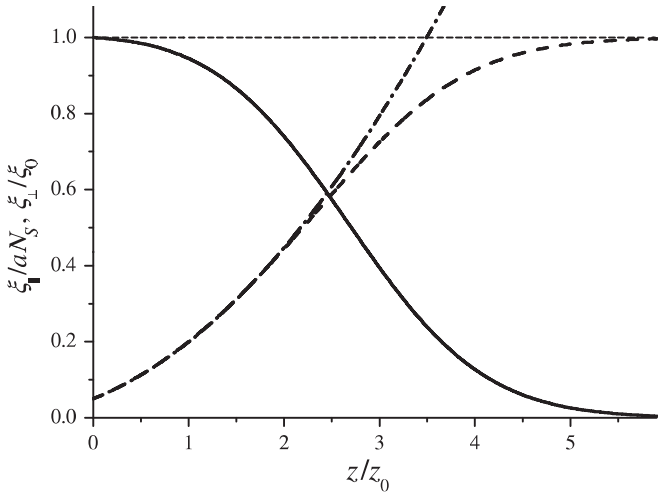

FIG. 3. Polymer network conformation. Relative radial contraction, $\xi_\perp/\xi_0$ (solid line), and relative axial stretching, $\xi_\parallel/aN_s$ (dashed and dot-dashed lines), vs the relative axial position, z/z_0. The results were obtained by the simulation (dashed and solid lines) and theoretical model (dot-dashed line). Parameters are $N_s = 400$, $\alpha = 1000$, and $\beta = 0.3$.

affect the effective viscosity of the solution, influencing the jet velocity. Furthermore, slipping of the solvent surface layer relative to the polymer network is also possible.

For these reasons we would like to restrict ourselves to the simplest model describing only the initial stage of polymer network evolution inside the electrospinning jet. Although the proposed model does not describe the final state of the polymer matrix in electrospun nanofibers, and is applicable only to the initial part of the jet where the stretching of a polymer system is not too high, it allows for analysis and understanding of the tendency in the evolution of the polymer during the electrospinning process.

Note that the transformation of subchains from a coil-like equilibrium state into a stretched state occurs as a continuous crossover, and no phase transition is observed, in contrast to the well-known coil-stretch transition, described by de Gennes [26]. Unlike stretching of an individual chain, during network stretching locally the dominant force that provides this transformation is the elastic force, whereas the hydrodynamic forces give rise to the global stretching of the network. As a result, the network subchains are subjected to the action of the network portion situated farther along the jet, a force independent of local stretching. In contrast, the force acting on an individual polymer chain under an ultrahigh velocity gradient increases with macromolecule stretching. Similar behavior, continuous crossover from a coil-like state into a stretched state was observed by Balabaev *et al.* upon examination of the state of an individual macromolecule under an external force acting on its ends [27].

D. Radial contraction

When analyzing the compression of the polymer network in a plane perpendicular to the jet, the process becomes stationary quite rapidly and can be presented as a one-dimensional (1D) chain of springs [see Fig. 2(c)] in a steady state, described by the following differential equation:

$$\frac{T}{\xi_0^2}\{[R_{n+1} - R_n - \xi_\perp] - [R_n - R_{n-1} - \xi_\perp]\} + a_{\text{eff}}\eta v_r(R_n) = 0, \tag{13}$$

which can be approximated by the following differential equation [using the velocity v_r from Eq. (1)]:

$$\frac{d^2R(\rho,z)}{d\rho^2} - \kappa^2(z)R(\rho,z) = 0, \tag{14}$$

where $\rho = r/z_0$, $\kappa(z) = \kappa_0[\xi_0/\xi_\perp(z)]\sqrt{1+z/z_0}$, and $\kappa_0^2 = z_0 v_0 a_{\text{eff}}\eta/mc_{\text{net}}^2 = (v_0^2/c_{\text{net}}^2 - 1)\,\alpha$, ($\kappa_0 \sim 10$–$10^2$).

The boundary conditions for Eq. (14) are

$$\frac{dR(\rho_0)}{d\rho} - z_0 + \frac{\xi_\perp(z)}{z_0}\kappa^2(z)\,R(\rho_0) = 0, \quad R(0) = 0, \tag{15}$$

where $\rho_0 \equiv \rho_0(z) = r_J(z)/z_0$ corresponds to the jet radius in the cross section z [see Eq. (2)], and $\xi_\perp$ is the lateral contraction of the mesh size due to the axial stretching $\xi_\parallel$:

$$\xi_\perp = \frac{3\xi_0}{2 + \left[1 - \left(a\xi_\parallel/\xi_0^2\right)^2\right]^{-1/2}}. \tag{16}$$

The solution of Eq. (14) with the boundary conditions (15) is

$$R(\rho,z) = \frac{z_0 \sinh[\kappa(z)\rho]\,/\cosh[\kappa(z)\rho_0]}{\kappa(z)\{1 + [\xi_\perp(z)/z_0]\,\kappa(z)\tanh[\kappa(z)\rho_0]\}}. \tag{17}$$

The polymer network radius, $R_P(z)$, is given at $\rho = \rho_0$ by the following form:

$$R_P(z) = \frac{z_0 \tanh[\kappa(z)\rho_0]}{\kappa(z)\{1 + [\xi_\perp(z)/z_0]\,\kappa(z)\tanh[\kappa(z)\rho_0]\}}. \tag{18}$$

For small values of argument $\kappa(z)\rho_0 \ll 1$ and $\kappa(z)\xi_\perp(z)/z_0 \ll 1$, Eq. (18) demonstrates no radial contraction of the polymer network, yielding

$$R_P(z) = z_0\rho_0(z) = r_J(z). \tag{19}$$

For large values of the argument of "tanh" ($\kappa(z)\rho_0 \gg 1$) one can assume that $\tanh[\kappa(z)\rho_0] \approx 1$, so that Eq. (18) can be simplified. Taking into account the fact that $\kappa(z)\xi_\perp(z)/z_0 \ll 1$, in the case of finite z/z_0 one can write

$$R_P(z) = \frac{\xi_\perp(z)}{\xi_0}\frac{z_0}{\kappa_0\sqrt{1+z/z_0}}, \tag{20}$$

and in the case of large z ($z/z_0 \gg 1$) the polymer network has the following form:

$$R_P(z) = \frac{z_0^2}{\kappa_0^2\xi_0(1+z/z_0)}, \tag{21}$$

indicating a constant ratio between the jet and polymer radii. However, the last asymptote lacks physical significance, as the effects dominant at this stage of the processes are not accounted for, thereby making the model inappropriate far from the jet start.

An approximation for the dependence of the polymer network radius, $R_P(z)$, on the jet radius, $r_J(z)$, can be given by

$$R_P(z) = \frac{\xi_\perp(z)}{\xi_0}r_J(z) \simeq \frac{3r_J(z)}{2 + \{1 - [a\hat{v}_z(\hat{z})/\xi_0]^2\}^{-1/2}}, \tag{22}$$

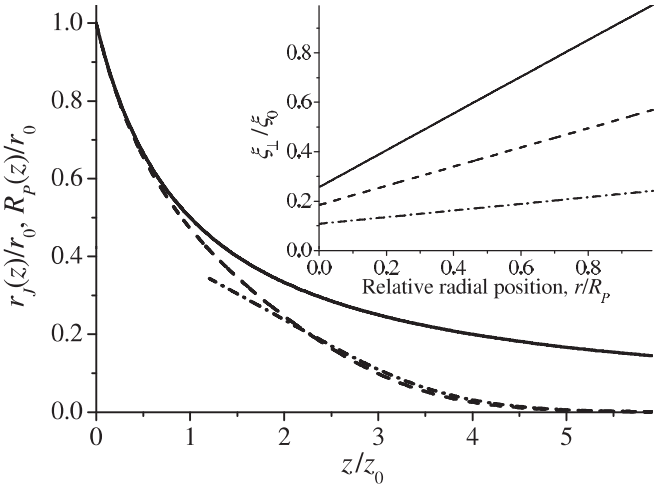

FIG. 4. Polymer network contraction. Relative jet radius r_J/r_0 (solid line) and polymer network radius R_P/r_0: dashed line Eq. (22) and dot-dashed line Eq. (20) as a function of the axial position, z/z_0. The inset displays radial contraction, $\xi_\perp/\xi_0$, obtained by simulations, as a function of the relative radial position, r/R_P, at three axial positions, $z = 0$ (solid line), $z/z_0 = 2.5$ (dashed line), and $z/z_0 = 3.5$ (dot-dashed). Parameters are the same as in Fig. 3.

showing that the axial stretching is the dominant factor determining the network radius, while the radial hydrodynamic compression has a negligible effect. When presenting the relationship, $R_P(z)/r_0$, as a function of position z along the jet and comparing it to Eq. (20), a rapid narrowing of the network radius is observed with respect to the jet radius (see Fig. 4). The expected outcome is a substantial rise in polymer concentration toward the jet center.

Summarizing the above results, one can conclude that no contraction of the polymer network occurs at the initial region of the jet. The intermediate asymptote demonstrates that the radial hydrodynamic effect is negligible, and that longitudinal stretching acts as the dominant factor affecting polymer network contraction, resulting in shortened distances between adjacent topological knots in the transversal direction. In the case of very large z ($z/z_0 \gg 1$), the form of the polymer network conforms to that of the jet. Note that the last asymptote is barely discernible in a real system, due to rapid solvent evaporation in this region, which acts as the dominant factor determining the state of the polymer system.

E. Conformational state of polymer subchains in the jet (numerical simulations)

The simplest way to examine the modification of the local conformational state of individual polymer chains along the jet is by application of the 3D random-walk model under an external field, with the help of numerical simulations. An effective potential, $U(x)$, between two adjacent topological knots connected by a polymer subchain, gives rise to "convective flux" (in addition to diffusive), which results in a nonzero end-to-end distance of subchains. The gradient of this potential, $\vec{\nabla} U(x)$, is an external force, $\vec{F}$, constituted of hydrodynamic and elastic forces acting on each subchain. Indeed, the direction of each step is determined by the stepping probabilities arising from the local effective potential

$$P_j^{\pm} = \frac{\exp(\pm F_j a/T)}{2\sum_j \cosh(F_j a/T)}; \quad j = z,\rho,\varphi, \tag{23}$$

where a is the above-introduced monomer (or Kuhn segment) scale.

In the equilibrium the effective external forces in all directions are the identical, $F_j^{(0)} \equiv F_0$, and result in the mesh size, ξ_0. Thus, the force F_0 is determined by the following equation:

$$\tanh(F_0 a/T) = 3/\sqrt{N_s} = 3a/\xi_0. \tag{24}$$

The stretching of a subchain along the jet flow direction can be accounted for by an increase in the potential gradient, $F_z = F_0 + \Delta F$. At the same time, this stretching results in transversal contraction of the polymer subchain due to redistribution of probabilities in the direction choice during the random walk. The additional potential gradient, ΔF, results in the stretching of a subchain, $\xi_\parallel$, which can be determined by the following equation:

$$\xi_\parallel = \frac{(\xi_0/a)\sinh[(F_0+\Delta F)a/T]}{\cosh[(F_0+\Delta F)a/T] + 2\cosh(F_0 a/T)}\xi_0. \tag{25}$$

Compression in the perpendicular (radial) direction corresponding to this stretching can be expressed as

$$\frac{\xi_\perp}{\xi_\parallel} = \frac{\sinh(F_0 a/T)}{\sinh[(F_0+\Delta F)a/T]}. \tag{26}$$

Note that Eq. (26) agrees with Eq. (16).

The potential gradient, ΔF_n, at subchain n comprises two components: a potential gradient corresponding to the elastic force, approximately equal to the potential gradient at the preceding subchain $n-1$, ΔF_{n-1}, and, an additional potential gradient, δF_n, corresponding to the hydrodynamic friction force acting on subchain n. Note that, as demonstrated above, the elastic force is the dominant factor acting on a subchain, and that it arises from the hydrodynamic interactions. Therefore, both the elastic and hydrodynamic forces acting on subchain n are determined by the jet velocity gradient.

The local velocity gradient, $\nabla v_{z,n}$, is practically constant within the scale of an individual subchain and yields an average velocity difference of magnitude $\frac{1}{2}\nabla v_{z,n}\xi_{\parallel,n}$ between the dilute fluid and the subchain ($\xi_{\parallel,n}$ is the mesh size of subchain in the flow direction). This velocity difference generates a friction force on each monomer (or Kuhn segment) of length a, with a corresponding average additional potential gradient of

$$\delta F_n = \tfrac{1}{2} k a \eta \xi_{\parallel,n} \nabla v_{z,n}, \tag{27}$$

where the dimensionless constant $k \propto 1$ is a geometric factor that depends on the segment's shape. Once the potential gradient, δF_n, is known for a subchain, the stepping probabilities in all six directions can be calculated from Eq. (23), and the random-walk algorithm can be applied by stepping sequentially through all the segments of the subchain.

The polymer network conformation, determined by the extension and contraction of each subchain, can be derived

by sequentially calculating the following: By knowing the state of the previous $(n-1)$ subchain, the position of the nth topological knot can be calculated as $z_n = z_{n-1} + \xi_{\parallel,n-1}$; the corresponding velocity gradient is then determined as $\nabla v_{z,n} = dv_z(z_n)/dz_n$, with the help of Eq. (1), and, assuming an extension of $\xi_{\parallel,n} \approx \xi_{\parallel,n-1}$ for the nth subchain, the additional potential gradient δF_n can be calculated from Eq. (27). The random-walk simulation with the effective force $F_n = F_0 + \sum_1^n \delta F_m$ allows one to determine the subchain extension, $\xi_{\parallel,n}$ [Eq. (25)], as well as the subchain radial contraction $\xi_{\perp,n}$ [Eq. (26)], due to redistribution of probabilities in the directions of choice during the random walks. This procedure starts at the first subchain, with the initial potential gradient F_0 [Eq. (24)] and is sequentially repeated for all subchains in the network.

The simulation uses only one dimensionless parameter $\beta = ka^2\eta v_0/T$ (~ 0.1–1). Each subchain is represented by a succession of random steps of size a. The jet parameters z_0 and v_0 are obtained from experimental measurements. The effective viscosity η is a free simulation parameter, and its resulting values, lying between the viscosity of a solvent ($\sim 10^3$ Pa·s) and the viscosity of a semidilute solution (~ 1 Pa·s), are physically plausible. The mesh sizes $\xi_\parallel$ and $\xi_\perp$, obtained from the simulation as a function of position along the jet, are depicted in Fig. 3. A difference between the theoretical model and the simulation is observed at high elongations, as the model does not account for the restriction on elongation due to the finite contour length of subchains.

A similar procedure is applied to the radial simulation, for several cross sections along the jet, starting with subchains at the jet perimeter, and continuing the sequential calculation toward the jet center. The radial mesh size, $\xi_\perp(r,z)$, obtained from the simulation as a result of the combined effect of axial stretching and radial compression, is depicted in the inset in Fig. 4. Compression due to radial hydrodynamic forces induces a further rise in polymer concentration toward the jet center, most notable at the initial region of the jet, in addition to the rise caused by axial stretching, as described before.

III. EXPERIMENTAL

A. Materials and methods

In-line fast x-ray phase-contrast imaging [28,29] was used to measure the radiation absorption of the straight region of an electrospinning jet. The experiment was carried out at the 32-ID Beamline, Advanced Photon Source (APS), Argonne National Lab, using a partially coherent undulator x-ray white beam. A scheme of the experimental setup, consisting of the x-ray imaging system and the electrospinning apparatus, is presented in Fig. 5(a).

The x-ray beam was generated from the synchrotron's electron storage ring with a dominant harmonic at 13 keV, corresponding to a wavelength of 0.95 Å [28]. The x-ray pulses were each 472 ns long, separated by a 3.68 μs time gap. A slow shutter opened the beam path at 1 Hz, and a fast shutter enabled isolation of single pulses. After penetrating the electrospinning jet, the transmitted radiation was imaged on a fast scintillator crystal (LYSO:Ce, 40 ns decay time), which converted the x-ray radiation to visible light. The scintillator's image was

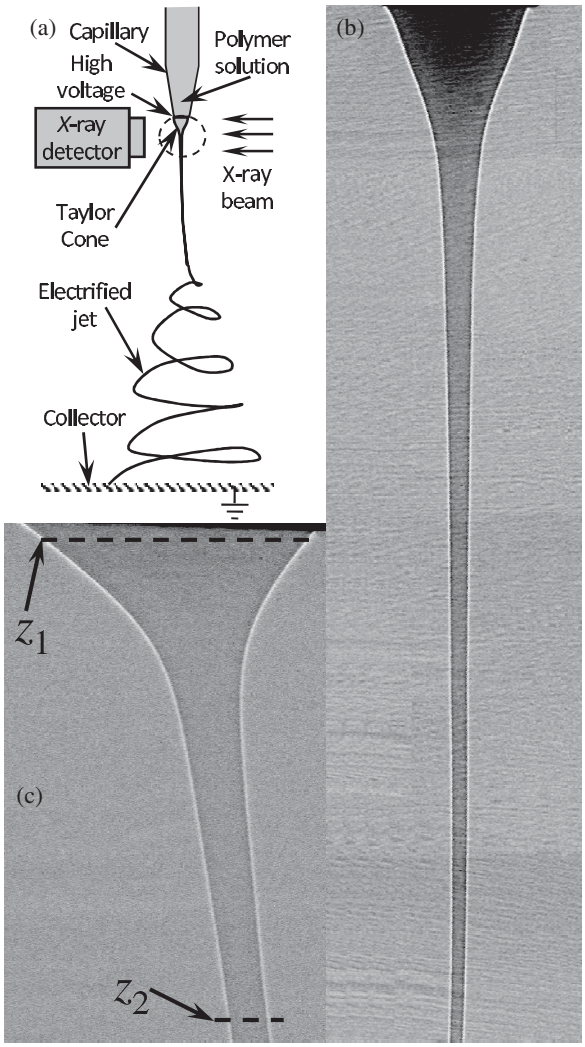

FIG. 5. (a) Schematics of electrospinning and fast in-process x-ray imaging. The imaged region is circled. (b) Rectilinear section of the jet (5 mm length), consisting of a sequence of 10 images. Electrospinning of a solution of 5 wt% PEO (Mw 600 kDa) in water; electric field 0.6 kV/cm with gap of 6.5 cm, flow rate 3.2 ml/h. (c) Zooming on the Taylor cone. The lines at $z_1 = 0.02$ mm and $z_2 = 0.5$ mm indicate the cross sections of the absorption measurements across the electrospinning jet. Electrospinning of a solution of 3 wt% PEO (Mw 600 kDa) in water; electric field 1.6 kV/cm with gap of 6.5 cm, flow rate 2 ml/h.

recorded by a 1280H×1024V CCD camera with pixel size of $6.7 \times 6.7\ \mu\text{m}^2$ via a folding mirror and a ×10 objective optics. The target (i.e., the scintillator) was distanced 10 cm from the jet, and the beam size on the target was large enough to cover the effective camera field-of-view of $0.857\text{H}\times 0.686\text{V}\ \text{mm}^2$.

A remotely controlled motorized stage enabled x,y,z positioning of the electrospinning chamber, during a single session, so that up to 8 mm of jet length could be imaged by capturing a sequence of images along the jet [see Figs. 5(a) and 5(b)]. Images were recorded with depth of 16-bit grayscale, at a rate of 1 Hz. Dark and background images were also collected and used for removal of the background spatial nonuniformity and for setting the background intensity to 1. Jet radius measurements, necessary

for the absorption analysis, were adjusted for the edge diffraction pattern [the white corona visible in Figs. 5(b) and 5(c)].

The polymers, purchased from Sigma-Aldrich, were PEO (Mw 600 kDa) dissolved in water at 3 wt% and 5 wt%, and PMMA (Mw 70 kDa) dissolved in $CHCl_3$ (chloroform) at 15 wt%. The polymer solution was injected by a syringe pump into a 25-gauge capillary needle installed on top of an enclosed plastic chamber, at volumetric feed rates ranging from 0.75 to 6 ml/h. A high-voltage power supply created a potential difference ranging from 4 to 14 kV, across a gap of 6.5 cm between the needle and the collector base, creating a nominal electric field of 0.6 to 2.2 kV/cm. The experiments were conducted at room temperature at a relative humidity of 40%.

Transmission measurements were derived from pixel intensity. The intensity of each pixel was averaged vertically within a vertical slice of up to of 13 pixels and adjusted for the residual local background offset. Horizontal pixel averaging was avoided to retain important features across the jet. The intensity profiles across the jet (T_{exp}) were normalized by the intensity calculated for the polymer solution at rest (T_{sim}), using a wave propagation simulation that took into account the overall optical effects due to absorption and scattering. The simulation was based on the Fresnel equation in the paraxial approximation [30]. The most relevant experimental parameters were included in the code, such as jet geometry and energy-dependent absorption coefficients and refraction indices, as well as source size, energy spectrum, and detector point-spread function. The resulting normalized intensity profiles across the jet represent the changes in the jet x-ray absorption due to polymer concentration variations.

B. Measurements of polymer concentration variations across the jet

Profiles of the radiation transmission T_{exp} were measured across the jet close to the jet start as well as farther along the jet, for PEO as well as for PMMA. Measured profiles of T_{exp} for PEO 3 wt%, overlaid on the simulated transmission of a stationary jet T_{sim} are plotted in Fig. 6. Close to the jet start, T_{exp} and T_{sim} almost coincide, as expected for homogeneous polymer solution [see Fig. 6(a)], whereas farther along the jet, T_{exp} rises above T_{sim} at the jet center, indicating a change in the local absorption coefficient [see Fig. 6(b)]. Since in this test case the polymer used has a lower absorption coefficient than its respective solvent, the decrease in absorption reflects a polymer concentration increase at the jet center.

It should be noted that the measured transmitted x-ray beam T_{exp} is the result of the incident beam attenuation due to both absorption and scattering of the materials contained in the jet. Because of the nonzero distance between the jet and the target, scattering effects of the collimated beam can become significant, especially for small objects [31] such as the electrospinning jet. Therefore, the radiation transmission can be written using the Beer–Lambert law in the following form:

$$T(r,z) = g(r,z)\exp\left[-d(r,z)\,\alpha(r,z)\right], \tag{28}$$

where $g(r,z)$ is a form factor describing the scattering effect; $d(r,z) = 2r_J(z)\sqrt{1-[r/r_J(z)]^2}$ is the length traveled by the beam through the jet at the radial position r and $r_J(z)$ is the local jet radius at position z; and $\alpha(r,z) = \varepsilon_P c_P(r,z) + \varepsilon_S c_S(r,z)$ is the absorption coefficient of polymer solutions, ε_P and ε_S denote the x-ray mass absorption coefficients of the polymer and solvent, respectively, and $c_P(r,z)$ and $c_S(r,z)$ denote the mass concentrations [32].

Since the wave propagation simulation also incorporates both absorption and scattering, for our purpose of detecting polymer concentration variations across the jet, we can compare the radiation transmissions obtained experimentally T_{exp} to the wave propagation simulation through the homogenous polymer solution T_{sim}. Assuming that both experiment and simulation result in the similar scattering effect ($g_{\text{exp}}(r,z)/g_{\text{sim}}(r,z) \cong 1$), normalization T_{exp} by T_{sim} reduces the influence of the scattering. Thus, the average variations in the measured absorption coefficient, $\Delta\alpha(r,z)$, with respect to the value of the fluid at rest, obtained by the wave

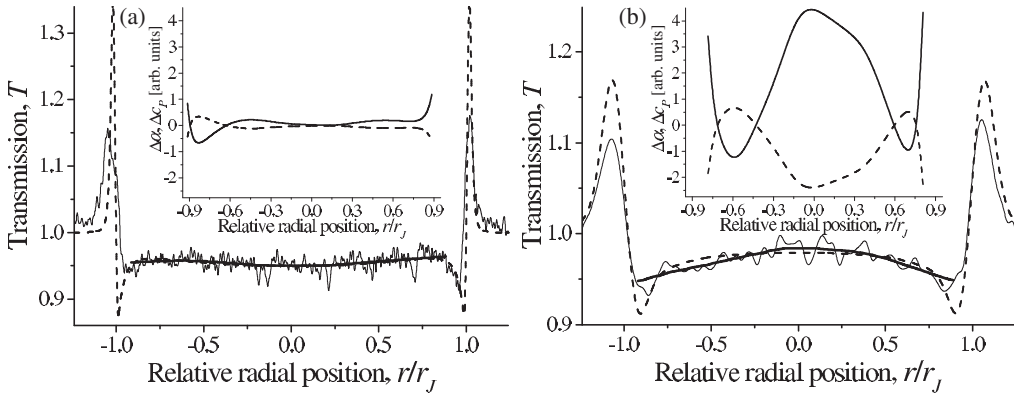

FIG. 6. Typical absorption measurements across the electrospinning jet of a solution of 3 wt% PEO (Mw 600 kDa) in water at the two z positions indicated in Fig. 5(c) (electric field 1.6 kV/cm, flow rate 2 ml/h). The measured transmission, T_{exp}, (thin solid line) and its smoothing (thick solid line) compared to simulated transmission, T_{sim} (dashed line). The inset displays calculated variations in x-ray absorption coefficient, $\Delta\alpha(r,z)$ (dashed line), and resulting variations in the local polymer mass concentration, $\Delta c_P(r,z)$ (solid line). (a) $z = 0.02$ mm, $r_J(z) = 120\ \mu$m; and (b) $z = 0.5$ mm, $r_J(z) = 22\ \mu$m.

propagation simulation can be calculated with the help of the following equation:

$$\Delta\alpha\,(r,z) = -\frac{1}{d\,(r,z)}\ln\left[\frac{T_{\mathrm{exp}}\,(r,z)}{T_{\mathrm{sim}}\,(r,z)}\right]. \tag{29}$$

Note that although Eq. (29) cannot fully compensate for the scattering effects, the obtained $\Delta\alpha\,(r,z)$ is sufficient, as it represents a trend, rather than an exact value. Typical results of the change in the absorption coefficient across the jet are presented in the insets of Fig. 6. Almost no change in the absorption coefficient across the jet was observed close to the jet start, whereas a distinct change in the absorption coefficient was observed farther along the jet.

Variations in the local polymer concentration can be calculated using the obtained variations in the absorption coefficient, $\Delta\alpha\,(r,z)$, from Eq. (29), as

$$\Delta c_P\,(r,z) = \frac{\Delta\alpha\,(r,z)}{\varepsilon_P - \varepsilon_S\,(\rho_S/\rho_P)}, \tag{30}$$

where ρ_P and ρ_S are the densities of the polymer and solvent, respectively.

For the PEO test case, the x-ray mass absorption coefficients and densities are $\varepsilon_P = 1.51\ \mathrm{cm}^2/\mathrm{g}$ and $\rho_P = 1.13\ \mathrm{g/cm}^3$ (PEO); and $\varepsilon_S = 2.29\ \mathrm{cm}^2/\mathrm{g}$ and $\rho_S = 1\ \mathrm{g/cm}^3$ (water) [33]. Substituting these x-ray material properties, the apparent change in polymer concentration can be calculated (insets of Fig. 6). While almost no change in absorption coefficient, and hence in polymer concentration, was observed across the jet close to the jet start [see inset in Fig. 6(a)], the absorption coefficient varied across the jet with respect to its initial value, when measured at points farther along the jet, indicating a nonuniform polymer concentration distribution [see inset in Fig. 6(b)]. A distinct decrease in absorption coefficient, and matching rise in concentration, was observed close to the jet center, while the absorption coefficient increased and concentration decreased, when measured at greater distances from the center, as expected from the redistribution of the polymer across the jet. Note also the sharp decrease in absorption coefficient at the jet boundary, which occurred irrespective of the position along the jet. This phenomenon may be caused by surface interaction between the polymer solution and the x-ray radiation. Similar behavior was observed in a PMMA test, demonstrating that polymer network stretching and lateral contraction are noticeable, even in cases of rapid solvent evaporation.

These experimental results are in agreement with our theoretical analysis that predicted fast network stretching and lateral contraction at high-velocity gradients, resulting in increased polymer concentration toward the jet center. The absorption measurements demonstrated that stretching is low and insignificant close to the jet start. However, at a distance of only 0.5 mm from the jet start, a significant rise in polymer concentration is observed at the jet center, indicating that stretching is already very high at this position. The theoretical analysis predicts a high stretching at the same region (see Fig. 3).

IV. CONCLUSIONS

The dynamics of the polymer network structure within the electrospinning jet of highly entangled, semidilute polymer solutions was studied both theoretically and experimentally. The theoretical modeling demonstrated that the polymer network can transform from a free state to an almost fully stretched state under extreme longitudinal acceleration, within less than 1 millimeter from the jet start. The stretching of the network is accompanied by substantial lateral contraction that leads to a rise in polymer concentration at the jet center, as confirmed by x-ray absorption measurements of the jet. This rise in polymer concentration can account for the formation of homogeneous fiber structure, as observed in polymer systems under certain electrospinning conditions.

At first glance, the short distance required for such a dramatic change in the conformational state of a polymeric subsystem in solution is unexpected from a physical point of view. Firstly, the well-known de Gennes criterion for coil-stretch transition, $\dot{\varepsilon}\tau_{\mathrm{relax}} > \theta_{\mathrm{cr}} = 0.5$ [26], is not valid in the region of macromolecule stretching during electrospinning (according to the experimental data for the system in question, $\dot{\varepsilon}\tau_{\mathrm{relax}} < \theta_{\mathrm{cr}}$). This discrepancy can be explained when considering the fact that the system presented here involves an entangled polymer network. In this case, the dominant local force, inducing macromolecule stretching, is the elastic force arising from the action of the portion of the polymer network situated farther along the jet, whereas the hydrodynamic forces give rise to the global network stretching. Conversely, the de Gennes criterion corresponds to an individual polymer macromolecule and is therefore not suitable for the estimation of the conformational state of the polymeric subsystem of the spinning jet.

In addition, the experimental observations demonstrate that further jet acceleration, but no further polymer chain elongation, is possible. The reasonable question is: What happens with the polymer subsystem of the jet during the further stage of the spinning. To date, no experimental data are available with regard to the internal evolution of the electrospinning jet at later stages of spinning, and this question remains an open problem. We surmise that disentanglement and topological reordering of the polymer network will be observed; these processes call for thorough examination.

Nevertheless, the obtained results allow predicting the stretched nonequilibrium conformational state of a polymer matrix inside electrospun nanofibers, although partial relaxation of this ordered microstructure can still occur after formation. Thus, the final state of the internal microstructure of electrospun nanofibers remains nonequilibrium, affecting their mechanical and thermodynamic properties. Note, however, that these unique properties cannot be explained only by nano-object microstructure or by processing effects. In our opinion, the formed microstructure sets a new internal scale within the nanofiber, and the unique properties of polymer nanofibers can be related to confinement of such microstructure [1].

ACKNOWLEDGMENTS

We gratefully acknowledge the financial support of the United States-Israel Binational Science Foundation (Grant

No. 2006061) and the RBNI-Russell Berrie Nanotechnology Institute. Use of the Advanced Photon Source, an Office of Science User Facility operated for the US Department of Energy (DOE) Office of Science by Argonne National Laboratory, was supported by the US DOE under Contract No. DE-AC02-06CH11357. AA acknowledges support from the Kamea Program, Israel Ministry of Absorption.

[1] A. Arinstein, M. Burman, O. Gendelman, and E. Zussman, Nat. Nanotechnol. **2**, 59 (2007).
[2] Y. Ji *et al*., Europhys. Lett. **84**, 56002 (2008).
[3] S. Cuenot, C. Frétigny, S. Demoustier-Champagne, and B. Nysten, Phys. Rev. B **69**, 165410 (2004).
[4] H. Schonherr and C. W. Frank, Macromolecules **36**, 1188 (2003).
[5] S. Cuenot, S. Demoustier-Champagne, and B. Nysten, Phys. Rev. Lett. **85**, 1690 (2000).
[6] G. B. McKenna, Eur. Phys. J. Spec. Topics **141**, 291 (2007).
[7] H. R. Brown and T. P. Russell, Macromolecules **29**, 798 (1996).
[8] P. G. de Gennes, Eur. Phys. J. E **2**, 201 (2000).
[9] M. Burman, A. Arinstein, and E. Zussman, Europhys. Lett. **96**, 16006 (2011).
[10] D. H. Reneker, A. L. Yarin, H. Fong, and S. Koombhongse, J. Appl. Phys. **87**, 4531 (2000).
[11] M. M. Hohman, M. Shin, G. Rutledge, and M. P. Brenner, Phys. Fluids **13**, 2201 (2001).
[12] Y. M. Shin, M. M. Hohman, M. P. Brenner, and G. C. Rutledge, Polymer **42**, 09955 (2001).
[13] P. Gupta, C. Elkins, T. E. Long, and G. L. Wilkes, Polymer **46**, 4799 (2005).
[14] D. H. Reneker, A. L. Yarin, E. Zussman, and H. Xu, Adv. Appl. Mech. **41**, 43 (2007).
[15] L. M. Bellan, H. G. Craighead, and J. P. Hinestroza, J. Appl. Phys. **102**, 094308 (2007).
[16] T. Han, A. L. Yarin, and D. H. Reneker, Polymer **49**, 1651 (2008).
[17] L. Larrondo and R. S. J. Manley, J. Polym. Sci. Polym. Phys. **19**, 921 (1981).
[18] J. S. Stephens, S. Frisk, S. Megelski, J. F. Rabolt, and D. B. Chase, Appl. Spectrosc. **55**, 1287 (2001).
[19] P. Dayal, J. Liu, S. Kumar, and T. Kyu, Macromolecules **40**, 7689 (2007).
[20] C. L. Casper, J. S. Stephens, N. G. Tassi, D. B. Chase, and J. F. Rabolt, Macromolecules **37**, 573 (2004).
[21] A. J. Guenthner, S. Khombhongse, W. Liu, P. Dayal, D. H. Reneker, and T. Kyu, Macromol. Theor. Simul. **15**, 87 (2006).
[22] P. Dayal and T. Kyu, Phys. Fluids **19**, 107106 (2007).
[23] S. Koombhongse, W. X. Liu, and D. H. Reneker, J. Polym. Sci. Polym. Phys. **39**, 2598 (2001).
[24] A. Arinstein and E. Zussman, J. Polym. Sci. Polym. Phys. **49**, 691 (2011).
[25] S. N. Reznik and E. Zussman, Phys. Rev. E **81**, 026313 (2010).
[26] P. G. de Gennes, J. Chem. Phys. **60**, 5030 (1974).
[27] N. K. Balabaev, I. P. Borodin, T. I. Borodina, and T. N. Khazanovich, Polym. Sci. A **52**, 655 (2010).
[28] Y. Wang, X. Liu, K.-S. Im, W.-K. Lee, J. Wang, K. Fezzaa, D. L. S. Hung, and J. R. Winkelman, Nat. Phys. **4**, 305 (2008).
[29] K. S. Im, K. Fezzaa, Y. J. Wang, X. Liu, J. Wang, and M. C. Lai, Appl. Phys. Lett. **90**, 091919 (2007).
[30] R. V. Reeves, J. D. E. White, E. M. Dufresne, K. Fezzaa, S. F. Son, A. Varma, and A. S. Mukasyan, Phys. Rev. B **80**, 224103 (2009).
[31] A. Sasov, in *Proceedings of the 9th European NDT Conference* (Berlin, Germany, 2006).
[32] R. J. Roe, *Methods of X-ray and Neutron Scattering in Polymer Science* (Oxford University Press, New York, 2000).
[33] E. Gullikson, http://henke.lbl.gov/optical_constants/.

5.2 X-ray imaging of electrospinning jets

Greenfeld, I., K. Fezzaa, M.H. Rafailovich, and E. Zussman, *Fast X-ray phase-contrast imaging of electrospinning polymer jets: Measurements of radius, velocity, and concentration.* Macromolecules, 2012. **45**(8): p. 3616-3626.[2]

Macromolecules

Article

pubs.acs.org/Macromolecules

Fast X-ray Phase-Contrast Imaging of Electrospinning Polymer Jets: Measurements of Radius, Velocity, and Concentration

Israel Greenfeld,*[,†] Kamel Fezzaa,[‡] Miriam H. Rafailovich,[§] and Eyal Zussman[†]

[†]Department of Mechanical Engineering, Technion - Israel Institute of Technology, Haifa 32000, Israel

[‡]Advanced Photon Source, Argonne National Laboratory, Argonne, Illinois 60439, United States

[§]Department of Materials Science and Engineering, State University of New York, Stony Brook, New York 11794-2275, United States

ABSTRACT: The study of electrospinning polymer solution jets, and the evolution of the polymer entangled network during electrospinning, is of interest for understanding of the microstructure of the resulting nanofibers. Fast X-ray phase-contrast imaging was applied to investigate the flow of the first 10 mm of a straight jet of electrospinning PEO and PMMA semidilute solutions. The jet radius, velocity, and absorbance were measured at high resolution (0.67 μm/pixel) and at extremely short exposure time (<0.5 μs), under a wide range of electrospinning conditions and solution concentrations. The flow field, measured by tracing silica microbeads, revealed laminar flow with axial velocities that implied significant mass loss due to evaporation. X-ray absorption measurements provided evidence for substantial polymer concentration rise along the jet, particularly at the jet boundaries, evidence of rapid evaporation. Furthermore, at high strain rates, the polymer concentration rose at the jet center as the velocity increased along the jet, implying polymer network lateral contraction due to axial stretching. Our findings confirm the theoretically predicted counteracting effects of evaporation and stretching on the polymer matrix within the jet.

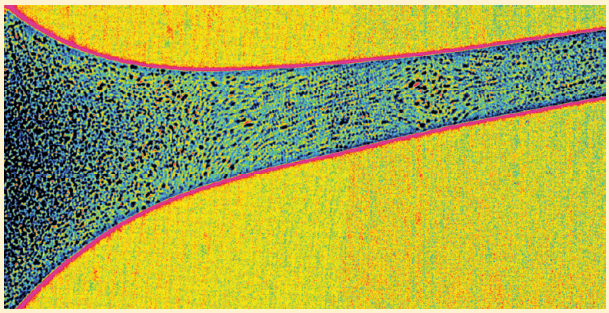

1. INTRODUCTION

Electrospinning is characterized by high strain rates of the order 10^3 s^{-1}.[1,1−7] Such stretching can potentially improve the structural order within as-spun nanofibers and enhance their mechanical properties.[8−12] At the same time, rapid solvent evaporation during electrospinning can lead to increased polymer concentrations at the jet boundary,[13−16] sometimes forming a solid skin and a heterogeneous and porous structure.[11,15,17] Hence, study of electrospinning polymer solution jets, and specifically of the evolution of the polymer entangled network during electrospinning,[11] is of interest in clarifying the microstructure of as-spun nanofibers. Experimental data on the jet dynamics during the initial stage of electrospinning, and particularly on the flow regime within the jet, are needed in order to characterize the hydrodynamic environment to which the polymer network is subjected. Furthermore, data on the distribution of the polymer within the jet can shed light on the conflicting processes of stretching and evaporation for different material properties and electrospinning conditions.

The geometry and velocity of electrospinning jets were studied by optical microscopy[1,5] and by tracing large particles (50−70 μm) using high-speed visible light imaging.[18] Stretching and orientation of polymer chains have been observed in electrospinning jets using birefringence,[19] Raman,[20] and X-ray diffraction[21] techniques. Imaging of electrospinning jets using in-line fast X-ray phase-contrast imparts several advantages. The method has been used to study flow dynamics, particularly fuel jets and sprays,[22−24] and offers an extremely short exposure time (<0.5 μs), essential for capturing the inherently unstable electrospinning jet, and, at the same time, provides high spatial resolution (0.67 μm/pixel). Owing to the weak interaction of X-ray with matter, it has high penetrability, and its essentially monochromatic beam enables measurement of transmission absorption and analysis of the polymer concentration within the jet. The method also provides enhanced phase boundary contrast, enabling accurate measurement of small objects, as well as accurate velocimetry using particles as small as 1 μm.[24] At the same time, the scattering of X-rays penetrating a small object is significant[25] and requires correction of absorption measurements.

In this work, we apply fast X-ray phase-contrast imaging toward analysis of up to 10 mm of the initial portion of electrospinning jets (the straight and stable section) to extrapolate high-resolution (0.67 μm/pixel) measurements of the jet radius, velocity, and absorbance. Semidilute solutions of PEO (poly(ethylene oxide)) and PMMA (poly(methyl methacrylate)) were measured under a wide range of electrospinning conditions (electric field and flow rate) and solution concentrations. The jet flow field, measured by tracing silica microbeads mixed in the polymer solutions, showed laminar flow with axial velocities that implied significant mass

Received: February 1, 2012
Revised: March 29, 2012
Published: April 10, 2012

loss due to evaporation. Absorption along and across the jet was calculated from beam transmission measurements, after correcting for the scattering effect. Substantial polymer concentration increase was observed along the jet, as early as 2−3 mm from the jet start, evidence of rapid evaporation. This concentration rise occurred particularly along the jet's boundaries. At the same time, high strain rates (e.g., due to high electric field), sufficiently distant from the orifice, led to a rise in polymer concentration at the jet center as well. This latter phenomenon is testimonial of the lateral inward contraction of the polymer network due to the axial stretching.

2. EXPERIMENTAL SECTION

2.1. Equipment Setup and Operation. The experiment was conducted at 32-ID Beamline, Advanced Photon Source (APS), Argonne National Lab, using a partially coherent undulator X-ray white beam. The experimental setup of the X-ray imaging system and the electrospinning chamber are presented in Figures 1a and 2a,b.

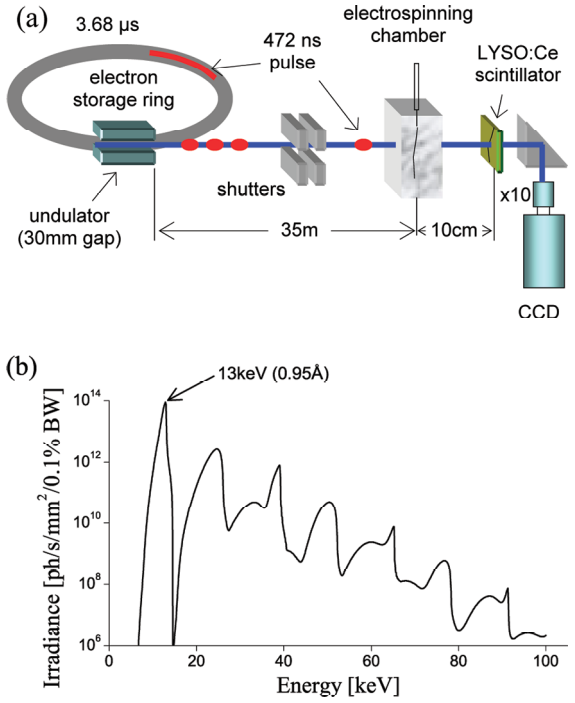

Figure 1. Experimental setup. (a) X-ray beam path: a millisecond shutter was set up in series with a very fast galvano-based shutter that opened the path for less than 100 μs each second. The beam penetrated the jet and was converted to a digital image via a scintillator. The CCD camera was timed to capture the first pulse after the very fast shutter opened. (b) X-ray beam flux: the dominant harmonic is indicated.

The X-ray beam was generated from the synchrotron's electron storage ring with a dominant harmonic at a beam energy of 13 keV, corresponding to a wavelength of 0.95 Å (Figure 1b). The dominant peak was ~100 times more intense than the harmonics, rendering the beam practically monochromatic, an essential feature in view of the strong dependence of material X-ray mass absorption coefficients on beam energy. The X-ray beam was emitted as short pulses, each 472 ns long, issued at intervals of 3.68 μs. A millisecond mechanical shutter opened the beam path at 1 Hz in order to protect the imaging system from overheating, and was followed by a very fast galvano-based shutter that opened the beam path for less than 100 μs each second.

The X-ray pulses penetrated the electrospinning jet, and their transmission was converted to visible light by a fast scintillator crystal (LYSO:Ce, 40 ns decay time), positioned at a distance of 10 cm from the spinning jet. A camera, timed to capture the first pulse passing through the very fast shutter, captured the image via a folding mirror and a ×10 objective optics, using a 1280H × 1024 V CCD detector with a pixel size of 6.7 × 6.7 μm^2. The beam size of 1 × 1 mm^2 was slightly larger than the camera's effective field-of-view. A typical X-ray image of the jet is shown in Figure 2c. Note the white corona at the jet boundaries due to edge diffraction. During particle tracing experiments, two-pulsed images were captured for each frame, separated by a time interval of 3.68 μs multiples, up to a maximum of 147.2 μs.

The electrospinning chamber (Figure 2a,b) consisted of a PMMA-based enclosure with Kapton-film windows. The chamber was mounted on a remotely controlled motorized stage, which allowed for control of *x,y,z* positioning of the electrospinning chamber, and for sequential capturing of images at 0.5 mm steps along the jet during a single session (see image example in Figure 2d). Because of the unstable nature of electrospinning jets and the small field-of-view of the camera, images could only be captured at distances of up to 10 mm from the jet start. The image frame was recorded 20 times at 1 s intervals for each stage position, with a gray scale depth of 16 bits. Dark images (no X-ray) and background images (no jet) were also collected to allow for image correction.

In order to avoid prolonged exposure of the jet to X-ray radiation that might degrade the polymer or affect the solvent, the following measures were taken. After allowing sufficient time for the jet flow to become steady, the camera was triggered to capture the first pulse released by the very fast shutter. In the absorption measurement experiments, only a single pulse was captured, and the jet was consequently exposed to the beam for 0.47 μs. In the particle tracing experiments, the beam path was left open until the second image was captured, and therefore the jet was exposed to 3−41 pulses, depending on the selected time interval, and consequently the cumulative exposure time varied between 1.4 and 19.4 μs. The corresponding fluence (time-integrated flux) of the beam spectrum shown in Figure 1b was several orders of magnitude below typical X-ray damaging fluences.[26] Also, owing to the beam small size, irradiation was restricted to the jet section that was currently imaged, about 1 mm long, while the rest of the jet was not exposed to the beam. Finally, the experimental evidence from the particle tracing experiments using different exposure times has shown that the measured jet radius and particles velocity were not sensitive to exposure time, implying that the beam did not influence the jet dynamics or evaporation.

2.2. Materials and Test Cases. PEO (M_w 600 kDa) and PMMA (M_w 70 kDa) were purchased from Sigma-Aldrich. PEO was dissolved in water at concentrations of 3 and 5 wt %; PMMA was dissolved in $CHCl_3$ (chloroform) at concentration of 15 wt %. Glycerol was purchased from Sigma-Aldrich. During velocimetry tests, the PEO solutions were mixed with silica (SiO_2) microbeads, purchased from Polysciences Europe GmbH, at volume fraction of 0.9 vol %. The microbeads size ranged from 1 to 10 μm (98% of microbeads), with a mean size of 1.94 ± 0.76 μm (STD), measured using ImageJ. The relevant properties of the materials and solutions used in the experiment are listed in Table 1.

The polymer solutions were injected using a standard syringe pump, into a 25 gauge capillary needle (internal diameter 0.26 mm) installed on top of the electrospinning chamber, at flow rates *Q* ranging from 1 to 8 mL/h. A 20 gauge needle (internal diameter 0.6 mm) was used for the PEO 5% particle tracing experiments. The polymer solution was drawn from the capillary needle by an electric field, created by a standard high-voltage power supply, with electric potential ranging from 4 to 14 kV. The gap between the needle and the collector tip was adjusted to fall within a range of 2.5−6.5 cm (Figure 2a), resulting in a nominal electric field *E* of 0.6−4 kV/cm. The experiments were conducted at room temperature, at a relative humidity of 40%. Tests 1−17 and their conditions are presented in Figure 3.

2.3. Particle Tracing. Velocity measurements and characterization of the flow regime inside the electrospinning jet were achieved by X-ray particle tracing. The measurements were carried out on PEO 3% and 5% solutions, mixed with silica microbeads (tests 14−18). The microbeads provided good X-ray image contrast, with an absorption coefficient ~10 times higher than that of the PEO solutions (refer to

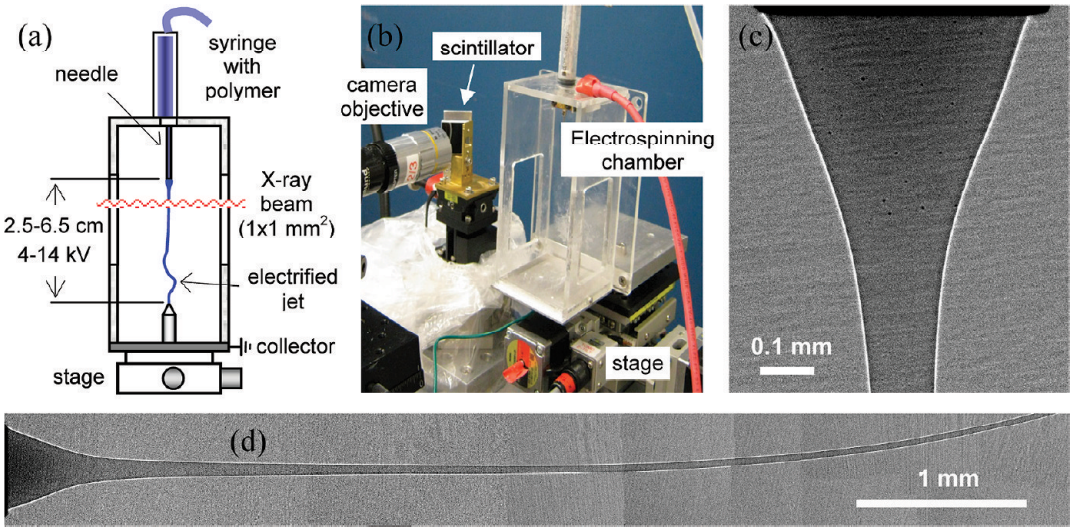

Figure 2. Electrospinning setup. (a) Electrospinning chamber: the polymer solution is pumped into the syringe and drawn by the electric field toward the collector. The initial rectilinear portion of the jet is imaged by sequentially moving the motorized stage upward at 0.5 mm steps. (b) Electrospinning chamber and imaging target (scintillator). (c) Representative X-ray image: electrospinning solution of 5 wt % PEO (M_w = 600 kDa) in water; electric field 1.6 kV/cm, flow rate 3.2 mL/h. (d) Same test case, presenting a jet section 6 mm long, reconstructed from 12 sequential images.

Table 1. Characteristic Properties of Tested Materials and Solutions[a]

material/polymer	M_w [Da]	solvent	c [%]	μ [Pa s]	γ [mN/m]	σ [mS/m]	ρ_p (ρ_s) [g/cm^3]	ε_p (ε_s)[b] [cm^2/g]	α_0 [1/cm]
glycerol	92		100	0.9	64[c]	0.006[d]	1.26	1.75	2.21
PMMA	70K	chloroform	15	~0.1	28[c]		1.2 (1.5)	1.45 (23.3)	28.9
PEO	600K	water	3	1.2[e]	72[e]	1.4[e]	1.12 (1)	1.51 (2.29)	2.28
PEO	600K	water	5	12[e]	75[e]	1.6[e]	1.12 (1)	1.51 (2.29)	2.26
silica (microbeads)							2.65	8.27	21.9

[a]Molecular weight M_w, concentration c, zero-shear viscosity μ, surface tension γ, conductivity σ, mass absorption coefficient of polymer (solvent) ε_p (ε_s), density of polymer (solvent) ρ_p (ρ_s), and absorption coefficient α_0. [b]Reference 27. [c]Reference 28. [d]SmartMeasurement.[29] [e]Estimate based on Theron et al.[30]

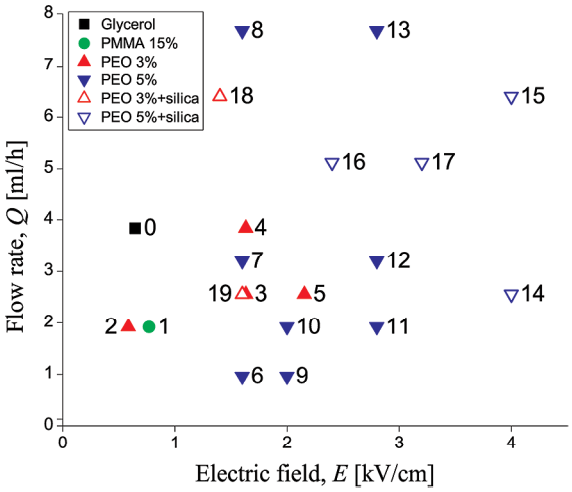

Figure 3. Map of X-ray tests and their respective solutions, flow rates Q, and applied electric fields E. Refer to Table 1 for corresponding material properties.

Table 1). Each jet section was exposed twice to X-ray radiation, within a short time interval, and both exposures were recorded on a single image. The time intervals used were 7.4, 18.4, 36.8, 73.6, and 147.2 μs. Velocity vectors were calculated by tracing particles, as shown in Figure 4, and adjusting for the lateral displacement of the jet during the time interval between exposures. Typically, shorter intervals were applied in regions of high velocity, whereas longer intervals were needed for regions of low velocity. The resulting velocity vectors were two-dimensional projections of a three-dimensional flow, but since the vertical velocity component was dominant this inaccuracy is negligible.

The small size of the particles (mean size ~2 μm) and their low volume fraction in the solution (0.9 vol %), as well as their homogeneous dispersion within the fluid (Figure 4), ensured minimal influence of the particles on the jet flow properties and accurate velocity measurement. Suspensions with particles volume fraction up to 1 vol % may be considered as dilute,[31] and therefore the effect of the particles on viscosity was negligible. Theoretical and experimental studies of the flow of particle-laden fluids in confined spaces[24,32] have shown that for small particles ($d/H \leq 0.2$, where d is the particle size and H the small dimension of the flow) and low Reynolds numbers ($Re = \rho v D_H/\mu < O(1)$, where ρ is the fluid density, v is the fluid velocity, and D_H is the hydraulic diameter), the particles will not cross streamlines while moving along the flow, and their velocity will be within less than 2% from the undisturbed fluid velocity. These conditions apply to the present tracing tests, where $d < 10$ μm, $H \cong D_H < 1$ mm, $\rho \cong 1$ g/cm^3, $v < 1$ m/s, and $\mu \leq 12$ Pa s, and therefore $d/H < 0.01$ and $Re < 0.1$.

The effects of particle gravity and buoyancy are negligible, in view of the high hydrodynamic forces in the electrospinning jet. The inertial force can be neglected as well (the ratio between the inertial force, $(\pi/6)\rho_p d^3 \dot{v}$, and the hydrodynamic force, $3\pi\mu d v$, acting on a particle assuming a spherical shape, is $\rho_p d^2 s/(18\mu) \cong 10^{-6} \ll 1$, where ρ_p = 2.65 g/cm^3 is the particle density and $s = \dot{v}/v < 10^3$ 1/s is the flow strain rate).

2.4. Radiation Transmission and Absorption. Characterization of the polymer concentration distribution within the jet was achieved by measuring the X-ray transmission through the jet and calculating

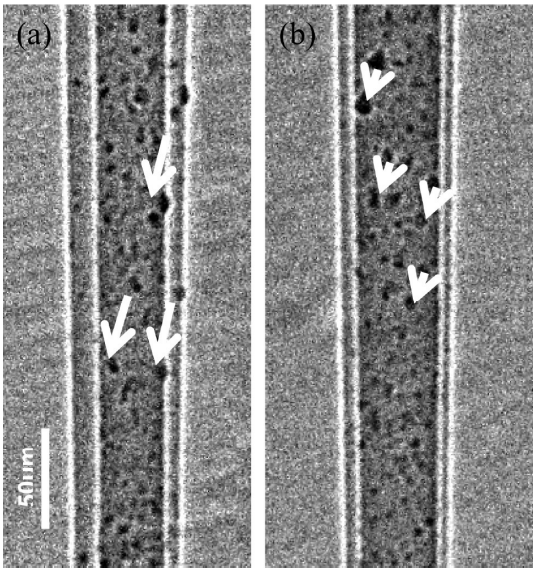

Figure 4. Particle tracing technique using two-pulsed X-ray images. The horizontal offset is due to the jet lateral displacement during the time interval between exposures. Representative velocity vectors (prior to correction of the lateral displacement) are indicated by arrows, correlating particles in the first image to the same particles in the second image. The solution was PEO 5% mixed with 0.9 vol % silica microbeads, electrospun under an electric field of 4 kV/cm and with a flow rate of 2.6 mL/h (test 14). The measurement was taken at distance z = 1.6 mm from the jet start, with a time interval between exposures of (a) Δt = 147.2 μs and (b) Δt = 73.6 μs.

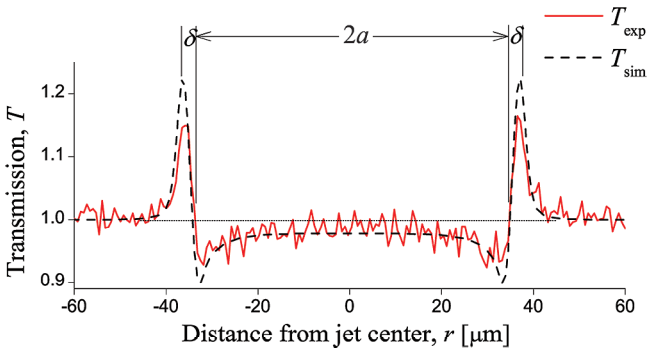

Figure 5. Example of the measured X-ray transmission T_{exp} at a cross section of the jet, based on test 3 (PEO 3%, 1.6 kV/cm, 2.6 mL/h) experimental data, overlaid on the simulated transmission T_{sim}. The estimated measurement error is 1.5%. The jet radius was measured at 1 pixel resolution (0.67 μm) both axially and radially. The radius a was obtained by measuring the distance between the two diffraction peaks, and subtracting δ = 1.5 μm, corresponding to the beam wavelength.

the corresponding absorption coefficient at each point. Using polymer–solvent pairs that have disparate mass absorption coefficients (refer to Table 1), the measured variations in the local absorption coefficient could be converted to polymer concentration variations.

Each raw image (see example in Figure 6a) was processed, using the recorded dark and background images, for the purpose of removing the background spatial nonuniformity and normalizing the background intensity to 1. The resulting transmission of each pixel, $T_{exp}(r,z)$, where r and z respectively denote the radial and axial positions of the pixel in the jet, was obtained by further adjustment for the residual local background offset. The measured transmission T_{exp} (Figure 6b) was normalized by a simulated transmission, $T_{sim}(r,z)$ (Figure 6c), that assumed a homogeneous jet without concentration variations. Normalization provided correction for scattering effects such as dispersion and edge diffraction. Polymer macromolecular orientation as a result of stretching had a negligible effect, since X-ray is absorbed by the atoms along the beam path regardless of their bonding state.[27,33]

The transmission T_{sim} was calculated by a wave propagation simulation designed to account for the overall optical effects of the partially coherent beam and the test setup, by combining absorption and scattering effects. The simulation was based on the Fresnel equation, which, in the paraxial approximation,[34] takes the form of a convolution of the object (projected sample) and a term called propagator. The code used FFTs to calculate the convolution in reciprocal space and then inverse FFTs to retrieve the intensity in real space at the detector location. The code included the most relevant experimental parameters, such as jet geometry and energy-dependent absorption coefficients and refraction indices, as well as source size, energy spectrum, and detector point spread function.

Figure 5 depicts T_{exp} and T_{sim} at a typical cross section of the jet. Note the slight increase in the measured transmission at the jet center, with respect to the simulated transmission. Since the polymer mass absorption coefficient is lower than that of the solvent (see Table 1), absorption decreases and polymer concentration increases. Note also the increase in the measured transmission close to the jet boundary ($r = \pm a$), reflecting a concentration increase near the edge as well.

Using the Beer–Lambert absorption law, and normalizing T_{exp} by T_{sim}, the average change in the apparent absorption coefficient, $\Delta\alpha_{app}(r,z)$, can be expressed by

$$\Delta\alpha_{app}(r,z) = -\frac{1}{d(r,z)} \ln \frac{T_{exp}(r,z)}{T_{sim}(r,z)} \quad (1)$$

where $d(r,z) = 2a(z)(1 - [r/a(z)]^2)^{1/2}$ is the beam penetration distance at a radial position r and $a(z)$ is the jet radius at an axial position z.[11] The measurement of the jet radius a was performed by detecting the edge diffraction white peaks and adjusting for a diffraction width of δ = 1.5 μm corresponding to the beam wavelength (refer to Figure 5).

The measured transmission of the X-ray beam, T_{exp}, is the result of incident beam attenuation consequential of both absorption and scattering of the materials within the jet. Scattering effects of the collimated beam become significant with nonzero distances between the jet and the imaging target (the scintillator) and are relatively larger at smaller jet diameters and at regions closer to the jet boundary. Thus, the apparent absorption coefficient α_{app}, obtained from pixel intensity measurements by eq 1, consists of an absorption term α_{abs} and a scattering term α_{scat}, such that $\alpha_{app} = \alpha_{abs} + \alpha_{scat}$.[33]

In the case of a homogeneous fluid without concentration variations, the scattering contribution can be assessed by comparing the solution absorption coefficient α_0 to the simulated apparent absorption coefficient extrapolated from jet geometry, $\alpha_{sim}(r,z) = -\ln T_{sim}(r,z)/d(r,z)$. While α_0 accounts for absorption only, $\alpha_{sim}(r,z)$ factors in both absorption and scattering. Assuming, as a first-order approximation, that the ratio between these two parameters is retained when concentration variations are present within the fluid, we can introduce a correction factor, $\alpha_0/\alpha_{sim}(r,z)$, to eq 1:

$$\Delta\alpha(r,z) \cong \frac{\alpha_0}{\alpha_{sim}(r,z)} \Delta\alpha_{app}(r,z) = \alpha_0 \left[\frac{\ln T_{exp}(r,z)}{\ln T_{sim}(r,z)} - 1 \right] \quad (2)$$

where $\Delta\alpha(r,z) = \alpha(r,z) - \alpha_0$ is the change in the local absorption coefficient with respect to the solution's initial absorption coefficient.

The absorption coefficient of polymer solutions is given by $\alpha(r,z) = \varepsilon_p c_p(r,z) + \varepsilon_s c_s(r,z)$,[33] where ε_p and ε_s denote the X-ray mass absorption coefficients of the polymer and solvent and c_p and c_s denote the mass concentrations. Using the relationship $c_s/\rho_s = 1 - c_p/\rho_p$, the change in the local polymer concentration, $\Delta c_p(r,z)$, is linearly dependent on $\Delta\alpha(r,z)$:[11]

$$\Delta c_p(r, z) = c_p(r, z) - c = \frac{\Delta\alpha(r, z)\rho_p}{\varepsilon_p\rho_p - \varepsilon_s\rho_s} \quad (3)$$

where c is the solution's initial concentration and ρ_p and ρ_s are the densities of the polymer and solvent, respectively. Using c as the concentration scale, the relative concentration change may be expressed by $\Delta c_p/c$ and the relative concentration by $c_p/c = 1 + \Delta c_p/c$.

The values of the parameters ρ_p, ρ_s, c, ε_p, ε_s, and α_0, used in the analysis of the experimental data, are provided in Table 1. An example of the two-dimensional distribution of $\Delta\alpha$ and Δc_p within the jet is shown in Figure 6d. Note that due to the pixel noise remaining after background removal, further data smoothing was required.

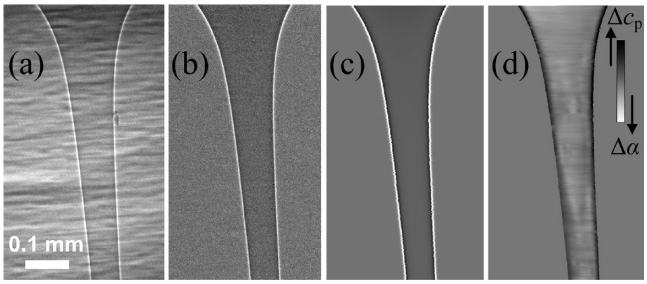

Figure 6. Radiation transmission and absorption processing steps. Example based on test 11 (PEO 5%, 2.8 kV/cm, 1.9 mL/h) data. (a) Raw image. (b) Image after background removal and normalization, T_{exp}. (c) Wave propagation simulation, T_{sim}, assuming a homogeneous jet. (d) Distribution of the absorption coefficient $\Delta\alpha$ (eq 2) and polymer concentration Δc_p (eq 3) (smoothed). Dark regions denote low absorption and high concentration, while bright regions denote high absorption and low concentration.

3. RESULTS AND DISCUSSION

3.1. Jet Radius. Jet radius measurements were carried out on electrospinning PEO 3% solutions (tests 2–5), PEO 5% solutions (tests 6–13), a PMMA 15% solution (test 1), and glycerol (test 0). Image examples shown in Figure 7

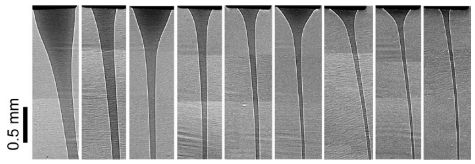

Test #	8	13	7	12	11	6	4	3	5
c %	5	5	5	5	5	5	3	3	3
E kV/cm	1.6	2.8	1.6	2.8	2.8	1.6	1.6	1.6	2.2
Q mL/h	7.7	7.7	3.2	3.2	1.9	1	3.8	2.6	2.6

Figure 7. Representative test cases of 3% and 5% PEO. The flow in each image was steady state, at test conditions provided in the table. The jet diameter narrows (from left to right) when the electric field is higher and the flow rate and solution concentration are lower.

demonstrate that the jet diameter narrows earlier along the jet when under higher electric fields and lower flow rates and polymer concentrations. Additionally, these process variables influence the opening angle and height of the Taylor cone at the beginning of the jet, as also shown by Reznik et al.[35] and Feng,[36] as well as the degree of wetting of the lower face of the stainless steel needle. The jet radius reduction ratios within up to 8 mm from the jet start ranged between 5 and 24 for the PEO tests, 10 for the PMMA test, and 31 for the glycerol test. The radius profiles versus the position along the jet are depicted in Figure 8.

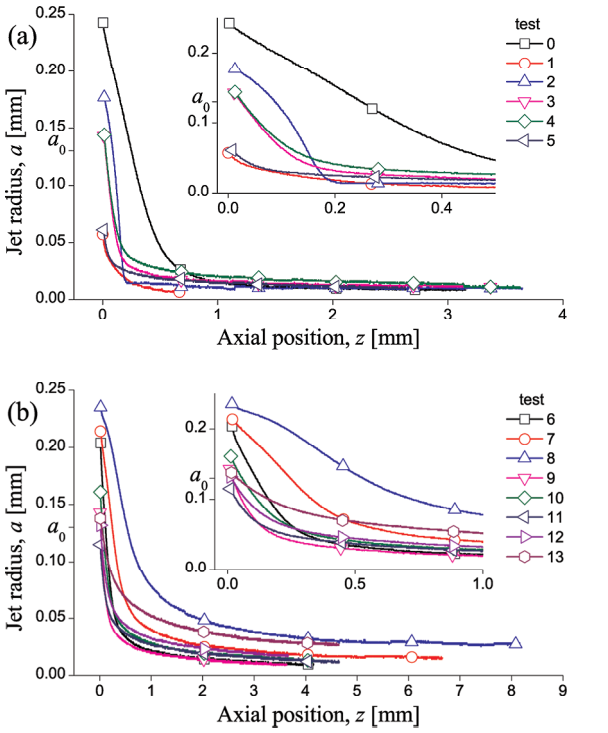

Figure 8. Measured jet radius a at position z along the jet. The jet profile is measured at 1 pixel resolution (0.67 μm), both axially and radially. The insets magnify the early portion of the jet. a_0 = 0.13 mm designates the capillary inner radius. (a) Glycerol (test 0), PMMA 15% (test 1), and PEO 3% (tests 2–5). (b) PEO 5% (tests 6–13).

Analysis of electrically driven fluid jets has shown that the jet reaches an asymptotic regime sufficiently far from the needle orifice. The dimensionless jet radius $\hat{a}$ can be expressed by a power law of the form $\hat{a} \sim \hat{z}^{-\beta}$, where $\hat{z}$ is the dimensionless distance from the orifice and β is a positive exponent.[37−41] The values of β vary, depending on the fluid type and analysis method. For Newtonian fluids, assuming a negligible viscosity effect, the exponent was estimated as $\beta = 1/4$.[37] Using a power-law rheologic constitutive equation, this estimate was generalized to non-Newtonian jets having a flow index >2, to $\beta \geq 1/2$,[38] which converged to $\beta = 1/2$ for jets with a high flow index. Other estimates for Newtonian fluids were $\beta = 1$ (hyperbolic shape), for both viscosity-dominated[40] and capillary-dominated[41] flows. The jet viscoelastic rheology was modeled by Reneker et al. using Maxwell damper-spring elements, providing a complete description of the jet dynamics throughout both the straight and bending-instability regions.[4] Running this model for the jet straight region, we observed a good asymptotic fit to a power law, with $\beta \cong 1/4$ over a wide range of the dimensionless parameters (voltage, elastic modulus, and electric charge). Solvent evaporation, added to the model by Yarin et al., was shown to have a major effect on the jet radius at the bending-instability region, while only a minor effect at the straight region.[42]

Using the orifice internal radius a_0 as the length scale, the power law takes the form

$$\frac{a}{a_0} = \frac{1}{k}\left(\frac{z}{a_0}\right)^{-\beta} \quad (4)$$

where the dimensionless parameter k determines the jet radius reduction rate. The radius measurements of all tests can be collapsed onto a common asymptotic curve ($k = 1$), by multiplying each profile displayed in Figure 8, by a suitable value of k. The results are depicted in Figure 9a and apply when

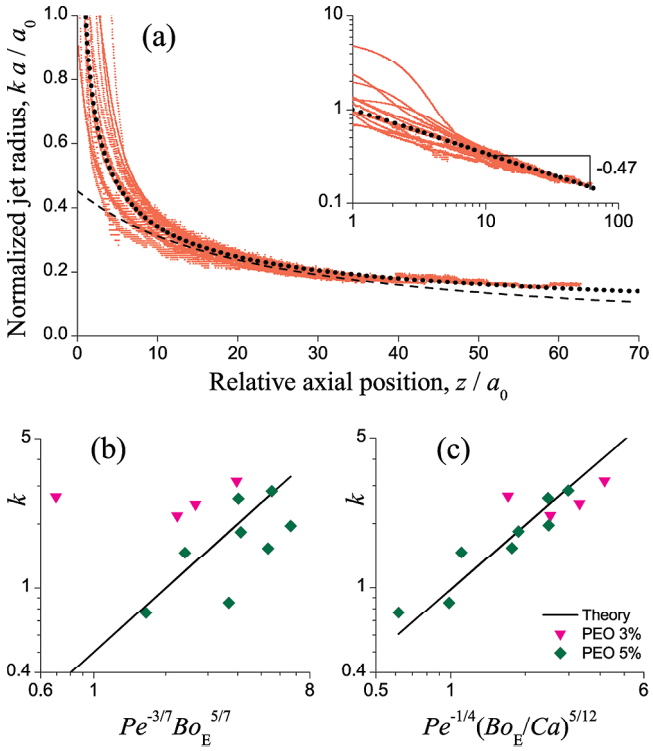

Figure 9. Comparison of measured jet radius to theory at distances of $z/a_0 > 10$ from the orifice. (a) Normalized jet radius ka/a_0 at position z/a_0 along the jet, for the combined data of tests 0–13, where each test set is multiplied by the constant k pertaining to that test. The power fit (dotted line) corresponds to $a/a_0 = (z/a_0)^{-0.47}$, where the exponent is measured in the inset graph. The hyperbolic fit (dashed line) corresponds to $a/a_0 = (z/a_0 + p)^{-1}$, where $p = 23.1$. (b) Measured coefficient k for tests 2–13 (PEO), compared to the theoretical dimensionless prediction (solid line) for capillary-dominated flow. The predicted value is adjusted by a constant of order 1. (c) As in (b), but for viscosity-dominated flow.

the distance from the orifice, z, is larger than ~10 times the orifice's internal radius, a_0. The slope of the asymptote was measured as $\beta = 0.47 \cong 1/2$ (inset in Figure 9a) and compared with a hyperbolic fit.

The parameter k depends on the flow type. The flow is considered viscosity-dominated when the viscosity, flow rate, and electric field are high, yielding smaller surface tension stresses than viscous and electric stresses. Conversely, the flow is considered capillary-dominated when the surface tension stresses are comparably higher than the viscous and electric stresses. Using dimensionless numbers, theoretical expressions for k are given by $k_{vis} \sim \varepsilon_m^{1/6} Pe^{-1/4}(Bo_E/Ca)^{5/12}$ for viscosity-dominated flow,[40] and $k_{cap} \sim \varepsilon_m^{2/7} Pe^{-3/7} Bo_E^{5/7}$ for capillary-dominated flow,[41] where $\varepsilon_m \cong 1$ is the permeability of the medium (air), $Pe = 2v_0/(\sigma a_0)$ is the Péclet number, $Bo_E = a_0E^2/\gamma$ is the electric Bond number, and $Ca = \mu v_0/\gamma$ is the capillary number. $v_0 = Q/(\pi a_0^2)$ is the jet initial velocity. The dimensional counterparts are the following: $k_{vis}^d \sim \varepsilon_m^{1/6} a_0^{2/3} v_0^{-2/3} \sigma^{1/4} \mu^{-5/12} E^{5/6}$ and $k_{cap}^d \sim \varepsilon_m^{2/7} a_0^{2/7} v_0^{-3/7} \sigma^{3/7} \gamma^{-5/7} E^{10/7}$. Note that k_{vis} is independent of the surface tension γ, while k_{cap} is independent of the viscosity μ. The measured values of k were compared with these theoretical predictions, assuming both capillary-dominated (Figure 9b) and viscosity-dominated (Figure 9c) flows. A good fit to the theoretical model was achieved when assuming viscosity-dominated flow.

Reznik et al.[41] provide an additional criterion for determining the flow type, using the dimensionless number $B = Bo_E CaI/Pe$, where I is the overall electric current led by the jet. When $B \leq 0.01$, the flow is dominated by capillarity, and when $B \geq 1$, the flow is dominated by viscosity. However, when $0.01 < B < 1$, both surface tension and viscous stresses influence the jet shape. Based on the data provided in Table 1, $0.1 < B < 0.9$ for the PEO 3% tests, which is within the interim regime, while $3 < B < 40$ for the PEO 5% tests, which falls within the viscosity-dominated regime. Thus, we can conclude that the experimental results for the PEO tests are in good agreement with the theoretical models. It should be clarified that this analysis applies to the straight section of the jet, before the onset of bending instability, which introduces a dramatic decrease in jet radius and an increase in jet surface area, causing rapid evaporation.[4,6,7,42–44]

At regions closer to the orifice, namely within the Taylor cone (Figure 10a), viscous stresses are lower and the effect of surface tension becomes more significant, while the effects of flow rate and electric field remain similar to those at the asymptotic region of the jet. We use the dimensionless number $Bo_E/Pe = (1/2)a_0^2 v_0^{-1} \sigma \gamma^{-1} E^2$ to express these effects for the

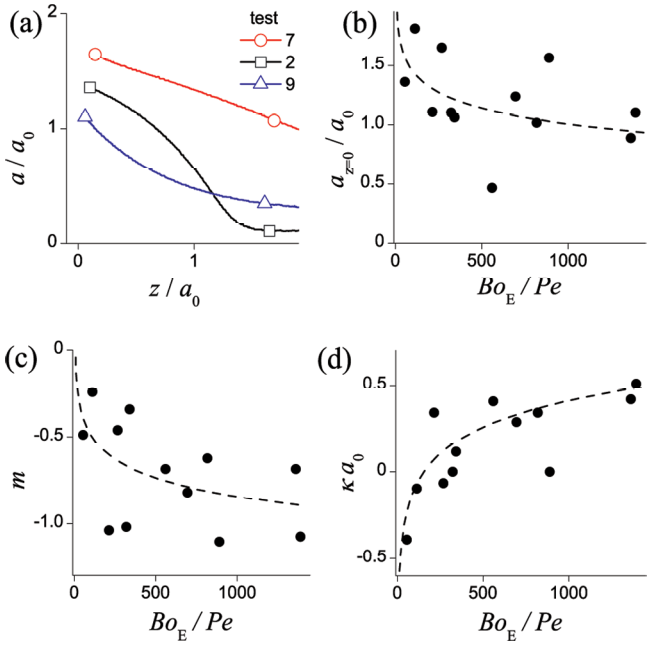

Figure 10. Jet radius profile near the orifice and its dependence on the dimensionless number Bo_E/Pe for tests 2–13 (PEO). (a) Typical cases of the jet radius a/a_0 at position z/a_0 along the jet: straight (test 7: PEO 5%, 1.6 kV/cm, 3.2 mL/h, $Bo_E/Pe = 267$), convex (test 2: PEO 3%, 0.6 kV/cm, 1.9 mL/h, $Bo_E/Pe = 55$), and concave (test 9: PEO 5%, 2 kV/cm, 1 mL/h, $Bo_E/Pe = 1390$). (b) Initial jet radius $a_{z=0}/a_0$. (c) Initial jet slope m. (d) Initial jet curvature κa_0.

dx.doi.org/10.1021/ma300237j | Macromolecules 2012, 45, 3616–3626

PEO tests (Figure 10). When the electric field was lower and the flow rate and surface tension were higher (smaller Bo_E/Pe), the wetting of the needle was larger (Figure 10b), the initial slope of the profile was smaller (Figure 10c), and the curvature of the profile became negative (Figure 10d). In other words, the Taylor cone became larger and convex. On the other hand, when $Bo_E/Pe > 1000$, the Taylor cone features tended to converge to the following conditions: no wetting $a_{z=0} \cong a_0$, slope $m = da/dz \cong -1$, and curvature $\kappa \cong 1/(2a_0)$.

The initial semivertical angle of the Taylor cone in these PEO tests varied between 13° and 48°. By comparison, Reznik et al.[35] have experimentally and theoretically shown that at an electric field with Bo_E above a critical value, jetting sets in, and the jet acquires an almost conical shape with a semivertical angle of 30°, significantly smaller than the 49.3° angle of the Taylor cone.

3.2. Jet Velocity. An upper-bound estimate for jet velocity v (Figure 11a,b) and strain rate s (velocity gradient) (Figure 11c)

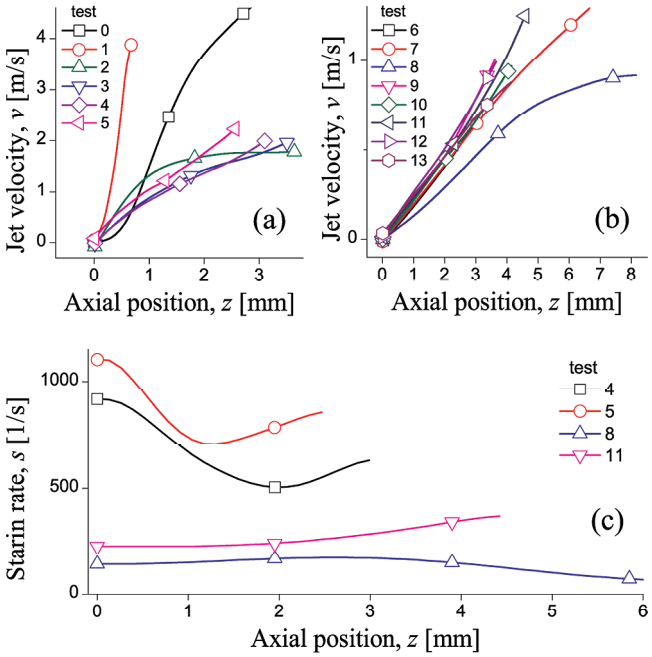

Figure 11. Estimated jet velocity $v = Q/(\pi a^2)$ at position z along the jet, assuming mass conservation. (a) Glycerol (test 0), PMMA 15% (test 1), and PEO 3% (tests 2–5). (b) PEO 5% (tests 6–13). (c) Examples of strain rate s.

can be obtained from the radius measurements by assuming mass conservation (i.e., no evaporation), that is, $v = Q/(\pi a^2)$, where Q is the volumetric flow rate. Typical estimated maximal values were $v \sim 2$ m/s and $s \sim 1000$ 1/s for the PEO 3% tests, $v \sim 1$ m/s and $s \sim 200$ 1/s for the PEO 5% tests, $v \sim 4$ m/s and $s \sim 7000$ 1/s for the PMMA 15% test, and $v \sim 5$ m/s and $s \sim 2000$ 1/s for the glycerol test. Note the nonmonotonic evolution of the strain rate in Figure 11c, which indicates the transition from the capillary-dominated region (Taylor cone) to the viscosity-dominated region.

Using the power law of eq 4, the asymptotic velocity sufficiently far from the orifice can be written as

$$\frac{v}{v_0} = k^2\left(\frac{z}{a_0}\right)^{2\beta} \cong \frac{k^2 z}{a_0} \qquad (5)$$

where, as before, $\beta = 0.47 \cong 1/2$. The corresponding dimensionless strain rate $\hat{s}$ saturates to approximately $\hat{s} = sa_0/v_0 \cong k^2$. Thus, for the studied viscosity-dominated test conditions, the jet strain rate, expressed by k_{vis}^2, increases with the electric field E and conductivity σ and decreases with the velocity v_0 (or flow rate Q) and viscosity μ (or solution concentration c). Note that the "grouping" of the graphs in Figure 11 is due to the sensitivity of k_{vis}^2 to the widely disparate viscosity values between the groups (see Table 1).

Measurements of the jet vertical velocity using particle tracing, v_p, are presented for PEO 5% tests 14 (4 kV/cm, 2.6 mL/h) and 15 (4 kV/cm, 6.4 mL/h) and are compared to velocity estimation based on the mass conservation assumption, v_c (Figure 12). The comparison revealed a large deviation

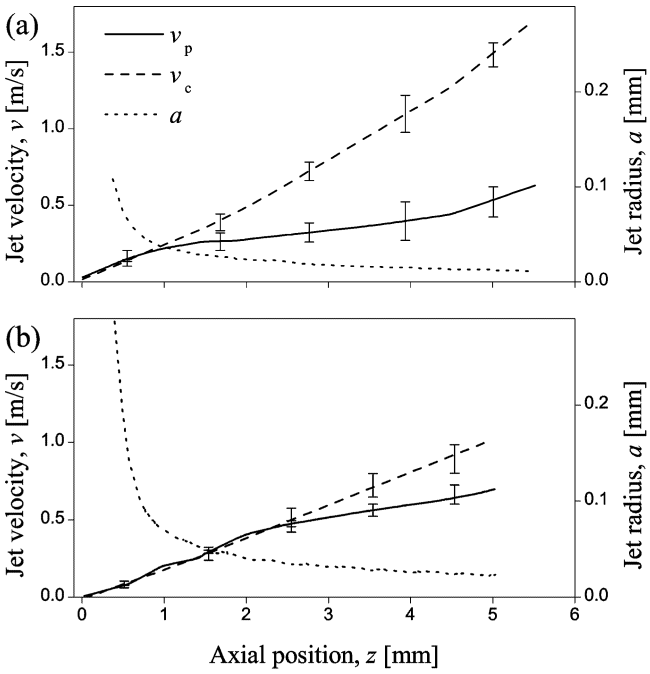

Figure 12. Examples of vertical velocity measurements using silica microbeads, v_p, compared to velocity estimation from the measured radius a assuming mass conservation, v_c. Electrospinning of PEO 5%, under an electric field of 4 kV/cm. (a) Test 14: flow rate of 2.6 mL/h, 589 data points. (b) Test 15: flow rate of 6.4 mL/h, 696 data points.

between the two measurement methods, which intensified with the distance from the orifice and was more pronounced at the lower flow rate (Figure 12a). The difference in strain rate is by a factor of ~2. v_p and v_c coincide close to the orifice, but they begin to separate at a jet diameter of $2a \cong 50$ μm, significantly larger than the particle mean size (~2 μm), thereby ruling out any possibility of adverse effects of the particles on flow. The possible impact of the X-ray beam, especially due to ionization of the air surrounding the jet, can also be ruled out in view of the good correlation between the methods at the beginning of the jet. It also seems unlikely that the dynamic evolution of the polymer network could affect the particles velocity to the extent observed.

Thus, this measurement and comparison suggest a very rapid evaporation, at a distance of only a few millimeters from the jet start. Note that the asymptotic ratio of jet surface area to volume, inversely proportional to the jet radius, is about twice as large in the 2.6 mL/h case compared to the 6.4 mL/h case, accounting for the higher evaporation rate in lower flow rate.

The solvent used in these tests was water, a nonvolatile solvent; however, the relative humidity was fairly low (40%).

The use of particles provides a high-resolution internal view of the flow field within the jet. The image in Figure 13a displays

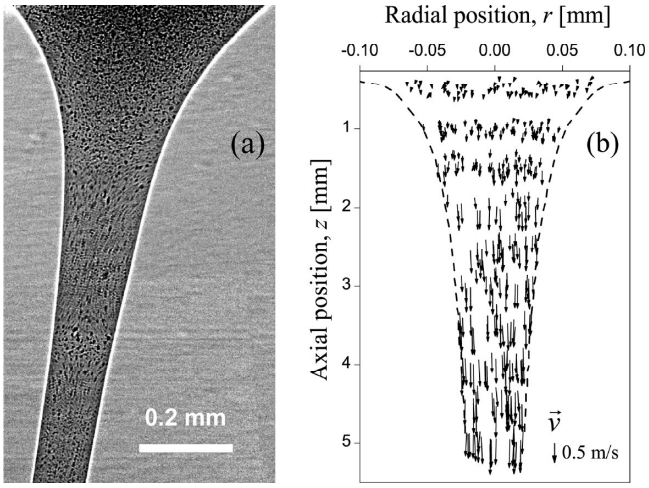

Figure 13. Typical flow field during electrospinning of PEO 5% solution in water, mixed with 0.9 vol % silica microbeads, under an electric field of 4 kV/cm and flow rate of 6.4 mL/h (test 15). (a) Two-pulsed X-ray image of a 1 mm long jet section, captured with a 73.6 μs time interval between exposures. (b) Velocity vector field, $\vec{v}$, generated by particle tracing in a 5 mm long jet section (note the uneven axis scales).

an example of the flow regime during the initial formation of the jet. As seen, flow lines emerge when the velocity is fast enough, and the flow appears to be laminar, as expected from the low Reynolds number. The flow field velocity measurements (Figure 13b) showed a predominantly vertical velocity that seemed to be uniformly distributed across the jet.

However, fitting the data of test 15 (PEO 5%, 4 kV/cm, 6.4 mL/h) to a parabolic shape, as suggested by Reznik et al.,[41] revealed a Poiseuille distribution of the vertical velocity across the jet (Figure 14a), with lower velocity at the jet center when compared to the jet boundary. By contrast, vertical velocity distribution was close to uniform in the lower flow rate case (test 14: PEO 5%, 4 kV/cm, 2.6 mL/h, Figure 14b), possibly

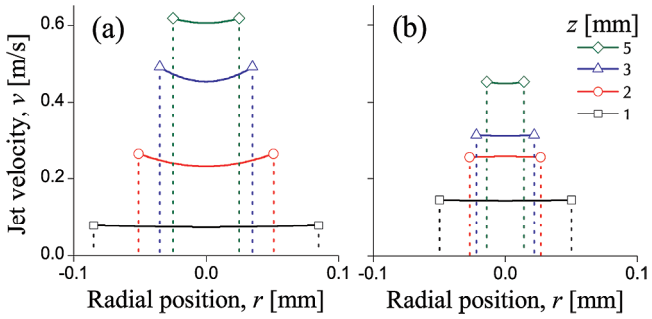

Figure 14. Examples of vertical velocity distribution across the jet, at given locations z along the jet, as a function of the radial distance r from the jet center. The values were averaged along the X-ray beam path and were obtained by parabolic fitting of the test data. Electrospinning was done for PEO 5% solution in water, mixed with 0.9 vol % silica microbeads, under an electric field of 4 kV/cm. (a) Test 15: flow rate of 6.4 mL/h ($\overline{R}^2 > 0.95$). (b) Test 14: flow rate of 2.6 mL/h ($\overline{R}^2 > 0.75$).

due to the smaller jet radius. The sign of the velocity profile curvature in test 15 was opposite to that predicted by Reznik et al. for a viscosity-dominated flow. This phenomena could be influenced by the nonuniform distribution of the polymer (section 3.3) .

3.3. Polymer Concentration Distribution. Measurements of X-ray absorption variations within the jet were carried out on PEO 3% solutions (tests 2–5), PEO 5% solutions (tests 6–13), and a PMMA 15% solution (test 1). The resulting concentration variations are attributed to the effects of evaporation and polymer network stretching. In view of the partial correction for scattering effects (eq 2), these results should be regarded as indicating trends.

As concentration variations are expected to assume circular symmetry at a jet cross section, measurement of radiation transmission through the center of a jet should yield the average absorption change of the jet at a given axial position z. The resulting evolution of the average absorption coefficient, $\Delta\alpha$, along the centerline of the jet of several test cases, is shown in Figure 15a. As seen, the absorption coefficient tends to

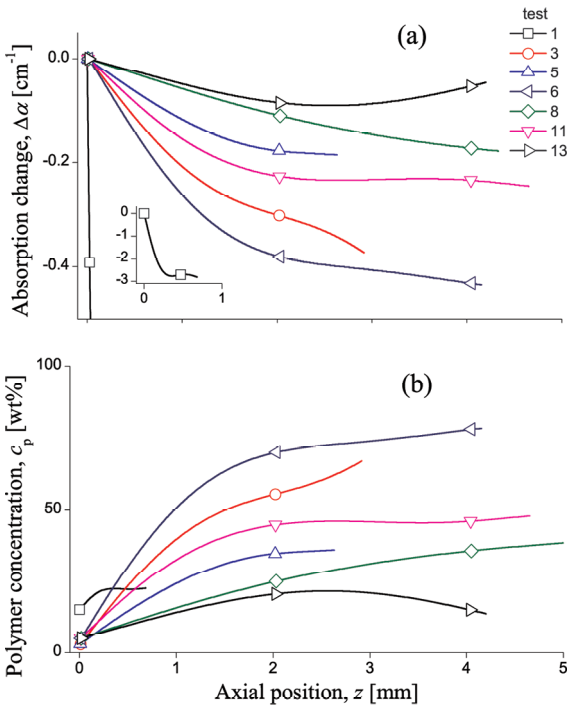

Figure 15. Measured average change in X-ray absorption and polymer concentration, in relation to the distance z from the orifice, based on radiation transmission measurements along the jet centerline. Test 1 is PMMA 15% (inset), tests 3 and 5 are PEO 3%, and tests 6–13 are PEO 5%. (a) Absorption coefficient change, $\Delta\alpha$. (b) Polymer concentration, c_p [wt %].

decrease with the distance from the orifice. At the jet beginning, the rate of decrease is high but slows at increasing distances and sometimes even reverses (e.g., test 13: PEO 5%, 2.8 kV/cm, 7.7 mL/h). Note the high absorption change in test 1 (PMMA 15%, 0.8 kV/cm, 1.9 mL/h, see inset in Figure 15a) due to the high disparity in mass absorption coefficients between PMMA and chloroform.

The polymers in these tests have lower X-ray mass absorption coefficients than their respective solvents (refer to Table 1), and therefore the decrease in the absorption coefficient reflects an increase in polymer concentration (Figure

15b). The results show a significant rise in concentration within the first few millimeters from the jet start, indicating substantial mass loss due to evaporation. This observation supports the similar finding obtained from the velocity measurements in section 3.2. The slowing down, and even reversal, of the concentration change rate along the jet may imply an onset of additional mechanisms, such as polymer chains disentanglement or skin solidification, which retards evaporation rates. Further evaporation may leave voids in the jet core and allow partial relaxation of the polymer matrix.[11]

A common behavior emerges when examining the polymer relative concentration change, $\Delta c_p/c$, recorded in tests 3–12 (PEO in water), as a function of the relative jet radius, a/a_0 (Figure 16). A steep rise in polymer concentration was

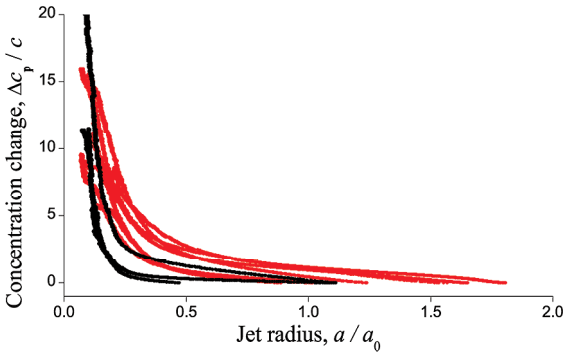

Figure 16. Relative concentration change $\Delta c_p/c$ vs relative jet radius a/a_0, derived from the X-ray absorption measurements at jet center of tests 3–5 (PEO 3%, black lines) and tests 6–12 (PEO 5%, red lines).

observed at $a/a_0 \cong 0.2$, marking a critical radius of ~25 μm, below which rapid evaporation is initiated. Interestingly, velocity measurements demonstrated a similar value, marking the radius at which rapid evaporation began (Figure 12). As noted by Yarin et al.,[42] rapid evaporation starts upon rapid increase in the ratio of the jet surface area to volume, which is inversely proportional to the jet radius.

The concentration change rate can be estimated from the slope of the plot in Figure 16 in the asymptotic region, using the power dependence

$$\frac{\Delta c_p}{c} \sim \left(\frac{a}{a_0}\right)^{-\phi} \tag{6}$$

where the measured exponent is $\varphi \cong 2 \pm 0.5$ for PEO tests 3–12. Since this concentration change is due to evaporation, the corresponding local mass loss rate is then $\sim c(a/a_0)^{-2}$ in the measured region or, in other words, inversely proportional to the jet cross-sectional area.

Absorption measurements across the jet at different axial positions (Figure 17) revealed nonuniform distribution of the polymer, with high concentration boundary layer formed as a result of evaporation. In addition, a peak emerged at the jet center, starting at cross sections $z \geq 1$ mm from the orifice. Our previous theoretical and experimental study[11] attributed this rise to polymer network stretching during electrospinning, which causes lateral contraction of the network, thereby increasing polymer concentration at the center. Polymer chains entangled in a network were shown to approach full extension when the jet vertical velocity was approximately $v/v_0 \cong N_s^{1-\nu}$, where N_s is the number of monomers in a subchain (a section

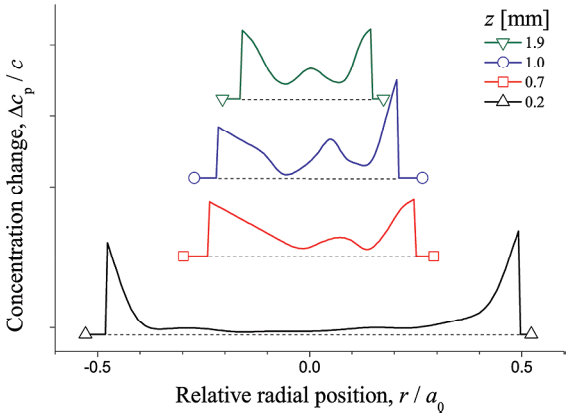

Figure 17. Typical polymer relative concentration change across the jet, $\Delta c_p/c$, vs the relative radial distance from the jet center, r/a_0, for several axial positions z along the jet. The data are derived from the X-ray absorption measurements of PEO 5%, under an electric field of 2.8 kV/cm and flow rate of 1.9 mL/h (test 11). The dashed horizontal lines represent zero concentration change, $\Delta c_p/c = 0$, corresponding to a homogeneous jet with uniform concentration $c_p = c$.

of a polymer chain between two adjacent entanglement nodes) and ν is Flory's exponent. Considering a PEO 5% solution, this criterion predicts significant stretching at a relative radius of $a/a_0 \cong 0.4$, which occurs close to the jet start, in good agreement with the result observed in Figure 17.

Evaporation and stretching impart contradicting effects on the polymer concentration distribution. Evaporation tends to increase concentration at the jet boundary, while stretching leads to its increase at the jet center. Fast stretching of the solution jet counteracts polymer network relaxation due to evaporation and skin formation and causes lateral inward contraction of the network. Material properties and electrospinning conditions influence the relative impact of stretching and evaporation on the polymer matrix and eventually determine the resulting macrostructure of nanofibers (see examples of homogeneous and porous structures in Greenfeld et al.[11]).

The balance between these two processes is demonstrated in Figure 18, which compares the concentration along the jet centerline to that along an offset of half-radius ($a/2$) from the centerline. The comparison is done within the same solution (PEO 5% in water) to avoid concentration effects on evaporation. Under an electric field of 2.8 kV/cm and flow rate of 1.9 mL/h (test 11, Figure 18a), the concentration at the center was higher than at the offset, for sufficiently small jet relative radius a/a_0, indicating noticeable stretching. When reducing the electric field to 2 kV/cm and leaving the flow rate unchanged (test 10, Figure 18b), the concentrations at the center and at the offset remained similar, evidence for balanced effects of evaporation and stretching on polymer distribution at the jet core. Finally, when leaving the electric field unchanged (as in test 11) and increasing the flow rate to 7.9 mL/h (test 13, Figure 18c), a higher concentration was observed at the offset than at the center, evidence for dominant evaporation.

Similar behavior was observed when testing PEO 3%. For example, test 5 (2.2 kV/cm, 2.6 mL/h) involved higher electric field and lower flow rate than test 4 (1.6 kV/cm, 3.8 mL/h) and yielded higher concentrations at the center when compared to the offset. These trends are in agreement with the theoretical prediction,[11] which has shown that the local axial stretching of polymer chains, and consequently their lateral contraction, are

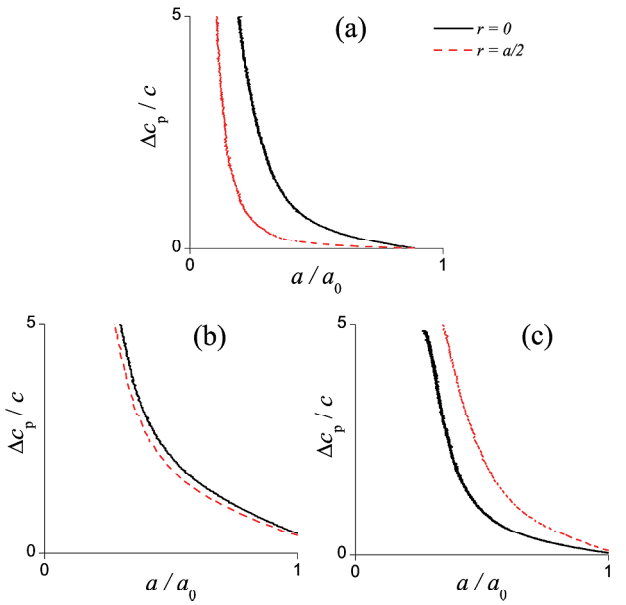

Figure 18. Comparison of the relative concentration change $\Delta c_p/c$ at the jet center ($r = 0$) to that measured at a radial offset from the center ($r = a/2$, averaged over the range $0.4a$ to $0.6a$), presented vs the relative jet radius a/a_0. The data were derived from the X-ray absorption measurements of PEO 5% in (a) test 11 (2.8 kV/cm, 1.9 mL/h), (b) test 10 (2 kV/cm, 1.9 mL/h), and (c) test 13 (2.8 kV/cm, 7.9 mL/h).

proportional to the jet relative local velocity v/v_0, and hence, in view of eq 5), are proportional to k_{vis}^2. Regardless of these findings, it should be noted that high concentration at the jet boundary was observed in all tests.

4. CONCLUSIONS

Fast X-ray phase-contrast imaging was applied for high-resolution investigation of the initial straight section of electrospinning polymer jets, extending up to 10 mm from the orifice. The experiment aimed at providing data on the flow field and polymer concentration distribution within the jet, which can help describe the state of the polymer network during electrospinning.

Details relating to jet radius, velocity, and strain rate were measured for a range of electrospinning conditions and polymer solutions. Particle tracing velocimetry allowed for flow regime viewing inside the jet, characterized by laminar flow and dominant vertical velocity. The velocity was found to be slower than an estimation based on mass conservation assumption, indicating a substantial mass loss due to evaporation at a very early stage of the process.

Measurement of pixel intensities were converted to X-ray radiation absorption coefficients that allowed for estimation of the polymer distribution within the jet. Concentrations were found to rapidly increase below a critical radius, evidence of rapid evaporation. The rate of mass loss due to evaporation seemed to be much higher than theoretical predictions.[42] In addition, the concentration variation across the jet revealed high concentrations at the jet boundary due to evaporation as well as a concentration rise at the jet center. The latter phenomenon is attributed to polymer stretching that causes lateral contraction of the polymer network toward the jet center and is in good agreement with theoretical models.[11] Moreover, it was shown that evaporation is dominant when stretching is weaker (e.g., at lower electric field and/or higher flow rate), canceling the concentration peaks measured at the jet center.

The balance between the effects of evaporation and stretching determines the polymer network nonequilibrium conformation during electrospinning and can help clarify the reasons for the diverse macrostructures and properties found in solid nanofibers. In particular, the size-dependent mechanical, thermomechanical, and thermodynamic properties of as-spun nanofibers,[8,9,12,45] such as the rise of the elastic modulus at small diameters, are attributed to the internal molecular and supermolecular structure of the polymer matrix in nanofibers.[11]

X-ray imaging during electrospinning can provide internal flow and concentration data, unattainable by other in-situ measurement methods. The current implementation of the method is, however, limited to the initial section of the jet that is sufficiently stable to be captured within the small field of view of the imaging system. Nevertheless, further investigation downstream, at narrower jet diameters on the order of micrometers, can provide evidence for polymer chains disentanglement and reveal nonuniform flow regime due to rapid evaporation, possibly with streamlines toward the jet boundary. Such observations may be important for electrospinning applications such as drug delivery and coatings.

AUTHOR INFORMATION

Corresponding Author

*Tel 972 4 957 1287; fax 972 4 957 1291; e-mail green_is@netvision.net.il.

Notes

The authors declare no competing financial interest.

ACKNOWLEDGMENTS

We gratefully acknowledge the financial support of the United States–Israel Binational Science Foundation (BSF Grant 2006061), the RBNI–Russell Berrie Nanotechnology Institute, and the Israel Science Foundation (ISF Grant 770/11). Use of the Advanced Photon Source, an Office of Science User Facility operated for the U.S. Department of Energy (DOE) Office of Science by Argonne National Laboratory, was supported by the U.S. DOE under Contract DE-AC02-06CH11357. We acknowledge Dr. Arkadii Arinstein for insightful discussions on polymer dynamics. We thank Dr. Rene Van-Hout for valuable advice on X-ray image processing.

REFERENCES

(1) Han, T.; Yarin, A. L.; Reneker, D. H. *Polymer* **2008**, *49* (6), 1651–1658.
(2) Gupta, P.; Elkins, C.; Long, T. E.; Wilkes, G. L. *Polymer* **2005**, *46* (13), 4799–4810.
(3) Reneker, D. H.; Yarin, A. L.; Zussman, E.; Xu, H. *Adv. Appl. Mech.* **2007**, *41*, 43–195.
(4) Reneker, D. H.; Yarin, A. L.; Fong, H.; Koombhongse, S. *J. Appl. Phys.* **2000**, *87* (9), 4531–4547.
(5) Bellan, L. M.; Craighead, H. G.; Hinestroza, J. P. *J. Appl. Phys.* **2007**, *102* (9), 094308.
(6) Hohman, M. M.; Shin, M.; Rutledge, G.; Brenner, M. P. *Phys. Fluids* **2001**, *13* (8), 2201–2220.
(7) Shin, Y. M.; Hohman, M. M.; Brenner, M. P.; Rutledge, G. C. *Polymer* **2001**, *42* (25), 9955–9967.
(8) Burman, M.; Arinstein, A.; Zussman, E. *Appl. Phys. Lett.* **2008**, *93* (19), 193118.
(9) Arinstein, A.; Burman, M.; Gendelman, O.; Zussman, E. *Nat. Nanotechnol.* **2007**, *2* (1), 59–62.

(10) Burman, M.; Arinstein, A.; Zussman, E. *Europhys. Lett.* **2011**, *96*, 16006.
(11) Greenfeld, I.; Arinstein, A.; Fezzaa, K.; Rafailovich, M. H.; Zussman, E. *Phys. Rev. E* **2011**, *84* (4), 041806.
(12) Zussman, E.; Arinstein, A. *J. Polym. Sci., Part B: Polym. Phys.* **2011**, *49* (10), 691−707.
(13) Guenthner, A. J.; Khombhongse, S.; Liu, W. X.; Dayal, P.; Reneker, D. H.; Kyu, T. *Macromol. Theory Simul.* **2006**, *15* (1), 87−93.
(14) Dayal, P.; Kyu, T. *Phys. Fluids* **2007**, *19* (10), 107106.
(15) Dayal, P.; Liu, J.; Kumar, S.; Kyu, T. *Macromolecules* **2007**, *40* (21), 7689−7694.
(16) Koombhongse, S.; Liu, W. X.; Reneker, D. H. *J. Polym. Sci., Part B: Polym. Phys.* **2001**, *39* (21), 2598−2606.
(17) Casper, C. L.; Stephens, J. S.; Tassi, N. G.; Chase, D. B.; Rabolt, J. F. *Macromolecules* **2004**, *37* (2), 573−578.
(18) Deitzel, J. M.; Krauthauser, C.; Harris, D.; Pergantis, C.; Kleinmeyer, J. *Polym. Nanofibers* **2006**, *918*, 56−73.
(19) Larrondo, L.; Manley, R. S. J. *J. Polym. Sci., Part B: Polym. Phys.* **1981**, *19* (6), 921−932.
(20) Stephens, J. S.; Frisk, S.; Megelski, S.; Rabolt, J. F.; Chase, D. B. *Appl. Spectrosc.* **2001**, *55* (10), 1287−1290.
(21) Priebe, M.; Kalbfleisch, S.; Tolkiehn, M.; Koster, S.; Abel, B.; Davies, R. J.; Salditt, T. *New J. Phys.* **2010**, *12*, 1−12.
(22) MacPhee, A. G.; Tate, M. W.; Powell, C. F.; Yue, Y.; Renzi, M. J.; Ercan, A.; Narayanan, S.; Fontes, E.; Walther, J.; Schaller, J.; Gruner, S. M.; Wang, J. *Science* **2002**, *295* (5558), 1261−1263.
(23) Wang, Y. J.; Liu, X.; Im, K. S.; Lee, W. K.; Wang, J.; Fezzaa, K.; Hung, D. L. S.; Winkelman, J. R. *Nat. Phys.* **2008**, *4* (4), 305−309.
(24) Im, K. S.; Fezzaa, K.; Wang, Y. J.; Liu, X.; Wang, J.; Lai, M. C. *Appl. Phys. Lett.* **2007**, *90* (9), 091919.
(25) Sasov, A. *European Conference for Non-Destructive Testing (ECNDT)* **2006**, *We.1.5.4*, 1−6.
(26) Richter, A. G.; Guico, R.; Shull, K.; Wang, J. *Macromolecules* **2006**, *39* (4), 1545−1553.
(27) Gullikson, E. X-Ray Interactions with Matter. http://henke.lbl.gov/optical_constants/.
(28) www.surface-tension.de. Surface tension values of some common test liquids.
(29) http://www.smartmeasurement.com. Conductivity of common fluids.
(30) Theron, S. A.; Zussman, E.; Yarin, A. L. *Polymer* **2004**, *45* (6), 2017−2030.
(31) Thomas, D. G. *J. Colloid Sci.* **1965**, *20* (3), 267−277.
(32) Staben, M. E.; Davis, R. H. *Int. J. Multiphase Flow* **2005**, *31* (5), 529−547.
(33) Roe, R. J., *Methods of X-ray and Neutron Scattering in Polymer Science*; Oxford University Press: New York, 2000; p xiv, 331 p.
(34) Reeves, R. V.; White, J. D. E.; Dufresne, E. M.; Fezzaa, K.; Son, S. F.; Varma, A.; Mukasyan, A. S. *Phys. Rev. B* **2009**, *80* (22), 224103.
(35) Reznik, S. N.; Yarin, A. L.; Theron, A.; Zussman, E. *J. Fluid Mech.* **2004**, *516*, 349−377.
(36) Feng, J. J. *Phys. Fluids* **2002**, *14* (11), 3912−3926.
(37) Kirichenko, V. N.; Petrianovsokolov, I. V.; Suprun, N. N.; Shutov, A. A. *Dokl. Akad. Nauk SSSR* **1986**, *289* (4), 817−820.
(38) Spivak, A. F.; Dzenis, Y. A. *Appl. Phys. Lett.* **1998**, *73* (21), 3067−3069.
(39) Hohman, M. M.; Shin, M.; Rutledge, G.; Brenner, M. P. *Phys. Fluids* **2001**, *13* (8), 2221−2236.
(40) Higuera, F. J. *J. Fluid Mech.* **2006**, *558*, 143−152.
(41) Reznik, S. N.; Zussman, E. *Phys. Rev. E* **2010**, *81* (2), 026313.
(42) Yarin, A. L.; Koombhongse, S.; Reneker, D. H. *J. Appl. Phys.* **2001**, *89* (5), 3018−3026.
(43) Thompson, C. J.; Chase, G. G.; Yarin, A. L.; Reneker, D. H. *Polymer* **2007**, *48* (23), 6913−6922.
(44) Fridrikh, S. V.; Yu, J. H.; Brenner, M. P.; Rutledge, G. C. *Phys. Rev. Lett.* **2003**, *90* (14), 144502.
(45) Ji, Y.; Li, C.; Wang, G.; Koo, J.; Ge, S.; Li, B.; Jiang, J.; Herzberg, B.; Klein, T.; Chen, S.; Sokolov, J. C.; Rafailovich, M. H. *EPL* **2008**, *84* (5), 56002.

5.3 Fiber nanostructure and mechanical properties

Camposeo, A.,* I. Greenfeld,* F. Tantussi, S. Pagliara, M. Moffa, F. Fuso, M. Allegrini, E. Zussman, and D. Pisignano, *Local mechanical properties of electrospun fibers correlate to their internal nanostructure.* Nano Letters, 2013. **13**(11): p. 5056−5062.[3]

* These authors contributed equally to this work.

NANO LETTERS

Letter

pubs.acs.org/NanoLett

Local Mechanical Properties of Electrospun Fibers Correlate to Their Internal Nanostructure

Andrea Camposeo,*[,†,‡,□] Israel Greenfeld,*[,§,□] Francesco Tantussi,[∥,⊥] Stefano Pagliara,[†,■] Maria Moffa,[†,‡] Francesco Fuso,[∥,⊥] Maria Allegrini,[∥,⊥] Eyal Zussman,[§] and Dario Pisignano*[,†,‡,¶]

[†]National Nanotechnology Laboratory of Istituto Nanoscienze-CNR, via Arnesano, I-73100 Lecce, Italy

[‡]Center for Biomolecular Nanotechnologies @UNILE, Istituto Italiano di Tecnologia, via Barsanti, I-73010 Arnesano, LE, Italy

[§]Department of Mechanical Engineering, Technion - Israel Institute of Technology, Haifa 32000, Israel

[∥]Dipartimento di Fisica "Enrico Fermi" and CNISM, Università di Pisa, Largo Bruno Pontecorvo 3, I-56127 Pisa, Italy

[⊥]Istituto Nazionale di Ottica INO−CNR, Sezione di Pisa, I-56127 Pisa, Italy

[¶]Dipartimento di Matematica e Fisica "Ennio De Giorgi", Università del Salento, via Arnesano, I-73100 Lecce, Italy

Supporting Information

ABSTRACT: The properties of polymeric nanofibers can be tailored and enhanced by properly managing the structure of the polymer molecules at the nanoscale. Although electrospun polymer fibers are increasingly exploited in many technological applications, their internal nanostructure, determining their improved physical properties, is still poorly investigated and understood. Here, we unravel the internal structure of electrospun functional nanofibers made by prototype conjugated polymers. The unique features of near-field optical measurements are exploited to investigate the nanoscale spatial variation of the polymer density, evidencing the presence of a dense internal core embedded in a less dense polymeric shell. Interestingly, nanoscale mapping the fiber Young's modulus demonstrates that the dense core is stiffer than the polymeric, less dense shell. These findings are rationalized by developing a theoretical model and simulations of the polymer molecular structural evolution during the electrospinning process. This model predicts that the stretching of the polymer network induces a contraction of the network toward the jet center with a local increase of the polymer density, as observed in the solid structure. The found complex internal structure opens an interesting perspective for improving and tailoring the molecular morphology and multifunctional electronic and optical properties of polymer fibers.

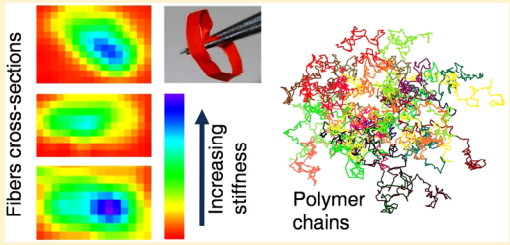

KEYWORDS: *Nanofibers, near-field microscopy, Young's modulus, conjugated polymers*

Fiber-shaped materials are the building blocks of many natural systems[1,2] and the enabling components of some of the most important modern technologies.[3−6] The advent of nanotechnologies has enabled the synthesis of micro- and nanoscale fibers by a variety of approaches, with a prominent control on shape and composition.[7] Experimental and theoretical research efforts have evidenced enhanced electronic, optical and mechanical properties of these innovative, almost one-dimensional (1D) nanomaterials compared to the bulk counterpart.[7−9]

Among 1D nanomaterials, polymer nanofibers deserve particular attention, because the use of polymers is continuously increasing in many fields, especially in low-end applications, where cost considerations prevail over performances. In this framework, polymeric 1D nanomaterials offer both low costs and physical properties enhanced by the nanoscopic morphology and peculiar assembly of macromolecules within nanofibers.[10−12] In particular, by reducing the fiber diameter below a critical value, an increase of the Young's modulus can be obtained,[10] demonstrating the possibility of tailoring the mechanical properties by controlling the geometry and supramolecular assembly in polymer nanosystems. Moreover, the peculiar packing of organic semiconductors in 1D nanostructures allows improved charge mobilities, polarized emission, enhanced amplified spontaneous emission and nonlinear optical properties to be observed, and a control of energy transfer phenomena to be obtained.[9−14] Therefore, predicting and managing the resultant polymer supramolecular assembly and the nanofiber internal structure is becoming increasingly relevant, aiming to ultimately optimize the performance of polymer-based systems and devices through smart engineering of the different processing steps.

Polymer nanofibers are mainly fabricated by elongating and stretching a polymer solution or melt by mechanical, capillary, or electrostatic forces.[11,15,16] This may result in extended chain conformation, very different with respect to standard solution or melt processing methods (spincoating, casting, rapid prototyping, etc.). The access to the fiber internal nanostruc-

Received: June 12, 2013
Published: October 3, 2013

ture of the polymer macromolecules is however challenging. So far, studies on the inner features of 1D polymeric systems have utilized small-area electron diffraction (SAED),[17] transmission electron microscopy,[18] infrared,[19] and Raman[20,21] spectroscopies, however either the limited spatial resolution or the inability to probe molecular orientation have prevented to resolve the internal structure of the analyzed systems, having submicrometer characteristic features.

In this work, we investigate the complex internal structure of conjugated polymer nanofiber materials. In particular, the nanoscale spatial variation of the fiber Young's modulus, and of the polymer density determined by near-field measurements, evidence the presence of a stiff and dense internal core with typical size of nearly 30% of the fiber diameter, embedded in a softer and less dense polymeric shell. These findings are supported by theoretical modeling and simulations of the molecular structural evolution during the elongational flow of semidilute polymer solutions at the base of electrospinning, which predict substantial stretching of the polymer network, accompanied by its contraction toward the jet center, as observed in the solid structure. The understanding and prediction of the internal structure of active fiber materials can be very important for the design and realization of novel advanced functional materials.

To our aim, a prototype conjugated polymer is used that constitutes an unequaled tool for probing optically the fiber internal nanostructure with nm-resolution. Fibers are made by electrospinning the poly[2-methoxy-5-(2-ethylhexyl-oxy)-1,4-phenylene-vinylene] (MEH-PPV), which is largely used in lasers,[22] field effect transistors,[23] and light-emitting diodes.[24] Randomly and uniaxially oriented free-standing, flexible mats of fibers (Figure 1a) are produced by dissolving the polymer in a mixture of good and poor solvents (see Methods).[25] The fibers emit visible light peaked at 605 nm as shown in Figure 1b, where we also show the temperature dependence of the emission. The photoluminescence (PL) peak blueshifts by about 10 nm upon increasing temperature, which can be attributed to a decreased conjugation length due to excitation of torsional and liberation modes.[26,27] More importantly, the blueshift observed in fibers is smaller than that in thin films by about a factor two,[26] evidencing reduced sensitivity to torsional distortions. This suggests irregular molecular assembly in the fibers compared to the film, which motivates to investigate their internal nanoscale structure much more in depth. Indeed, the stretching process, whose dynamics is determined by competing forces related to the applied electric field and molecular interactions (surface tension and viscoelesticity), as well as by rapid solvent evaporation, can result in complex internal nanostructuring.[28]

To study the effects of such phenomena on individual fibers, we determine their mechanical and densitometric properties by nanoscale indentation experiments and scanning near-field optical microscopy (SNOM). The local Young's modulus of a fiber deposited on quartz can be obtained with atomic force microscopy (AFM) by measuring the nanoscale deformation induced by a controlled load, applied along a direction perpendicular to the fiber longitudinal axis and to the substrate (Figure S3 in the Supporting Information). The mechanical response of the nanofiber upon indentation depends on its elastic properties, which are mainly related to the local density, degree of crystallinity and arrangement of the polymer molecules. Interestingly, the MEH-PPV fibers feature a spatially nonuniform effective elastic modulus (E_{fiber}), whose resulting

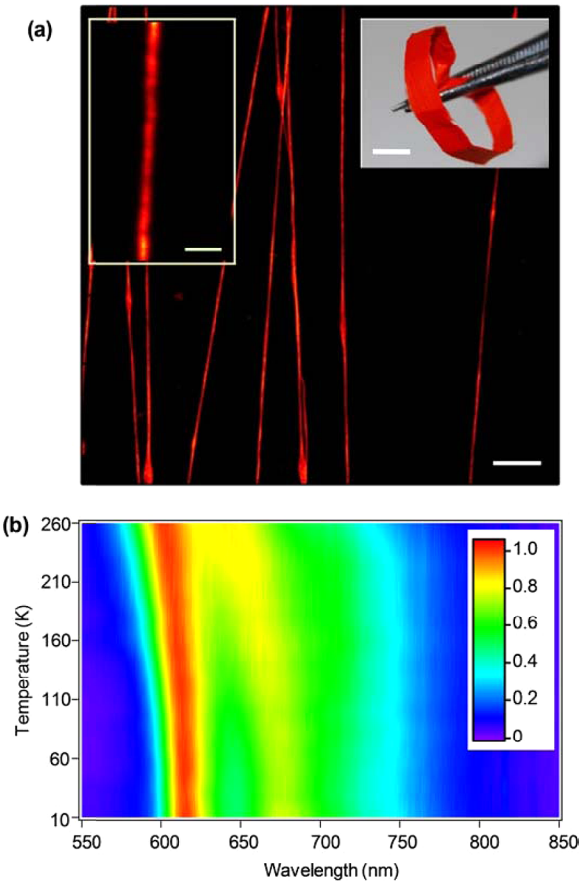

Figure 1. (a) Fluorescence confocal micrographs of MEH-PPV fibers. Scale bar: 10 μm. Left inset scale bar: 2 μm. Right inset: photograph of a uniaxially oriented nanofiber mat (scale bar, 4 mm). (b) MEH-PPV fiber emission spectra vs sample temperature. Color scale: normalized PL intensity.

value is affected by the polymer structure underlying the indentation region. Overall, in an axial region (whose width is roughly 30% of the fiber diameter), E_{fiber} is about twice the value measured in the peripheral region which constitutes the external layer of each fiber. However, due to the low thickness of the fibers (typically <200 nm), these measurements are affected by the mechanical properties of the substrate underneath.[29,30] To rule out such effects, indentation experiments are better performed on the cross-sectional surface of cleaved fibers. To this aim, we first embed MEH-PPV fibers in a photocurable polymer, and freeze the resulting solid composite in liquid nitrogen. Following careful fracturing, the fiber cross-sectional surfaces are clearly visible both by emission confocal microscopy and by AFM (Figure 2a,b). Examples of Young's modulus maps measured on the fiber cross sections are shown in Figure 2c–e, where data clearly evidence the presence of a stiffer internal region nearby the fiber longitudinal axis, extending over about 30% of the cross sectional area. This axial region exhibits a Young's modulus up to 80–120 MPa, larger than that in the surrounding sheath by about a factor 2.

This has to be clearly correlated to the internal nanostructure and density, which we also investigate by SNOM in order to probe simultaneously morphology and optical properties with subwavelength resolution.[31−34] Figure 3a displays the map of the transmittance, $T(x, y) = I_s(x, y)/I_{sub}$, obtained by raster scanning the sample, measuring the intensity of the transmitted

dx.doi.org/10.1021/nl4033439 | Nano Lett. 2013, 13, 5056–5062

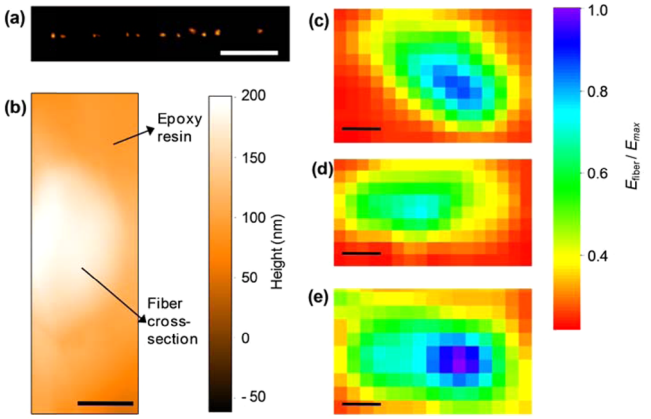

Figure 2. (a) Confocal emission image of the cross-sectional surface of an array of MEH-PPV fibers. Scale bar: 10 μm. (b) Tapping mode topography micrograph of the cross-sectional surface of an individual MEH-PPV nanofiber (bright region). The fiber is embedded in a UV-cured polymer. Scale bar: 200 nm. (c–e) Examples of cross-sectional Young's modulus (normalized to the maximum value, E_{max}) maps measured by AFM indentation measurements (force–distance curves). The orange-red regions correspond to the cured polymer embedding the fibers. Scalebars: (c) 500, (d) 200, and (e) 300 nm, respectively.

light, $I_s(x, y)$, and normalizing to the light transmitted by the transparent regions of a quartz substrate (I_{sub}). The measured T values are superimposed to the simultaneously acquired fiber topography and used to calculate the average absorption coefficient along the local beam path. In Figure 3b, we display the absorption coefficient, α/α_{max}, normalized to the maximum absorption value measured in the single fiber (α_{max} in the range $3–3.5 \times 10^4$ cm^{-1}). It is remarkable that the map showing the spatial variation of the absorption coefficient is not flat, as would be in case of homogeneous distribution of the absorbers. Instead, comparison of the line profiles of the absorption coefficient and the fiber height (Figure 3c) clearly indicates a higher concentration of absorbing chromophores at the fiber core. Such a nonuniform distribution of the absorbing chromophores has been observed in all the investigated fibers (see Supporting Information). Overall, both mechanical and optical data evidence that the electrospun conjugated polymer fibers are characterized by a core–sheath structure with a denser and stiffer core, which can significantly impact on technological and optoelectronic applications.

In order to rationalize the origin of such a complex internal structure of the nanomaterial, we develop a model of the polymer elongational dynamics during electrospinning, where the flow of the solution jet exerts strong stretching forces. Owing to inherent bonding defects, which substitute rigid conjugated links by flexible tetrahedral links along the chain backbone, the conjugated macromolecules can be described as flexible chains[35] with specific adjustments pertaining to their high segmental aspect ratio.[36] The conjugated polymer chain is so treated as a linear, flexible, freely jointed chain, whose rigid segments are chain sections between neighboring bonding defects. Scaling is used to incorporate the interactions relevant to the solvent type and to describe the entangled polymer network conformation in the semidilute solution.[35] An example of a simulated polymer network at rest is shown in Figure 4a. During electrospinning, each subchain (a chain section between two neighboring entanglements) is acted upon by the hydrodynamic force induced by the solvent, as well as by the entropic forces applied by its neighboring subchains. The resulting conformational evolution has been previously modeled for fully flexible chains, using a beads-and-springs lattice model and a 3D random walk simulation.[35] This is readily applicable to conjugated subchains, using as input the calculated initial network mesh size (ξ_0 = 20 nm) and number of segments per subchain (N_s = 14), corresponding to the polymer volume fraction (φ = 0.025), and assuming a defects concentration of 10% of monomers, together with the jet velocity. Since evaporation is negligible at the early stage of electrospinning, the jet velocity can be derived (see details in Methods) from the measured radius, a, of the jet (Figure 4b). The simulation provides the dependence of the polymer network radius, a_p, on the longitudinal spatial coordinate, z (Figure 4b). The polymer subchains contract laterally as a consequence of the redistribution of probabilities between the axial and radial directions of the random walk. The lateral contraction of individual subchains affects the conformation of the whole polymer network, narrowing its radius a_p faster than the narrowing of the jet radius a. The simulated conformation of the whole network and its evolution along the jet (Figure 4b) demonstrate the dominant effect of axial stretching on lateral contraction, while only a negligible effect of radial

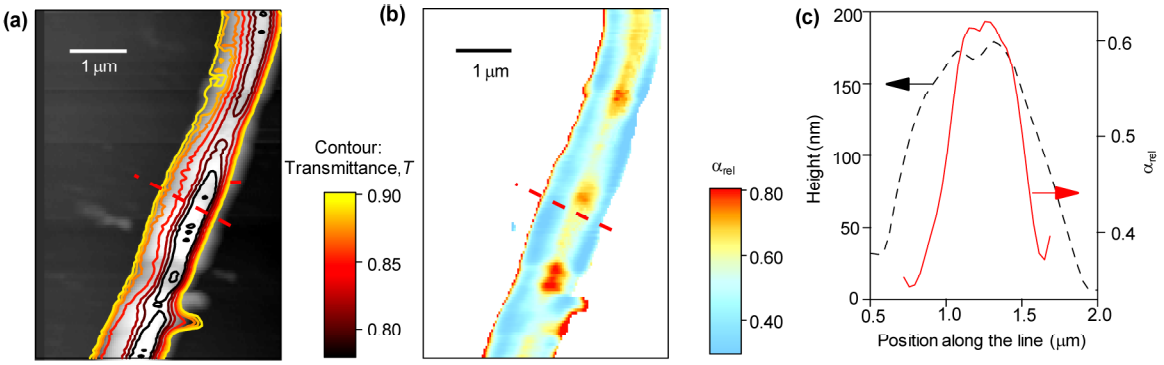

Figure 3. (a) Contour plot of the SNOM transmission superimposed to the corresponding topography. The topography map is produced by the shear-force method during the scan of a single MEH-PPV fiber deposited on quartz, and the optical transmission is acquired simultaneously by collecting the signal passing through the sample. Transmission is averaged over all polarization states of the near-field probing radiation. The color scale refers to the contour plot. (b) Map of the nanoscale variation of optical absorption. (c) Line profile analysis showing the cross sections of the topography (dashed line) and the corresponding relative optical absorption, α/α_{max} (continuous line) along the dashed segment in maps (a) and (b).

dx.doi.org/10.1021/nl4033439 | Nano Lett. 2013, 13, 5056–5062

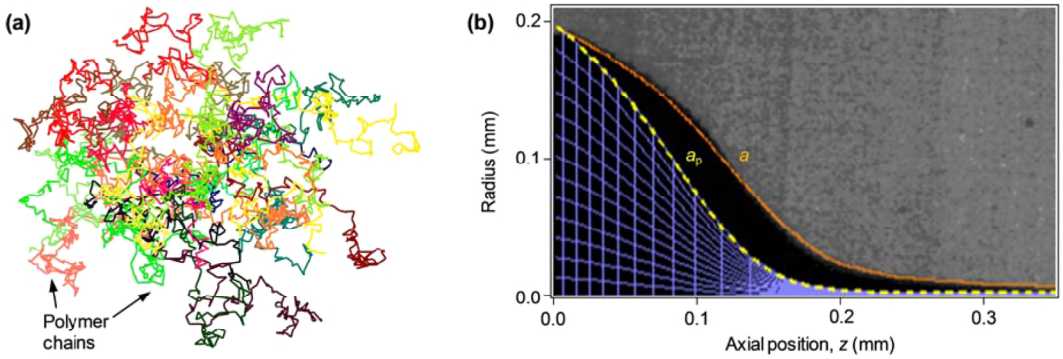

Figure 4. (a) Example of a section of a network at rest, made of 30 conjugated polymer chains, each consisting of 146 segments (MW = 380,000 g/mol). The size of the network section is about 150 nm, and its average mesh size is 20 nm. (b) Image of the measured steady state jet profile and corresponding jet radius a vs axial position z (continuous line). The modeled polymer network radius, a_p vs z, is also shown (dashed line), together with the network mesh (viewed mesh density is diluted ×300 in each direction). The maximal jet radius is larger than the needle internal radius, a_0 = 96 μm, due to wetting of the needle face. Electric field = 1.8 kV/cm, flow rate = 10 μL/min, MEH-PPV volume fraction ϕ = 0.025.

hydrodynamic compression, evidenced in the almost uniform radial mesh size. The network compacts around the jet center, thereby increasing polymer concentration near the center. Experimental evidence of this effect has been reported for optically inert polymers such as poly(ethylene oxide) and poly(methylmethacrylate), by measuring the polymer jet absorption profile during electrospinning with fast X-ray phase contrast imaging,[37] whereas it was previously unexplored in active, light-emitting or conductive nanofibers. In fact, our model generalizes the stretching and compacting phenomenon[35,37] for all types of linear polymers, using the degree of chain flexibility as a tuning parameter. In the case of semiflexible conjugated polymers whose backbone structure is rigid, the bonding defects concentration determines chain flexibility (i.e., each rigid segment consists of several monomers), whereas fully flexible polymer chains are a particular case of the model with max defects concentration (i.e., each rigid segment consists of one monomer). Consequently, the model and simulation predict that the stretching phenomenon should be prominent in conjugated polymers because of their longer rigid segments. Hence, MEH-PPV is an excellent choice as a model system allowing us to measure for the first time the nanostructure of solid fibers by optical means, owing to its high absorption as well as expectedly higher traces of the effects of electrospinning-induced stretching.

The network conformation during electrospinning depends on the balance between stretching and evaporation.[37] Dominant evaporation can cause rapid solidification of the jet surface, retarding evaporation from the core, and resulting in a tubular structure.[28,38] On the other hand, dominant strain rates will cause higher polymer density in the center due to stretching. Our model shows that the stretching of conjugated chains occurs earlier than in fully flexible chains, and one can therefore expect a dense core in the solid fiber. Indeed, the distance from the needle where full chain extension is accomplished is below 1 mm for semiflexible conjugated polymers, as demonstrated by overlaying the simulated polymer network on the image of the actual jet (Figure 4b). Moreover, the theoretical modeling of the network shows that the jet radius reduction ratio at the position where full extension is reached is lower by a factor of typically 2−5 (depending on the solvent quality) compared to fully flexible chains, confirming an earlier network stretching in conjugated polymers.

In addition, crystallization is enhanced in regions of strong stretching and alignment. Interchain interaction and $\pi-\pi$ stacking are known to lead to high extent of local crystallinity.[39] When neighboring chain sections are aligned in the same direction, they correlate to each other according to Onsager's rods theory and may eventually crystallize. This phenomenon will be more pronounced in conjugated polymers with longer rigid chain sections between bonding defects. The model shows that unlike flexible polymers conjugated chains intermix within a single correlation volume in the network, increasing the probability of interchain overlap. The model specifically predicts that such correlation is likely to occur during electrospinning of MEH-PPV with typical production-induced bonding defects concentration (5−10% of monomers), at the solution concentrations used in our experiments.

Here, the measurements of the material properties of as-spun MEH-PPV solid nanofibers provide convincing evidence that the polymer matrix conformation described for the liquid phase of the jet is essentially retained in the solid nanofiber. In particular, SNOM measurements (Figure 3) show higher optical absorption at the fiber center and lower absorption closer to its boundary, indicative of higher polymer concentration at the fiber core. The regions of lower concentration close to the boundary have a large fraction of free volume and are most probably porous, possibly even encouraging nucleation and growth of crystalline structures.[40]

Moreover, traces of an early solidification of a skin during the spinning[41] can be seen in the slight absorption rise very close to the fiber boundary and on its surface (visible for instance in Figure 3b). These observations suggest that during electrospinning the solvent content at the jet core is low as a result of network stretching and inward contraction, whereas closer to the jet boundary the solvent content is high and evaporation through the solidified skin leaves voids and porosity in the inner matrix close to the boundary. This is consistent with the measured spatial variation of the Young's modulus (Figure 2), since lower values are measured far from the fiber axis, where a less dense polymer network is present with higher free-volume content. This process-induced core−sheath structure impacts on many physical properties, determining, for instance, an increase of the effective conjugation length in conjugated polymer nanofibers.[42]

Conclusions. In summary, the elongational dynamics of polymer semidilute solutions under electrostatic fields is

dx.doi.org/10.1021/nl4033439 | *Nano Lett.* 2013, 13, 5056−5062

predicted to include a fast axial stretching of the polymer network accompanied by a radial contraction toward the core, resulting in a higher polymer concentration and axial orientation at the fiber center. Our modeling shows that this morphology should be more pronounced in the semiflexible conjugated polymers due to their longer rigid chain segments, but evidence from X-ray imaging of electrospinning jets indicates that it is also expected in fully flexible polymers. As demonstrated by the SNOM analysis and the AFM indentation measurements, the polymer conformation during the electrospinning process is retained in the solid matrix. This process-induced core−sheath structure impacts on many physical properties, determining, for instance, an increase of the Young's modulus close to the fiber core. In perspective, the found graded-density internal structure and the different mechanical properties of the core and the sheath of polymer fibers open interesting opportunities for many applications. In organic semiconductors, the presence of a core with close-packed molecules can improve charge transport, whereas the sheath with less dense molecules can determine the suitable conditions to enhance amplification of the light guided in the fiber. Both charge transport and light amplification can be therefore improved in a single nanostructure. For scaffold applications, the complex internal structure can be exploited to engineering multifunctional fibers, where the high density core can provide enhanced mechanical strength and/or feed stimuli (electrical, thermal, etc.), whereas the porous external layer can be a suitable soft substrate for cell adhesion, contaminant removal, or drug delivery.

Methods. *Nanofiber Production.* The nanofibers are produced by electrospinning a solution of MEH-PPV (MW 380,000 g/mol, American Dye Source Inc., Baie-d'Urfé, Canada), dissolved in dimethyl sulfoxide and tetrahydrofuran (1:4 w:w, see Supporting Information). A 70 μM polymer solution is stored into a 1.0 mL plastic syringe tipped with a 27-gauge stainless steel needle and injected at the end of the needle at a constant rate of 10 μL/min by a microprocessor dual drive syringe pump (33 Dual Syringe Pump, Harvard Apparatus Inc., Holliston, MA). The positive lead from a high-voltage supplier (XRM30P, Gamma High Voltage Research Inc., Ormond Beach, FL) is connected to the metal needle applying a bias of 5 kV. The collector is made of two Al stripes biased at a negative voltage of −6 kV and positioned at a mutual distance of 2 cm and at a distance of 6 cm from the positively charged needle. All the electrospinning experiments are performed at room temperature with air humidity in the range 40−50%. Aligned arrays of free-standing fibers are deposited across metallic stripes and then collected on a 1 × 1 cm^2 quartz substrate. Arrays of uniaxially aligned MEH-PPV nanofibers are also fabricated by using a rotating collector.

Polymer Jet Imaging. For imaging the polymer jet profile, a stereomicroscope (Leica MZ 12.5) and a high speed camera (Photron, FASTCAM APX RS, 1024 pixel ×1024 pixel, 10000 frame s^{-1}) are used. A typical collected single frame image is shown in Figure 4b. The dependence of the jet velocity, v, and radius, a, on the axial coordinate z, is given by the following relation[35,37]

$$\frac{v}{v_0} \cong \left(\frac{a}{a_0}\right)^{-2} \cong \left(1 + \frac{z}{z_0}\right)^{2\beta} \quad (1)$$

Given the initial velocity v_0 = 5.8 mm/s and radius a_0 = 96 μm, fit of the jet radius data yields z_0 = 22 μm, and β = 0.94.

Nanofiber Characterization. Fluorescence confocal microscopy is performed by using a A1R MP confocal system (Nikon), coupled to an inverted microscope (Eclipse Ti, Nikon). The fibers are excited by an Ar^+ ion laser (λ_{exc} = 488 nm) through an oil immersion objective with numerical aperture of 1.4. PL spectra are collected by exciting the MEH-PPV fibers with a diode laser (λ_{exc} = 405 nm) and collecting the emission by an optical fiber coupled to a monochromator, equipped with a Charge Coupled Device detector (Yobin Yvon). The fiber samples are mounted in a He closed-cycle cryostat under vacuum (10^{-4} mbar) for variable temperature measurements.

AFM and Mechanical Compression Experiments. AFM imaging is performed by using a Multimode system equipped with a Nanoscope IIIa electronic controller (Veeco Instruments). The nanofiber topography is measured in tapping mode, utilizing Si cantilevers featuring a resonance frequency of 250 kHz. To map the local Young's modulus of the nanofibers (see Supporting Information for details), force−distance curves are collected by using nonconductive, Au-coated silicon nitride cantilevers with a nominal spring constant of 0.32 N/m, tip radius of 20 nm, and resonant frequency of 52.5 kHz. The fiber is supported underneath by the substrate, assuring no bending or buckling during measurements, and the force is applied perpendicularly to the fiber longitudinal axis and to the substrate. The system is calibrated by measuring the force−distance curve of a stiff sample (Si/SiO_2, quartz). For mapping the local mechanical properties on the fiber cross-sectional surface, arrays of uniaxially aligned MEH-PPV fibers are embedded in a photocurable polymer (NOA68, Norland Products Inc.), that is cured by exposure to UV light for 3 min. The curing UV intensity is kept at about 1 mW/cm^2 to avoid degradation of the active polymer. The samples are frozen in liquid nitrogen and fractured along a direction perpendicular to the fiber alignment axis. Samples are then inspected by confocal and AFM microscopies in order to select those showing smooth cross-sectional surfaces for subsequent mechanical measurements.

SNOM Analysis. Optical properties at nanoscale are investigated with a scanning near-field optical microscope. The instrument operates in the emission-mode: the sample interacts with the near-field produced by a tapered optical fiber probe (Nanonics) featuring a 50 nm diameter apical aperture (nominal). The system allows the fiber topography (i.e., height profile) to be measured simultaneously to optical transmission in each scan, by the shear-force method. This allows a topography map [$h(x,y)$] to be obtained, which is then used as a local measurement of the fiber thickness. A semiconductor laser with wavelength λ = 473 nm, coupled to the tapered fiber, is used to measure the local absorption of the nanofibers. To this aim, the signal transmitted by the sample is collected by an aspheric lens and sent onto a miniaturized photomultiplier (Hamamatsu R-5600), connected to a lock-in amplifier. In order to avoid any artifact related to variations of the fiber thickness, the absorption coefficient is calculated as $\alpha(x, y) = -\ln[T(x, y)]/h(x, y) = \sigma\rho(x, y)$, where $h(x, y)$ indicates the local nanofiber thickness, deducible from the topography map measured simultaneously to the optical transmission map (Figure 3a and Figure S2, see Supporting Information for more details). Linear absorption is assumed as dominant and the Lambert−Beer law is used to estimate absorption, in turn related to the absorption cross section at the incident laser

wavelength (σ) and to the local density of absorbing chromophores, $\rho(x, y)$.

■ ASSOCIATED CONTENT

Supporting Information

Additional technical details on nanofiber morphological and mechanical properties, Young's modulus mapping, and SNOM analysis. This material is available free of charge via the Internet at http://pubs.acs.org.

■ AUTHOR INFORMATION

Corresponding Authors

*E-mail: andrea.camposeo@nano.cnr.it.
*E-mail: green_is@netvision.net.il.
*E-mail: dario.pisignano@unisalento.it.

Present Address

■(S.P.) Sector of Biological and Soft Systems, Department of Physics, Cavendish Laboratory, University of Cambridge, J.J. Thomson Avenue, Cambridge CB3 0HE, United Kingdom.

Author Contributions

□A.C. and I.G. contributed equally to this work.

Notes

The authors declare no competing financial interest.

■ ACKNOWLEDGMENTS

V. Fasano and G. Potente are acknowledged for confocal and SEM images, respectively. The authors also gratefully thank S. Girardo for high-speed imaging of the polymer jet and E. Caldi for assistance in the SNOM measurements. We gratefully acknowledge the financial support of the United States-Israel Binational Science Foundation (BSF Grant 2006061), the RBNI-Russell Berrie Nanotechnology Institute, and the Israel Science Foundation (ISF Grant 770/11). The research leading to these results has received funding from the European Research Council under the European Union's Seventh Framework Programme (FP/2007-2013)/ERC Grant Agreement 306357 (ERC Starting Grant "NANO-JETS").

■ REFERENCES

(1) Vollrath, F.; Knigth, D. P. Liquid crystalline spinning of spider silk. *Nature* **2001**, *410*, 541−548.
(2) Cattaneo Vietti, T.; Bavestrello, G.; Cerrano, C.; Sara, M.; Benatti, U.; Giovine, M.; Gaino, E. Optical fibres in an Antarctic sponge. *Nature* **1996**, *383*, 397−398.
(3) Kao, C. K. Sand from centuries past: Send future voices fast. *Rev. Mod. Phys.* **2010**, *82*, 2299−2303.
(4) Dvir, T.; Timko, B. P.; Kohane, D. S.; Langer, R. Nanotechnological strategies for engineering complex tissues. *Nat. Nanotechnol.* **2011**, *6*, 13−22.
(5) Shannon, M. A.; Bohn, P. W.; Elimelech, M.; Georgiadis, J. G.; Mariñas, B. J.; Mayes, A. M. Science and technology for water purification in the coming decades. *Nature* **2008**, *452*, 301−310.
(6) Lu, W.; Zu, M.; Byun, J.-H.; Kim, B.-S.; Chou, T.-W. State of the art of carbon nanotube fibers: opportunities and challenges. *Adv. Mater.* **2012**, *24*, 1805−1833.
(7) Xia, Y.; Yang, P.; Sun, Y.; Wu, Y.; Mayers, B.; Gates, B.; Yin, Y.; Kim, F.; Yan, H. One-dimensional nanostructures: synthesis, characterization and applications. *Adv. Mater.* **2003**, *15*, 353-389.
(8) Scholes, G. D. Rumbles, G. Excitons in nanoscale systems. *Nat. Mater.* **2006**, *5*, 683−696.
(9) Kim, F. S.; Ren, G.; Jenekhe, S. A. One-dimensional nanostructures of π-conjugated molecular systems: assembly, properties, and applications from photovoltaics, sensors, and nanophotonics to nanoelectronics. *Chem. Mater.* **2011**, *23*, 682−732.
(10) Arinstein, A.; Burman, M.; Gendelman, O.; Zussman, E. Effect of supramolecular structure on polymer nanofibre elasticity. *Nat. Nanotechnol.* **2007**, *2*, 59−62.
(11) Shen, S.; Henry, A.; Tong, J.; Zheng, R.; Chen, G. Polyethylene nanofibres with very high thermal conductivities. *Nat. Nanotechnol.* **2010**, *5*, 251−255.
(12) Wang, S.; Kappl, M.; Liebewirth, I.; Müller, M.; Kirchhoff, K.; Pisula, W.; Müllen, K. Organic field-effect transistors based on highly ordered single polymer fibers. *Adv. Mater.* **2012**, *24*, 417−420.
(13) Martini, I. B.; Craig, I. M.; Molenkamp, W. C.; Miyata, H.; Tolbert, S. H.; Schwartz, B. J. Controlling optical gain in semiconducting polymers with nanoscale chain positioning and alignment. *Nat. Nanotechnol.* **2007**, *2*, 647−652.
(14) Nguyen, T.-Q.; Wu, J.; Doan, V.; Schwartz, B. J.; Tolbert, S. H. Control of energy transfer in oriented conjugated polymer-mesoporous silica composites. *Science* **2000**, *288*, 652−656.
(15) De Marco, C.; Mele, E.; Camposeo, A.; Stabile, R.; Cingolani, R.; Pisignano, D. Organic light-emitting nanofibers by solvent-resistant nanofluidics. *Adv. Mater.* **2008**, *20*, 4158−4162.
(16) Reneker, D. H.; Chun, I. Nanometer diameterfibres of polymer, produced by electrospinning. *Nanotechnology* **1996**, *7*, 216−223.
(17) Dersch, R.; Liu, T.; Schaper, A. K.; Greiner, A.; Wendorff, J. H. Electrospun nanofibers: internal structure and intrinsic orientation. *J. Polym. Sci., Part A: Polym. Chem.* **2003**, *41*, 545−553.
(18) Ma, M.; Krikorian, V.; Yu, J. H.; Thomas, E. L.; Rutledge, G. C. Electrospun polymer nanofibers with internal periodic structure obtained by microphase separation of cylindrically confined block copolymers. *Nano Lett.* **2006**, *6*, 2969−2972.
(19) Liang, W.; Martin, C. R. Template-synthesized polyacetylene fibrils show enhanced supermolecular order. *J. Am. Chem. Soc.* **1990**, *112*, 9666−9668.
(20) Bellan, L. M.; Craighead, H. G. Molecular orientation in individual electrospun nanofibers measured via polarized Raman spectroscopy. *Polymer* **2008**, *49*, 3125-3129 (2008).
(21) Pagliara, S.; Vitiello, M. S.; Camposeo, A.; Polini, A.; Cingolani, R.; Scamarcio, G.; Pisignano, D. Optical Anisotropy in Single Light-Emitting Polymer Nanofibers. *J. Phys. Chem. C* **2011**, *115*, 20399−20405.
(22) Hide, F.; Díaz-García, M. A.; Schwartz, B. J.; Andersson, M. R.; Pei, Q.; Heeger, A. J. Semiconducting polymers: a new class of solid-state laser materials. *Science* **1996**, *273*, 1833−1836.
(23) Asadi, K.; Gholamrezaie, F.; Smits, E. C. P.; Bloma, P. W. M.; de Boer, B. Manipulation of charge carrier injection into organic field-effect transistors by self-assembled monolayers of alkanethiols. *J. Mater. Chem.* **2007**, *17*, 1947−1953.
(24) Yamamoto, H.; Wilkinson, J.; Long, J. P.; Bussman, K.; Christodoulides, J. A.; Kafafi, Z. H. Nanoscale Organic Light-Emitting Diodes. *Nano Lett.* **2005**, *5*, 2485−2488.
(25) Di Benedetto, F.; Camposeo, A.; Pagliara, S.; Mele, E.; Persano, L.; Stabile, R.; Cingolani, R.; Pisignano, D. Patterning of light-emitting conjugated polymer nanofibres. *Nat. Nanotechnol.* **2008**, *3*, 614−619.
(26) Neves, A. A. R.; Camposeo, A.; Cingolani, R.; Pisignano, D. Interaction scheme and temperature behavior of energy transfer in a light-emitting inorganic-organic composite system. *Adv. Funct. Mater.* **2008**, *18*, 751−757.
(27) da Silva, M. A. T.; Dias, I. F. L.; Duarte, J. L.; Laureto, E.; Silvestre, I.; Cury, L. A.; Guimarães, P. S. S. Identification of the optically active vibrational modes in the photoluminescence of MEH-PPV films. *J. Chem. Phys.* **2008**, *128*, 094902.
(28) Arinstein, A.; Zussman, E. Electrospun polymer nanofibers: mechanical and thermodynamic perspectives. *J. Polym. Sci., B: Polym. Phys.* **2011**, *49*, 691−707.
(29) Cappella, B.; Silbernagl, D. Nanomechanical Properties of Mechanical Double Layers: A Novel Semiempirical Analysis. *Langmuir* **2007**, *23*, 10779−10787.
(30) Silbernagl, D.; Cappella, B. Reconstruction of a hidden topography by single AFM force-distance curves. *Surf. Sci.* **2009**, *603*, 2363−2369.

(31) Eisele, D. M.; Knoester, J.; Kirstein, S.; Rabe, J. P.; Vanden Bout, D. A. Uniform exciton fluorescence from individual molecular nanotubes immobilized on solid substrates. *Nat. Nanotechnol.* **2009**, *4*, 658−663.
(32) O'Carrol, D.; Iacopino, D.; Redmond, G. Luminescent conjugated polymer nanowire Y-junctions with on-branch molecular anisotropy. *Adv. Mater.* **2009**, *21*, 1160−1165.
(33) Pomraenke, R.; Ropers, C.; Renard, J.; Lienau, C.; Lüer, L.; Polli, D.; Cerullo, G. Structural Phase Contrast in Polycrystalline Organic Semiconductor Films Observed by Broadband near-Field Optical Spectroscopy. *Nano Lett.* **2007**, *7*, 998−1002.
(34) Stiegler, J. M.; Huber, A. J.; Diedenhofen, S. L.; Gomez Rivas, J.; Algra, R. E.; Bakkers, E. P. A. M.; Hillenbrand, R. Nanoscale Free-Carrier Profiling of Individual Semiconductor Nanowires by Infrared near-Field Nanoscopy. *Nano Lett.* **2010**, *10*, 1387−1392.
(35) Greenfeld, I.; Arinstein, A.; Fezzaa, K.; Rafailovich, M. H; Zussman, E. Polymer dynamics in semidilute solution during electrospinning: a simple model and experimental observations. *Phys. Rev. E* **2011**, *84*, 041806.
(36) Hu, D.; Yu, J.; Wong, K.; Bagchi, B.; Rossky, P. J.; Barbara, P. F. Collapse of stiff conjugated polymers with chemical defects into ordered, cylindrical conformations. *Nature* **2000**, *405*, 1030−1033.
(37) Greenfeld, I.; Fezzaa, K.; Rafailovich, M. H.; Zussman, E. Fast X-ray Phase-Contrast Imaging of Electrospinning Polymer Jets: Measurements of Radius, Velocity, and Concentration. *Macromolecules* **2012**, *45*, 3616−3626.
(38) Stachewicz, U.; Bailey, R. J.; Wang, W.; Barber, A. H. Size dependent mechanical properties of electrospun polymer fibers from a composite structure. *Polymer* **2012**, *53*, 5132−5137.
(39) Craig, I. M.; Tassone, C. J.; Tolbert, S. H.; Schwartz, B. J. Second-harmonic generation in conjugated polymer films: A sensitive probe of how bulk polymer crystallinity changes with spin speed. *J. Chem. Phys.* **2010**, *133*, 044901.
(40) Diao, Y.; Harada, T.; Myerson, A. S.; Hatton, T. A.; Trout, B. L. The role of nanopore shape in surface-induced crystallization. *Nat. Mater.* **2011**, *10*, 867−871.
(41) Koombhongse, S.; Liu, W.; Reneker, D. H. Flat polymer ribbons and other shapes by electrospinning. *J. Polym. Sci., Part B: Polym. Phys.* **2001**, *39*, 2598−2606.
(42) Li, D.; Babel, A.; Jenekhe, S. A.; Xia, Y. Nanofibers of conjugated polymers prepared by electrospinning with a two-capillary spinneret. *Adv. Mater.* **2004**, *16*, 2062−2066.

SUPPORTING INFORMATION

Nanofiber Morphology. Figure S1 displays the MEH-PPV fiber morphology as obtained by scanning electron microscopy (SEM) and atomic force microscopy (AFM). SEM analysis is performed by using a Nova NanoSEM 450 field emission system (FEI) operating with an acceleration voltage of 5 kV and an aperture size of 30 μm. A thin layer of Cr (<10 nm) is thermally evaporated on top of the samples before SEM imaging. Figures S1a,b display the SEM images of MEH-PPV fibers deposited on quartz substrates and then analysed by near-field optical analysis. The fibers have mean diameters of about 500 nm.

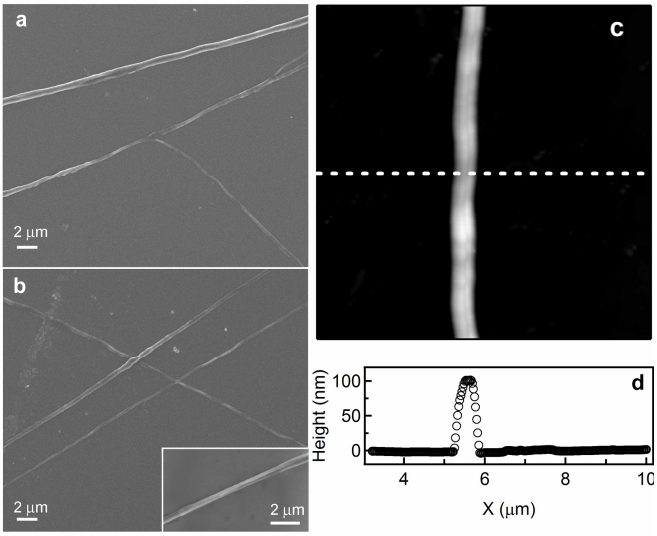

Figure S1. (a, b) SEM images of MEH-PPV fibers. (c, d) AFM topographic map (c) and height profile (d) of a MEH-PPV fiber (width 450 nm and height 100 nm.).

The surface topography of the nanofibers is investigated by AFM, employing a Multimode head (Veeco Instruments, Plainview, NY) equipped with a Nanoscope IIIa controller and operating in tapping mode. Phosphorous-doped Si tips are employed, with an 8-10 nm nominal curvature radius and a resonant frequency of 250 kHz. Figures S1c,d display a typical AFM topography map of a MEH-PPV fiber, evidencing a ribbon-shape. Similar results are obtained by measuring the fiber topography by the shear-force method with the scanning near field optical microscope (Fig. S2).

Force-Indentation measurements. The nanoscale spatial variation of the nanofiber elastic modulus is measured by acquiring force (F_{load}) *vs* distance curves, by using a Multimode AFM system equipped with a Nanoscope IIIa electronic controller (Veeco Instruments). The force vs. distance curves are then converted to force vs. deformation plots (F_{load} vs. δ).[S1,S2] The dependence of the applied load on the deformation of the sample (δ) is approximated by the Hertz model:[S3]

$$F_{load} = \left(\frac{4}{3}\sqrt{R}\right)\left(\frac{1-\nu_t^2}{E_t} + \frac{1-\nu_{fiber}^2}{E_{fiber}}\right)^{-1} \delta^{\frac{3}{2}} \qquad \text{(S1)}$$

where R is the tip radius, ν_t and ν_f are the Poisson's ratio of the cantilever (ν_t =0.27) and of the fiber (ν_f =0.35), respectively, and E_t and E_{fiber} are the Young's modulus of the cantilever (E_t =160 GPa) and of the nanofiber, respectively. The nanofiber Young's modulus is obtained by fitting the force vs. indentation curves to Eq. S1.[S4]

Indentation measurements on the surface of fibers (Fig. S3) are performed by applying the load, F_{load}, along a direction perpendicular to the quartz substrate and to the fiber longitudinal axis, assuring the absence of bending or buckling of the fiber during the measurement. Indeed, AFM images of the investigated region, acquired before and after indentation measurements, do not evidence variations of the fiber morphology and position. Due to the finite thickness of the fiber deposited on the quartz substrate, these measurements can be affected by the presence of the stiffer substrate. B. Cappella et al.[S5] have reported a dependence of the measured effective elastic modulus on the thickness of the polymer film deposited on glass. In particular they have observed an increase of the effective elastic modulus upon decreasing the film thickness, since for thinner films the indentation measurement is sensitive also to the mechanical properties of the substrate.

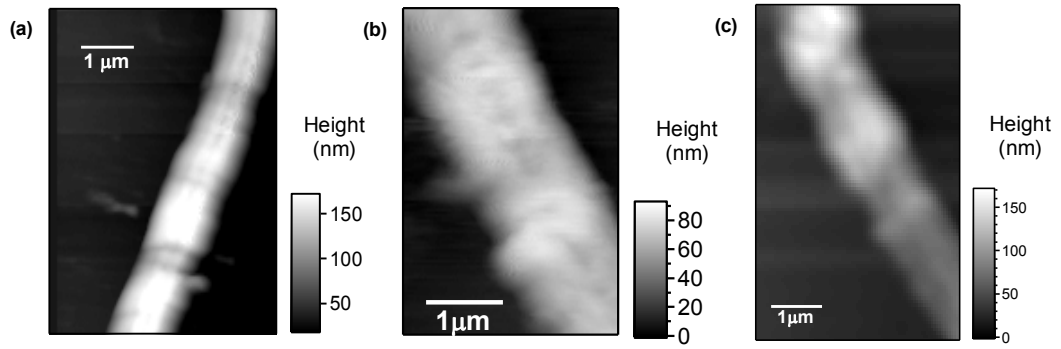

Figure S2. Examples of topography maps of MEH-PPV fibers obtained by the shear-force method. The map reported in (a) corresponds to the topography of the fiber displayed in Fig. 3. The fiber height is < 170 nm, whereas the width is about 1 μm, in accordance with the ribbon shape of the fiber evidenced by both AFM and SEM measurements (Fig. S1).

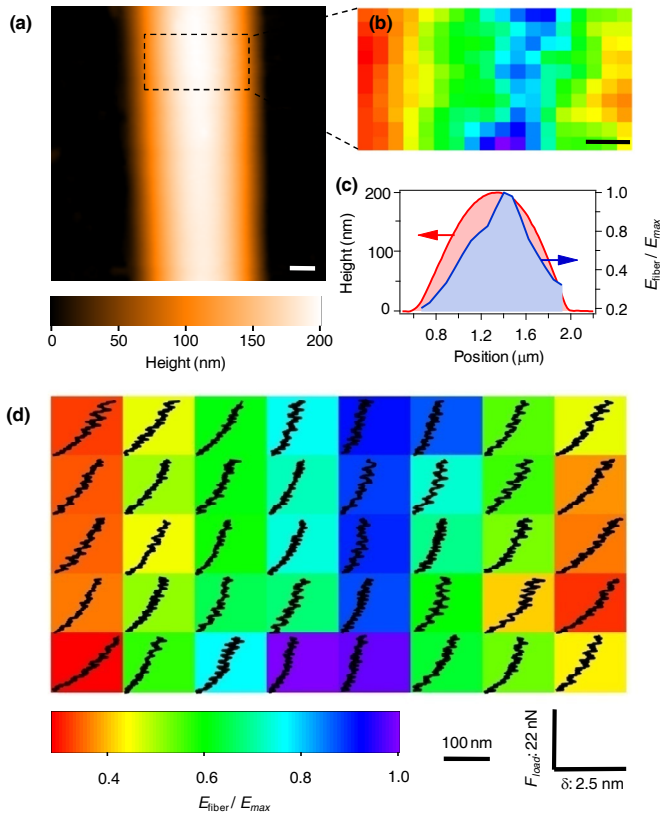

Figure S3. Indentation measurements on the surface of fibers. (a) AFM micrograph of a single MEH-PPV spun fiber. Scalebar: 250 nm. (b) Corresponding Young's modulus (E_{fiber}) map, normalized to the maximum value (E_{max}). Scalebar: 200 nm, color scale shown in the bottom of the Figure. The map is obtained by determining the force-distance curves in the region highlighted by a dashed box in (a). (c) Line profiles showing the cross-sections of the topography (red continuous line) and of E_{fiber} (blue continuous line). (d) Example of applied load (F_{load}) vs. deformation (δ) curves measured in different points of the fiber surface. Each pixel area is 140×140 nm^2, and the pixel color shows the local normalized Young's modulus. The curves shown in each pixel have higher slopes for stiffer regions, according to (x, y) axes (δ and F_{load}), respectively, shown in the bottom-right corner. The overall analyzed area is highlighted in (a) by a dashed box.

They also proposed a semi-empirical analysis that allows to obtain the mechanical properties of the polymer film, taking into account its finite thickness.[S6] The force-distance measurements performed on a fiber deposited on quartz substrate provide therefore an effective elastic modulus, possibly affected by the substrate.

In particular, for a fiber composed by uniformly distributed polymer, *larger* effective values are expected at the fiber border, due to the reduced thickness and to the relatively major contribution from the substrate. Instead, we find a *decrease* of the elastic modulus at the fiber border (Fig. S3), that can be related to the presence of a softer fiber sheath, as confirmed by the fiber cross-section measurements discussed in the main paper (Fig. 2). In Fig. S4, two examples of force *vs*. indentation (δ) curves, measured at the fiber core and sheath, respectively, are shown.

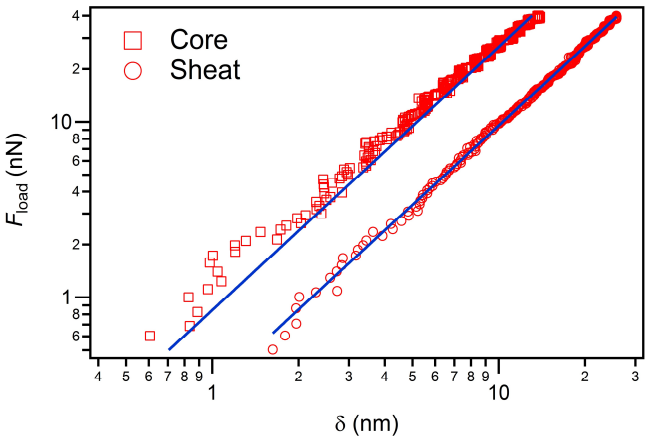

Figure S4. Examples of force vs. indentation (δ) curves measured on the fiber cross-section surface in the core (squares) and sheath (circles). The difference of the resulting E_{fiber} is evidenced by the different intercepts of the curves with the F_{load} axis in the bi-logarithmic plot. The continuous lines are fits to the data by Eq. S1.

SNOM measurements. The spatial variation of the polymer density in the fibers is evaluated by near-field absorption microscopy, a measurement allowing to estimate the absorption coefficient, that depends on the local density of the absorbing chromophores, according to the Lambert-Beer law. In order to obtain maps of the absorption coefficient (α), the light transmitted through the fiber illuminated by the optical near field of a tapered fiber is measured simultaneously to its topography. This is accomplished by the shear-force method,[S7] allowing both the fiber-sample distance to be kept constant and the fiber height profile to be obtained in each scan. Examples of fiber topography maps obtained by this method are shown in Fig. S2. The map of the absorption coefficient is then calculated as: $\alpha(x, y) = - \ln[T(x, y)]/h(x, y)$, where $T(x,y)$ is the map of the fiber transmission coefficient and $h(x,y)$ is the local, measured fiber thickness, which is fully taken into account in this way. Examples of transmittance and absorption coefficient maps obtained in various MEH-PPV fibers are shown in Fig. S5.

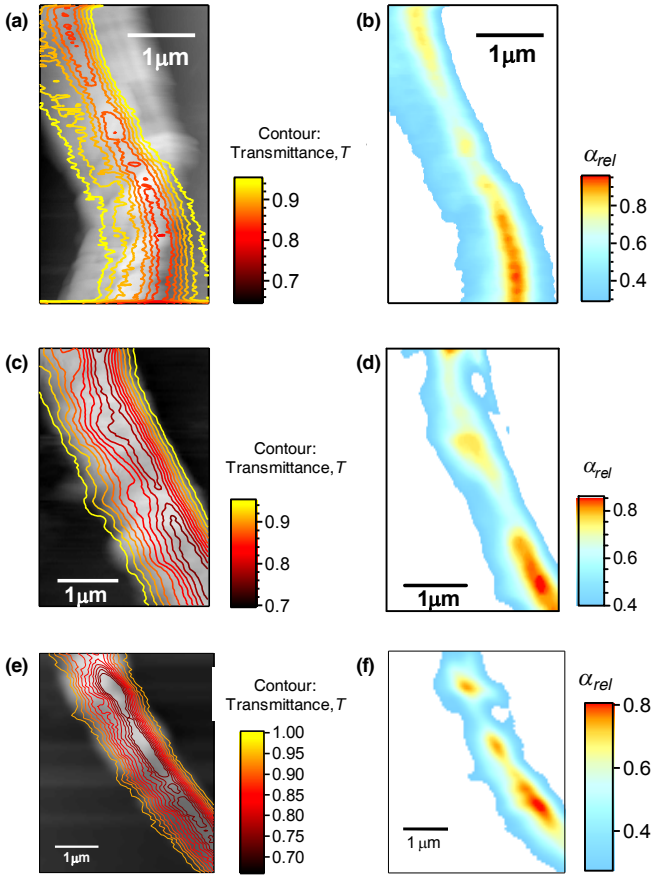

Figure S5. (a, c, e) Examples of fiber topography maps, with superimposed contour plots of the SNOM transmission data, and corresponding maps of the nanoscale variation of optical absorption (b, d, f) respectively.

References.

S1. Tan, S.; Sherman Jr., R. L.; Ford, W. T. Nanoscale compression of polymer microspheres by atomic force microscopy. *Langmuir* **2004**, *20*, 7015-7020.

S2. Touhami, A.; Nysten, B.; Dufrene, Y. F. Nanoscale mapping of the elasticity of microbial cells by atomic force microscopy. *Langmuir* **2003**, *19*, 4539-4543.

S3. Butt, H. J.; Cappella, B.; Kappl, M. Force measurements with the atomic force microscope: technique, interpretation and applications. *Surf. Sci. Rep.* **2005**, *59*, 1-152.

S4. Lin, H.-N. ; Lin, H.-L.; Wang, S.-S.; Yu, L.-S.; Perng, G.-Y.; Chen, S.-A.; Chen, S.-H. Nanoscale charge transport in an electroluminescent polymer investigated by conducting atomic force microscopy. *Appl. Phys. Lett.* **2002**, *81*, 2572.

S5. Cappella, B.; Silbernagl, D. Nanomechanical properties of mechanical double layers: a novel semiempirical analysis. *Langmuir* **2007**, *23*, 10779-10787.

S6. Silbernagl, D.; B. Cappella. Reconstruction of a ridde topography by single AFM force-distance curves. *Surf. Sci.* **2009**, *603*, 2363-2369.

S7. Karrai, K.; Grober, R. D. Piezoelectric tip-sample distance control for near field optical microscopes. *Appl. Phys. Lett.* **1995**, *66*, 1842.

5.4 Control of chain orientation in fibers

Camposeo, A.,* I. Greenfeld,* F. Tantussi, M. Moffa, F. Fuso, M. Allegrini, E. Zussman, and D. Pisignano, *Mechanistic insight and nanoscale control of the orientational and polarization properties of active polymer fibers.* Submitted for publication, 2013.[4]

* These authors contributed equally to this work.

Mechanistic insight and nanoscale control of the orientational and polarization properties of active polymer fibers

Andrea Camposeo[1,2†*], Israel Greenfeld[3†*], Francesco Tantussi[4], Maria Moffa[2,5], Francesco Fuso[4,6], Maria Allegrini[4,6], Eyal Zussman[3], Dario Pisignano[1,2,5]

[1] *National Nanotechnology Laboratory of Istituto Nanoscienze-CNR, Università del Salento, via Arnesano, I-73100 Lecce (Italy)*
[2] *Center for Biomolecular Nanotechnologies @UNILE, Istituto Italiano di Tecnologia, via Barsanti, I-73010 Arnesano, LE (Italy)*
[3] *Department of Mechanical Engineering, Technion - Israel Institute of Technology, Haifa 32000, Israel*
[4] *Dipartimento di Fisica "Enrico Fermi" and CNISM, Università di Pisa, Largo Bruno Pontecorvo 3, I-56127 Pisa (Italy)*
[5] *Dipartimento di Matematica e Fisica "Ennio De Giorgi", Università del Salento, via Arnesano I-73100 Lecce, (Italy)*
[6] *Istituto Nazionale di Ottica INO-CNR, Sezione di Pisa, Largo Bruno Pontecorvo 3, I-56127 Pisa (Italy)*

† *These authors contributed equally to this work.*
* *E-mail: andrea.camposeo@nano.cnr.it, green_is@netvision.net.il*

Polymer fibers are currently exploited in tremendously important technologies.[1-4] Their innovative properties are mainly determined by the behavior of the polymer macromolecules under the elongation induced by external mechanical or electrostatic forces, characterizing the fiber drawing process.[5,6] Although enhanced physical properties were observed in polymer fibers produced under strong stretching conditions,[5,7] studies of the process-induced nanoscale organization of the polymer molecules are not available, and most of fiber properties are still obtained on an empirical basis. Here we reveal the orientational properties of semiflexible polymers in electrospun nanofibers, which allow the polarization properties of active fibers to be finely controlled. Modeling and simulations of the conformational evolution of the polymer chains during electrostatic elongation of semidilute solutions demonstrate that the molecules stretch *almost fully* within less than 1 mm from jet start, increasing polymer axial orientation at the jet center. The nanoscale mapping of the local dichroism of individual fibers by polarized near-field optical microscopy unveils for the first time the presence of an internal spatial variation of the molecular order, namely the presence of a core with axially aligned molecules and a sheath with almost radially oriented molecules. These results allow important and specific fiber properties to be manipulated and tailored, as here demonstrated for the polarization of emitted light.

Fibers are typically formed upon the solidification of a tiny filament drawn from a viscous solution or melt. The formation and thinning of such filament is characterized by a complex dynamics, determined by the different acting forces and by the rheological properties of the fluid.[8-10] Understanding how polymer chains modify their conformation at nanoscale, forming ordered structures under external forces, and to what extent they keep their configuration in solid nanostructures, is fundamental for many applications and for controlling the resulting physical properties of the elongated nanostructures.[11] For example, polymers are typically considered bad thermal conductors, despite the fact that individual polymeric chains can display very high thermal conductivity (about 350 W m^{-1} K^{-1} for polyethylene). Alignment of polymer chains in 1-dimensional (1D) nanostructures provides a way to improve thermal conductivity in an attempt to get values close to the single molecule limit and comparable to those of pure metals.[5] Similarly, charge mobilities (μ) in organic semiconductors thin films are typically low (most often < 10^{-1} V cm^{-2} s^{-1}), although in single π-conjugated polymer chains μ can be of the order of hundreds of V cm^{-2} s^{-1}.[12] In the bulk, mobility is mainly limited by the disordered supramolecular assembly, which limits transistor device performances, whereas 1D nanostructures show an increase of 1 to 3 orders of magnitude of μ,[13,14] mainly due to the enhanced order of polymer chain backbones. The alignment of π-conjugated polymer molecules is also effective to improve the amplification of light by stimulated emission,[15] and ordered conjugated chains show polarization of emitted light, as well as macroscopic quantum spatial coherence of the exciton state up to tens of micrometers.[16] In general, stretching of a semidilute polymer solution by an electrostatic field is very effective to prime the formation of polymer nanofibers, potentially resulting in a structure mostly composed of ordered and aligned polymer chains.[17-19] Little is known however about the nanoscale features induced by the elongational dynamics, and about how these features can be exploited to achieve a mechanistic prediction of the macroscale properties of the solid nanostructures.

In this work, we employ the unique features of scanning near-field optical microscopy (SNOM) to investigate at nanoscale polymer fibers, produced by electrospinning of semidilute solutions. In particular, absorption measurements with nm-spatial resolution and polarization modulation provide insight into the nanoscale variation of the

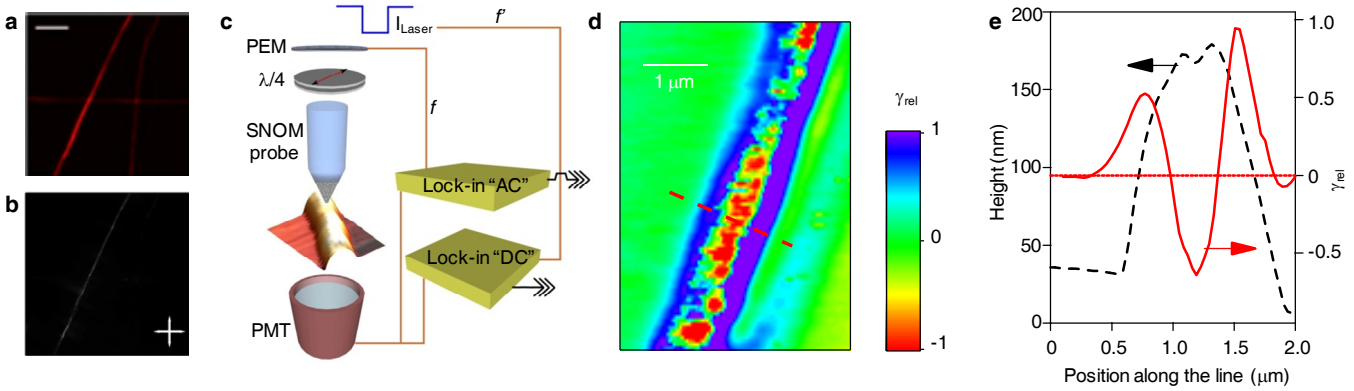

Figure 1. Experimental analysis of nanoscale molecular orientation in active fibers. a, Fluorescence confocal micrograph of conjugated polymer fibers. Scalebar: 10 μm. **b**, Confocal map of the exciting laser intensity transmitted by the fibers, collected simultaneously to the emission map in **a**. The polarization of the excitation laser is aligned parallel to the longitudinal axis of the horizontal fibers, whereas the axis of the analyzer (polarization filter used for the analysis of the polarization of the light transmitted by the nanofiber) is positioned perpendicularly to the incident laser polarization. The horizontal and vertical white arrows indicate the direction of the incident laser polarization and of the analyzer axis, respectively. **c**, Schematics of the polarization-modulation SNOM measurement. Light coupled into the SNOM probe is modulated in intensity (I_{Laser}) and polarization with frequency f' and f , respectively (f/f' >10, see Supplementary Information for details). PEM: photoelastic modulator, PMT: photomultiplier. **d**, Map of the relative dichroic ratio ($\gamma_{rel} = \gamma / \gamma_{max}$) of a single MEH-PPV fiber. The dichroic ratio is zero for non-optically active regions (background contribution subtracted, see Supplementary Information) and gets negative or positive values according to the decreased or increased optical transmission along two mutually orthogonal directions. In the shown map, negative values correspond to preferred optical transmission for incident light polarized approximately along the fiber axis. **e**, Line profile analysis displaying the cross-sections of topography got simultaneously with the optical data (dashed line) and the relative dichroic ratio (continuous line) along the dashed segment in **d**. The change in sign of γ_{rel} when crossing the fiber (dotted horizontal line corresponding to $\gamma_{rel} = 0$) indicates alignment of the polymer along the fiber axis.

molecular alignment, evidencing an unexpected change from axial to radial molecular orientation upon moving from the fiber axis to its surface. The formation of such complex structures occurs close to the polymer jet start, as demonstrated by modeling the evolution of the conformation of the polymer chains network.

The investigated fibers are formed from a π-conjugated polymer, having absorption and emission in the visible range (Fig. S1 in the Supplementary Information), dissolved in a mixture of good and poor solvents (see methods).[20] This allows the chain order to be investigated by optical methods in the bright light-emitting nanofibers (Fig. 1a). In Fig. 1b we show the confocal transmission micrograph of excitation laser light, collected by crossed polarizers (analyzer axis perpendicular to the incident laser polarization), for poly[2-methoxy-5-(2-ethylhexyl-oxy)-1,4-phenylene-vinylene] (MEH-PPV) nanofibers positioned at 0°, 65°and 90° with respect to the incident laser polarization. The fibers aligned along either the direction of the laser polarization or that of the analyzer (0°and 90°, respectively) do not display any transmitted signal, whereas the fiber positioned at 65° displays a significant transmitted signal. This effect, typically observed in anisotropic materials, indicates the optical anisotropy of the fibers and is expectedly the result of a preferential alignment of the conjugated polymer molecules along the fiber length.

To investigate these properties at nanoscale, we use near-field microscopy.[21-23] In particular, polarized near-field absorption microscopy, here applied for the first time to active organic nanofibers, provides a direct measurement of the spatial variation of polymer alignment. This method (Figure 1c) allows us to map the local dichroism, γ, which represents the normalized difference between the transmission of radiation polarized along two mutually orthogonal directions. The map, displayed in Fig. 1d, is determined by the distribution and anisotropy of absorbing chromophores (see Supplementary Information). Here, the most important finding is the spatial variation of the optical dichroism and, consequently, of the molecular alignment as highlighted in Fig. 1e, showing topographical and cross-sectional profiles of the fiber. Unexpectedly, the sign of the relative dichroic ratio, γ_{REL}, is *not constant* throughout the nanofiber, because of regions showing preferential absorption of light polarized along or across the fiber axis (for the scan shown, they correspond to negative or positive γ_{REL}, respectively). These results suggest the presence of a core, with width ~40% of fiber diameter, where chromophore dipoles preferentially align along the fiber length, whereas molecules closer to the fiber surface show a preferential radial orientation.

To learn more about the origin of the found spatial variation of the molecular alignment, we develop a model of the polymer network and simulations of its dynamics.

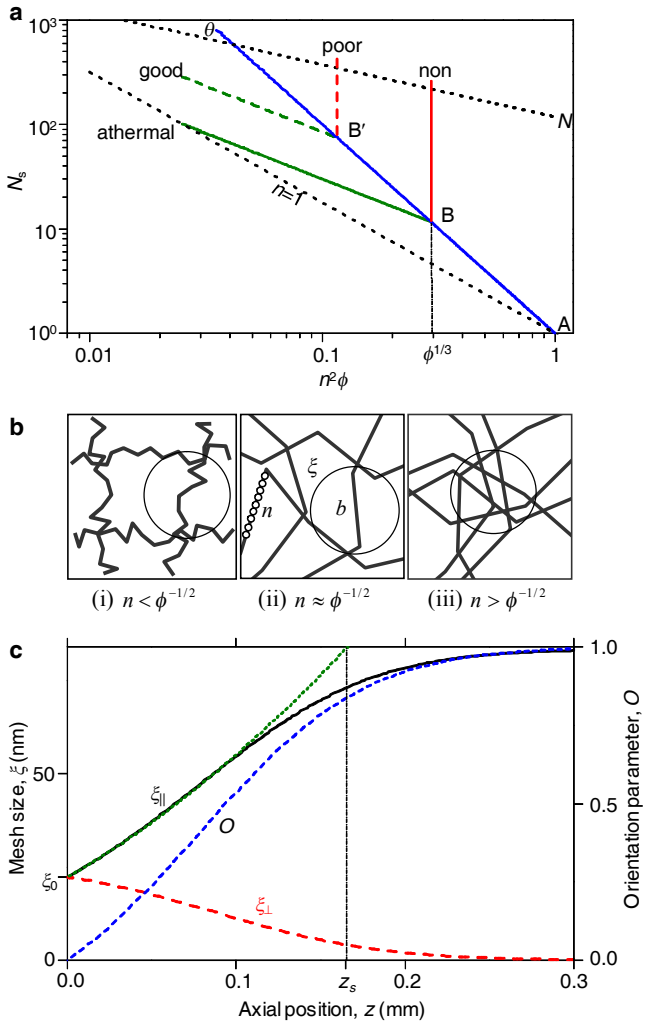

Figure 2. Modeling of polymer chains during elongational flow in nanofabrication. a, The number of rigid segments per subchain (N_s) *vs* $n^2\varphi$ (n the number of beads per segment and ϕ the polymer volume fraction) and solvent quality. The solvent quality grades are designated by θ, good, poor, athermal and non solvent. The θ-solvent curve marks the crossover between good and poor solvents. The dotted lines constitute the upper and lower limits for $\phi = 0.025$. Polymer molecular weight =380,000, equivalent to N_{beads}=730. Points B and B', plotted for $\phi = 0.025$ for Flory's interaction parameter $\chi \cong 0$ and $\chi \cong 0.38$, respectively, mark the transition from ideal subchains (right) to real subchains (left). Prefactors are omitted for sake of simplicity. **b,** Crossover (Point A in **a**) of the polymer network conformation with respect to the scale of the correlation length ξ (circles) and the segment length b: (i) regular semi-dilute, $\xi > b$, (ii) crossover, $\xi \approx b$, and (iii) different chains intermix within a single correlation volume, $\xi \approx b$. **c,** Simulation of subchains during electrospinning. The axial mesh size $\xi_{\parallel}$, radial mesh size $\xi_{\perp}$, and orientation parameter O are plotted *vs* the axial position, z, along the jet. $\xi_{\parallel}$ is compared to the theoretical model (dotted line). The position close to full subchain extension is designated by z_s. Parameters used: ideal chain, $\phi = 0.025$, $n = 5$ beads, $d = 1.2$ nm, $\xi = 20$ nm, $N_s = 14$ segments. Jet dynamics is from Fig. S4 (see Supplementary Information).

A flexible polymer chain is modeled as a series of N rigid segments, each of length $b=nd$ (n spherical beads of diameter d).[24] The segment length b represents the average distance between two neighboring bonding defects along the chain backbone, where a bonding defect introduces local flexibility in the chain.[25] The corresponding defects concentration, using two chemical monomers per bead, is $(2n)^{-1}$ of monomers. In the context of the model, the chain's conformational correlation is lost above the scale of a segment due to the bonding defects, and therefore the rigid segment b is regarded as a Kuhn segment, and a freely jointed chain model is assumed. With such approach, fully flexible polymers are a particular case of the model ($n = 1$),[26] and generality is retained by using the segmental aspect ratio parameter, n, to specify the degree of chain flexibility. Thus, ordering effects described by the model, such as macromolecules alignment and crystallization, are *universal*, even though they are more pronounced in some systems, such as conjugated polymers with semiflexible chains and presence of bonding defects along the chain. In general, the high entanglement of chains creating a connective network determines the viscoelastic property of semidilute solutions. An entanglement can be simply defined as a topological constraint that inhibits intercrossing of two chains. The conformation of the entangled polymer network in the semidilute solution and the interactions relevant to the solvent type are described by scaling laws. When the segmental aspect ratio is high, an entanglement strand (i.e., a chain section between two adjacent entanglements) has the same length scale as the network correlation length (mesh size), ξ, the end-to-end distance of an unperturbed subchain containing N_s rigid segments. Given the aspect ratio n, polymer volume fraction ϕ, and solution properties expressed by Flory's exponent ν and Flory's interaction parameter χ, the number of rigid segments in a subchain for good solvent is (see also the Supplementary Information):

$$N_s \approx \left(\frac{n}{1-2\chi}\right)^{3(2\nu-1)/(3\nu-1)} \left(n^2\phi\right)^{-1/(3\nu-1)}, \qquad (1)$$

and the corresponding correlation length is $\xi \approx b\left[(1-2\chi)/n\right]^{2\nu-1} N_s^{\nu}$.[27] The exponent ν is 0.5 for ideal chains, corresponding to θ-solvents, and ~0.6 for real chains, corresponding to good and athermal solvents.

The mapping of N_s as a function of $n^2\varphi$ for different solvent qualities is depicted in Figure 2a. The effect of various solvents quality is discussed in detail in the Supplementary Information. The θ-solvent curve represents

the borderline between good and poor solvents, where chain conformation is ideal. The good and poor solvent curves represent swollen and shrunk chain conformations, respectively. Point B' marks the position to the right of which the chain conformation is dominated by the thermal energy and is therefore ideal [see Eq. (S7) in the Supporting Information]; its rightmost position is at the athermal limit (point B). Accordingly, points B' and B slide along the θ curve for particular values of φ and χ. When the calculated N_s is above the N limit (upper dotted line, designating the overlap concentration φ^*), the polymer network is not sufficiently entangled for elastic stretching. The limit n=1 (lower dotted line) designates the minimal selectable n value.

For the solvent blend used in our experiments (tetrahydrofuran:dimethyl sulfoxide, THF:DMSO 4:1 wt:wt), the interaction parameter can be estimated as $\chi \cong 0.38$,[28] and for our polymer volume fraction, $\varphi = 0.025$, the transition from ideal to real chain conformation occurs at $n \cong 2.7$ beads (point B' in Fig. 2a). The corresponding defects concentration (19% of monomers) is much higher than typical values (<10%, equivalent to n>5),[25] and therefore the conformation of subchains is close to ideal (θ-solvent line in Fig. 2a, right to point B'). At the high temperature limit (athermal solvent), the transition from ideal to real conformation occurs at $n \cong \phi^{-1/3} \cong 3.4$ beads (point B in Fig. 2a), equivalent to 15% defects. Thus, as a chain is stiffer (higher n) it is more likely to be practically ideal, regardless of the solvent quality, provided that sufficient entanglement exists.

At low concentration, when $n < \phi^{-1/2}$ (left to point A in Fig. 2a), the subchain consists of many segments and does not interact with other chains [Figure 2b(i)]. When $n \approx \phi^{-1/2}$ (point A), the correlation length ξ has the same length scale as the segment length b [Figure 2b(ii)]. However, when chains are not fully flexible, the correlation volume is not completely occupied by a single segment, and further increase of n and/or ϕ is possible. The network then crosses over to a state where different chains intermix within a single correlation volume [Figure 2b(iii)], increasing the probability of interchain overlap. The increased interaction between neighboring rigid segments may lead to nematic ordering and enhanced orientation, according to Onsager theory. For the volume fraction used in the experiment, ϕ=0.025, this crossover occurs at $n \cong 8.6$ beads, corresponding to defects concentration of ~6% of monomers.

On these bases, the evolution of the polymer conformation under dynamic tension can be modeled by a beads-and-spring lattice model and a 3D random walk simulation, previously developed for fully flexible subchains and here generalized to semi-flexible chains.[26] To this aim, the calculated number of segments per subchain, N_s, the initial correlation length, ξ_0, and the pertaining experimental conditions are used as input to the simulations. Specifically, the jet velocity is derived from the measured jet radius a, subjecting each subchain to a hydrodynamic force induced by the solvent, as well as to entropic elastic forces applied by its neighboring subchains.[26] The simulation results are presented in Figure 2c. It is seen that under these conditions the subchains fully extend within less than 1 mm from the jet start (position z_s), while contracting laterally, and their segments become fully oriented along the jet axis. The theoretical expression for the axial stretching (dotted line in Figure 2c), derived for linear elasticity, is given by:[26] $\xi_{II} \approx (v/v_0)\xi_0 = (a_0/a)^2 \xi_0$. Here we also include the dependence of the jet velocity, v, on the jet radius, a, under volume conservation conditions.

An example of the conformational evolution of a single subchain under the same conditions is shown in Fig. 3. The polymer chain is entangled with other chains in the solution (Fig. 3a-b).

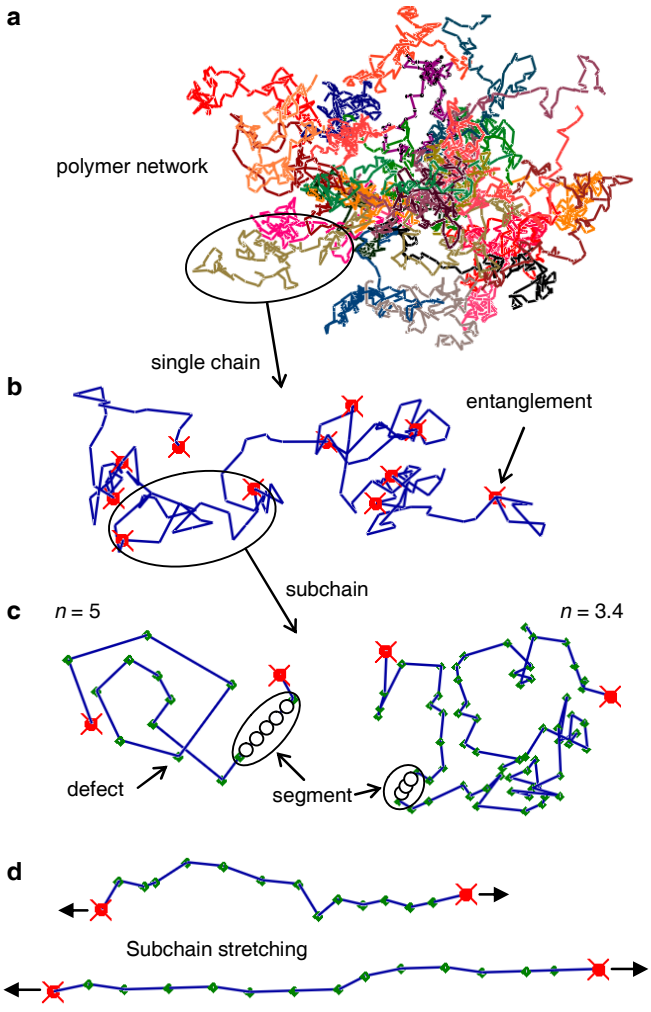

Figure 3, Simulated ideal chain conformations during electrospinning. **a,** Polymer network at rest. **b**, A single chain with N = 146. **c**, Examples of single subchains, left N_s = 14 (n = 5, 10% defects), right N_s = 67 (n = 3.4, 15% defects). **d**, stretched subchains, N_s = 14, z = 0.08 mm and $z = z_s$ = 0.16 mm**.**

Each subchain (an entanglement strand) starts from an equilibrium conformation at the jet start (Fig. 3c), proceeds through intermediate stretching, and approaches full extension and lateral contraction (Fig. 3d). The subchain conformation is sensitive to the average concentration of defects. A change in the defects concentration from 10% of monomers to 15% raises the subchain size from 14 to 67 segments and increases the correlation length. The lateral contraction of individual subchains affects the conformation of the whole polymer network, narrowing its radius a_p faster than the narrowing of the jet radius a. The network radius is approximated by $a_p \approx (\xi_\perp / \xi_0) a$,[26] where $\xi_\perp$ is the radial mesh size depicted in Figure 2c. The dominant effect

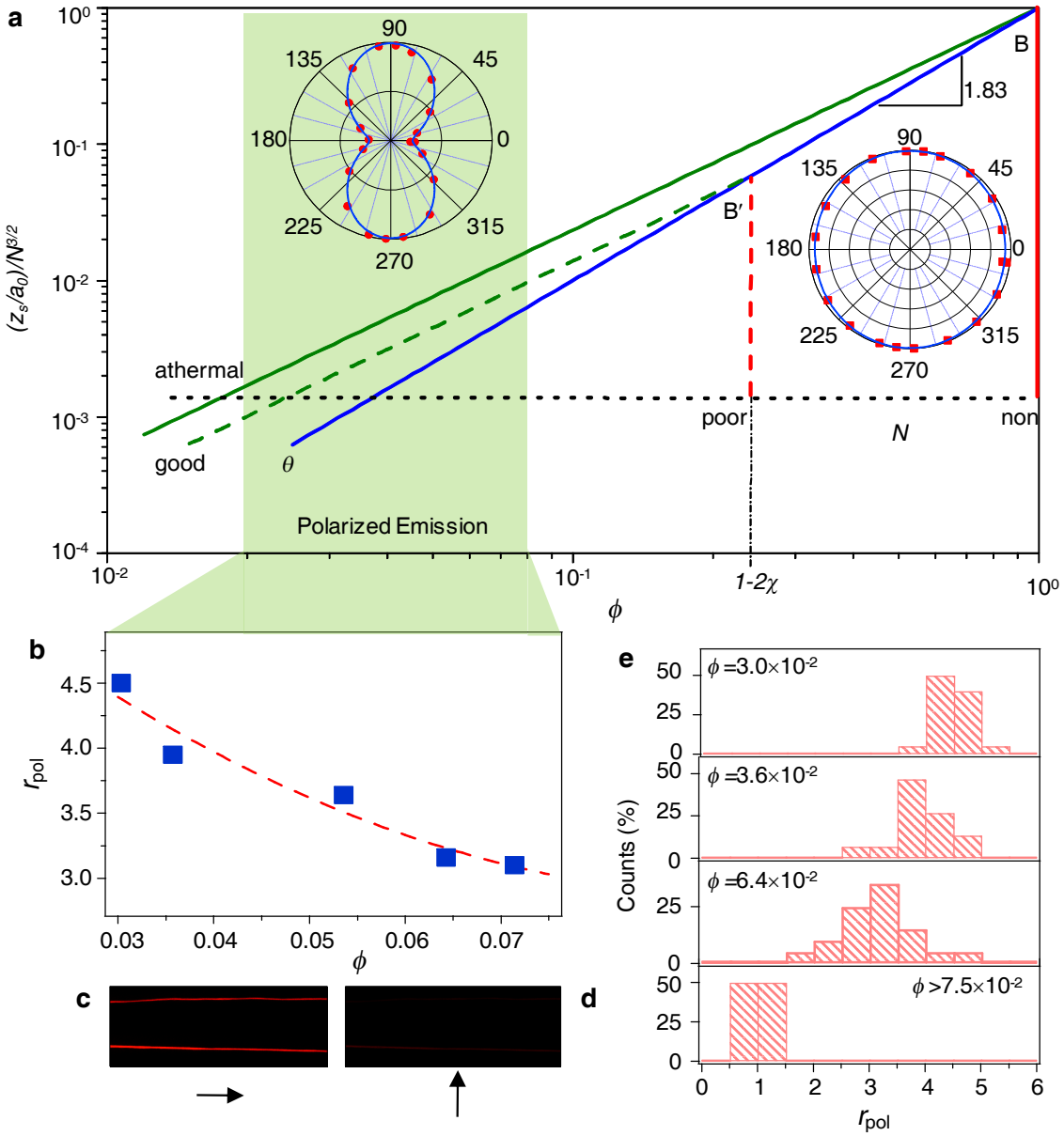

Figure 4. Polymer network during elongational flow and polarization properties. a, Mechanistic prediction plot, showing the axial position where subchains approach full extension, $z_s / a0$, normalized by $N^{3/2}$ (N is the chain's number of segments), versus the polymer volume fraction ϕ and solvent quality. The dotted line constitutes the lower limit imposed by N_s<N. Prefactors are omitted for sake of simplicity. Points B and B' are explained in Figure 2a. Insets: Plot of the normalized nanofiber emission intensity vs. the angle between the nanofiber and analyzer axes, measured on fibers electrospun from a solution with ϕ = 0.03 (left inset) and on a film of sprayed film for comparison (right inset). **b**, Polarization ratio, r_{pol} vs. solution volume fraction, ϕ. The dashed line is a guide for the eyes. An unpolarized sample (sprayed film) has r_{pol} = 1. **c-d,** Confocal images of nanofiber polarized emission. The laser-excited emission is filtered through an analyzer with axis parallel and perpendicular to the fiber axis, respectively. The arrows highlight the direction of the analyzer axis. **e-g**, Experimental distributions of the nanofiber polarization ratio, r_{pol}, at different polymer concentrations.

is of axial stretching and lateral contraction, resulting in compacting of the network toward the jet core. Thus, the model and simulation axial alignment at the jet center, while closer to the jet boundary the stretching effect is not dominant and other mechanisms prevail.

Full extension is approached when $\xi_{||} \approx bN_s$, i.e. at the axial position z_s and a corresponding jet radius a_s. The radius reduction ratio at full stretching is expressed for good solvents by $a_0/a_s \approx [n/(1-2\chi)]^{(2\nu-1)/(3\nu-1)}(n^2\phi)^{-(1-\nu)/[2(3\nu-1)]}$, whereas the axial position of full stretching, omitting the effect of n, scales as (details in the Supplementary Information):

$$\frac{z_s}{a_0} \sim N^{3/2} \begin{cases} \phi^{\frac{\nu+2}{2(3\nu-1)}} & \text{athermal solvent} \\ \phi^{11/6} & \theta\text{-solvent.} \end{cases} \qquad (2)$$

The estimated z_s for various solvent qualities, allowing the axial position of full stretching and consequently the resulting fiber properties for each particular nanofabrication experiment to be predicted, is shown in Fig. 4a. Typically $z_s < 1$ mm and a_0/a_s=2-10, close to the jet start. Considering that the final radius reduction ratios in electrospinning are typically 10^2-10^4, substantial stretching occurs quite early in the process. For given polymer concentration and molecular weight, when n is larger (i.e. longer segments, equivalent to lower defects concentration), full stretching is approached at a higher jet radius and lower z_s; however, at the same time, the number of entanglements per chain N/N_s is higher and therefore solution viscosity will be larger, increasing z_s. In contrast to the radius reduction ratio a_0/a_s, the axial position z_s is strongly affected by the jet rheology, resulting in a concentration dependence with a large positive exponent, as well as added dependence on the molecular weight (Fig. 4a).

In addition to its dependence on the molecular weight and concentration as expressed in Eq. (2), z_s strongly depends on the intensity of the electrostatic field E and the jet initial velocity v_0. It can be shown that this dependence may be approximated by $z_s \sim v_0^{1/2}E^{-1}$, meaning that a high strain rate, caused by high E and low v_0, should result in earlier stretching.

A substantial axial stretching of chains is therefore predicted during the initial stage of the elongational flow, causing lateral contraction of the polymer network toward the center of the jet, as well as orientation of chain segments along the jet axis. Similar results obtained for fully flexible chains (particular case with n=1) have been confirmed by X-ray imaging of high strain rate electrified jets.[26, 29] In electrospinning, the electric field provides the flow of the semi-dilute solution with a characteristic increasing velocity along the jet axis, with a strain rate that continuously increases the elastic stretching of the polymer network and reduces network relaxation. Our model shows that full chain stretching is approached at a higher jet radius as the chain is stiffer, at a region where the mass loss rate due to evaporation is still low. When stretching is less dominant (e.g. at low electric field and high flow rate), the rapid solvent evaporation can adversely affect the polymer matrix, creating a porous nanofiber macrostructure.[26, 29] Also, the high chain stretching forces predicted by the model may accelerate disentanglement and topological reordering of chains, resulting in elongation of subchains and allowing some relaxation and hence reduction in the molecular alignment. Other effects, such as the asymmetric ribbon-shaped collapse of the fibers, may also affect the morphology. These additional processes can influence the network structure and the extent of chains stretching, but are not supposed to change the general conformational trend.

Our polarization modulation measurements (Fig. 1), showing a change in the sign of the dichroic ratio along the fiber radius, indicate a preferred axial alignment of molecules at the fiber core, whereas molecules closer to the fiber boundary possess a preferred radial alignment. Thus, at the jet center axial stretching is dominant, and one can anticipate a propensity for interchain interaction and π-π stacking and consequently high extent of local crystallinity.[30] At the boundary region of the jet, where the polymer concentration is reduced, entanglement is low or nonexistent, allowing partial or full relaxation of chains back to their coil-shaped equilibrium state. We propose that the solidified fiber surface morphology impacts nucleation and crystallization of the conjugated polymer chains trapped in the shell, causing heterogeneous crystallization and crystal growing out-of-plane in a radial inward direction. Nanopores which are typically lying on the fiber surface as a result of phase separation may affect the nucleation kinetics.[31] Alternatively, crystallization can possibly start from the dense core and grow outward, as observed in electrospun low-density polyethylene (LDPE).[32]

Overall, full extension of the network occurs at an earlier stage of the jet (lower z_s), when the solution initial concentration, the polymer molecular weight, and the solvent quality are lower, accounting for lower network entanglement. Under such conditions, the likelihood that the extended conformation, and the associated axial molecular alignment, will partially remain in the polymer structure after solidification is higher. This prediction of the model enables tailoring the physical properties of the fibers. In particular, the far-field, macroscale emission from fibers is expected to be polarized along the longitudinal axis of the nanostructures, with a degree of polarization dependent on process variables. The $z_s(\phi)$ diagram of Fig. 4a clearly relates the chain alignment, and hence the resulting polarization, to the polymer volume fraction (i.e. solution concentration). Indeed, by our approach we obtain a fine tuning of the polarization ratio of the fiber emission ($r_{pol} = I_{||}/I_{\perp}$, given by the ratio between the photoluminescence intensity parallel, $I_{||}$, and perpendicular, $I_{\perp}$, to the fiber axis, respectively), increasing up to about 5 by gradually decreasing the solution concentration down to a volume fraction ϕ=0.03, as shown in Fig. 4b-e, demonstrating the possibility to tailor and manipulate specific fiber properties by the relevant process

parameters. Note that the highlighted solution concentration range in Fig. 4a denotes a semi-dilute entangled solution (above the overlap concentration φ^*), that enables elastic stretching of the polymer network in accordance with the theoretical model. Within that region, a higher solution concentration means higher entanglement density. Finally, we point out that conjugated polymer fibers frequently show red-shifted absorption compared to spincast films (Fig. S1a and Ref. 33), a property consistent with a longer effective conjugation length consequence of the stretched conformation. Indeed, while aggregation is favored in films, the elongational dynamics of semidilute solutions leads to extended structures having interchain alignment. The bonding defects concentration, $(2n)^{-1}$ of monomers, determines chain flexibility and appears as a possible key factor in controlling the desired morphology. The found complex internal structure and assessment of the key influencing process variables open new perspectives for tailoring the molecular morphology and resulting properties of polymer fibers.

Methods

Conjugated polymer nanofibers. Fibers are produced by electrospinning a solution (70-200 μM polymer) of MEH-PPV (molecular weight 380,000 g/mol, American Dye Source Inc). Spray films of micro-beads and micro-fibers are obtained at concentrations > 200 μM. The polymer is dissolved in a 1:4 (weight:weight) mixture of DMSO and THF. The electrospinning system consists of a microprocessor dual drive syringe pump (33 Dual Syringe Pump, Harvard Apparatus Inc.), feeding the polymer solution through the metallic needle at constant rate (10 μL/min). A 11 kV bias is applied between the needle and a metallic collector (needle-collector distance 6 cm), made of two Al stripes positioned at a mutual distance of 2 cm. The MEH-PPV nanofibers are collected on a 1×1 cm^2 quartz substrate for optical investigation. For the emission polarization measurements, arrays of uniaxially aligned nanofibers are produced by using a rotating collector (4000 rpm).

Polarized emission. Optical images of the fibers are obtained by confocal microscopy, using an inverted microscope (Eclipse Ti, Nikon) equipped with a confocal laser scanning head (A1R MP, Nikon). An Ar^+ ion laser (λ_{exc}=488 nm) excites the fibers through an oil immersion objective with numerical aperture, N.A. =1.4. The intensity of the light transmitted through the sample, measured by a photomultiplier, is recorded synchronously to the confocal acquisition of the laser-excited fluorescence. The polarization of the emission of individual nanofibers at different polymer concentrations is characterized by a micro-photoluminescence system, composed by a diode laser excitation source (λ=405 nm) coupled to an inverted microscope (IX71, Olympus). The collimated laser beam is focussed on the sample through a 20× objective (N.A.=0.5, spot size 30 μm). The PL emitted by individual nanofibers is collected by an optical fiber and analyzed by a monochomator (USB 4000, Ocean Optics). The polarization of the emission is analyzed by a polarization filter mounted on a rotating stage and positioned between the emitting MEH-PPV nanofiber and the collecting optics. The system response is precisely analyzed in order to avoid artefacts due to the collection and measurement apparatus.

SNOM. A polarization-modulation near field microscopy system is used to analyze the linear dichroism of the sample. The SNOM system, operating in emission mode, excites samples in the optical near-field of a tapered optical fiber probe (Nanonics), with a nominal aperture of 50 nm, delivering a near-field power up to the tens of nW range (λ=473 nm). The polarization modulation relies on a photoelastic modulator (PEM-100, Hinds Instruments), behaving as a waveplate with periodically modulated retardation. The modulator is followed by a $\lambda/4$ waveplate and the whole system is conceived in order to send into the optical fiber probe radiation linearly polarized along a direction periodically oscillating in the transverse plane (see Figure S3 of the Supplementary Information). The photomultiplier signal is split and sent into two different digital dual lock-in amplifiers (Stanford Research SR830DSP). The first one, referenced to the polarization modulator frequency, f, provides with an output (hereafter called AC) representative of the sample response to polarized radiation, whereas the second lock-in, referenced to a slow modulation frequency, f' (f/f' >10), of the laser amplitude, is used to determine the optical transmission averaged over all polarization states (DC output). The dichroic ratio of sample, $\gamma = (I_{//} - I_{\perp})/(I_{//} + I_{\perp})$, where $I_{//}$ and $I_{\perp}$ are the transmitted intensity for polarization aligned along two mutually orthogonal directions, respectively, is quantitatively evaluated from the ratio AC/DC. This requires to model the behaviour of the whole optical chain and to account for the residual optical activity of its components, including the optical fiber probe (see Supplementary Information).

References

1. Dvir, T., Timko, B. P., Kohane, D. S. & Langer, R. Nanotechnological strategies for engineering complex tissues. *Nat. Nanotech.* **6**, 13-22 (2011).
2. Shannon, M. A. et al. Science and technology for water purification in the coming decades. *Nature* **452**, 301-310 (2008).
3. Lu, W., Zu, M., Byun, J.-H., Kim, B.-S. & Chou, T.-W. State of the art of carbon nanotube fibers: opportunities and challenges. *Adv. Mater.* **24**, 1805-1833 (2012).
4. Veedu, V. P. et al. Multifunctional composites using reinforced laminae with carbon-nanotube forests. *Nat. Mater.* **5**, 457-462 (2006).
5. Shen, S., Henry, A., Tong, J., Zheng, R. & Chen, G. Polyethylene nanofibres with very high thermal conductivities. *Nat. Nanotech.* **5**, 251-255 (2010).
6. Reneker, D. H. & Chun, I. Nanometer diameter fibres of polymer, produced by electrospinning. *Nanotechnology* **7**, 216-223 (1996).

7. Arinstein, A., Burman, M., Gendelman, O. & Zussman, E. Effect of supramolecular structure
on polymer nanofibre elasticity. *Nat. Nanotech.* **2**, 59-62 (2007).
8. Collins, R. T., Jones, J. J., Harris, M. T. & Barasan, O. A. Electrohydrodynamic tip streaming and emission of charged drops from liquid cones. *Nat. Phys.* **4**, 149-154 (2008).
9. Bhat, P. P., Appathurai, S., Harris, M. T., Pasquali, M., McKinley, G. H. & Basaran, O. A. Formation of beads-on-a-string structures during break-up of viscoelastic filaments. *Nat. Phys.* **6**, 625-631 (2010).
10. Yarin, A. L., Koombhongse, S. & Reneker D. H. Taylor cone and jetting from liquid droplets in electrospinning of nanofibers. *J. App. Phys.* **90**, 4836-4846 (2001).
11. Facchetti, A. Organic semiconductors: Made to order. *Nat. Mater.* **12**, 598-600 (2013).
12. Prins, P. et al. High intrachain hole mobility on molecular wires of ladder-type poly(*p*-phenylenes). *Phys. Rev. Lett.* **96**, 146601 (2006).
13. Kim, F. S., Ren, G., Jenekhe, S. A. One-dimensional nanostructures of π-conjugated molecular systems: assembly, properties, and applications from photovoltaics, sensors, and nanophotonics to nanoelectronics. *Chem. Mater.* **23**, 682-732 (2011).
14.Wang, S. et al. Organic field-effect transistors based on highly ordered single polymer fibers. *Adv. Mater.* **24**, 417-420 (2012).
15. Martini, I. B. et al. Controlling optical gain in semiconducting polymers with nanoscale chain positioning and alignment. *Nat. Nanotech.* **2**, 647-652 (2007).
16. Dubin, F. et al. Macroscopic coherence of a single exciton state in an organic quantum wire. *Nat. Phys.* **2**, 32-35 (2006).
17. Dersch, R., Liu, T., Schaper, A. K., Greiner, A. & Wendorff, J. H. Electrospun nanofibers: internal structure and intrinsic orientation. *J. Polym. Sci. Pol. Chem.* **41**, 545-553 (2003).
18. Bellan, L. M. & Craighead, H. G. Molecular orientation in individual electrospun nanofibers measured via polarized Raman spectroscopy. *Polymer* **49**, 3125-3129 (2008).
19. Pagliara, S. et al. Optical anisotropy in single light-emitting polymer nanofibers. *J. Phys. Chem. C* **115**, 20399-20405 (2011).
20. Di Benedetto, F. et al. Patterning of light-emitting conjugated polymer nanofibres. *Nat. Nanotech.* **3**, 614-619 (2008).
21. Eisele, D. M., Knoester, J., Kirstein, S., Rabe, J. P. & Vanden Bout, D. A. Uniform exciton fluorescence from individual molecular nanotubes immobilized on solid substrates. *Nat. Nanotech.* **4**, 658-663 (2009).
22. O'Carrol, D., Iacopino, D. & Redmond G. Luminescent conjugated polymer nanowire Y-junctions with on-branch molecular anisotropy. *Adv. Mater.* **21**, 1160-1165 (2009).
23. Pomraenke, R. et al. Structural phase contrast in polycrystalline organic semiconductor films observed by broadband near-field optical spectroscopy. *Nano Lett.* **7**, 998-1002 (2007).
24. $d \cong 1.2$ nm (each bead consisting of 2 chemical monomers).
25. Hu, D. et al. Collapse of stiff conjugated polymers with chemical defects into ordered, cylindrical conformations. *Nature* **405,** 1030-1033 (2000).
26. Greenfeld, I., Arinstein, A., Fezzaa, K., Rafailovich, M. H. & Zussman, E. Polymer dynamics in semidilute solution during electrospinning: a simple model and experimental observations. *Phys. Rev. E* **84**, 041806 (2011).
27. The pre-factors, of the order of unity, are omitted for clarity.
28. Mark, J. E. *Physical properties of polymers handbook* p. xv (AIP Press: Woodbury, N.Y., 1996). Since THF is a good solvent for MEH-PPV while DMSO is a poor solvent, the interaction parameter may be slightly higher than 0.38.
29. Greenfeld, I., Fezzaa, K., Rafailovich, M. H. & Zussman, E. Fast X-ray phase-contrast imaging of electrospinning polymer jets: measurements of radius, velocity, and concentration. *Macromolecules* **45**, 3616-3626 (2012).
30. Craig, I. M., Tassone, C. J., Tolbert, S. H. & Schwartz, B. J. Second-harmonic generation in conjugated polymer films: A sensitive probe of how bulk polymer crystallinity changes with spin speed. *J. Chem. Phys.* **133**, 044901 (2010).
31. Diao, Y., Harada, T., Myerson, A. S., Hatton, T. A. & Trout, B. L. The role of nanopore shape in surface-induced crystallization. *Nat. Mater.* **10**, 867–871 (2011).
32. Liu, Y., Chen, S., Zussman, E., Korach, C. S., Zhao, W. & Rafailovich M. Diameter-dependent modulus and melting behavior in electrospun semicrystalline polymer fibers. *Macromolecules* **44**, 4439-4444 (2011).
33. Li, D., Babel, A., Jenekhe, S. A. & Xia, Y. Nanofibers of conjugated polymers prepared by electrospinning with a two-capillary spinneret. *Adv. Mater.* **16**, 2062-2066 (2004).

Acknowledgments

We gratefully acknowledge the financial support of the United States-Israel Binational Science Foundation (BSF Grant 2006061), the RBNI–Russell Berrie Nanotechnology Institute, and the Israel Science Foundation (ISF Grant 770/11). The research leading to these results has received funding from the European Research Council under the European Union's Seventh Framework Programme (FP/2007-2013)/ERC Grant Agreement n. 306357 (ERC Starting Grant "NANO-JETS"). The authors also gratefully thank S. Pagliara for preparation of samples for SNOM, E. Caldi for assistance in the SNOM measurements, S. Girardo for imaging of the polymer jet and V. Fasano for confocal images.

Author contributions

A. C., M. A., E. Z. and D. P. conceived and designed the research. I. G. developed the model and performed the simulations. M. M. and A.C. fabricated the samples and performed absorption and polarized emission characterization. F.T., F. F. and M. A. collected and analyzed the SNOM data. A.C., F. F. and I. G. wrote the manuscript. All authors discussed the results and commented on the manuscript.

SUPPLEMENTARY INFORMATION

1. Theoretical modeling rational

The distinctive photophysical properties of conjugated polymers are strongly affected by the structural conformation of the polymer solid matrix,[S1-S5] more specifically by the ordering and orientation of chain sections, typically with a conjugation length of ~10-15 monomers in MEH-PPV.[S1,S6] Individual conjugated polymer chains in a dilute solution can assume various conformations, and hence different optical properties, depending on solvent quality and bonding defects. Theoretically, when defects are not present, the chain is semi-flexible and takes the form of a toroid or rod. However, chemical defects introduced by polymer synthesis and reactivity substitute conjugated links by tetrahedral links along the chain backbone, creating defect coil or cylindrical shapes as a result of the increased flexibility. The defects concentration is in the order of 2.6% to 10% of monomers.[S1,S2,S5] Generally, in good solvents conjugated chains are swollen and polymer-solvent interactions are dominant, whereas in poor solvents polymer-polymer intrachain and interchain interactions are stronger, favoring aggregation and π-π stacking, respectively.[S2-S4]

The processing of thin conjugated polymer films from dilute solutions by spin coating, dip coating and casting has a relatively low impact on chain conformations in view of the weak dynamics. Such conformations, extensively investigated both theoretically and experimentally,[S1-S5] are partly retained after solvent evaporation due to memory effect[S4] but are still close to the chain equilibrium state. By contrast, electrospinning of semidilute solutions of conjugated polymers is characterized by strong stretching generated by the high electrostatic field, resulting in extended chain conformations and longer conjugation lengths, evidenced by red-shifted optical absorption of fibers and smaller phase separation length scale.[S7] It is therefore a specific aim of the present study to provide a modeling approach for the conformational evolution of the conjugated polymer chains during electrospinning, including its dependence on solution properties and jet dynamics. It is further intended to describe the impact of the modeled conformation on the solid nanofiber microstructure and photophysical properties in light of MEH-PPV optical observations.

The model is generalized by tuning the degree of chain flexibility with the segmental aspect ratio parameter, and therefore applies to a wide range of linear flexible polymers, including to conjugated polymers with different levels of defects concentration, as well as to fully flexible polymers which are a particular case of the model.

2. Chain conformation in solution

Considering a polymer chain having N rigid segments, each of length $b = nd$ (n spherical beads of diameter d). In a semi-dilute solution, a chain section (subchain) within a correlation volume is essentially unperturbed by other chains, and therefore its end-to-end distance for good solvent can be expressed by Flory's radius:

$$\xi \approx b\left(\frac{\mathrm{v}}{b^3}\right)^{2\nu-1} N_s^{\nu}. \qquad \text{(S1)}$$

where v is the excluded volume and ν is Flory's exponent. Remembering that a correlation volume encloses a single subchain and that correlation volumes are space filling, the polymer volume fraction in the solution is:

$$\phi \approx \frac{N_s n d^3}{\left(2\xi/\sqrt{6}\right)^3} = \left(\tfrac{3}{2}\right)^{3/2} N_s n^{-2}\left(\frac{b}{\xi}\right)^3. \qquad \text{(S2)}$$

The correlation length is obtained by substituting N_s from Equation (S2) into Equation (S1):

$$\xi \approx b\left(\frac{b^3}{\mathrm{v}}\right)^{(2\nu-1)/(3\nu-1)} \left(n^2\phi\right)^{-\nu/(3\nu-1)}, \qquad \text{(S3)}$$

with a pre-factor of order unity, $\left(\tfrac{3}{2}\right)^{3\nu/(6\nu-2)}$. This relation can be obtained also by de Gennes scaling approach. The corresponding number of segments is:

$$N_s \approx \left(\frac{b^3}{\mathrm{v}}\right)^{3(2\nu-1)/(3\nu-1)} \left(n^2\phi\right)^{-1/(3\nu-1)}. \qquad \text{(S4)}$$

with a pre-factor of order unity, $\left(\tfrac{3}{2}\right)^{3/(6\nu-2)}$. The excluded volume of a non-spherical segment can be expressed by $\mathrm{v} \approx b^2 d\left(1-2\chi\right)$, where χ is Flory's interaction parameter, and therefore:

$$\frac{b^3}{\mathrm{v}} \approx \frac{b^3}{b^2 d\left(1-2\chi\right)} \approx \frac{n}{\left(1-2\chi\right)}. \qquad \text{(S5)}$$

The final expression for the number of segments for good solvent is:

$$N_s \approx \left(\tfrac{3}{2}\right)^{3/(6\nu-2)}\left(\frac{n}{1-2\chi}\right)^{3(2\nu-1)/(3\nu-1)} \left(n^2\phi\right)^{-1/(3\nu-1)}, \qquad \text{(S6)}$$

which reduces to $N_s \approx \left(\tfrac{3}{2}\right)^3\left(n^2\phi\right)^{-2}$ segments for an ideal chain ($\nu = 1/2$).

Figure 2a displays the dependence of N_s on $n^2\phi$, for different solvent types. The θ-solvent curve ($\nu = 1/2$, $\chi = 1/2$) marks the crossover between good and poor solvents, for which the subchain is a random walk of segments (ideal chain conformation). In good solvents ($\nu = 3/5$, $\chi < 1/2$), the subchain is swollen (real chain conformation)

and therefore the values of N_s and ξ are lower. The corresponding curve starts at point B', and the athermal limit curve ($\chi = 0$) starts at point B. In poor solvents ($\nu = 1/3$, $\chi > 1/2$), the subchain is shrunk and therefore N_s and ξ are higher, up to the non-solvent limit ($\chi = 1$) where subchains are fully collapsed and phase-separated from the solvent. The corresponding curves start at point B' and B, respectively. N_s is smaller at high aspect ratio (low defects concentration) and is proportional to $n^{-(5-6\nu)/(3\nu-1)}$, i.e. n^{-4} for a θ-solvent and $n^{-1.75}$ for good and athermal solvents.

For chain sections where the excluded volume interaction energy is weak, the conformation is dominated by the thermal energy and is therefore diffusive and ideal. The transition from real to ideal conformation occurs at the length scale of a thermal blob possessing b^6/v^2 segments. Thus, the number of segments in a thermal blob is:

$$N_{sT} \approx \frac{b^6}{\mathrm{v}^2} \approx \left[\frac{n}{1-2\chi}\right]^2, \tag{S7}$$

which reduces to $N_{sT} \approx n^2 \approx \phi^{-2/3}$ for athermal solvents ($\chi = 0$). For solvents other than a θ-solvent, point B' in Figure 2a marks the position where the subchain is of the same length scale as the thermal blob. For larger n (smaller N_s), excluded volume interactions are weak and the thermal energy is dominant; the θ-solvent curve applies and subchains have an ideal conformation. For smaller n (larger N_s), excluded volume interactions are dominant outside the thermal blob; the good solvent or poor solvent curves apply and subchains have an intermediate swollen or collapsed conformation, respectively. The minimal thermal blob size is at the athermal limit (point B), where the athermal solvent or non-solvent curves apply and subchains have a fully swollen or collapsed conformation, respectively. Note that point B slides to the right as the volume fraction increases.

Given the molecular weight or the number of beads in the complete chain, N_{beads}, the chain's number of segments is $N = N_{beads}/n$. The average number of entanglements per chain, $N/N_s \sim n^{3(2-3\nu)/(3\nu-1)}$, decreases for smaller n (i.e. higher defects concentration and chain flexibility) and the solution may turn dilute. Thus, stiffer chains can establish a level of entanglement sufficient for electrospinning at lower concentration and molecular weight. For poor solvents, N_s is close to N, not assuring sufficient entanglements for electrospinning.

The model uses the correlation length as representative for the entanglement length, a chain section between two consecutive entanglements along the chain. In a semi-dilute solution, the elastic modulus of the polymer network is proportional to the number density of entanglement strands. In an athermal solvent, an entanglement strand containing N_e segments is related to the correlation length by $N_e \approx N_e(1)N_s$, where $N_e(1)$ is the number of segments in an entanglement strand in a melt. Although the entanglement strand length is always longer than the correlation length, in conjugated polymers they are of similar length scale because of the high segmental aspect ratio. Using the known expression for the number of chains within the confinement volume of a single strand in a melt, $P_e \approx \left(b^3/\mathrm{v}_0\right)\sqrt{N_e(1)}$, where $\mathrm{v}_0 \approx d^2 b$ is the segment volume, the number of strands in a conjugated polymer strand in a melt is:

$$N_e(1) \approx \left(\frac{P_e \mathrm{v}_0}{b^3}\right)^2 \approx \left(\frac{P_e}{n^2}\right)^2. \tag{S8}$$

Since $P_e \cong 20$ for all flexible polymers regardless of their segmental aspect ratio, $N_e(1) \approx 1$ when $n \geq \sqrt{P_e} \cong 5$, and therefore practically, for typical defects concentration, $N_e \approx N_s$ as used in the modeling.

3. Network stretching during electrospinning

Using Eq. (1) the expression for chain extension, $\xi_{\mathrm{II}} \approx (v/v_0)\xi_0 = (a_0/a)^2 \xi_0$,[S8] the jet radius reduction ratio at full stretching is expressed for good solvents by:

$$\begin{aligned} \frac{a_0}{a_s} &\approx \left(\frac{bN_s}{\xi_0}\right)^{1/2} \approx \left(\frac{n}{1-2\chi}\right)^{(1-2\nu)/2} N_s^{(1-\nu)/2} \\ &\approx \left(\frac{n}{1-2\chi}\right)^{(2\nu-1)/(3\nu-1)} \left(n^2\phi\right)^{-(1-\nu)/[2(3\nu-1)]}. \end{aligned} \tag{S9}$$

Thus, a_0/a_s is reduced as the chain is stiffer, by a factor of $n^{(2-3\nu)/(3\nu-1)}$, i.e. n^{-1} for a θ-solvent (for which ν=1/2) and $n^{-0.25}$ for good and athermal solvents (ν=3/5).

Finally, in order to find the axial position z_s where subchains approach full extension, it is necessary to estimate the dependence of the velocity parameter z_0 in Eq. (S20) on the parameters that determine the jet rheology, predominantly the solution viscosity η. Additional influencing parameters, such as the electric field and conductivity, flow rate, and needle diameter, are assumed constant in the current analysis. Sufficiently far from the orifice ($z/z_0 >> 1$), the jet velocity gradient is proportional to z_0^{-2} (using the exponent β=1 in Eq. S20). Since, for a given tensile stress (e.g. due to electric field), the gradient is approximately proportional to η^{-1}, the velocity parameter scales as $z_0 \sim \eta^{1/2}$. Written in dimensionless parameters, $z_0/a_0 \sim \eta_{sp}^{1/2}$, where $\eta_{sp} \cong \eta/\eta_s$ is the specific viscosity (η_s is the solvent viscosity, $<<\eta$). Hence, The dependence of the axial position on the jet radius

(see Eq. S20 in the following Sec. 6) can be approximated by:

$$\frac{z}{a_0} \cong \frac{z_0}{a_0}\left(\frac{a}{a_0}\right)^{-1} \sim \eta_{sp}^{1/2}\frac{a_0}{a}, \qquad \text{(S10)}$$

where the specific viscosity can be obtained from the known expressions for semi-dilute solutions,[S9] $\eta_{sp} \approx N^3\phi^{3/(3\nu-1)}$ for an athermal solvent and $\eta_{sp} \approx N^3\phi^{14/3}$ for a θ-solvent (prefactors are omitted).

Using the radius reduction ratio from Equation (S9) and the viscosity expressions, z_s scales as:

$$\frac{z_s}{a_0} \sim N^{3/2}\begin{cases}\phi^{\frac{\nu+2}{2(3\nu-1)}} & \text{athermal solvent}\\ \phi^{11/6} & \theta \text{ solvent,}\end{cases} \qquad \text{(S11)}$$

depicted in Figure 4a. The concentration dependence of z_s is $\phi^{1.63}$ for an athermal solvent and $\phi^{1.83}$ for a θ-solvent. Note that this expression is written for fully flexible chains ($n=1$), with the intention to demonstrate the trends of the dependence on the concentration, solvent quality, and molecular weight.

4. Nanofiber optical properties

The absorption spectra are measured by using a UV/visible spectrophotometer (Lambda950, PerkinElmer) and an integrating sphere (Labsphere). PL spectra are acquired by exciting the nanofibers with a diode laser (λ=405 nm, polarization parallel to the fiber axis) and collecting the emission through a fiber-coupled monocromator (iHR320, Jobin Yvon) equipped with a charged coupled device (Jobin Yvon). In Figure S1a we compare the absorption spectrum of a mat of MEH-PPV nanofibers with a reference spincast film. The films display a maximum absorption at about 510 nm, whereas a peak red shift of about 5 nm is measured for fibers, which indicates a slight increase of the effective conjugation length attributable to a more ordered molecular packing.[S7]

The absorption linear dichroism (LD) spectrum is shown in Figure S1b. The plot, obtained from polarized absorption measurements performed on uniaxially aligned MEH-PPV nanofibers, evidences a predominant absorption for light polarized along the fiber longitudinal axis, a fingerprint of a preferential alignment of the polymer backbones along the fiber length. The LD values are positive on average, with a peak at about 575 nm, corresponding to the (0-0) vibronic replica of the π-π* electronic transition. Figure S1c displays the photoluminescence (PL) linear dichroism defined as the difference between the intensity of the light emitted by fibers with polarization parallel or perpendicular to the fiber axis (LD_{PL}= $I_{PL//}$ - $I_{PL\perp}$). The measured polarization anisotropy of the emission further supports the anisotropic packing of MEH-PPV molecules in the electrospun fibers.

5. Near-field Optical Microscopy set-up

The analysis of the optical activity at the local scale is performed by using a polarization-modulated scanning near-field optical microscope (SNOM) developed on the basis of a multi-purpose head.[S10] The instrument operates in the emission-mode: the sample interacts with the near-field produced by a tapered optical fiber probe (50 nm nominal diameter apical aperture). Radiation is collected below the sample by

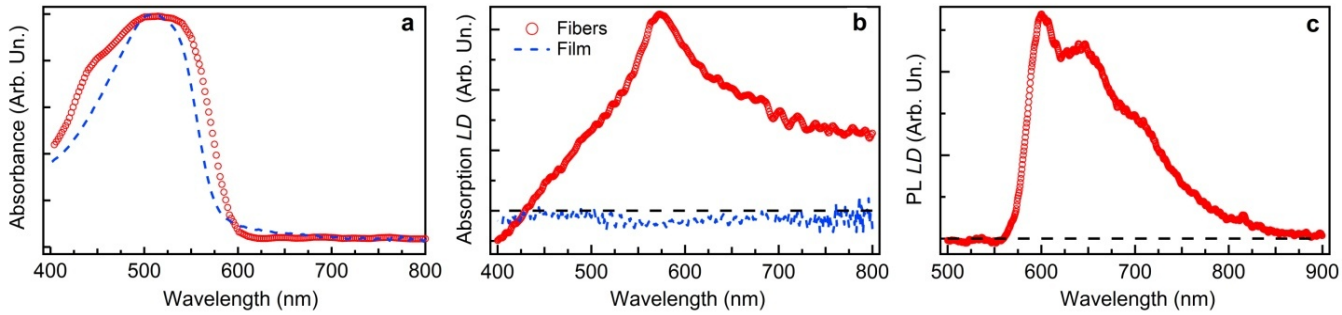

Figure S1. **a**, Absorption spectra of a reference MEH-PPV film (dashed line) and of the nanofibers (circles). **b**, LD spectra. The LD spectra (empty circles) are obtained by measuring the polarized absorption spectra, with incident light polarization aligned parallel ($A_{\parallel}$) and perpendicular ($A_{\perp}$) to the fiber alignment axis, respectively. The LD spectra are then calculated by LD= $A_{\parallel}$ - $A_{\perp}$. The signal at λ>600 nm is due to scattering from the nanofibers. The LD spectrum of a reference spincast film is also shown (dashed line), displaying average null LD values. **c**, PL linear dichroism spectrum (LD_{PL}), calculated by PL spectra exciting the fibers with the laser polarized along the fiber axis and collecting the PL through a polarization filter with axis parallel ($I_{PL//}$) and perpendicular ($I_{PL\perp}$) to the fiber axis, respectively (i.e., LD_{PL}= $I_{PL//}$ - $I_{PL\perp}$). The horizontal black dashed lines mark null values.

an aspheric lens and directed onto a miniaturized photomultiplier. The configuration is hence similar to that of conventional optical transmission measurements, but for the use of the near-field, the key component enabling spatial resolution below the diffraction limit.

Producing maps of the linear dichroism requires the ability to measure the response of the sample upon excitation with controlled polarization states. To this aim, polarization modulation (PM) methods are typically employed.[S11] The main motivation is the long duration of SNOM scans, that makes mechanical drifts likely to occur. As a consequence, subsequent scans of the same region recorded with rotated polarizations can be hardly carried out. PM circumvents the problem by continuously manipulating the polarization state at every point of a single scan. In addition, signal-to-noise ratio is improved thanks to demodulation through lock-in amplifiers, that makes the measurement of small dichroism variations feasible.[S12]

Core of the polarization modulation system is a photoelastic modulator (PEM, Hinds Instruments PEM-100) which acts as a waveplate whose retardation is periodically modulated at f = 50 kHz.[S13] As shown in Fig. S2, the modulator is followed by a $\lambda/4$ waveplate. Being the linear polarization of the excitation laser directed at 45° with respect to the PEM optical axes, the polarization entering the $\lambda/4$ waveplate is periodically modified through linear to elliptical and circular states. After passage through the waveplate, oriented at -45^0 with respect to the PEM axes, the polarization is converted back to linear, but its in-plane direction gets now periodically modulated. In typical operating conditions, the freely adjustable, maximum retardation produced by the PEM is set to $A = \pi$. Consequently, the whole range of directions (0-360°) is spanned two times in a single modulation period $T = 1/f$. Lock-in demodulation at twice the frequency f brings information (hereafter called AC signal) on the response of the sample to polarized radiation. Since the intensity of the signal collected by the photodetector can be affected by a number of effects, including instrumental drifts, variations in the coupling efficiency with the near-field, as well as polarization-independent absorption, the AC signal must be normalized. A reference can be easily obtained by averaging the photodetector output over all polarization states. In our setup this is achieved by using an independent lock-in amplifier connected at the photo-detector output and referenced to a slow ($f' < f/10$) amplitude modulation of the excitation laser, that produces a signal (hereafter called DC) time-averaged over all polarization states. The normalized AC/DC signal contains information on the linear dichroism of the sample.

Measurements at the local scale involve the use of near-field radiation. Different previous reports have demonstrated the ability of polarization modulated SNOM in achieving a polarization-related contrast mechanism and in determining the optical activity of a variety of samples.[S14-S21] However, especially when near-field probes based on tapered optical fibers are used, as in our case, special care must be devoted to account for the residual optical activity. In fact, birefringence of the fiber, as well as any other spurious effect stemming from the optical bench components (mirrors, beam splitters), can heavily affect the results, in particular their quantitative evaluation. In order to remove those unwanted

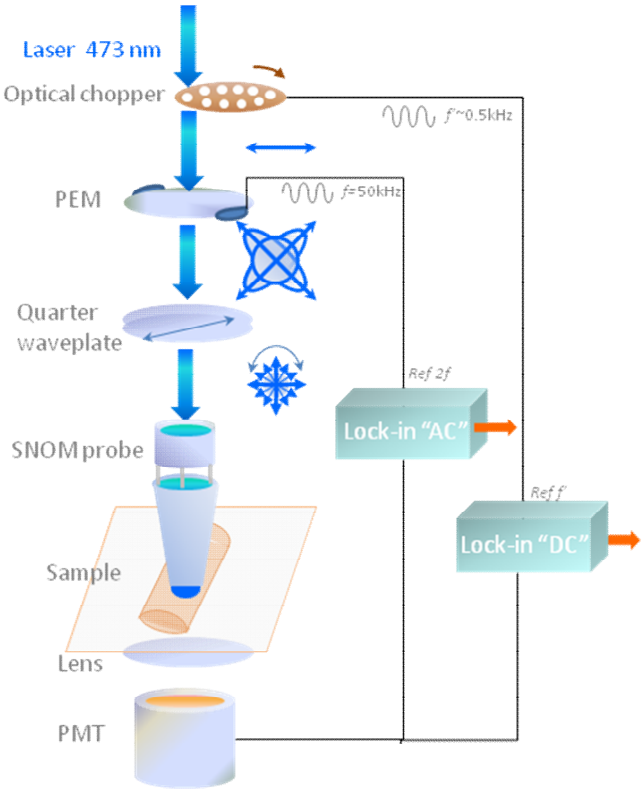

Figure S2. Representation of polarization modulated SNOM. Close to some of the optical components, the polarization of the excitation radiation is schematically shown. Note that, in the actual setup the optical chopper, depicted as a rotary wheel, is replaced by an acousto-optic shutter in order to prevent mechanical noise on the microscope table.

contributions, prior to the measurements we analyze bare substrates, expected to show negligible optical activity. Both demodulated signals (lock-in outputs) and time-resolved data are compared to results obtained through calculations aimed at simulating the polarization-dependent behavior of the optical components in the experimental chain. Such calculations have been based on the Jones matrix formalism (more complicated methods, such as those based on the Mueller formalism, did not lead to significant advantages).

Within this frame, the time-dependent polarization of the light at the PEM output can be represented by the following vector, whose components are the electric field amplitude along two mutually orthogonal in-plane directions (x and y) in the reference frame of the optical bench:

$$V = \frac{1}{\sqrt{2}}\begin{pmatrix} e^{i\Delta(t)} \\ 1 \end{pmatrix}, \qquad \text{(S12)}$$

with $\Delta(t) = A\sin(2\pi ft+\delta)$, where δ represents a constant phase factor accounting for instrumental delays. The modifications to the polarization produced by each component are described by 2x2 matrices. The whole system behavior is then given by the product of all considered matrices. For instance, the $\lambda/4$ waveplate, aligned as in our setup, can be described by the following matrix:

$$W = \frac{1}{\sqrt{2}}\begin{pmatrix} \cos\theta & -\sin\theta \\ \sin\theta & \cos\theta \end{pmatrix}\begin{pmatrix} 1 & 0 \\ 0 & i \end{pmatrix}\begin{pmatrix} \cos\theta & \sin\theta \\ -\sin\theta & \cos\theta \end{pmatrix}, \qquad \text{(S13)}$$

with $\theta = -\pi/4$. A generic birefringent component, with its optical axes rotated by a generic angle β with respect to the reference system, can be represented by the matrix M:

$$M = \frac{1}{\sqrt{2}}\begin{pmatrix} \cos\beta & -\sin\beta \\ \sin\beta & \cos\beta \end{pmatrix}\begin{pmatrix} e^{-i\Delta\phi} & 0 \\ 0 & 1 \end{pmatrix}\begin{pmatrix} \cos\beta & \sin\beta \\ -\sin\beta & \cos\beta \end{pmatrix}, \qquad \text{(S14)}$$

where $\Delta\phi$ is the optical retardation produced by the birefringent component. The matrix M can conveniently describe the spurious birefringence induced by the probe.

The components of the electric field, D , collected by the photodetector (in the absence of any optically active sample) are given by the product:

$$D = MWV, \qquad \text{(S15)}$$

which is time-dependent due to the explicit dependence of V on t. Assuming photodetector response independent of polarization, as confirmed by specific calibration measurements showing negligible variations of the output signal for radiation polarized along two mutually orthogonal directions, the intensity $I(t) = |D(t)|^2$ can then be simulated and compared to the signal measured by the photodetector in the experiment, duly amplified and acquired by a fast digital oscilloscope averaging over many modulation cycles in order to enhance the signal-to-noise ratio. By adjusting the calculation parameters to achieve the best agreement between the simulated and the observed temporal shape of the signal, the retardation $\Delta\phi$ can be estimated.

In our experiments we select probes showing a residual birefringence, $\Delta\phi < 0.1$ rad. Moreover, since the birefringence can be altered by naturally occurring mechanical stresses of the fiber, particular care is taken to keep stable the eventual mechanical stress and to minimize long term drifts, as experimentally confirmed by measuring the AC signal fluctuations in scans of bare substrates (measured well below 10% on the duration of a whole scan, typically lasting for several tens of minutes). Once the spurious birefringence has been characterized, the dichroism of the sample can be determined by using a matrix S describing a generic linearly dichroic material with its axes rotated at a generic angle α:

$$S = \begin{pmatrix} \cos\alpha & -\sin\alpha \\ \sin\alpha & \cos\alpha \end{pmatrix}\begin{pmatrix} e^{-k_1 z} & 0 \\ 0 & e^{-k_2 z} \end{pmatrix}\begin{pmatrix} \cos\alpha & \sin\alpha \\ -\sin\alpha & \cos\alpha \end{pmatrix}, \qquad \text{(S16)}$$

where k_1 and k_2 are the absorption coefficients for radiation polarized along two mutually orthogonal directions representing the optical axes of the sample, and z is the thickness of the absorbing material, that can be experimentally inferred by the topography maps. The response of the whole system produces the time-dependent electromagnetic field D_S:

$$D_S = SMWV. \qquad \text{(S17)}$$

In order to compare with experimental data (at a fixed point of the scan, to remove the dependence on z), lock-in demodulation at frequency $2f$ (or f) of the intensity $I_S(t) = |D_S(t)|^2$ measured by photodetector can be easily simulated, corresponding in practice to the measured AC/DC ratio. Thanks to the use in the experiment of dual lock-in amplifiers, any possible dephasing between the reference and the signal modulation, for instance caused by the parameter δ (see Eq. S12), can be neglected.

The absorption coefficients can in turn be linked to the dichroic ratio of the material:

$$\gamma = (I_{//} - I_{\perp})/(I_{//} + I_{\perp}) \qquad \text{(S18)}$$

where

$$I_{\parallel} = I_0(1 - e^{-k_1 z}) \text{ and } I_{\perp} = I_0(1 - e^{-k_2 z}) \qquad \text{(S19)}$$

We note that the above defined dichroic ratio can get either positive or negative values, depending on whether $k_1 < k_2$, or vice versa. The ability to retrieve the sign of γ is indeed very useful when the spatial distribution of the dichroic behavior in isolated systems has to be investigated, as in our case. In fact, this allows to identify regions with radically different polarization-dependent absorption, as due, for instance, to peculiar alignment of molecules.

The procedure leads to a calibration curve where the simulated AC/DC ratio is plotted as a function of γ that can be used to put a scale bar into the experimentally produced maps. Figure S3 shows an example of the resulting curve. We estimate the uncertainty of our procedure, accounting for all the error sources in our simple calculation model, of the order of ±10%.

As shown in Fig. S3, non-zero AC/DC is expected at $\gamma = 0$. The occurrence of such a background pedestal, which is an obvious consequence of the spurious optical activity of the optical bench, is well confirmed in the experimental maps, where the bare substrate actually displays non-zero AC/DC. Thanks to the calibration curve, the effect disappears in the maps calibrated in units of γ, or γ_{rel}, as shown

in Fig. 1d. We note also that the angle α entering Eq. S17 is measured in the in-plane directions (x', y') of the sample reference frame, different from the reference frame (x, y) used to determine all the other angular quantities appearing in Eqs. S12-16. The rotation of the reference axes can be experimentally estimated by selecting a constant linear

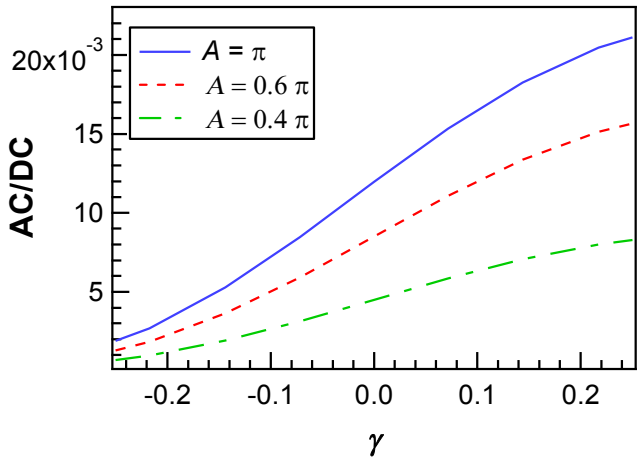

Figure S3. Example of a calibration curve, as defined in the text, relating the simulated AC/DC ratio with the dichroic ratio of the material. In this example, which fits experimental data, the residual birefringence of the probe is computed as $\Delta\phi$ = 0.06 rad and the angle α appearing in Eq. S16 is $\alpha \sim \pi/2$. Different curves are calculated assuming different values of the maximum PEM retardation A, as specified in the legend.

polarization at the entrance of the fiber probe with a known direction, by placing a rotatable linear polarizer in front of the photodetector and by looking at the maximum (or minimum) signal. Being the photodetector mounted in the SNOM microscope, the direction of the reference axes in the SNOM frame can be deduced.

However, such a technique can be rather cumbersome from the experimental point of view, in particular because it requires removal and replacement of the sample. An *in-situ* procedure can be carried out instead, based on the circumstance that the calibration curves depend on the maximum retardation A set for the PEM. This is shown, for instance, in Figure S3, where calibration curves for three different choices of A are plotted. Hence, by repeating the same SNOM scan with different A-values and comparing the so-obtained AC/DC maps, it is possible to infer on the value of α entering Eq. S17. For the measurements shown in the paper, α is slightly larger than $\pi/2$. Being the nanofiber axis roughly aligned along the vertical direction of the scan, measurements are referenced to polarization directions aligned roughly along and across the nanofiber, that is, k_1 and k_2 roughly corresponds to absorption along the longitudinal and radial directions of the fiber, respectively. As a consequence, negative and positive dichroic ratios correspond to prevalent absorption of radiation polarized along or across the fiber, respectively.

6. Imaging of the electrospinning jet profile

For imaging the polymer jet profile a high speed camera (Photron, FASTCAM APX RS, 1024 pixel ×1024 pixel, 10000 frame s^{-1}) coupled to a stereomicroscope (Leica MZ 12.5) is used. A typical image of the measured jet shape is shown in Figure S4. The dependence of the jet radius, a, on the axial coordinate, z, is modelled by the following relation: [S8,S22]

$$\left(\frac{a_0}{a}\right) \cong \left(1+\frac{z}{z_0}\right)^{\beta}, \qquad \text{(S20)}$$

Fitting the jet profile to Equation (S20) provides values of $z_0 = 22$ μm, and $\beta = 0.94$, using the initial radius $a_0 = 96$ μm.

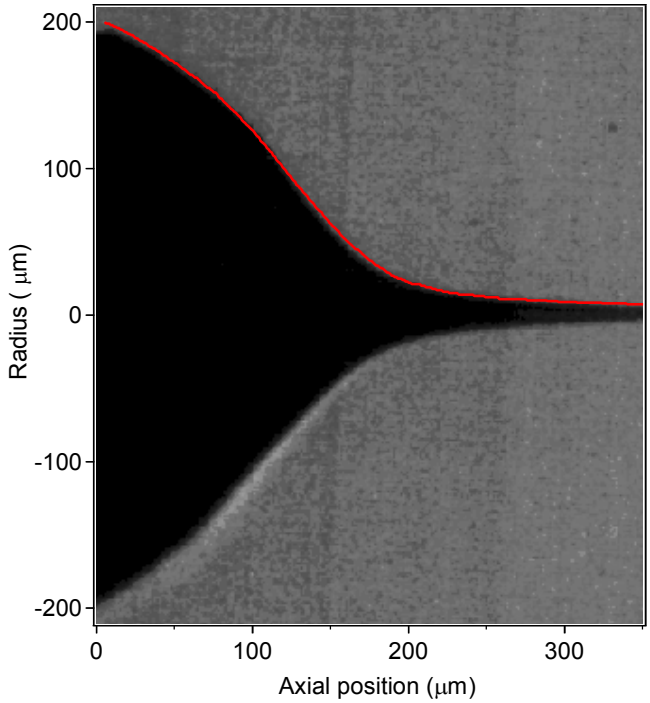

Figure S4. Image of the jet profile. The continuous red line is the measured profile, used for fitting by Eq. S20.

References

S1. Hu, D. H. et al. Collapse of stiff conjugated polymers with chemical defects into ordered, cylindrical conformations. *Nature* **405**, 1030-1033 (2000).
S2. Ebihara, Y. & Vacha, M. Relating conformation and photophysics in single MEH-PPV chains. *J. Phys. Chem. B* **112**, 12575-12578 (2008).

S3. Nguyen, T. Q., Doan, V. & Schwartz, B. J. Conjugated polymer aggregates in solution: Control of interchain interactions. *J. Chem. Phys*. **110**, 4068-4078 (1999).
S4. Cossiello, R. F., Susman, M. D., Aramendia, P. F. & Atvars, T. D. Z. Study of solvent-conjugated polymer interactions by polarized spectroscopy: MEH-PPV and Poly(9,9 '-dioctylfluorene-2,7-diyl). *J. Lumin.* **130**, 415-423 (2010).
S5. Shie, S. C., Lee, C. K., Hua, C. C. & Chen, S. A. A predictive coarse-grained model for semiflexible polymers in specific solvents. *Macromolecular Theory and Simulations* **19**, 179-189 (2010).
S6. Hu, D. H., Yu, J. & Barbara, P. F. Single-molecule spectroscopy of the conjugated polymer MEH-PPV. *J. Am. Chem. Soc.* **121**, 6936-6937 (1999).
S7. Li, D., Babel, A., Jenekhe, S. A. & Xia, Y. Nanofibers of conjugated polymers prepared by electrospinning with a two-capillary spinneret. *Adv. Mater.* **16**, 2062-2066 (2004).
S8. Greenfeld, I., Arinstein, A., Fezzaa, K. Rafailovich M. H. & Zussman, E. *Phys. Rev. E* **84**, 041806 (2011).
S9. Rubinstein, M. & Colby, R. H. Polymer physics. Oxford University Press: Oxford; New York, 2003; p. xi, 440 p.
S10. Gucciardi, P., Labardi, M., Gennai, S., Lazzeri, F. & Allegrini, M. Versatile scanning near-field optical microscope for material science applications. *Rev. Sci. Instrum.* **68**, 3088 (1997).
S11. Gucciardi, P., Micheletto, R., Kawakami, Y. K., & Allegrini, M. in "Near-field optical microscopy for imaging of polarization anisotropy in photonic nanostructures", edited by B. Bhushan and H. Fuchs (Springer, Berlin Heidelberg New York, 2006) Chap. 10, pp. 321–360.
S12. Drake, A. F. Polarization modulation – the measurement of linear and circular dichroism. *J. Phys. E: Sci. Instrum.* **19**, 170 (1986).
S13. Wang, B. Measurement of Circular and Linear Birefringence in Chiral Media and Optical Materials Using the Photoelastic Modulator. *SPIE Proceedings* **3424**, 120 (1998).
S14.Vaez-Iravani, M. & Toledo Crow, R. Pure linear polarization imaging in near field scanning optical microscopy. *Appl. Phys. Lett.* **63**, 138 (1993).
S15. Lacoste, T., Huser, T., Prioli, R. & Heinzelmann, H. Contrast enhancement using polarization-modulation scanning near-field optical microscopy (PM-SNOM). *Ultramicroscopy* **71**, 333 (1998).
S16. Ramoino, L. et al. Polarization-modulation near-field optical microscope for quantitative local dichroism mapping. *Rev. Sci. Instrum.* **73**, 2051 (2002).
S17. Ambrosio, A. et al. Near-field optical microscopy of polymer-based films with dispersed terthiophene chromophores for polarizer applications. *Nanotechnology* **15**, 5270 (2004).
S18. Micheletto, R., Kawakami, Y., Manfredotti, C., Garino, Y. & Allegrini, M. Dichroism of diamond grains by a polarization modulated near field optical setup. *Appl. Phys. Lett.* **89**, 121125 (2006).
S19. Micheletto, R., Allegrini, M. & Kawakami, Y. Artefacts in polarization modulation scanning near-field optical microscopes. *J. Opt. A: Pure Appl. Opt.* **9**, 431 (2007).
S20. Savoini, M., Biagioni, P., Duò, L., & Finazzi, M. All-optical subdiffraction multilevel data encoding onto azo-polymeric thin films. *Opt. Lett.* **34**, 761 (2009).
S21. Tantussi, F. et al. Pure optical and reversible optically driven nanowriting of azobenzene block copolymers. *Appl. Phys. Lett.* **100**, 08313 (2012).
S22. I. Greenfeld, K. Fezzaa, M. H. Rafailovich & E. Zussman, *Macromolecules* **45**, 3616-3626 (2012).

5.5 Entanglement loss and short nanofibers

Greenfeld, I. and E. Zussman, *Polymer entanglement loss in extensional flow: evidence from electrospun short nanofibers.* Journal of Polymer Science Part B-Polymer Physics, 2013. **51**(18): p. 1377–1391.[5]

The cover page of the journal issue featured an image from the published paper.

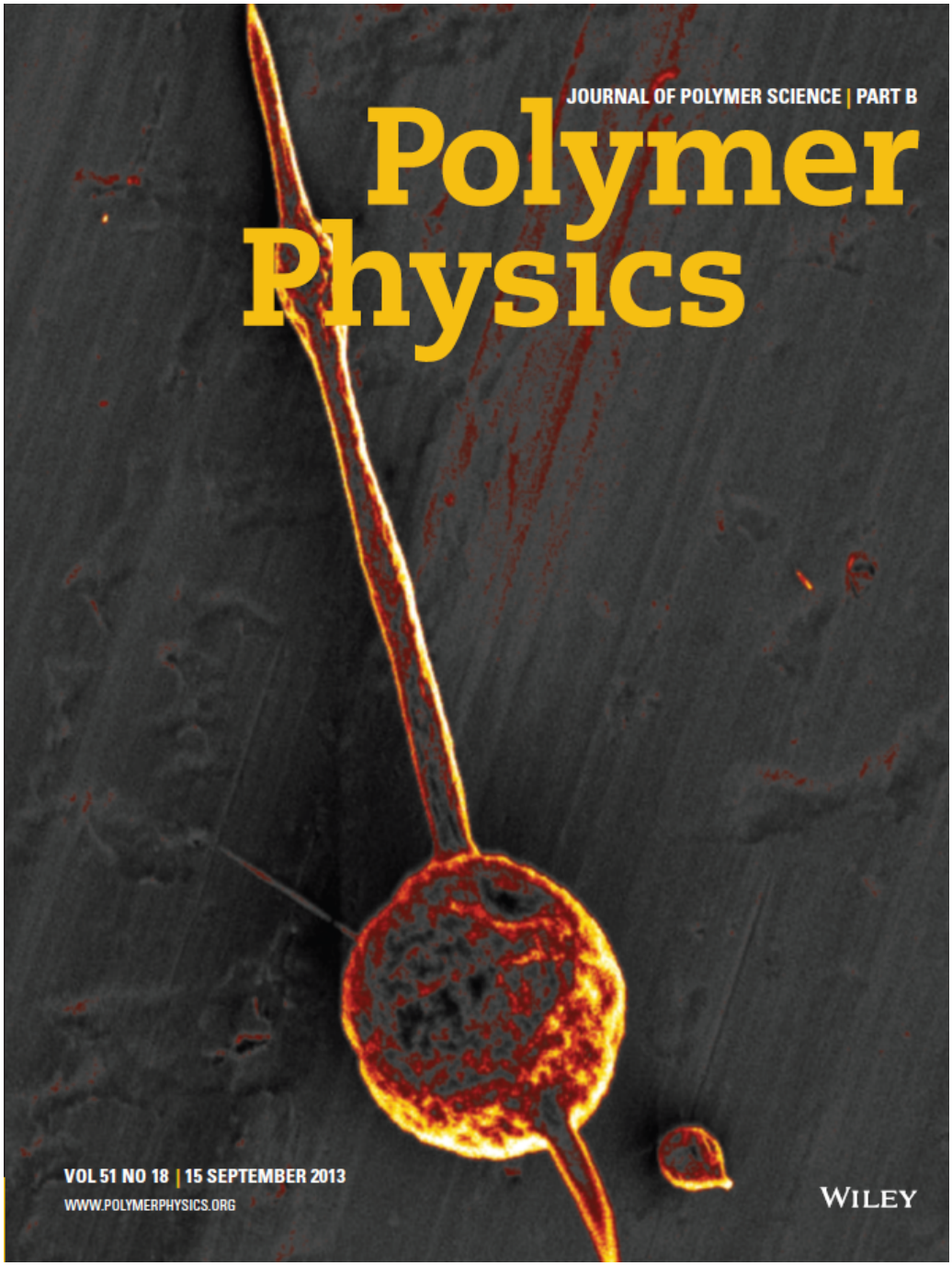

Polymer Entanglement Loss in Extensional Flow: Evidence from Electrospun Short Nanofibers

Israel Greenfeld, Eyal Zussman

Department of Mechanical Engineering, Technion - Israel Institute of Technology, Haifa 32000, Israel
Correspondence to: I. Greenfeld (E-mail: green_is@netvision.net.il)

Received 24 May 2013; revised 16 June 2013; accepted 17 June 2013; published online 17 July 2013
DOI: 10.1002/polb.23345

ABSTRACT: High strain rate extensional flow of a semidilute polymer solution can result in fragmentation caused by polymer entanglement loss, evidenced by appearance of short nanofibers during electrospinning. The typically desired outcome of electrospinning is long continuous fibers or beads, but, under certain material and process conditions, short nanofibers can be obtained, a morphology that has scarcely been studied. Here we study the conditions that lead to the creation of short nanofibers, and find a distinct parametric space in which they are likely to appear, requiring a combination of low entanglement of the polymer chains and high strain rate of the electrospinning jet. Measurements of the length and diameter of short nanofibers, electrospun from PMMA dissolved in a blend of $CHCl_3$ and DMF, confirm the theoretical prediction that the fragmentation of the jet into short fibers is brought about by elastic stretching and loss of entanglement of the polymer network. The ability to tune nanofiber length, diameter and nanostructure, by modifying variables such as the molar mass, concentration, solvent quality, electric field intensity, and flow rate, can be exploited for improving their mechanical and thermodynamic properties, leading to novel applications in engineering and life sciences. © 2013 Wiley Periodicals, Inc. J. Polym. Sci., Part B: Polym. Phys. **2013**, *51*, 1377–1391

KEYWORDS: beads; disentanglement; electrospinning; fibers; fracture; networks; nanotechnology; nanofibers; inorganic polymers; jet; PMMA; short nanofibers; viscoelastic properties

INTRODUCTION The high strain rate of an extensional flow, such as the flow of an electrospinning semidilute polymer solution jet, can result in fragmentation as a consequence of loss of the polymer network entanglement, leading to appearance of short nanofibers varying from a few tens of nanometers to a few microns in diameter. Short nanofibers are a unique morphology of electrospun polymeric nanofibers, in addition to the continuous nanofibers and nanobeads morphologies. Typically, long continuous nanofibers or beads are the preferred outcome in electrospinning applications, while short nanofibers are an undesirable defect. However, electrospun short polymeric nanofibers are expected to find important applications in engineering and life sciences.[1] Although short nanofibers can be produced by methods such as solution precipitation[2] or ultrasonication of continuous fibers,[3] their creation by electrospinning without any post-processing offers unique structures and enhanced mechanical properties.

Discontinuous beaded fibers and elongated beads are known to appear in low-concentration solutions, when the concentration is sufficiently high to avoid excessive dilution and creation of beads from droplets.[4–6] By gradually increasing the concentration, continuous fibers begin to appear. Bead-free short fibers with aspect ratios of 10–200 were obtained by varying the polymer–solvent system and molecular weight.[1] Polymer entanglement was identified as the key factor affecting the transition from the bead morphology, through that of elongated beads or short fibers, to that of continuous fibers.[1,4,6]

Short nanofibers have been scarcely explored, and further study is needed to measure the dominant factors that influence their creation and properties. Furthermore, the nanoscale mechanism that leads to short nanofiber formation requires clarification, particularly with regards to how disentanglement initiates the fragmentation of the electrospinning jet.

Short nanofibers can be created in a semi–dilute entangled solution, depending on the polymer architecture (linear or branched), molar mass, solution concentration and solvent quality. Generally, at given electric field intensities and flow rates, lower concentrations and poorer solvents decrease chain entanglement, and consequently increase the likelihood that short nanofibers will appear during electrospinning (Fig. 1). Also, short nanofibers are frequently accompanied by beads-on-string and free beads [Fig. 1(b,d)], a phenomena associated with low viscosity and high surface tension.

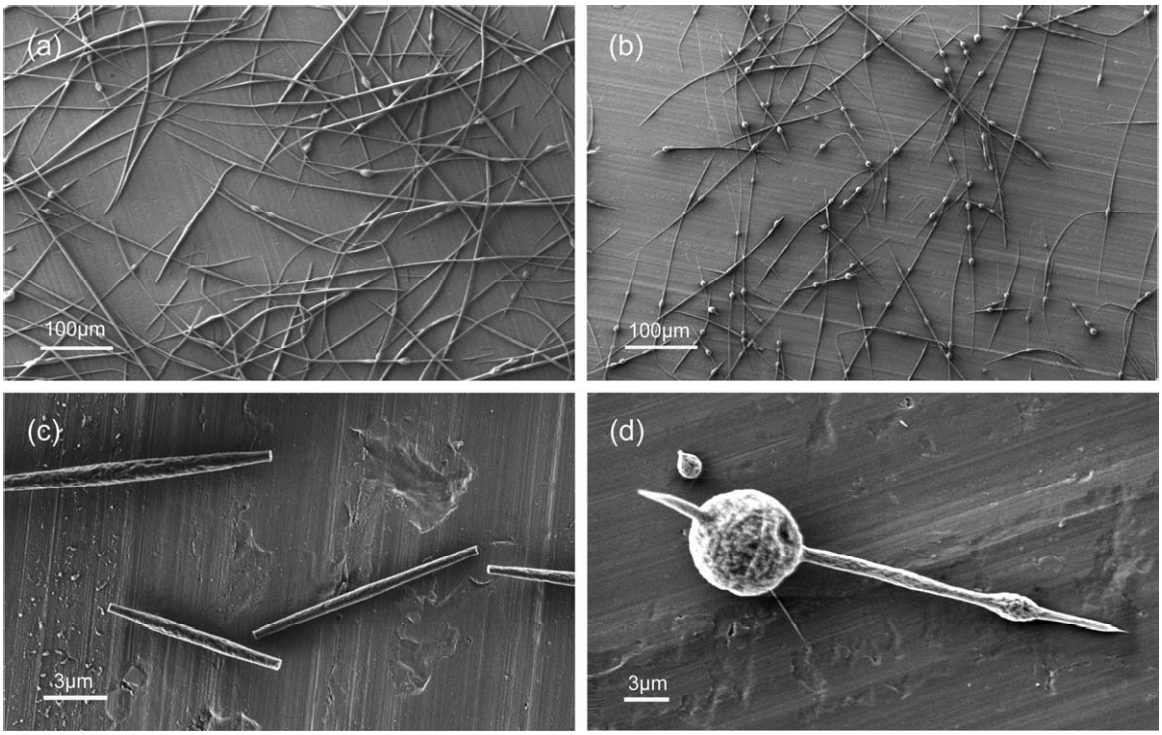

FIGURE 1 SEM micrographs of electrospun short nanofibers, with (right) and without (left) beads-on-string. Electrospinning conditions: molar mass 15 kDa PMMA, electric field 0.75 kV/cm, and flow rate 1 mL/h. Polymer concentration (vol %)/$CHCl_3$:DMF solvent composition (vol %) were: (a) 31.3/70:30, (b) 32.2/50:50, (c) 29.3/50:50, and (d) 27.5/30:70.

When the polymer network is not highly entangled, the high strain rate caused by the electrostatic field can stretch and disentangle chains from the network, and break the jet into short segments. Entanglement loss is governed by two opposing variables, both dependent on the degree of polymerization N of the polymer chain. The entanglement number, the number of topological constraints along the chain, scales with N, while the chain relaxation time in an entangled network scales with N^3. When the jet strain rate is low, rapid relaxation of the network prevents entanglement loss and viscosity is dominant. However, at high strain rates, relaxation is not sufficiently fast and elasticity is dominant, making chain extension and disentanglement possible. Hence, lower N (shorter chain) reduces entanglement, but at the same time reduces relaxation time; thus, the net effect on entanglement loss relies upon the strain rate.

At the same time, the rapid solvent evaporation characteristic of electrospinning partially solidifies the jet, sometimes creating a solid skin,[7–9] and retards entanglement loss and jet breaking, but also prevents the jet segments from contracting back into droplets by relaxation and surface tension. Electrospinning involves many material, process and ambient variables that impact the final outcome; for the purpose of this study, we chose to focus on those affecting entanglement and strain rate.

We electrospun PMMA, a linear thermoplastic polymer, dissolved in a solvent blend of $CHCl_3$ and DMF, at semi–dilute concentrations slightly above the entanglement concentration. By tuning the process and material parameters, a distinct, albeit small, parametric space where short nanofibers appeared was clearly identified, and its boundaries with the other electrospun morphologies (continuous fibers, beads-on-string, and beads) were defined. The proposed disentanglement mechanism that leads to jet fragmentation was substantiated by examining SEM images of fiber fractures and by measuring the parametric dependence of the length and diameter of short nanofibers. Further substantiation was obtained by theoretical predictions that describe the entanglement loss process, assuming known jet rheology and affine extension of the polymer network. The experimental and theoretical investigations focused on the control of the molar mass, concentration, solvent quality, electric field, and flow rate variables, and correlated well over a wide parametric space.

EXPERIMENTAL

Materials and Methods

Electrospinning was carried out by pumping a polymer solution into a syringe, and drawing it by a strong electric field toward a collector. The polymer solution was injected into a capillary needle using a syringe pump, at flow rates ranging from 0.1 to 2 mL/h. The solutions were drawn by an electric potential of 4.5 to 50 kV, across a needle-collector (upper-lower electrodes) gap that was adjusted between 4 and 30

TABLE 1 Properties of Tested Polymer and Solvents[a]

Polymer	ρ [g/cm^3]	M_w [Da][b]	M_w [Da][c]	M_n [Da][c]	$Đ$
PMMA	1.20	15,000	12,700	10,100	1.26
PMMA	1.20	101,000	82,300	43,600	1.89
PMMA	1.20	350,000	288,400	162,500	1.77

Solvent	ρ[g/cm^3]	M_w [Da]	η_s [mPa s]	γ [mN/m][d]	σ[mS/m]	χ
DMF	0.95	73	0.92	37	0.25	1.16 [f]
$CHCl_3$	1.48	119	0.54	27	0.002 [e]	0.44 [e]

[a] Density ρ, weight-average molar mass M_w, number-average molar mass M_n, dispersity $Đ=M_w/M_n$, zero-shear solvent viscosity η_s, surface tension γ, electrical conductivity σ, and Flory's interaction parameter χ (with PMMA).
[b] Manufacturer's data.
[c] GPC results.
[d] Ref. 10. Surface tension measurements (Wilhelmy method) of PMMA 15 kDa dissolved in $CHCl_3$:DMF 50:50 vol % resulted in 32.7 ± 0.5 mN/m over a wide range of concentrations.
[e] Ref. 11
[f] Mark.[12]
[g] Selvakumar et al.[13]

cm, yielding an average electric field of 0.6–6.2 kV/cm. The collector was a wheel of 20-cm diameter, rotating at tangential speeds of up to 26 m/s. Samples were collected on aluminum foils placed on the wheel edge and on glass slides close to the wheel, and were imaged by scanning electron microscopes (resolution down to 3 nm/pixel) and an optical microscope (resolution down to 0.4 μm/pixel), respectively. Under certain material and process conditions, the jet fragmented and short nanofibers were collected. The experiments were conducted at a temperature of 25 ± 1.2 °C, and at a relative humidity of $50 \pm 10\%$.

The polymer, PMMA (poly(methyl methacrylate)) purchased from Sigma-Aldrich, came in three different molar masses (15, 101, and 350 kDa). PMMA is a transparent thermoplastic polymer (T_g=105°C), with a tensile strength of 70 N/mm^2, and is brittle in its pure composition at room temperature. The solvents were a blend of $CHCl_3$ (chloroform) and DMF (dimethyl formamide), at volume ratios between 0:100 and 70:30 vol %. The polymer was dissolved in the solvent blend, at concentrations varying between 3 and 40 wt %. The relevant properties of the polymer and solvents are presented in Table 1.

To avoid over-parameterization, the electric field intensity and polymer concentration were used as free parameters, while the other parameters were assigned the following nominal conditions: solvent composition $CHCl_3$:DMF 50:50 vol %, flow rate 1 mL/h, collector velocity 2.8 m/s, and gap distance between the electrodes 10 cm. These nominal conditions were modulated within a limited range to assess their influence as well. The polymer concentration c was selected so that the solution would be within the semi–dilute entangled regime, generally with a relative concentration c/c_e (c_e is the entanglement concentration) between 1 and 2,

TABLE 2 Measured Overlap and Entanglement Concentrations for PMMA Dissolved in $CHCl_3$:DMF 50:50 vol %[a]

M_w [kDa]	c^* [g/mL]	φ^* [vol %]	c_e [g/mL]	ϕ_e [vol%]
15	0.086	7.2	0.254	21.2
101	0.039	3.2	0.118	9.8
350	0.019	1.6	0.058	4.8

[a] Molar mass M_w, overlap concentration c^*, overlap volume fraction φ^*, entanglement concentration c_e, and entanglement volume fraction ϕ_e. Calculated from the measured viscosity by intersecting the power fit curves of adjacent concentration regimes (Appendix A), and using $\varphi=c/\rho$. Estimated accuracy is ±10%.

a range in which chain entanglement is fairly low but still spinnable. This range is known as a transition zone between beads and continuous fibers, producing a mixture of nanobeads, nanofibers, and elongated beads.[4] The current work shows that, under certain conditions, solutions in this relative concentration range yield short nanofibers as well. The overlap concentration c^* and the entanglement concentration c_e for each molar mass were obtained by measuring the solution specific viscosity as a function of the polymer concentration (Appendix A), and are presented in Table 2.

The ratio between the entanglement concentration and the overlap concentration is similar for the three molar masses, $\phi_e/\phi^* \cong 3$ (expressing the concentration in terms of the volume fraction $\varphi=c/\rho$). The dependence of ϕ_e on the degree of polymerization N (in terms of Kuhn monomers, $N=M_w/598$ for PMMA) was obtained by power fitting the results from Table 2:

$$\phi_e \approx N^{-0.46}, \quad (1)$$

compared to theoretical predictions of $N^{-0.75}$ for θ-solvent and $N^{-0.76}$ for a good solvent.[14]

Jet and Fiber Fragmentation

Short nanofibers form when the jet breaks into fragments before complete solvent evaporation and fiber solidification (Fig. 2). The fragmentation of the jet can be viewed on both the macroscopic and microscopic scales. Macroscopically, the tensile stress continuously grows along the jet, and is larger when the electric field intensity is higher. The stress in an electrically driven fluid jet is generated by the electrostatic force applied on charged ionic species, which are induced into the electrically conductive fluid by the electric field. The stress in the jet is proportional to sE, where E is the electrostatic field intensity, and s is the surface density of the electric charge. At the free end of the jet the stress is zero, but at a distance x from the free end it is proportional to E^2x^2,[15] giving rise to a viscoelastic stress that scales with E^2.

Eventually, if the stress exceeds the jet tensile strength, the jet will break at weak points [Fig. 2(a)]. At the break point, the stress is fully relieved, but is gradually restored upstream to the breakpoint until, sufficiently far from the

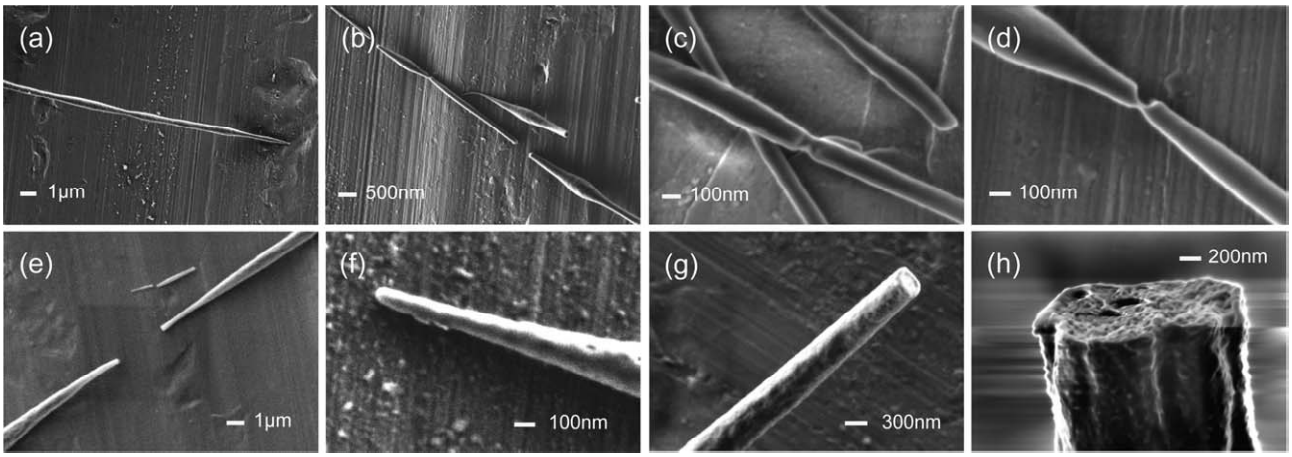

FIGURE 2 SEM micrographs of short nanofibers formation: (a) Diameter fluctuations. (b) Fragmentation. (c) Necking. (d) Break. (e) Separated fragments. (f) Round tip. (g) Fractured tip. (h) Fracture surface.

break, the effect of the break on the stress in the jet is no longer significant. As a result, the next break occurs at a distance from the previous break point, creating a fragment—a short nanofiber—and, when repeated, a sequence of fragments [Fig. 2(b)]. This mechanism is analogous to the fragmentation of a rigid fiber embedded in a soft matrix under tension (Cox and Kelly-Tyson models),[16,17] in which the fiber stress is proportional to the interfacial stress between the matrix and the fiber, and rises linearly with the distance from the break. In the Cox model, the fragment length is proportional to the fiber strength and inversely proportional to the interfacial stress. The analogy to jet fragmentation is attained by replacing the fiber strength by a power of the entanglement number, and the interfacial stress by E^2.

Typical breaking starts with necking [Fig. 2(c)] that gradually increases [Fig. 2(d)] until full break [Fig. 2(e)]. Since pure PMMA is brittle in its solid state, the presence of necking confirms that fragmentation occurs while the jet has not yet fully solidified, and material flow is still possible. The fragment tip is typically round [Fig. 2(f)], but sometimes, when solidification is more advanced, the fiber ultimately breaks in a cohesive facture [Fig. 2(g,h)].

Fragmentation of the liquid jet can be explained by a microscopic-scale mechanism. An extensional flow of a polymer solution induces hydrodynamic forces on the polymer network, resulting in stretching of the network.[18] Chains disentangle from the polymer network in fast extensional flows such as electrospinning, by a dynamic process involving stretching, reptation along an effective confining tube, and relaxation.[4,19–22] The entanglement loss is faster when the flow's strain rate is high, the chains are short, and the polymer concentration is low. Eventually, chains can detach from the network, leading to the network's complete separation. Upon separation, the tension in chains close to the break is relieved, and their relaxation leads to regaining some of the lost entanglement. As the stress, and consequently the disentanglement, is gradually restored far from the break, the next break point occurs at a distance from the previous break point. In addition, network entanglement heterogeneities, due to local variations in the polymer degree of polymerization and solution concentration, may cause jet failure.

The evolution of the axial stress and the entanglement number (number of entanglements along the chain) is schematically illustrated in Figure 3. The mechanism is repetitive, and therefore the length and diameter of the created short nanofibers should be consistent for given conditions. The cyclic nature of the entanglement number lies at the base of the diameter fluctuations seen in Figure 2(a), which are macroscopically explained by axisymmetric Rayleigh instability of highly conducting, viscoelastic polymer solutions,[23–26] leading to a wavy contour and formation of beads.

Hence, it is suggested that jet fragmentation is caused by disentanglement of chains, to the extent that the network loses its continuity and breaks up at intervals. Such breaking can only be experimentally observed if the entanglement loss is

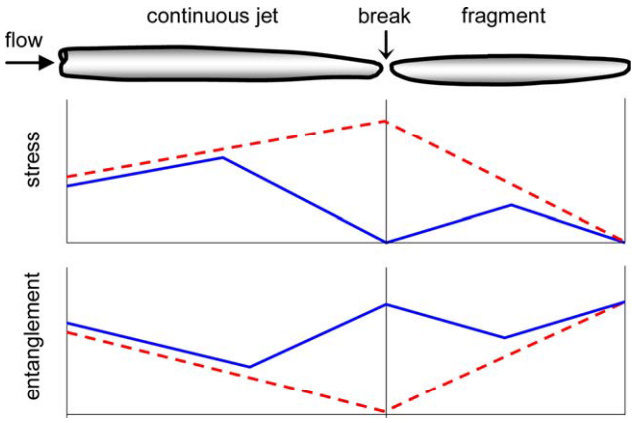

FIGURE 3 Illustration of the proposed evolution of the jet's axial stress and entanglement number (number of entanglements along the chain), before (dashed line) and after (solid line) jet break. [Color figure can be viewed in the online issue, which is available at wileyonlinelibrary.com.]

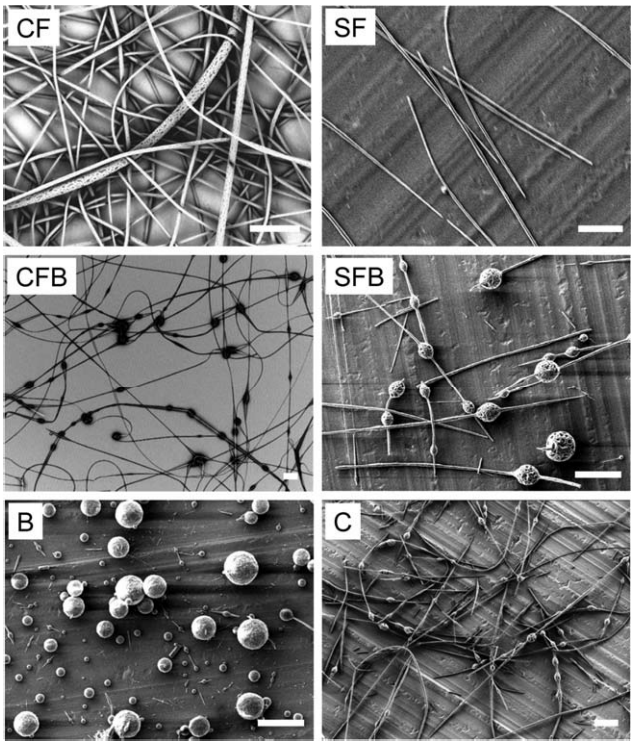

FIGURE 4 Representative SEM micrographs of the distinct nanofiber morphology regions: continuous fibers (CF), short fibers (SF), beads on continuous fibers (CFB), beads on short fibers (SFB), beads (B), and transition (mixed morphologies) (C). The scale bars are 20 μm.

fully completed within the gap between the needle and the collector. This mechanism, described in detail in the Theoretical Section, offers a good explanation for the necking and breaking process, as well as reasonable theoretical predictions for the process and material dependence of short nanofiber features.

Occurrence of Short Nanofibers and Beads

Overall, 76 experiments at varying electrospinning parameters were run, out of which 38 experiments produced short nanofibers. The observed morphologies can be categorized to continuous fibers, short fibers, beads on continuous fibers, beads on short fibers, and stand-alone beads, as shown in Figure 4. Under transitional conditions, mixed morphologies were observed.

The data set of the tests run under the nominal conditions (see Materials and Methods Section) is depicted in Figure 5, mapping the occurrence of the different morphologies as a function of the electric field intensity E and the polymer volume fraction φ normalized by a power of the degree of polymerization N. The exponents of N were tuned until the best separation between the morphology regions was achieved, enabling estimation of the boundaries by power curves. The following trends are observed for the occurrence of short nanofibers [Fig. 5(a)]. At a given molar mass (i.e., N), short nanofibers occur at lower concentration and higher electric field. As the molar mass is increased, short nanofibers are less frequent or do not appear at all. At molar mass of 350 kDa short nanofibers only appeared when a lower $CHCl_3$:DMF ratio was used. In terms of the proposed microscopic mechanism, chains are more likely to disentangle completely when they are shorter (lower molar mass), when the polymer network is less entangled because of low concentration and/or poorer solvent (causing chains to contract), and when the external electrostatic force is higher.

Beads-on-string occur at lower concentration and molar mass as well [Fig. 5(b)]. However, contrary to short nanofibers, beads-on-string occur at low electric field intensity, when the surface tension is strong enough to overcome the viscous forces driven by the electrostatic tension. Standalone beads appear as the concentration is reduced, particularly below the entanglement concentration φ_e. The boundary of the beads-on-string region is expressed by two power curves with different slopes: the upper curve relates to beads on

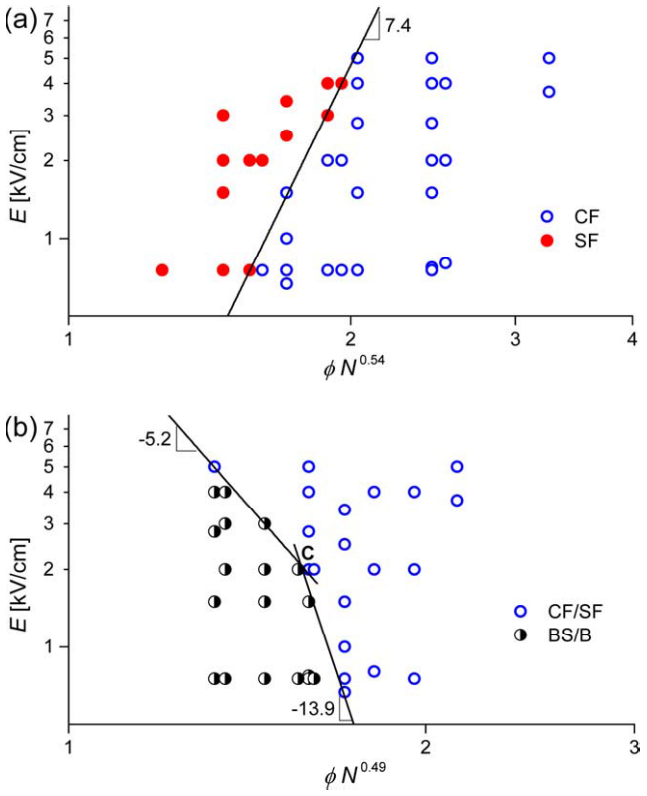

FIGURE 5 Occurrence of short fibers (a) and beads-on-string (b) in electrospun PMMA dissolved in $CHCl_3$:DMF 50:50 vol %. The flow rate was 1 mL/h and the molar mass was 15,000, 101,000, and 350,000 Da. The morphology regions are mapped over the electric field E, the polymer volume fraction ϕ, and the degree of polymerization N. The boundaries between the regions are depicted by power curves. Estimated accuracy of exponents: ±10%. Point C in (b) marks the transition from the electrostatic regime (upper section) and the viscoelastic regime (lower section)—explained in the text. [Color figure can be viewed in the online issue, which is available at wileyonlinelibrary.com.]

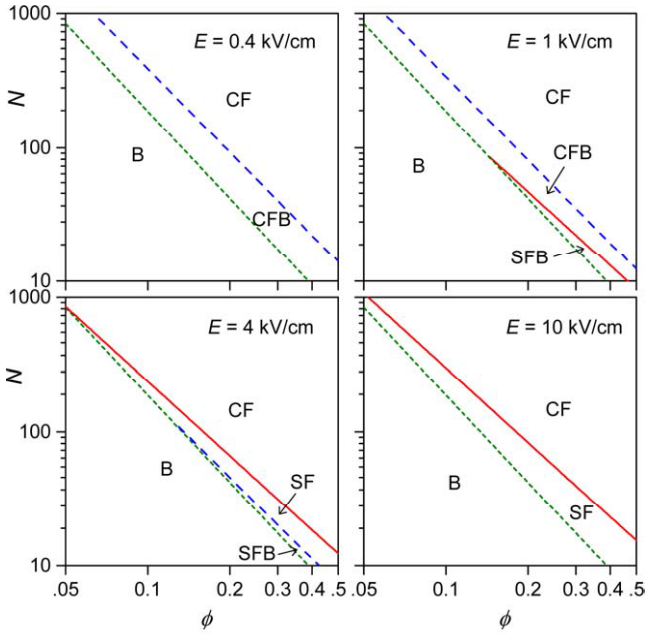

CF continuous fibers, SF short fibers, CFB beads on continuous fibers, SFB beads on short fibers, B beads

FIGURE 6 Generalized plot of the morphology regions, based on the experimental data set of Figure 5, mapped over the degree of polymerization N and the polymer volume fraction ϕ, for four different values of the electric field E. The lines correspond to eqs 1 and 2. [Color figure can be viewed in the online issue, which is available at wileyonlinelibrary.com.]

short fibers while the lower curve relates to beads on continuous fibers. Indeed, two different mechanisms are involved, since with continuous fibers the surface tension stress is opposed by the viscoelastic stress in the jet, while in short fibers the jet is fragmented and the opposing stress is electrostatic. As the electrostatic stress is lower than the viscoelastic stress, beading is more likely to occur in short fibers, as observed in the test results. Further analysis of the beading mechanism is beyond the scope of this article, as this issue has been broadly investigated both experimentally and theoretically.[4,23–25,27,28]

The morphology boundaries measured in Figure 5 can be used to formulate the electrospinning conditions for occurrence of short nanofibers (SF), beads on short fibers (SFB), and beads on continuous fibers (CFB):

$$\begin{aligned} &E^{-1}N^{4.0}\phi^{7.4} < \text{const.} \quad \text{SF} \\ &\text{EN}^{2.5}\phi^{5.2} < \text{const.} \quad \text{SFB} \\ &\text{EN}^{6.7}\phi^{13.9} < \text{const.} \quad \text{CFB}, \end{aligned} \tag{2}$$

when all the other process and material parameters that determine the constants are kept unchanged. These equations are depicted in Figure 6, together with eq 1 that marks the boundary of the standalone beads region. Note that the short fibers region is a fairly narrow strip that disappears completely at the low value of the electric field intensity (upper-left pane). The acceptable working ranges for E, N, and φ necessary for jetting are not shown. Obviously, the borderlines between the regions are not as sharp as shown, but a clear picture emerges, depicting distinct morphologies and respective process and material conditions that lead to them.

Equation 2 can be expressed in terms of the relative concentration ϕ/ϕ_e, using the measured molar mass dependence of the entanglement concentration ϕ_e from eq 1:

$$\begin{aligned} &E^{-1}N^{0.6}(\phi/\phi_e)^{7.4} < \text{const.} \quad \text{SF} \\ &EN^{0.1}(\phi/\phi_e)^{5.2} < \text{const.} \quad \text{SFB} \\ &EN^{0.3}(\phi/\phi_e)^{13.9} < \text{const.} \quad \text{CFB}. \end{aligned} \tag{3}$$

These conditions are not entirely dependent on the number of entanglements n_e along the chain (theoretically[14] $n_e \approx (\phi/\phi_e)^{1.3}$), as they depend on N and E as well. In other words, the shorter the chain and the less it is entangled, the entanglement loss will be faster and the likelihood of short nanofibers and beads-on-string will be higher. These equations are depicted in Figure 7, where E/N^{α} is plotted as a function of the relative concentration. The plot details may vary for different data sets (different polymer, solvent, jet initial velocity, etc.), but the overall layout of the plot is universal. For example, better solvent quality (higher $CHCl_3$:DMF ratio) increases entanglement and will therefore pull the plot upward. The effect of additional parameters is addressed in the next sections. Note that short fibers can only occur at normalized

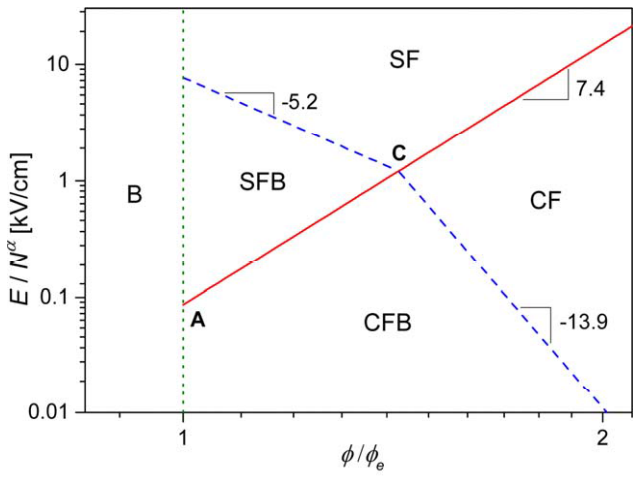

CF continuous fibers, SF short fibers, CFB beads on continuous fibers, SFB beads on short fibers, B beads, C transition point

FIGURE 7 Universal plot of the morphology regions, based on the experimental data set of Figure 5, mapped over the electric field E and the relative polymer concentration φ/φ_e. E is normalized by N^{α}, where N is the degree of polymerization and α is 0.6 (solid line), −0.1 (upper dashed line), and −0.3 (lower dashed line). The lines correspond to eq 3. [Color figure can be viewed in the online issue, which is available at wileyonlinelibrary.com.]

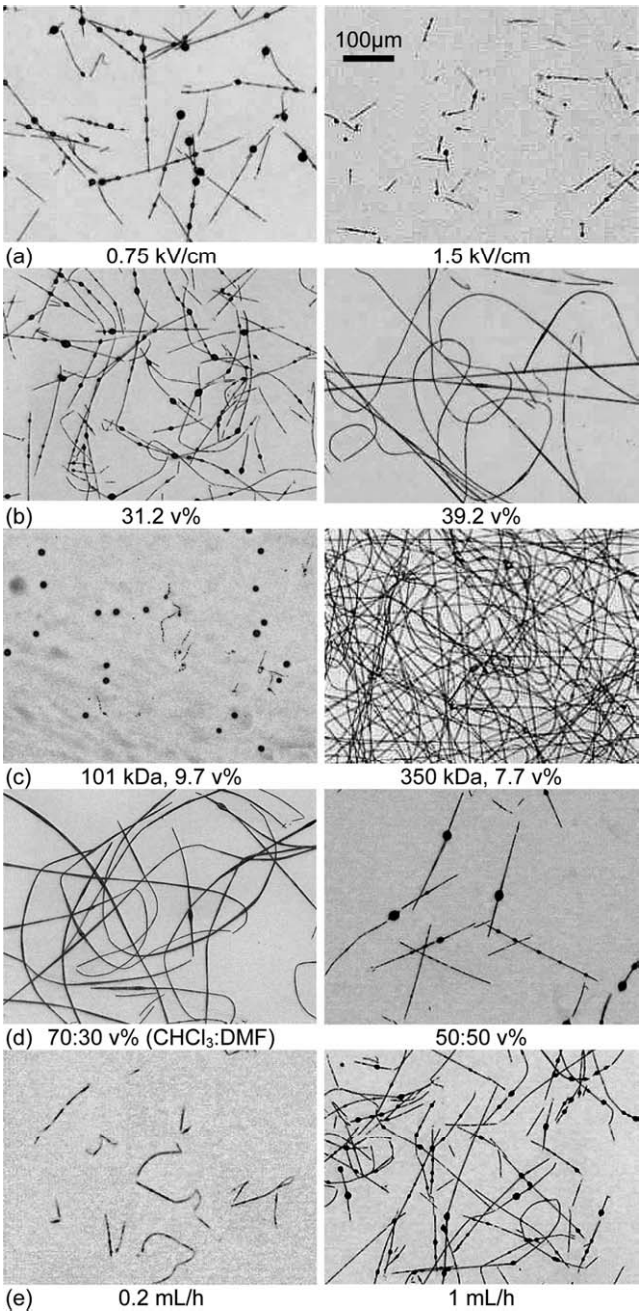

FIGURE 8 Effect of solution properties and process parameters on short nanofiber length (optical micrographs): (a) electric field (15 kDa, $CHCl_3$:DMF 50:50 vol %, 1 mL/h, 29.3 vol %), (b) polymer concentration (15 kDa, 50:50 vol %, 1 mL/h, 2 kV/cm), (c) molar mass (50:50 vol %, 0.75 kV/cm, 1 mL/h), (d) DMF fraction (15 kDa, 1 mL/h, 0.75 kV/cm, 31.2 vol %), and (e) flow rate (15 kDa, 50:50 vol %, 2 kV/cm, 31.2 vol %).

electric field intensity above point A, and short fibers without beads can occur only above the transition point C.

Short Nanofiber Length and Diameter

When the conditions for short nanofibers are met, the fragment length is the most distinctive property. The length depends on the material and process parameters, as demonstrated in Figure 8. Generally, the fragment length is shorter upon increasing the electric field intensity [Fig. 8(a)], decreasing the polymer concentration [Fig. 8(b)], decreasing the molar mass [Fig. 8(c)], decreasing the $CHCl_3$:DMF ratio [Fig. 8(d)], and decreasing the flow rate [Fig. 8(e)]. In line with the proposed entanglement loss mechanism, all of these conditions contribute to rapid chain disentanglement, and consequently to shorter fiber fragments. The polymer network is less entangled for shorter chains, lower concentrations, and poorer solvents (e.g., lower $CHCl_3$:DMF ratio), while higher electric field intensities and lower feed velocities increase the extensional strain rate, together leading to more rapid disentanglement and shorter fiber fragments. When the parametric conditions are reversed, the fragment length will increase, until continuous fibers are restored at the boundary described in the previous section. Note the randomly oriented scattering of fragments on the revolving collector, seen in Figure 8, which indicates that fragmentation occurs before reaching the collector, during the free flight of the jet.

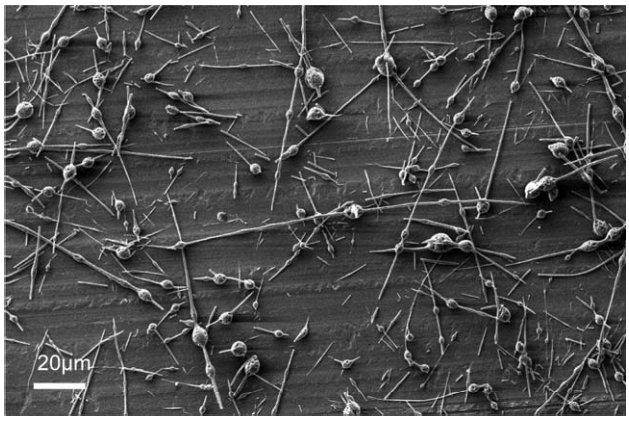

FIGURE 9 SEM micrograph demonstrating the dispersity of short nanofiber lengths and diameters. Conditions: molar mass 15 kDa, polymer concentration 29.3 vol %, solvents composition $CHCl_3$: DMF 50:50 vol %, electric field 3 kV/cm, and flow rate 1 mL/h.

The tested samples yielded short nanofibers of lengths ranging from 1 to 1000 μm and of diameters ranging from 50 nm to 3 μm. When observing a representative experimental sample in the image of Figure 9, and its length and diameter measurements in Figure 10(a), it becomes clear that even when all material and process parameters are fixed, the dispersion of fragment lengths and diameters is high, correlating well with lognormal distribution[1] [Fig. 10(b)]. Tiny fragments are by far more frequent than large fragments, and therefore, the number-average (mean) length L_n and diameter D_n are biased downward and their measurement is not stable. Instead, we use the weight-average length and diameter, $L_w = \sum L_i^2 / \sum L_i$ and $D_w = \sum D_i^2 / \sum D_i$ (analogous to the weight-average molar mass M_w), which give a higher weight to larger fragments. As shown further on, the experimental material and process dependencies match well with the weight-average length and diameter. Note that the fragment aspect ratio rises with fragment length [inset of Fig. 10(a)].

One is tempted to associate the high dispersity of fragment sizes with the fairly high molar mass dispersity of the polymer

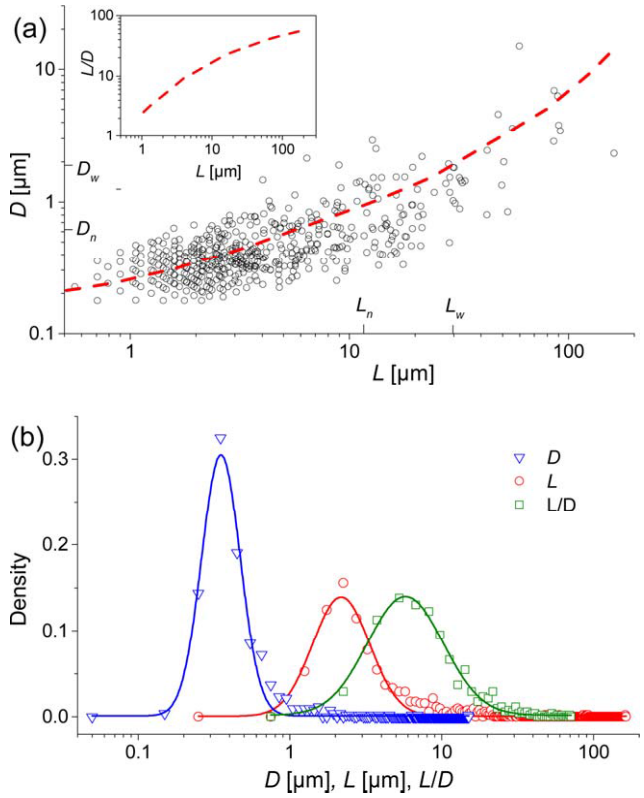

FIGURE 10 Example of the dispersity of short nanofiber lengths L, diameters D, and aspect ratios L/D. The measurements were taken from the SEM micrograph of Figure 9. (a) Measured diameter and length of the fragments. The number-average (L_n, D_n) and weight-average (L_w, D_w) values are indicated on the axes. The dispersity is $Đ_L = L_w/L_n = 2.7$ and $Đ_D = D_w/D_n = 3.1$. The inset shows the measured aspect ratio. The correlation between L and D is >0.6. (b) Distribution density of diameter, length and aspect ratio, with lognormal fit. [Color figure can be viewed in the online issue, which is available at wileyonlinelibrary.com.]

used in the experiment (Table 1), but the average molar mass at different jet cross sections should not diverge significantly. Rather, large fluctuations in the local jet diameter, due to the jet's dynamic instability, splitting and branching,[29] as well as local concentration variations, due to rapid solvent evaporation, are more likely to spawn such size dispersity.

The dependence of the length and diameter on the material and process parameters was analyzed for the experimental data sets in Table 3, all of which yielded short nanofibers. Variations were applied to the molar mass, flow rate, solvents ratio, electric field intensity, and polymer concentration. The fragments weight-average length varied over a wide range of 10^1–10^3 μm, whereas the diameter varied within a much narrower range of 0.7–3 μm.

Dependence of the fragment length and diameter on the electric field is estimated by power fitting of the data from samples in which only the electric field intensity was modified [Fig. 11(a)]. Similarly, the concentration dependence is

TABLE 3 Experimental Data Sets Used for Diameter and Length Measurements[a]

M_w [kDa]	Q [mL/h]	$CHCl_3$:DMF [vol%]	E [kV/cm]	φ [vol%]
15	1	50:50	2	39.2
|	|	|	|	32.2
|	|	|	|	31.2
|	|	|	|	29.3
|	|	|	3	|
|	|	|	1.5	|
|	|	|	0.75	|
|	|	|	|	31.2
|	|	|	|	32.2
|	|	|	|	34.2
|	|	30:70	2	27.5
|	|	|	0.75	|
|	|	70:30	|	31.3
|	|	0:100	|	29.8
|	|	|	2	|
|	0.2	50:50	|	31.2
|	|	|	3	|
|	|	30:70	0.75	27.5
|	2	70:30	2	31.3
|	|	|	4	|
101	1	50:50	|	14.6
|	|	|	3	|
|	|	|	0.75	9.7
350	|	0:100	|	3.2
|	|	|	4	|

[a] Weight-average molar mass M_w, flow rate Q, solvent volume ratio $CHCl_3$:DMF, electric field E, and polymer volume fraction φ.

estimated by power fitting of samples in which only the concentration was modified, separately for two values of electric field intensity [Fig. 11(b)]. The dependence on the other three parameters (molar mass, flow rate, and solvent ratio) was estimated by multivariate power fitting of the data, using the already estimated electric field and concentration exponents from Figure 11.

The results of the length power fit are combined in the following scaling expression:

$$L_{\mathrm{FIT}} \approx v_0^{1.4} E^{-1.1} N^{3.9} \kappa^{2.1} \phi^{7.5}, \quad (4)$$

where v_0 is the jet initial velocity, E is the applied electric field, κ is the solvents blend quality, N is the degree of polymerization, and ϕ is the polymer volume fraction. Similarly, the results of the diameter power fit are combined in the following scaling expression:

$$D_{\mathrm{FIT}} \approx v_0^{0.1} E^{-0.07} N^{-0.4} \kappa^{-0.2} \phi^{0.19}. \quad (5)$$

Note that v_0 substitutes the flow rate Q, considering that the experiments were carried out with a fixed needle internal

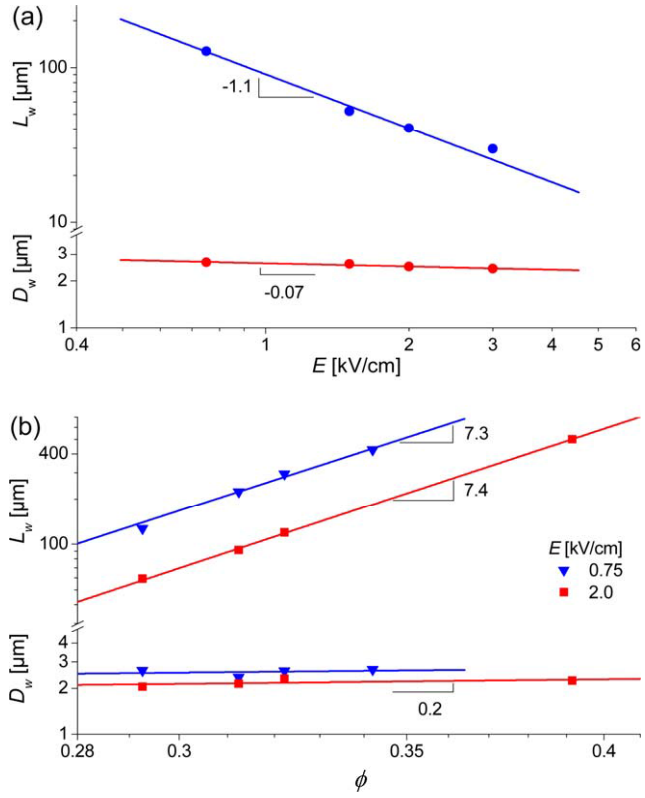

FIGURE 11 Short nanofiber weight-average length L_w and diameter D_w, measured for molar mass 15,000 kDa, flow rate 1 mL/h, and $CHCl_3$:DMF ratio 50:50 vol %. Power fit curves and corresponding exponents are shown. (a) Length and diameter *versus* the electric field E, for polymer concentration 29.3 vol %. (b) Length and diameter *versus* the polymer volume fraction φ, for two cases of electric field. Based on the experimental data sets of Table 3. [Color figure can be viewed in the online issue, which is available at wileyonlinelibrary.com.]

diameter. The solvents blend quality is approximated by the dimensionless term $\kappa=(2\chi-1)^{-1}$, where χ is the concentration-weighted interaction parameter of the two solvents with the polymer, $\chi=\phi_{DMF}\chi_{DMF}+(1-\phi_{DMF})\chi_{CHCl3}$ (ϕ_{DMF} is the DMF volume fraction in the solvents blend). The values of χ_{DMF} and χ_{CHCl3} are given in Table 1. Figure 12 demonstrates the quality of the power fit and confirms the scaling approach, which is further validated by the analysis in the next section.

Higher v_0 and lower E result in a reduced velocity gradient and therefore longer L, while they have a negligible effect on D. Higher κ (better solvent blend - higher $CHCl_3$:DMF ratio) result in longer L and smaller D. The solvent quality dependence of L is apparent, as a better solvent increases chain swelling and consequently entanglement, resulting in slower entanglement loss and longer fragments. However, the solvent quality dependence of D is opposite; when the network is more entangled, due to a better solvent, its extension ratio upon breaking is higher, and therefore its condensed diameter is smaller.

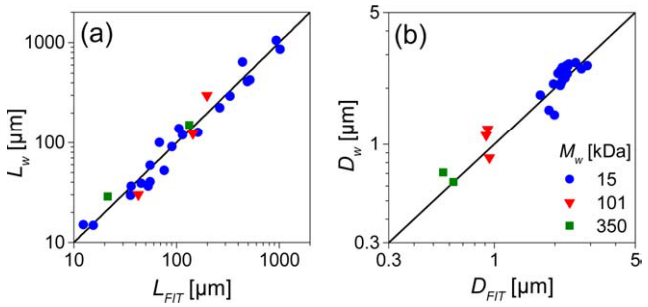

FIGURE 12 Measured weight-average short nanofiber length L_w (a) and diameter D_w (b), *versus* the corresponding power-fit curves L_{FIT} (eq 4) and D_{FIT} (eq 5). Based on the experimental data sets of Table 3. [Color figure can be viewed in the online issue, which is available at wileyonlinelibrary.com.]

Writing eqs 4 and 5 in terms of the relative concentration ϕ/ϕ_e, using eq 1 (omitting all other terms):

$$L_{FIT} \sim N^{0.5}(\phi/\phi_e)^{7.5}$$
$$D_{FIT} \sim N^{-0.5}(\phi/\phi_e)^{0.19}, \quad (6)$$

we observe that higher entanglement number $n_e \approx (\phi/\phi_e)^{1.3}$ yields larger L due to increased viscosity and reduced velocity gradient, and that L increases with the degree of polymerization N. The shorter the chain and the less it is entangled, the more rapid entanglement loss will be, and fragment lengths will be consequentially shorter. The effect of N on the diameter is opposite, as a longer chain means higher chain extensibility, whereas the effect of n_e is minor. In contrast, the diameter of continuous fibers is highly dependent on n_e, as will be shown in the next section.

The upper limit of the fragment length L scales with the gap distance between the electrodes d [Fig. 13(a)], and therefore eq 4 can be used to define the condition for the occurrence of short nanofibers:

$$Kd > v_0^{1.4}E^{-1.1}N^{3.9}\kappa^{2.1}\phi^{7.5}, \quad (7)$$

where K is a constant prefactor. This equation compares well with the boundary of short nanofibers occurrence of eq 2, const. $> E^{-1}N^{4.0}\phi^{7.4}$, which was derived in a completely different way. Moreover, since the occurrence boundary scales with the position at which the jet separates, z_s [Fig. 13(a)], this observation leads to the conclusion that the short nanofiber length should be proportional to the breaking position, $L \sim z_s$, even though their orders of magnitude may be quite disparate. This result is used in the next section for estimating the fragment length (eq 15).

THEORETICAL DESCRIPTION

Disentanglement of Polymer Chains

The highly entangled polymer network within the electrospinning semidilute solution ensures the continuity of the jet and the eventual formation of continuous nanofibers. As suggested, the occurrence of short nanofibers is brought about

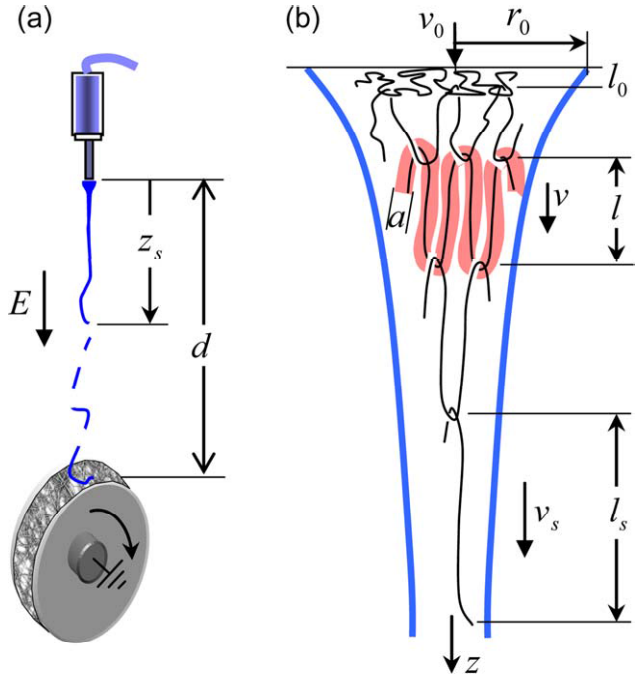

FIGURE 13 Illustration of electrospinning and jet fragmentation (a), and network disentanglement (b). The blue (outer) curves in (b) are the jet boundary, and the pink (thick) curve represents the confining tube. Elastic extension of chains, followed by stress relief resulting from chain reptation along a confining tube, gradually disentangle chains from the network. The subscript *s* denotes the jet break point. [Color figure can be viewed in the online issue, which is available at wileyonlinelibrary.com.]

by substantial entanglement loss during the electrospinning process. The entanglements, topological constraints that prevent intercrossing of chains, effectively divide each polymer chain into entanglement strands, which are elastically extended under the applied extensional forces. At equilibrium, chains can reptate within a confining tube, which represents the constraining potential of nearby chains on the strand, allowing monomers to fluctuate within its confining diameter. Under strain, chains can relieve the high elastic tension by sliding along the tube, and be partially disentangled from the network. When the jet strain rate is sufficiently high and the chain relaxation time is sufficiently slow, the chains cannot effectively relax back to their network equilibrium state. Under such conditions, the end-to-end distance of strands will gradually increase, and the number of entanglements along chains will be reduced, eventually resulting in a complete separation of the network and breaking of the jet. The process is illustrated in Figure 13.

The analysis assumes an affine deformation of the polymer network, namely, that the relative extension of each strand is the same as the relative extension of the jet at the same axial position. Thus, the entanglement nodes are supposedly moving at the same velocity as the jet, with negligible local velocity lag or lead with respect to the jet. This approach is reminiscent of the affine tube model of rubber elasticity, except that the contour length of strands is not fixed, but rather increases in consequence of chain sliding along the confining tube. Thus, the extended length of the strand is the result of both elastic stretching and disentanglement. Using this concept, an extended strand having a distance l between its two entanglements, located at a jet position z and axial velocity v, is extended at a velocity of

$$\frac{dl}{dt} \approx l\frac{dv}{dz} \approx \frac{l}{v}\frac{dv}{dt}, \tag{8}$$

or, by rearranging the terms, $\dot{l}/l \approx \dot{v}/v$. Integrating and setting the initial strand length $l_0 = a$ (a is the tube diameter) and the initial jet velocity v_0:

$$\frac{v}{v_0} \approx \frac{l}{l_0} = \frac{l}{a}. \tag{9}$$

A similar expression was obtained by dynamic modeling of network stretching during electrospinning,[18] assuming rubber elasticity with a fixed strand contour length.

Jet Breaking

At the jet start, when the solution is almost at rest, the initial strand length (end-to-end distance) is equivalent to the chain's confining tube diameter, and is given by $a \approx bN_{e1}^{1/2}\phi^{-\nu/(3\nu-1)}$ for an athermal solvent and $a \approx bN_{e1}^{1/2}\phi^{-2/3}$ for a θ-solvent.[14] b is the Kuhn monomer length, N_{e1} is the number of Kuhn monomers in an entanglement strand in the melt (a fixed value for a given polymer, of order 10^0-10^1), ϕ is the polymer volume fraction, and $\nu \cong 0.588$ is the swelling exponent for a good solvent. As a result of the high strain rate, the strand approaches full extension close to the jet start,[18] and, since the strain rate is not relieved throughout the jet, the strand retains a high extension even after partial disentanglement and relaxation. Under such conditions, the end-to-end distance of a strand consisting of N_e monomers can be approximated by $l \cong bN_e$. At low strain rates and fast relaxation times, the strand length may be shorter, or $l \cong bN_e^x$, where $\nu < x < 1$; however, for simplicity, in the following analysis we assume full extension. Thus, upon complete chain disentanglement at jet position z_s, the strand approaches the length of the entire chain, $l_s \cong bN$, and the corresponding jet velocity v_s from eq 9 is:

$$\frac{v_s}{v_0} \approx \frac{l_s}{a} \approx \frac{N}{N_{e1}^{1/2}}\begin{cases}\phi^{\frac{\nu}{3\nu-1}} & \text{athermal solvent}\\ \phi^{2/3} & \theta\text{-solvent.}\end{cases} \tag{10}$$

To obtain a length scale for the network separation, the velocity profile $v(z)$ should be specified. Theoretical and experimental analyses of electrically driven fluid jets have shown that the jet velocity, sufficiently far from the jet start, assumes an asymptotic profile that can be expressed by a power law of the position z along the jet.[30–35] For example,

$$\frac{v}{v_0} \cong k^2\left(\frac{z}{r_0}\right)^{2\beta}, \tag{11}$$

where k is a dimensionless parameter, of order $10^{-1}-10^1$, that determines the scale of velocity increase, r_0 is the initial jet radius, of order 10^{-1} mm, and β is an exponent shown to

vary between 0.25 and 1 (β=0.5 is used throughout the rest of the analysis)[30].

The dependence of the flow parameter k on the material and process parameters, can be estimated by substituting the velocity gradient from eq 11, which scales as $\nabla v \sim (v_0/r_0)k^2$, by the strain rate, which scales as $\dot{\varepsilon} \sim E^2/\eta$, yielding $k \sim r_0^{1/2}\eta^{-1/2}v_0^{-1/2}E$. A theoretical derivation based on jet rheology yields $k \cong \varepsilon_m^{1/6}r_0^{2/3}\sigma^{1/4}\eta^{-5/12}v_0^{-2/3}E^{5/6}$ (in CGS electrostatic units), where $\varepsilon_m \cong 1$ is the permeability of the medium (air).[34,35] Substituting the solution viscosity $\eta \cong \eta_s\eta_{sp}$ ($\eta >> \eta_s$, where η_s is the solvent viscosity and η_{sp} is the solution specific viscosity), the flow parameter may be redefined as $k=k_0\eta_{sp}^{-5/12}$. Thus, the jet breaking position, or the jet axial position at which disentanglement is completed, z_s, can be expressed as a function of the corresponding jet velocity v_s:

$$\frac{z_s}{r_0} \approx k^{-2}\frac{v_s}{v_0} \approx k_0^{-2}\eta_{sp}^{5/6}\frac{l_s}{a} \qquad k_0 \cong \varepsilon_m^{1/6}r_0^{2/3}\sigma^{1/4}\eta_s^{-5/12}v_0^{-2/3}E^{5/6}. \tag{12}$$

Using the known expressions for the viscosity of a semidilute solution,[14] $\eta_{sp} \approx \left(N^3/N_{e1}^2\right)\phi^{3/(3\nu-1)}$ for an athermal solvent and $\eta_{sp} \approx \left(N^3/N_{e1}^2\right)\phi^{14/3}$ for a θ-solvent, and substituting l_s/a from eq 10, the breaking position is:

$$\frac{z_s}{r_0} \approx k_0^{-2}\frac{N^{7/2}}{N_{e1}^{13/6}}\begin{cases}\kappa^{\frac{17(2\nu-1)}{2(3\nu-1)}}\phi^{\frac{2\nu+5}{2(3\nu-1)}} & \text{good solvent}\\ \phi^{41/9} & \theta\text{-solvent}.\end{cases} \tag{13}$$

Note that the expression is expanded to good solvents by incorporating the dimensionless term $\kappa=\nu/b^3$ (ν is the excluded volume), which expresses the solvent quality based on the interaction between monomers in a given solvent; this term rises as the solvent improves, up to the athermal limit where it is equal to 1.

The analysis assumes a homogenous polymer network. Local variations in polymer concentration and deformation, and the dispersity of the polymer degree of polymerization, can influence the results. Discussion on the effects of deformation, disentanglement and evaporation on the solution viscosity, which are not accounted for in the current theoretical analysis, is provided in Appendix B.

Short Nanofiber Occurrence and Length

The jet position z_s where the polymer network separates marks the location where short nanofibers are being created. If $z_s > d$ (d is the gap distance between the electrodes), the jet will not fragment and the nanofibers will be continuous, whereas when $z_s < d$ short nanofibers will appear. Hence, the condition for occurrence of short nanofibers is:

$$\frac{d}{r_0} > \frac{z_s}{r_0}, \tag{14}$$

where z_s is given by eq 13.

Upon breaking, the jet tensile stress at position z_s is relieved, but is gradually restored upstream. Chains will partially relax under the reduced stress, and there will be an entanglement gain, consequently delaying the next break point. This mechanism repeats itself, producing a sequence of fragments. The short fiber length L and the jet breaking position z_s scale similarly with the material and process parameters, as shown in the Experimental Section, inferring that L is proportional to z_s:

$$\frac{L}{r_0} \approx \frac{z_s}{r_0} \approx \frac{\eta_s^{5/6}v_0^{4/3}}{\sigma^{1/2}r_0^{4/3}E^{5/3}}\frac{N^{7/2}}{N_{e1}^{13/6}}\begin{cases}\kappa^{\frac{17(2\nu-1)}{2(3\nu-1)}}\phi^{\frac{2\nu+5}{2(3\nu-1)}} & \text{good solvent}\\ \phi^{41/9} & \theta\text{-solvent}.\end{cases} \tag{15}$$

where z_s is obtained from eq 13 and k_0 is explicitly written. Since $z_s \sim d \sim 10^2$ mm and $L \sim 10^{-1}$ mm, a constant prefactor of order 10^{-3} should be added. The concentration dependence of L is $\phi^{4.0}$, for a good solvent, and $\phi^{4.6}$, for a θ-solvent, and, with the effect of deformation on the viscosity (Appendix B), $\phi^{5.3}$ and $\phi^{5.7}$, respectively. The solvent quality dependence of L is $\kappa^{2.0}$. These predictions compare reasonably well with the experimental findings in eqs 2, 4, and 7, specifically $L_{FIT} \approx v_0^{1.4}E^{-1.1}N^{3.9}\kappa^{2.1}\phi^{7.5}$. The two main differences between this prediction and the experiment lie in the concentration and the electric field intensity. The exponent of ϕ does not reflect the full effects of deformation, disentanglement and evaporation on the solution viscosity (Appendix B). The jet rheology assumes a uniform electric field,[35] while in reality, the field magnitude and gradient increase sharply close to the syringe and collector, in a manner similar to the electric field generated by two point charges.[36] The fibers' experimental and theoretical lengths are compared in Figure 14(a).

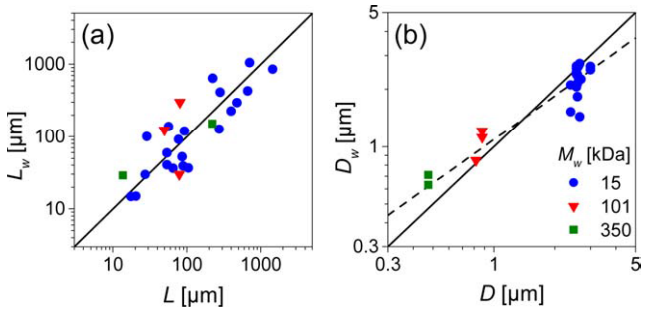

FIGURE 14 Comparison of experimental and theoretical short nanofibers dimensions, based on the experimental data sets of Table 3. The prefactors were adjusted as free parameters. (a) Measured length L_w *versus* the theoretical length L (eq 15). (b) Measured diameter D_w *versus* the theoretical diameter D (eq 18). The dashed line marks the deviation with respect to the molar mass (M_w) dependence, explained in the text. [Color figure can be viewed in the online issue, which is available at wileyonlinelibrary.com.]

The length is dependent on both the entanglement number of the solution, $n_e \approx (\phi/\phi_e)^{1.3}$, and the degree of polymerization N, as can be seen when expressed in terms of the relative concentration, using the theoretical entanglement concentration[14] $\phi_e \sim N^{1-3\nu}$, for a good solvent, and $\phi_e \sim N^{-3/4}$, for a θ-solvent:

$$\frac{L}{r_0} \sim k_0^{-2} \begin{cases} N^{0.41}(\phi/\phi_e)^{4.0} & \text{good solvent} \\ N^{0.08}(\phi/\phi_e)^{4.6} & \theta\text{-solvent}. \end{cases} \quad (16)$$

In line with the analogy to Cox model for the fragmentation of a rigid fiber embedded in a soft matrix under tension, discussed in the Experimental Section, this equation can be reduced to $L \sim n_e^{3.5}/E^{1.7}$ (for a θ-solvent), in which $n_e^{3.5}$ is replaced by the fiber strength and $E^{1.7}$ by the interfacial stress.

Short and Continuous Nanofiber Diameter

Prior to stretching, the condensed polymer network diameter scales with $r_0\sqrt{\phi}$ for initial jet radius r_0. The local condensed diameter, D_c, is reduced by a factor of $\sqrt{l/a}$, as a result of network stretching and disentanglement, and therefore (using eq 9):

$$\frac{D_c}{r_0} \approx \sqrt{\frac{\phi a}{l}} \approx \phi^{1/2}\left(\frac{v}{v_0}\right)^{-1/2}. \quad (17)$$

An alternative expression is $D_c \approx r\sqrt{\phi}$, where r is the local jet radius.

The diameter of short nanofibers can be obtained by inserting the value of l_s/a from eq 10:

$$\frac{D}{r_0} \approx \frac{N_{e1}^{1/4}}{N^{1/2}} \begin{cases} (\phi/\kappa)^{\frac{2v-1}{2(3v-1)}} & \text{good solvent} \\ \phi^{1/6} & \theta\text{-solvent}. \end{cases} \quad (18)$$

The concentration dependence of short nanofiber diameter is $(\phi/\kappa)^{0.12}$, for a good solvent, and $\phi^{0.17}$, for a θ-solvent. This prediction compares reasonably well with the experimental finding, $D_{FIT} \approx v_0^{0.1}E^{-0.07}N^{-0.4}\kappa^{-0.2}\phi^{0.19}$ (eq. 5). Unlike the length, the theoretical diameter is independent of the jet dynamics (i.e. the initial velocity and electric field). However, the exponents of v_0 and E were not zero in the experiment, implying additional secondary influences. Note the dominance of the degree of polymerization N (larger N leads to smaller D), whereas the other parameters have a weak or null effect. Since the size of a chain (its end-to-end distance) in a semidilute, good-solvent solution is $R \approx bN^{1/2}(\kappa/\phi)^{(v-1/2)/(3v-1)}$,[14] eq 18 can be written as $D \approx bN_{e1}^{1/4}(r_0/R)$, an inverse dependence of D on R.

The fibers' experimental and theoretical diameters are compared in Figure 14(b). The predicted exponent of N deviates from that obtained from the experiment, as reflected in the dashed line in Figure 14(b). This deviation implies that the entanglement strand does not reach full extension ($l_s \sim N$) upon network separation, as assumed in the theoretical prediction, but rather corresponds to $l_s \sim N^{0.8}$, a substantial extension when compared to the chain's equilibrium end-to-end distance.

In terms of the relative concentration, the short fiber diameter is proportional to:

$$\frac{D}{r_0} \sim \begin{cases} N^{-0.59}(\phi/\phi_e)^{0.12} & \text{good solvent} \\ N^{-0.62}(\phi/\phi_e)^{0.17} & \theta\text{-solvent}. \end{cases} \quad (19)$$

The dependence on N has a negative exponent, as in the experiment, since longer chains allow higher extensibility of the network.

To obtain the diameter of continuous nanofibers, the jet velocity upon reaching the collector is obtained from eq 11 with $z=d$, and is substituted into eq 17:

$$\frac{D}{r_0} \approx k_1^{-1}\frac{N^{5/4}}{N_{e1}^{5/6}} \begin{cases} \kappa^{\frac{15(2v-1)}{4(3v-1)}}\phi^{\frac{3(2v+1)}{4(3v-1)}} & \text{good solvent} \\ \phi^{22/9} & \theta\text{-solvent}. \end{cases} \quad (20)$$

where $k_1=k_0\sqrt{d/r_0}$ and k_0 is defined in eq 12. The concentration dependence of the continuous nanofiber diameter is $\phi^{2.1}$, for a good solvent, and $\phi^{2.4}$, for a θ-solvent, and, with the effect of deformation on the viscosity (Appendix B), $\phi^{2.8}$ and ϕ^3, respectively. The solvent quality dependence of D is $\kappa^{0.9}$. Note that, compared to short nanofibers, the exponent of the degree of polymerization N is positive, (larger N leads to larger D), and that the concentration dependence is much higher, reflecting the dominant effect of the jet dynamics.

In terms of the relative concentration, the continuous fiber diameter is proportional to:

$$\frac{D}{r_0} \sim k_1^{-1} \begin{cases} N^{-0.38}(\phi/\phi_e)^{2.1} & \text{good solvent} \\ N^{-0.58}(\phi/\phi_e)^{2.4} & \theta\text{-solvent}. \end{cases} \quad (21)$$

The results are consistent with the trends in numerous published works, which showed that the diameter of continuous fibers is smaller for lower concentration,[6,37,38] higher electric field intensity,[37,39] lower flow rate,[40] and larger gap distance between the electrodes.[41] More specifically, similar relative concentration dependencies of continuous fiber diameters were measured by Mckee et al.[38] on linear and branched PET-*co*-PEI copolymers and by Gupta et al.[6] on PMMA, yielding $(\phi/\phi_e)^{2.6}$ and $(\phi/\phi_e)^{3.1}$, respectively. These measurements compare well with our theoretical prediction. However, in addition to the dependence on the entanglement number, $n_e \approx (\phi/\phi_e)^{1.3}$, the prediction includes a strong dependence on the degree of polymerization as well, the introduction of which can improve the fit of the data in these references. Furthermore, note that different combinations of material and process variables can lead to the same nanofiber diameter, but with different nanostructure.

The evolution of the fiber length and diameter as a function of the relative polymer concentration is depicted in Figure 15 for a θ-solvent. If $k_1 > 1$ (e.g., low initial velocity, high electric field intensity, and/or large gap distance), short fibers occur and their diameter grows weakly with increasing relative concentration, while their length grows sharply. When the concentration is increased beyond the transition point, $\phi/\phi_e \geq k_1^{0.44}N^{-0.02} \cong k_1^{0.44}$, continuous fibers are created and the diameter growth slope increases abruptly. If $k_1 \leq 1$, only continuous fibers are created. Unlike continuous fibers, the diameter of short fibers is independent of the gap distance between the electrodes d and the parameter k_0 (whose initial velocity and electric field dependencies are

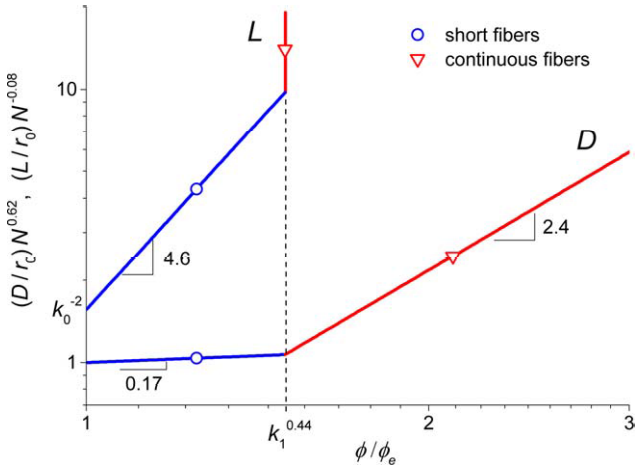

FIGURE 15 Nanofiber length L/r_0 and diameter D/r_0 *versus* the relative concentration φ/φ_e, based on eqs 16, 19, and 21 with approximations (θ-solvent). The length is normalized by $N^{0.08}$ and the diameter by $N^{-0.62}$, where N is the degree of polymerization. Prefactors are ignored. $k_1 = k_0\sqrt{d/r_0}$, where the parameter k_0 is defined in eq 12, d is the gap distance between the electrodes, and r_0 is the jet initial radius. The slopes of the two morphology regions—short nanofibers and continuous nanofibers—are marked. [Color figure can be viewed in the online issue, which is available at wileyonlinelibrary.com.]

$\sim v_0^{-2/3}E^{5/6}$). In continuous fibers, the process of disentanglement is not carried out until complete separation of the network, since it is terminated at the collector, and therefore the amount of entanglement loss, and hence the diameter, depend on the flow dynamics and the gap size. In short fibers, once the condition for their occurrence is met, entanglement loss is driven to completion and the diameter is therefore independent of these parameters.

CONCLUSIONS

High strain rate extensional flow of a semidilute polymer solution can result in fragmentation caused by polymer entanglement loss. We found evidence for this phenomenon in the appearance of short nanofibers during electrospinning. Short nanofibers, of lengths ranging from 1 to 1000 μm and of diameters ranging from 50 nm to 3 μm, were electrospun from solutions of PMMA dissolved in a blend of $CHCl_3$ and DMF. The short nanofibers appeared at solution concentrations slightly above the entanglement concentration, when the electric field intensity was high and the flow rate low. When starting from material properties that yield continuous nanofibers, short nanofibers were obtained by decreasing the molar mass, concentration, and solvent quality, all of which contribute to reduced polymer network entanglement. Under such favorable low entanglement and high strain rate conditions, the elastic stretching of the polymer network accelerates the entanglement loss, eventually leading to separation of the network and fragmentation of the jet. The experimental results and theoretical predictions correlate well, confirming the proposed disentanglement mechanism. The analysis identifies the conditions for short nanofiber occurrence, with and without beads-on-string, and explains how their length and diameter depend on the material and process variables.

The high elastic stretching and entanglement loss required to create short nanofibers are likely to lead to an ordered, aligned solid nanostructure with improved mechanical properties. At the same time, since fragmentation occurs before full solidification and collection of the fibers, the polymer network may partially relax in solvent rich areas, and voids may be left in the matrix after evaporation.[9,18,30] A nonuniform structure can result in both the axial and radial directions, with regions of aligned rigid structure and regions of amorphous porous structure. Furthermore, the analysis shows that different combinations of material and process variables can lead to the same nanofiber diameter, but not necessarily to the same internal nanostructure, a result that can be exploited for controlling the mechanical properties.

The ability to tune short nanofiber dimensions can be exploited to improve their as-spun mechanical and thermodynamic properties, such as the elastic modulus, as already demonstrated in continuous nanofibers, whose known size-dependent properties[42–45] are attributed to the molecular and supermolecular structure of the polymer matrix[18]. Such size tuning, combined with the possible biaxial nonuniform nanostructure, may find interesting applications in tissue engineering,[46] drug delivery, composites reinforcement, filtration, electrical and thermal conduction, and light amplification.

APPENDIX A: VISCOSITY MEASUREMENT

To determine the overlap concentration c^* and the entanglement concentration c_e for each molar mass, the solution specific viscosity was measured as a function of the polymer concentration (Fig. A1). The c^* and c_e (Table 2) were measured by intersecting the slopes of the three known concentration regimes, and compared well with c^* estimated from the measured intrinsic viscosity, $c^* = [\eta]^{-1}$, and with the literature[6]. The individual curves of each molar mass were normalized by their corresponding c_e and collapsed into a universal curve as a function of ϕ/ϕ_e (Fig. A1), where the mass concentration c was substituted by the dimensionless volume fraction $\phi = c/\rho$. The measured slopes were 1.1, 2.0, and 4.5 for the dilute, semidilute unentangled, and semidilute entangled regimes, respectively, close to both theoretical[14] (1, 2 and 4.7 for θ-solvent and 1, 1.3 and 3.9 for good solvent) and experimental values.[6]

APPENDIX B: EFFECT OF NETWORK DEFORMATION ON VISCOSITY

The theoretical prediction does not account for the effects of network deformation, chain disentanglement, and solvent evaporation on the solution viscosity. These complex effects are not introduced in the current analysis, but are briefly

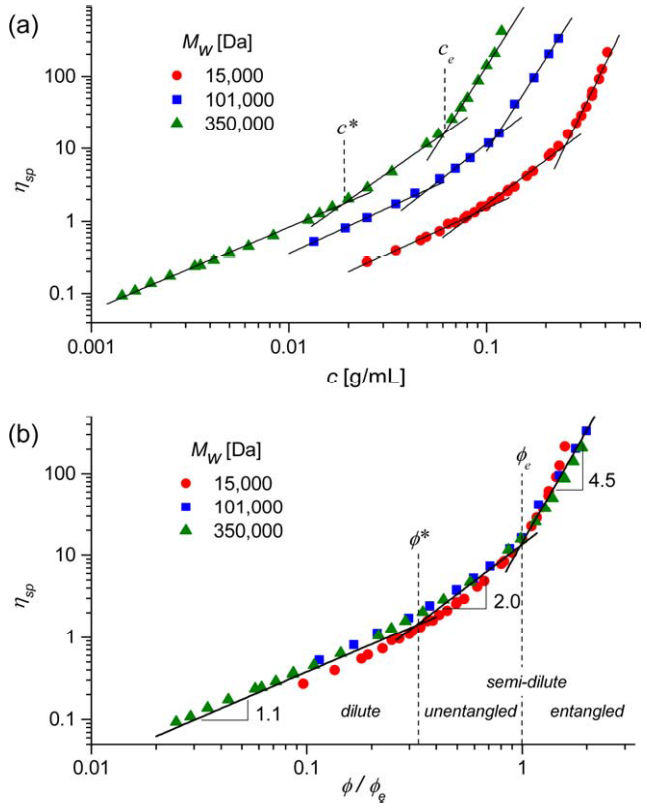

FIGURE A1 Measured specific viscosity, $\eta_{sp}=\eta/\eta_s-1$ (η and η_s are the solution and solvent viscosities, respectively), for PMMA dissolved in $CHCl_3$:DMF 50:50 vol % at 25 °C. (a) Viscosity *versus* solution concentration c. The concentration regimes were identified by power fit curves, the intersections of which provided the overlap concentration c^* and the entanglement concentration c_e for each molar mass. (b) Viscosity *versus* relative solution concentration ϕ/ϕ_e ($\phi=c/\rho$). The concentration regimes and the exponents of the power fit curves are indicated. [Color figure can be viewed in the online issue, which is available at wileyonlinelibrary.com.]

discussed below. The confining tube varies in consequence of the large network deformation and the rearrangement of chains and their interactions with neighboring chains. For example, the non-affine tube model of rubber elasticity predicts that the deformation dependence of the tube diameter is $a_{\mathrm{def}} \cong a\lambda^{1/2}$, where a is the undeformed tube diameter, and λ is the deformation factor.[47] When an entanglement strand, consisting of N_e monomers, approaches its full elastic extension, $\lambda \approx bN_e/(bN_e^{1/2}) \approx N_e^{1/2} \approx a/b \approx N_{e1}^{1/2}\phi^{-2/3}$ (θ-solvent), and therefore the deformed tube diameter increases by a factor of $\lambda^{1/2} \approx N_{e1}^{1/4}\phi^{-1/3}$. Since the dependence of the solution viscosity on the tube diameter is $\eta \sim a^{-4}$, the viscosity decreases by a factor of $\lambda^2 \approx N_{e1}\phi^{-4/3}$.

Further change is expected following the elongation of strands by disentanglement, which in turn decreases the viscosity by increasing the effective tube diameter. At the same time, the concurrent lateral network contraction, resulting from axial stretching,[18] may have an opposite effect because of a reduction in the deformation factor in the lateral direction. Also, while the longer chains in the population retain the continuity of the network, disentangled shorter chains effectively reduce viscosity. Finally, rapid evaporation, characteristic of electrospinning, increases the concentration and consequently the solution viscosity.

ACKNOWLEDGMENTS

The authors gratefully acknowledge the vital part of Dr. Ulrike Wangenheim in executing the short nanofibers experiment and the preliminary observations, and the valuable advice and support of Prof. Robert H. Schuster in planning the experiment, both from the Deutsches Institut für Kautschuktechnologie in Hannover, Germany. We thank Ron Avrahami from the Technion for assistance in carrying out the experiment. We acknowledge Dr. Arkadii Arinstein from the Technion for insightful discussions on polymer dynamics. We gratefully acknowledge the financial support of the United States-Israel Binational Science Foundation (BSF Grant 2006061), the RBNI−Russell Berrie Nanotechnology Institute, and the Israel Science Foundation (ISF Grant 770/11).

REFERENCES AND NOTES

1 C. J. Luo, E. Stride, S. Stoyanov, E. Pelan, M. Edirisinghe, *J. Polym. Res.* **2011**, *18*, 2515–2522.

2 A. Sutti, T. Lin, X. G. Wang, *J. Nanosci. Nanotechnol.* **2011**, *11*, 8947–8952.

3 K. Mukhopadhyay, C. D. Dwivedi, G. N. Mathur, *Carbon* **2002**, *40*, 1373–1376.

4 S. L. Shenoy, W. D. Bates, H. L. Frisch, G. E. Wnek, *Polymer* **2005**, *46*, 3372–3384.

5 S. Megelski, J. S. Stephens, D. B. Chase, J. F. Rabolt, *Macromolecules* **2002**, *35*, 8456–8466.

6 P. Gupta, C. Elkins, T. E. Long, G. L. Wilkes, *Polymer* **2005**, *46*, 4799–4810.

7 A. J. Guenthner, S. Khombhongse, W. X. Liu, P. Dayal, D. H. Reneker, T. Kyu, *Macromol. Theory Simul.* **2006**, *15*, 87–93.

8 A. Arinstein, E. Zussman, *Phys. Rev. E* **2007**, 76.

9 U. Stachewicz, R. J. Bailey, W. Wang, A. H. Barber, *Polymer* **2012**, *53*, 5132–5137.

10 Available at: www.surface-tension.de. **2006**, accessed on February 2013.

11 Available at: http://www.smartmeasurement.com. 2001–2002, accessed on February 2013.

12 J. E. Mark, Physical Properties of Polymers Handbook; AIP Press: Woodbury, N.Y., **1996**.

13 M. Selvakumar, D. K. Bhat, N. G. Renganathan, *J. Appl. Polym. Sci.* **2009**, *111*, 452–460.

14 M. Rubinstein, R. H. Colby, Polymer Physics; Oxford University Press: Oxford; New York, **2003**.

15 G. Taylor, *Proc. R. Soc. London Ser. A: Math. Phys. Sci.* **1966**, *291*, 145–158.

16 H. L. Cox, *Br. J. Appl. Phys.* **1952**, *3*, 72.

17 A. Kelly, W. R. Tyson, *J. Mech. Phys. Solids* **1965**, *13*, 329–350.

18 I. Greenfeld, A. Arinstein, K. Fezzaa, M. H. Rafailovich, E. Zussman, *Phys. Rev. E* **2011**, *84*, 041806.

19 Y. H. Wen, C. C. Hua, *J. Rheol.* **2009**, *53*, 781–798.

20 L. A. Archer, *J. Rheol.* **1999**, *43*, 1617–1633.

21 D. W. Mead, R. G. Larson, M. Doi, *Macromolecules* **1998**, *31*, 7895–7914.

22 V. R. Mhetar, L. A. Archer, *J. Polym. Sci. Part B: Polym. Phys.* **2000**, *38*, 222–233.

23 W. W. Zuo, M. F. Zhu, W. Yang, H. Yu, Y. M. Chen, Y. Zhang, *Polym. Eng. Sci.* **2005**, *45*, 704–709.

24 M. M. Hohman, M. Shin, G. Rutledge, M. P. Brenner, *Phys. Fluids* **2001**, *13*, 2201–2220.

25 Y. M. Shin, M. M. Hohman, M. P. Brenner, G. C. Rutledge, *Polymer* **2001**, *42*, 9955–9967.

26 E. Zussman, D. Rittel, A. L. Yarin, *Appl. Phys. Lett.* **2003**, *82*, 3958–3960.

27 H. Fong, I. Chun, D. H. Reneker, *Polymer* **1999**, *40*, 4585–4592.

28 H. Fong, D. H. Reneker, *J. Polym. Sci. Part B: Polym. Phys.* **1999**, *37*, 3488–3493.

29 D. H. Reneker, A. L. Yarin, H. Fong, S. Koombhongse, *J. Appl. Phys.* **2000**, *87*, 4531–4547.

30 I. Greenfeld, K. Fezzaa, M. H. Rafailovich, E. Zussman, *Macromolecules* **2012**, *45*, 3616–3626.

31 V. N. Kirichenko, I. V. Petrianovsokolov, N. N. Suprun, A. A. Shutov, *Doklady Akademii Nauk SSSR* **1986**, *289*, 817–820.

32 A. F. Spivak, Y. A. Dzenis, *Appl. Phys. Lett.* **1998**, *73*, 3067–3069.

33 M. M. Hohman, M. Shin, G. Rutledge, M. P. Brenner, *Phys. Fluids* **2001**, *13*, 2221–2236.

34 F. J. Higuera, *J. Fluid Mech.* **2006**, *558*, 143–152.

35 S. N. Reznik, E. Zussman, *Phys. Rev. E* **2010**, *81*, 026313.

36 A. Theron, E. Zussman, A. L. Yarin, *Nanotechnology* **2001**, *12*, 384–390.

37 S. Y. Gu, J. Ren, *Macromol. Mater. Eng.* **2005**, *290*, 1097–1105.

38 M. G. McKee, G. L. Wilkes, R. H. Colby, T. E. Long, *Macromolecules* **2004**, *37*, 1760–1767.

39 S. Kedem, J. Schmidt, Y. Paz, Y. Cohen, *Langmuir* **2005**, *21*, 5600–5604.

40 S. Kidoaki, K. Kwon, T. Matsuda, *J. Biomed. Mater. Res. Part B: Appl. Biomater.* **2006**, *76B*, 219–229.

41 S. C. Baker, N. Atkin, P. A. Gunning, N. Granville, K. Wilson, D. Wilson, J. Southgate, *Biomaterials* **2006**, *27*, 3136–3146.

42 Y. Ji, C. Li, G. Wang, J. Koo, S. Ge, B. Li, J. Jiang, B. Herzberg, T. Klein, S. Chen, J. C. Sokolov, M. H. Rafailovich, *Europhys. Lett.* **2008**, *84*, 56002.

43 M. Burman, A. Arinstein, E. Zussman, *Appl. Phys. Lett.* **2008**, *93*, 193118.

44 A. Arinstein, M. Burman, O. Gendelman, E. Zussman, *Nat. Nanotechnol.* **2007**, *2*, 59–62.

45 E. Zussman, A. Arinstein, *J. Polym. Sci. Part B: Polym. Phys.* **2011**, *49*, 691–707.

46 R. Ravichandran, J. R. Venugopal, S. Sundarrajan, S. Mukherjee, R. Sridhar, S. Ramakrishna, *Nanotechnology* **2012**, 23.

47 M. Rubinstein, S. Panyukov, *Macromolecules* **2002**, *35*, 6670–6686.

6. Discussion and conclusions

Research scope. An extensional flow of a semi-dilute polymer solution under a high strain rate can cause substantial stretching and disentanglement of the polymer network. The theoretical and experimental investigation conducted in this research uses the technique of electrospinning, a flow with high strain rate and rapid evaporation, to study the effects of such a strong extensional flow on the dissolved polymer network. Electrospun polymer nanofibers are of particular interest, in view of their small size and broad potential applications in engineering and life sciences. Their unique mechanical properties, such as a size-dependent elasticity which rises highly above that of bulk material, and the need to explain these properties, provide the incentive for this research.

In this work, the dynamic evolution of the entangled polymer network in an electrospinning jet was modeled and simulated, predicting substantial longitudinal stretching and radial contraction of the network, a transformation from an equilibrium state to an almost fully-stretched state (Section 5.1). X-ray phase-contrast imaging of electrospinning jets verified this prediction, observing an onset of polymer concentration increase at the jet center, close to the jet start (Section 5.2). Scanning near field optical microscopy (SNOM) of electrospun conjugated optically active polymer nanofibers revealed a dense elongated molecular conformation at the fiber core, confirming that the stretched structure remains after jet solidification (Section 5.3). The stretching dynamics of such conjugated polymers was analyzed by generalizing the theoretical model and simulation to semi-flexible polymer chains, allowing quantification of the various effects of electrospinning and their validation by SNOM (Section 5.4). Finally, the effect of the high strain rate on polymer entanglement loss was evidenced in jet fragmentation and appearance of short nanofibers, which compared well with a disentanglement model (Section 5.5). The main consequence of the study is better understanding of the mechanisms leading to the observed molecular structures of nanofibers, with the goal of providing a quantitative explanation for their unique mechanical properties.

Polymer dynamics during electrospinning (Section 5.1). Polymer chains dissolved in a sufficiently concentrated semi-dilute solution create an entangled network (Figure 5.1-2), a prerequisite for the polymer solution successful spinability. Given the solution concentration, the network mesh size (i.e., average subchain length) is determined, allowing the modeling of the network as a 3D beads and

springs lattice, where each bead represents the mass and volume of a subchain, and the springs represent the linear entropic elasticity of the subchains connected to each bead. Using the known rheology of electrified jets, the dynamics of such a network can be described by difference-differential equations. The solution predicts an affine stretching of the network, presented in Equation (5.1-12) and depicted by the dot-dashed line in Figure 5.1-3. Random walk simulations expand the analysis to large chain elongations with non-linear elasticity, and shows that the subchains approach full extension not far (<1 mm) from the jet start (the dashed line in Figure 5.1-3). The criterion established for such full extension is when the jet velocity rises above its initial value by a factor equal to the square root of the number of monomers in the subchain (p. 58) (equivalently, equal to the inverse of the polymer volume fraction).

The transformation of subchains from a coil-like equilibrium state into a stretched state occurs as a continuous crossover, and no phase transition is observed, in contrast to the well-known coil stretch transition in unentangled chains (Sections A.3 and 4.1.4). The dominant local force on a subchain is the elastic force arising from the action of the linked subchains, whereas the local hydrodynamic forces, whose accumulation along the network gives rise to the global elastic stretching, are negligible. Theoretically, in view of the analogy between a vertical sequence of subchains in a network and a very long chain, discussed in Section 4.1.5, a network stretch transition is possible if the jet strain rate is very low (see left curve in Figure 4-16); however, under such conditions, the flow will be dominated by viscosity and network relaxation rather than elasticity.

The strong increase in the longitudinal mesh size results in a decrease in the radial mesh size, due to redistribution of the random walk stepping probabilities (the solid line in Figure 5.1-3). The result is a lateral contraction of the network toward the jet center, simulated in Figure 5.3-4 and Figure 4-21(a), which is proportional to the decrease in the subchains radial mesh size (Figure 5.1-4). This particular outcome was validated by X-ray absorption measurements of electrospinning jets, which indicated a significant increase in polymer concentration close to the jet center (Figure 5.1-6).

The validity of the network modeling is restricted to the initial stage of the jet (first few millimeters), where elastic elongation is still possible, and therefore the model does not describe the final state of the polymer matrix in electrospun nanofibers. Additional processes, such as rapid evaporation and entanglement loss, which can result in chain relaxation, are not accounted for in the model, and are further investigated in later sections. Nevertheless, the results strongly indicate non-

equilibrium, ordered nanostructures that could remain in the nanofibers after solidification, structures which may set a new internal scale, and affect the nanofiber elasticity through confinement.

The random walk simulation, developed specifically for this research (Section 4.1), provides a flexible and effective tool for analysis and visualization of polymer networks and individual chains in high strain rate flows. The tool was used extensively to investigate the conformation of the polymer chains and the network during electrospinning, under varying process variables such as molar mass, flow strain rate, and solution viscosity. It is shown that, although several simplifications were applied in the simulation, the use of an effective potential field induced by the flow represents well the physics of the polymer chains.

X-ray imaging of electrospinning jets (Section 5.2). The theoretically predicted longitudinal stretching and lateral contraction of the polymer network, as well as the additional effects of rapid evaporation, were investigated experimentally by fast X-ray, phase-contrast, high-resolution imaging of the first 10 mm of electrospinning jets, using solutions of PEO and PMMA.

The power law jet rheology [Equations (5.2-4) and (5.2-5)], assumed in the theoretical model, was validated by detailed measurements of the jet profile under a wide range of electrospinning conditions and polymer solutions, demonstrating that the jet diameter narrows faster under higher electric fields, lower flow rates, and lower polymer concentrations (Figure 5.2-9). Comparison of velocity measurements obtained by particle tracing velocimetry to estimates based on volume conservation assumption, showed an abrupt deviation 1-2 mm from the jet start, a possible indication for full extension of the network that retards the jet velocity, as well as an indication for a substantial mass loss due to evaporation (Figure 5.2-12). The flow regime inside the jet was found to be laminar, with observed streamlines [Figure 5.2-13] and an almost uniform vertical velocity across the jet (Figure 5.2-14).

Taking advantage of the different X-ray mass absorption coefficients of the polymer and solvent, variations in polymer concentration were observable by mapping the variations in X-ray absorption along and across the jet. Concentrations were found to rapidly increase below a critical jet radius of ~25 μm (equivalent to radius reduction ratio of 0.2) (Figure 5.2-16), a possible evidence for full network extension and of rapid evaporation that occurs much earlier than theoretical predictions found in the literature. The estimated mass loss rate due to evaporation was found to be proportional to the inverse square of the radius reduction ratio

[Equation (5.2-6)]. Concentration variation across the jet revealed high concentrations at the jet boundary due to evaporation, as well as a concentration rise at the jet center within ~1 mm from the jet start (Figure 5.2-17), in agreement with our model and simulation.

Evaporation becomes dominant when stretching is weaker (e.g. at lower electric field and/or higher flow rate), reducing or canceling the concentration peaks measured at the jet center (Figure 5.2-18). Such tuning of parameters demonstrates the balance between the effects of evaporation and stretching, which determines the polymer network non-equilibrium conformation during electrospinning, and explains the diversity of macrostructures and properties found in solid nanofibers (see examples in Figure 5.1-1). Specifically, dominant stretching is expected to yield uniform structures with axially oriented molecules and better mechanical properties, whereas dominant evaporation may result in porous nonuniform structures.

The technique of X-ray imaging during electrospinning was specifically developed for this research, including the algorithms and methods for processing and analyzing the recorded data (Section 4.2). These experiments provided information on internal flow and concentration variations unattainable by other in-situ measurement methods. Fast X-ray phase contrast imaging provides high penetrability at very short exposures, allowing absorption measurements of the unsteady jet, as well as enhanced phase boundary contrast, allowing high resolution viewing of the narrow jet and particles within it.

Fiber nanostructure and mechanical properties (Section 5.3). The theoretical and experimental results presented so far apply to the first stage of the electrospinning jet. The gradual solidification of the jet during the further stages, which results in viscosity increase, crystal growth, and partial relaxation of chains from their non-equilibrium state back toward their coil state, raises a key question whether the beneficial outcome of stretching and molecular packing remains in the solid fiber.

The opportunity presented itself in electrospinning of the conjugated polymer MEH-PPV. This optically active, electrically conductive polymer is of high interest because of its potential applications in semi-conducting devices such as field effect transistors, light emitting diodes, and active layer in lasers. Two properties make this polymer an excellent candidate for examining the posed question. First, MEH-PPV has high absorption in the visible waveband [Figure 5.4-S1(a)], specifically around the wavelength of the laser used in the experiment, lending itself to optical probing.

Second, conjugated polymer chains are not flexible, as in freely jointed chains, but are rather semi-flexible as a result of the high bending rigidity of the chain backbone, which is composed of alternating single and double covalent bonds. Owing to inherent bonding defects, which substitute rigid conjugated links by flexible tetrahedral links, the conjugated chains can be described as flexible chains having longer Kuhn (rigid) segments [Figure 5.4-3(c)]. Consequently, as shown by our generalized modeling and simulation (more details later), the stretching and lateral contraction phenomena should be more pronounced in this class of polymers.

Measurements by high resolution, scanning near-field optical microscopy (SNOM) revealed a core-sheath structure, in which the fiber core has a higher density, whereas closer to the fiber boundary the density is lower (Figure 5.3-3). This observation was strengthened by force-indentation measurements of the elastic modulus at the cross-section of the fiber, using atomic force microscopy (AFM), which showed a higher modulus at the fiber center with respect to the boundary (Figure 5.3-2), indicative of higher density and possibly molecular ordering. These results confirm that the close-packed molecular conformation of the polymer network in the liquid jet, demonstrated by the simulation of the semi-flexible conjugated polymer (Figure 5.3-4), is essentially retained in the solid fiber.

In perspective, the found graded-density internal structure can possibly improve charge transport by the fiber core, whereas the lower density sheath can determine the amplification of light guided in the fiber. Similarly, for scaffold applications, the core can provide the needed strength, rigidity, and conductivity, while the boundary layer has enhanced material absorption and adhesion properties.

Control of chain orientation in fibers (Section 5.4). A valid concern is whether the observed dense region at the fiber core consists of an ordered structure or an amorphous structure. In an ordered structure, the mechanical properties of the nanofiber should be improved with respect to bulk material. Moreover, in conjugated polymers such as MEH-PPV, ordering and orientation of chain sections results in a longer effective conjugation length, and consequently longer chromophores (chain parts responsible for color absorption or excitation) and improved optical and electrical properties. We exploited the unique optical properties of conjugated polymers to investigate this concern by measurements of optical absorption and polarization modulation.

The most common process used in producing conjugated polymer macrostructures is spincasting. Electrospinning of conjugated polymers is usually

avoided due to their low miscibility, or carried out by mixing other polymers in the solution or by using the core-shell technique. However, while amorphous aggregation of the polymer is favored in films, the elongational dynamics of electrospinning leads to extended structures having interchain alignment. Measurements of the absorption spectra of nanofibers, compared to those of spincast films, showed a peak red shift [Figure 5.4-S1(a)], which indicates an increase of the effective conjugation length attributable to a more ordered molecular packing. Additionally, the absorption and photoluminescence linear dichroism spectrums [Figure 5.4-S1(b,c)], measured on uniaxially aligned MEH-PPV nanofibers, evidence a predominance for light polarized along the fiber longitudinal axis, a fingerprint of a preferential alignment of the polymer backbones along the fiber length.

The nanoscale mapping of the local dichroism of individual fibers, measured by polarized near-field optical microscopy [Figure 5.4-1(c) and Figure 5.4-S2], unveiled for the first time the presence of an internal spatial variation of the molecular order [Figure 5.4-1(d,e)]. Specifically, these results confirm the presence of a core (of width ~40% of fiber diameter) with axially aligned molecules, and reveal a sheath (envelope) with almost radially oriented molecules. The unexpected radial orientational preference in the fiber sheath is attributed to relaxation of polymer chains in the lower density region, combined with radial crystallic growth.

A key question is how and to what extent the process can be controlled in order to achieve desired nanostructures within the fiber. For that purpose, the polymer network dynamic model and simulation, described in Section 5.1, were generalized by tuning the degree of chain flexibility with the segmental aspect ratio (i.e., the number of monomers in a segment). Thus, the generalized model applies to a wide range of linear flexible polymers, including conjugated polymers with different bonding defect concentrations, as well as fully flexible polymers that are a particular case of the model in which the segmental aspect ratio is 1.

When the aspect ratio is larger (lower defects concentration), the subchains become shorter and more rigid, in other words the network mesh size is smaller [Figure 5.4-2(a)]; specifically, the number of subchain segments is reduced by a power of 4 of the aspect ratio [Equation (5.4-1)]. When the polymer volume fraction is sufficiently high, subchains start to interact within a single correlation volume (explained in Section A.2), a condition not existing in fully flexible chains, thereby enhancing the likelihood of nematic ordering and molecular orientation [Figure 5.4-2(b)]. The results of the model and simulation for a representative conjugated polymer

(10% defects concentration) are presented in Figure 5.4-2(c), and typical free and extended chain conformations are depicted in Figure 5.4-3, exhibiting a similar behavior as in fully flexible chains, but with a strong dependence on the aspect ratio.

The model predicts that full extension of the network occurs at an earlier stage of the jet when the concentration, molar mass, and solvent quality are lower, accounting for lower network entanglement [Figure 5.4-4(a)]. Specifically, the jet position where subchains approach full extension is proportional to the polymer volume fraction by the power of 1.8 and the molar mass by the power of 1.5 [Equation (5.4-2)]. Under favorable stretching conditions that expedite full network extension, it is more likely that the extended conformation, and the associated axial molecular alignment, will partially remain in the polymer structure after solidification. Indeed, the measured far-field, macroscale emission from fibers was found to be polarized along the longitudinal axis of the nanostructures, with a degree of polarization dependent on process variables. Specifically, the photoluminescence polarization ratio increased up to 5 times the ratio of amorphous polymer, by gradually decreasing the solution concentration down to a volume fraction of 0.03 [Figure 5.4-4(b,e)], a clear indication for the inverse dependence of the longitudinal molecular alignment on concentration. Thus, the confirmed model provides tools for tailoring of the photophysical properties of the fibers.

Entanglement loss and short nanofibers (Section 5.5). As already pointed out, the validity of the network modeling is restricted to the initial stage of the jet, where elastic elongation is still possible and the network can be assumed to maintain its degree of entanglement. However, the effects of entanglement loss due to the high strain rate cannot be neglected when considering the final polymer conformation. When carrying out the electrospinning process to its extreme conditions, jet fragmentation (Figure 5.5-2 and Figure 5.5-3) was observed in the appearance of short nanofibers (Figure 5.5-1), allowing quantification of the polymer entanglement loss under a high strain rate extensional flow.

Using PMMA of several molar masses, dissolved at different concentrations in solvent blends of varying quality, and tuning the electric field intensities and flow rates, the occurrence of short nanofibers, as well of that of beads-on-string, was clearly identified and mapped (Figure 5.5-7). Also, the dependence of the short nanofiber length and diameter on the material and process variables was characterized in the form of scaling expressions [Figure 5.5-11 and Equations (5.5-4) and (5.5-5)]. Short nanofibers appeared at solution concentrations slightly above the entanglement

concentration, when the electric field intensity was high and the flow rate low. In other words, short nanofibers appeared, and their length was shorter, when the polymer molar mass, concentration, and solvent quality were lower and the flow strain rate was higher. Under such favorable low entanglement and high stretching conditions, the elastic extension of the polymer network accelerates the entanglement loss, eventually leading to separation of the network and fragmentation of the jet.

Using the known jet rheology and the premise of affine extension of the polymer network, a disentanglement model was developed. The underlying assumption is that the entanglement nodes are moving at the same velocity as the jet, while chains are allowed to disentangle but remain highly stretched [Figure 5.5-13 and Equation (5.5-9)]. The experimental results and theoretical predictions correlate well (Figure 5.5-14), confirming the proposed disentanglement mechanism.

An important outcome of the analysis is the dependence of the fiber diameter on the material and process parameters, identifying the conditions that lead to the minimal possible radius (Figure 5.5-15). The diameter of short nanofibers grows weakly with increasing relative concentration, while their length grows sharply. When the concentration is increased beyond a transition point, continuous nanofibers are created and the diameter's growth slope increases abruptly. While the diameter of a continuous nanofiber depends on the solution's relative concentration by a power of 2.4, the corresponding power in short nanofibers is only 0.17, marking a distinct transition between the two morphologies [Equations (5.5-21) and (5.5-19), respectively]. The reason for these differences is that in continuous nanofibers, the process of disentanglement is not carried out until complete separation of the polymer network as in short nanofiber, since it is terminated at the collector, and therefore the amount of entanglement loss, and hence the diameter, depend on the flow dynamics and the electrodes gap size.

The high elastic stretching and entanglement loss required to create short nanofibers are likely to lead to an ordered, aligned solid nanostructure with improved mechanical properties. At the same time, since fragmentation occurs before full solidification, the polymer network may partially relax in solvent rich areas and leave voids in the polymer matrix. Hence, a nonuniform structure can result in both the axial and radial directions, with regions of aligned rigid structure and regions of amorphous porous structure. The prospect of nanofiber size tuning, and hence their morphology, in accordance with Equations (5.5-4,5,15,18,20), can be exploited to improve their as-spun mechanical and thermodynamic properties, such as the elastic

modulus. Combined with the possible biaxial nonuniform nanostructure, it may find interesting applications in tissue engineering, drug delivery, composites reinforcement, filtration, electrical and thermal conduction, and light amplification.

Perspective on nanofibers elasticity. This research focused on the analysis of the polymer matrix conformation during a strong extensional flow of a polymer solution, using the technique of electrospinning as a test bed. When stretching is dominant, the structures revealed in electrospun nanofibers are dense and ordered, with a preference for molecular alignment along the fiber longitudinal axis, and chains are partially disentangled from the matrix. Although the question why nanofiber elasticity is size-dependent is left outside the scope of this thesis, it can be put in general perspective.

The increase in elastic modulus as the nanofiber diameter becomes smaller is well established experimentally (Figure 2-10). Also, we showed how the nanofiber diameter can be tuned by modifying the material and process conditions, such as the molar mass, concentration, electric field, and electrodes gap [Figure 5.5-15 and Equation (5.5-20)]. The diameter can be decreased by this method to the point just before fragmentation, resulting in the smallest achievable fiber diameter in given conditions, and potentially yielding the highest modulus possible for these conditions.

The anisotropic molecular orientation in itself provides only a partial explanation for the size-dependent elasticity. Indeed, substantial molecular orientation was observed in nanofibers (Figure B-9), especially when the strain rate of the electrospinning jet was high, as for example achieved by reducing the concentration [Figure 5.4-4(b,e)]. Molecular orientation is known to increase the elastic modulus when chains can be extended freely, as in the case of rubber under high elongation (Figure A-12), when chains are fully extended in crystallic structures (Figure A-14), or when chains are extended by mechanical drawing (Figure A-13). However, the modulus change in these cases is not size-dependent.

On the other hand, rigid supramolecular structures, created by correlation between neighboring polymer segments, may be of the same size scale as the fiber diameter (Figure 2-11), and can cause an increase in the effective elastic modulus as a result of confinement. However, the confinement approach overlooks the question how specific fiber diameter and internal morphology were reached. The fiber diameter expression in Equation (5.5-20) reveals that a desired fiber diameter can be reached by different combinations of material and process conditions. For example, increasing the molar mass, while decreasing the concentration and/or increasing the electrodes

gap distance, can result in the same fiber diameter. More importantly, the molecular structure within the nanofiber can be different, as illustrated in Figure 6-1, when electrospun under different conditions. For example, at a given fiber diameter, a subchain between 2 entanglements in the solid matrix is longer (equivalently, the number of entanglements per unit volume is lower) when the fiber is electrospun from a higher-concentration solution [can be derived from Equation (5.5-17)].

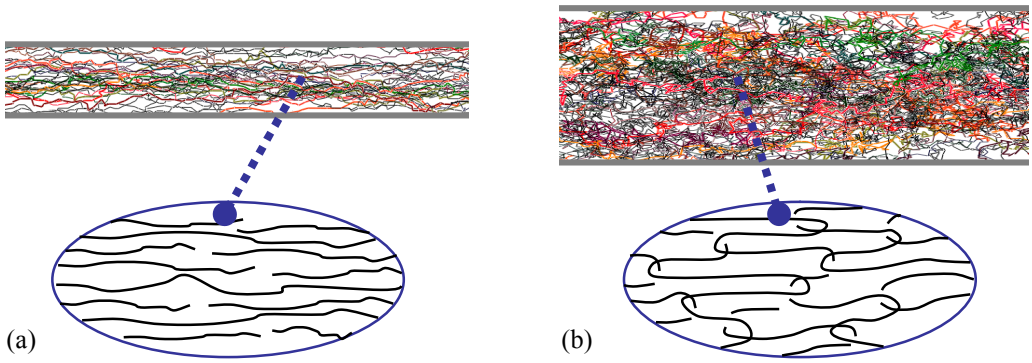

Figure 6-1. Illustration of possible molecular structures in electrospun nanofibers. (a) Unentangled chains, expected in short nanofibers. (b) Entangled chains, typical of continuous nanofibers.

Furthermore, the subchain length is inversely proportional (equivalently, the entanglements density is proportional) to the fiber diameter squared, a similar diameter dependence to that of the elastic modulus in Figure 2-10. Regarding the entanglements in the solid matrix as elastically compliant locally, nanofibers with longer subchains (equivalently, lower entanglements density) may be expected to have a higher tensile modulus. Unlike rubber whose subchains are more flexible when they are longer, the elasticity of subchains below the glass transition temperature is not entropic. Rather, the elasticity depends on the orientation and elastic compliance of the chains' backbone bonds and interchain interactions, and therefore the determining factor could possibly be the entanglements density. The situation is analogous to the increase in modulus when reinforcing a compliant polymer matrix with stiff elongated fibers, and should also impact other mechanical properties such as strength.

This logic quantitatively links the electrospinning conditions to both the fiber diameter and the solid nanostructure, and provides a pathway for future investigation of the link between the nanostructure and the elastic modulus, thereby getting closer to answering the question how electrospinning affects nanofiber elasticity.

Appendix A. Background on polymer structure and elasticity

The physics of polymers deals with the static and dynamic conformation of polymer molecules in various states, and is described in books by notable researchers: Flory *Polymer Chemistry*[76], De Gennes *Scaling concepts in polymer physics*[20], Rubinstein *Polymer physics*[21], Grosberg *Statistical physics of macromolecules*[22], and Graessley *Polymeric liquids & networks: dynamics and rheology*[77]. The scientific foundation for the mechanical properties of solid polymers is described in the books by Arridge[17], Nielsen[18] and Ward[19]. The following review provides the basic concepts of polymer physics and is based mainly on these references.

A.1 Single chain conformation

A **polymer** is a very large molecule or macromolecule, consisting of many repeating units (monomers) joined by covalent chemical bonds (Figure A-1). A polymer molecule may have branches of various formations, or can be a long linear chain. For simplicity, the following review deals with linear chains.

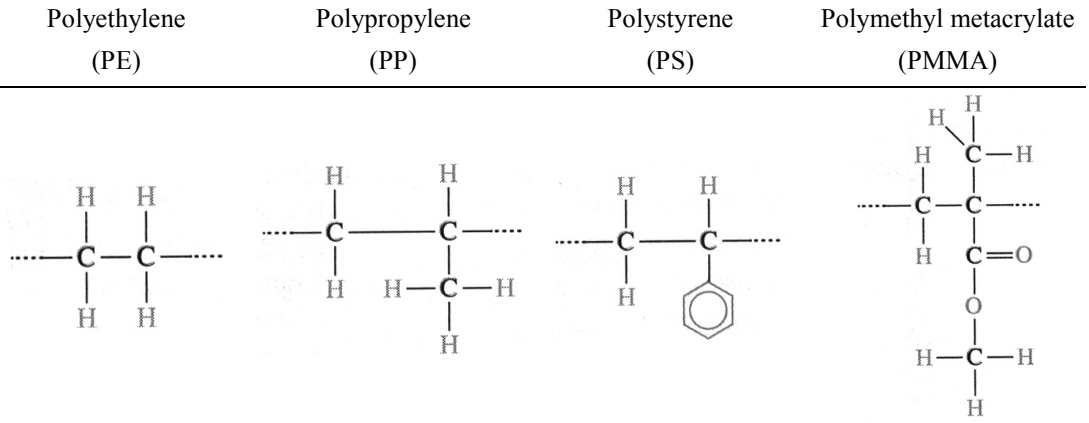

Figure A-1. Examples of synthetic polymers and their repeating units (monomers). Based on ref[78].

The number of monomers N in a single macromolecule, called the polymer degree of polymerization, can reach the order of 10^5, with molar masses ranging from 10^4 to 10^6 g/mol. A monomer may consist of several backbone atoms (usually carbon), with two hydrogen atoms bonded to each carbon atom. Some of the hydrogen atoms are replaced by side groups, such as the CH_3 group (methyl) in PP and the Benzene ring in PS (Figure A-1), affecting the polymer properties. The number of backbone atoms in a single macromolecule is designated as n.

Polymer chains are flexible, and therefore can adopt varied conformations of statistical nature, occupying a volume much larger than the volume of their

constituents. **Flexibility** is due to the variation in the torsion (rotation) angle φ *o*f the carbon-to-carbon (C-C) covalent bonds (Figure A-2). While the bond tetrahedral angle θ is almost constant at 68°, the torsion angle may be in one of three different states – *Gauche*$_-$, *Gauche*$_+$, and *Trans* (rigid), depending on the energy difference $\Delta\varepsilon$ between these states, the energy barrier ΔE between them, and the thermal energy k_BT (k_B - Boltzmann constant, T - temperature). $\Delta\varepsilon$ determines the static flexibility, while ΔE the dynamic flexibility, or the characteristic time for transition between the states.

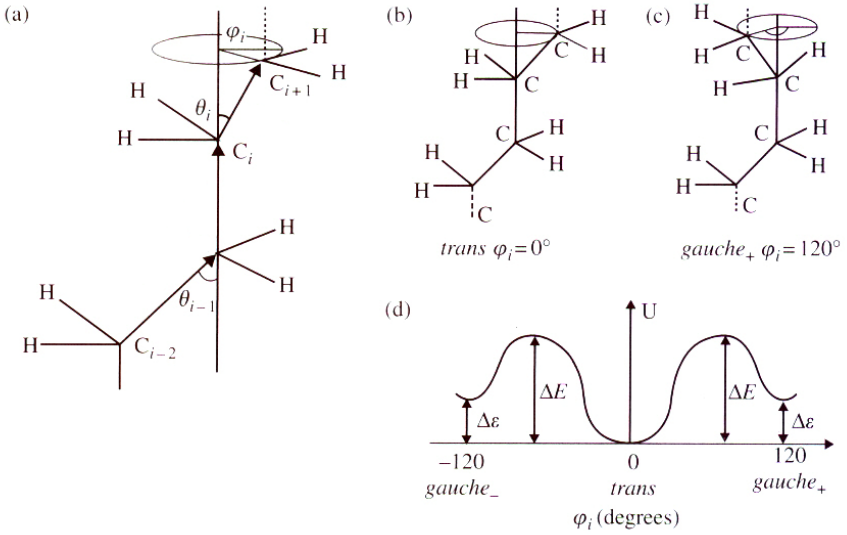

Figure A-2. Bond flexibility due to variation in torsion angles: (a) Tetrahedral angle θ and torsion angle φ for a sequence of three backbone bonds, (b) Trans state, (c) Gauche$_+$ state, and (d) torsion angle energies.[21]

At a small scale, segments of the chain may be rigid, with a characteristic length, the persistence length, given by

$$l_p = le^{\Delta\varepsilon / k_BT}, \tag{A.1}$$

where l is the length of the C-C bond, equal to 1.54 Å.[20] Assuming the conditions for flexibility exist, the persistence length may be assumed as the monomer size. At a larger scale than l_p, the chain may be considered as flexible. Thus, even though the chain depends locally on its chemical properties, globally it depends on physical observable properties such as chain length and concentration.

A polymer chain often possesses the property of self-similarity, or **scale invariance**, up to a certain degree of magnification (Figure A-3). This property enables universal scaling laws, such as the power dependence of the chain average coil size on the number of monomers, as shown in Equations (A.5) and (A.10).

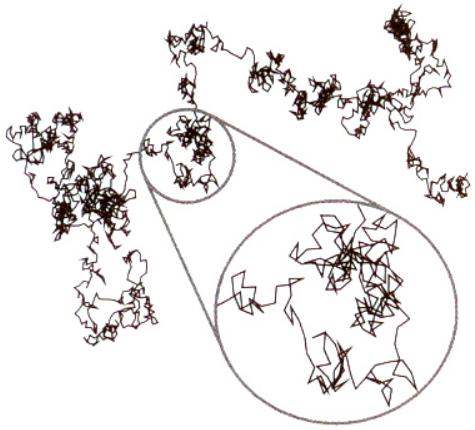

Figure A-3. Computer simulation of a polymer chain, showing the self-similarity or scale invariance of the chain.[21]

When the interactions between distant monomers of a chain in a solution (a mixture of polymer and solvent) are ignored (or balanced), the polymer chain is called an **ideal chain**. The mean-square end-to-end distance R_0 of a linear ideal chain is

$$\left\langle R_0^{\,2} \right\rangle \cong C_\infty n l^2 = N_k l_k^2 \equiv N a^2, \quad \text{and therefore} \quad R_0 = a N^{1/2}, \tag{A.2}$$

where n is the number backbone bonds, l the bond length, and C_∞ Flory's characteristic ratio for long chains, which accounts for the fact that adjacent atoms are not freely jointed but are rather bound to the possible states of the bond angles.[21] The values of the dimensionless factor C_∞ range from 5 to 10 for typical long chains.

The length l_k is defined as the **Kuhn segment** (also called Kuhn length or Kuhn monomer), and the number of Kuhn segments in the chain is N_k, thus rendering the chain as freely jointed with the same end-to-end distance. The size of a Kuhn segment is from 0.8 to 1.8 nm for typical polymers. The Kuhn segment approach takes into account the details of the local restricted bond angles and the steric hindrance (restrictive effect of polymer side groups), and is therefore more accurate and measurable than the persistence length approach.[22]

For simplicity, as shown in the rightmost expression of Equation (A.2), we define a as the length of a reference rigid element:[21]

$$a \equiv l_k = \frac{\left\langle R_0^2 \right\rangle}{R_{\max}} = \frac{C_\infty l}{\cos(\theta/2)} \cong 1.17 C_\infty \cdot l, \tag{A.3}$$

and N as the number of such elements in the chain:

$$N \equiv N_k = \frac{R_{\max}^2}{\left\langle R_0^2 \right\rangle} = \frac{n\cos^2(\theta/2)}{C_\infty} \cong \frac{0.69}{C_\infty} n, \qquad \text{(A.4)}$$

where $R_{\max} = nl\cos(\theta/2)$ is the fully extended length of the chain. We shall use different names for a (sometimes referred to as b) – chain element, Kuhn segment, Kuhn monomer, or just monomer – but they all designate the smallest rigid element of the chain, and accordingly N is the number of such elements in a chain.

The mean-square **radius of gyration** R_g of a linear ideal chain is defined as the averaged square distance from all monomers to the polymer center of mass, and is a convenient measure for the polymer occupying size

$$\left\langle R_g^2 \right\rangle = Na^2/6, \quad \text{and therefore} \quad R_g = \frac{a}{\sqrt{6}} N^{1/2}. \qquad \text{(A.5)}$$

As an example, for a polystyrene chain of n = 40,000 backbone C-C bonds, with C_∞ = 9.5, l = 1.54 Å, and θ = 68° [21], we obtain: a = 1.76 nm, N = 2894, R_0 = 94.7 nm and R_g = 38.7 nm. In comparison, R_{max} = 6160 nm, much larger than R_0, and, if we ignore the correction factor C_∞, $R_0(C_\infty=1)$ = 30.8 nm, much smaller than R_0. Thus, the chain resembles a coil rather than a linear line. The relative sizes are illustrated in Figure A-4, where $\vec{R}$ is the end-to-end distance.

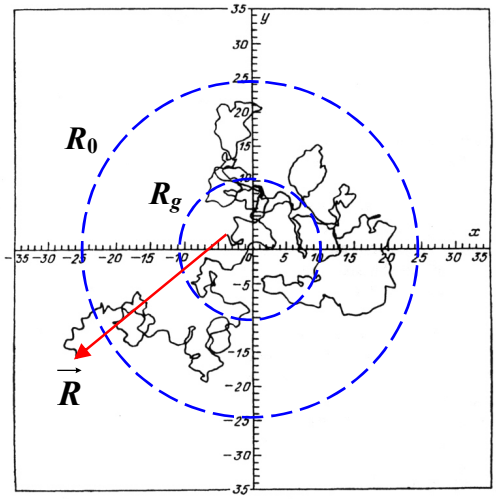

Figure A-4. Computer simulation of coil conformation of a single ideal chain of 626 freely jointed segments of unit length. Adapted from ref[22].

The statistical distribution of end-to-end distances $\vec{R}$ (in three dimensions) of a linear ideal chain, can be obtained by N steps of **random walk** (RW) of fixed step length a, where each step is independent and of the same probability in all directions.

Random walk on a Cartesian lattice can describe each possible chain conformation of a freely jointed chain, and therefore its statistics applies to long ideal chains. The result is a Gaussian distribution $P\left(\vec{R},N\right)$ of the three-dimensional end-to-end distance (Figure A-6):[21]

$$P\left(\vec{R},N\right)=\left(\frac{3}{2\pi R_0^2}\right)^{3/2}\exp\left(-\frac{3\vec{R}^2}{2R_0^2}\right) \quad \text{where} \quad R_0^2=Na^2 \,. \tag{A.6}$$

The distribution of each Cartesian component of $\vec{R}$ is normal, with mean at zero. The probability that the end-to-end distance $R=\left|\vec{R}\right|$ will be within a spherical shell of radius R and thickness dR is (depicted in Figure A-5)

$$P\left(R,N\right)4\pi R^2\mathrm{d}R=\left(\frac{3}{2\pi R_0^2}\right)^{3/2}\exp\left(-\frac{3R^2}{2R_0^2}\right)4\pi R^2\mathrm{d}R \,. \tag{A.7}$$

Equation (A.6) can also be obtained by solving the diffusion equation (or Schrödinger equation)[20, 22]

$$\frac{\partial P}{\partial N}=\frac{a^2}{6}\frac{\partial^2 P}{\partial R^2}-\frac{U(R)}{k_B T}P \,, \tag{A.8}$$

where the time t is replaced by the step number N, and the field potential $U(R)$ is nullified. Equation (A.8) has the benefit of providing an analytical solution for solvable boundary conditions and for a known (or estimated) mean field potential. In other cases, random walk simulations are useful, and were extensively used in this research, by applying an effective potential calculated from the local hydrodynamic and elastic forces acting on the polymer network during electrospinning (Sections 4.1 and 5.1[1]).

A **real chain** in a solution has interactions between distant monomers, expressed as repulsion between monomers, leading to swelling of the coil. At the same time, the elastic entropic forces of Equation (A.16) tend to draw the coil back to its Gaussian conformation. Additionally, monomer-solvent interaction forces are effective. When the attraction forces balance the effect of repulsion, the chain is nearly ideal, and the solvent is termed θ-solvent. A similar situation happens for chains in a polymer melt (a concentrated solution), where the repulsion forces due to interactions within the chain are balanced by the repulsion forces due to interactions with other chains in the melt.

If the repulsion is stronger than the attraction (good solvent), the chain tends to swell, while if it is weaker (poor solvent), the chain tends to contract. The Flory theory[79] for good solvent is based on equating the attractive and repulsive forces, yielding the Flory radius R_F (mean-square end-to-end distance) of

$$R_F \approx a\left(\frac{\mathrm{v}}{a^3}\right)^{2\nu-1} \cdot N^{\nu} \approx a\left(\frac{\mathrm{v}}{a^3}\right)^{1/5} N^{3/5}, \tag{A.9}$$

where v is the excluded volume parameter and ν is the Flory exponent.

If the attraction forces of monomer-monomer and monomer-solvent balance, leaving just the repulsive forces, the solvent is termed athermal solvent, $\mathrm{v}/a^3 \approx 1$, and the chain is a self-avoiding random walk (SAW, a walk that never visits the same site more than once) with radius

$$R_F \approx aN^{\nu} \approx aN^{3/5}, \quad \text{and} \quad R_g \approx \frac{a}{\sqrt{6}} N^{\nu}. \tag{A.10}$$

Using the same example as before, for a polystyrene chain of n = 40,000 C-C bonds, with $C_\infty = 9.5$, $l = 1.54$ Å, and $\theta = 68°$ [21], we obtain: R_F = 210 nm, compared to R_0 = 94.7 nm, a considerable swelling.

The statistical distribution $P(R,N)$ of end-to-end distances R of a long linear real chain is given by:[21]

$$\begin{aligned} P(R,N) &\sim \left(\frac{R}{R_F}\right)^{g} \exp\left[-\alpha\left(\frac{R}{R_F}\right)^{\delta}\right] \\ &\cong 0.278\left(\frac{R}{R_F}\right)^{0.28} \exp\left[-1.206\left(\frac{R}{R_F}\right)^{2.43}\right] \quad \text{where} \quad R_F \approx aN^{3/5}, \end{aligned} \tag{A.11}$$

and is compared (Figure A-6) to the Gaussian distribution of an ideal chain from Equation (A.6). There is a distinct difference between the distributions – while in ideal chains the most probable end-to-end distance is zero, in real chains it is seldom zero because of swelling.

The R_g Equations (A.5) and (A.10) for ideal and real chains were validated by various scattering experiments (light, small-angle X-ray, and neutron), such as Kirste et al.'s small-angle neutron scattering measurement of ideal chains in a melt of predeuterated PMMA[80], and Flory's light scattering measurement of real chains in a dilute solution[76].

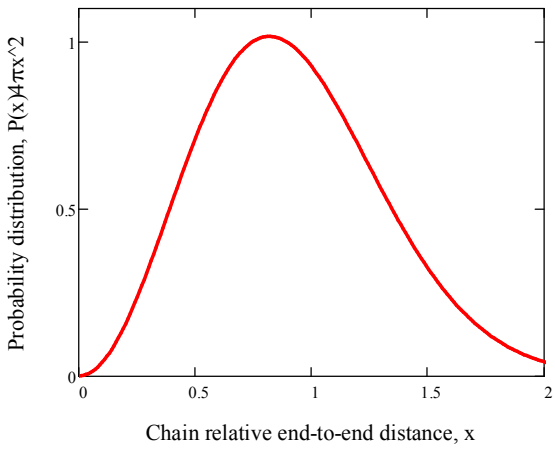

Figure A-5. Normalized probability distribution function of three dimensional relative end-to-end distances $x=R/R_0$ of long ideal chains (Equation (A.7)).

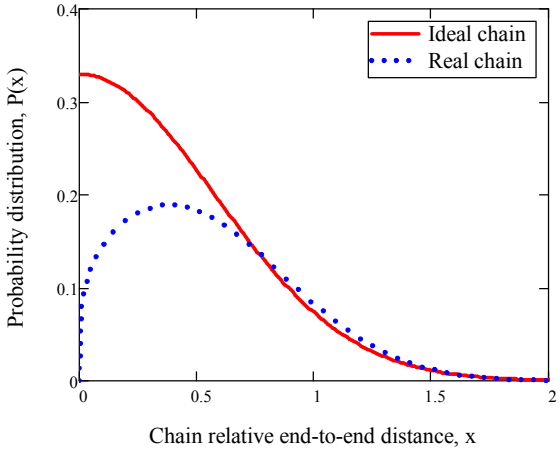

Figure A-6. Probability distribution function of 3D relative end-to-end distances $x=R/R_0$ and $x=R/R_F$ of long ideal chains (Equation (A.6)) and real chains (Equation (A.11)), respectively.

Equations (A.2) and (A.10) provide a good example of a **scaling law**, where the exponent ν is a universal parameter that depends only on the type of polymer solution, and is the same for all coils. The exponent ν varies between 1/3 (poor solvent) and 3/5 (more accurately 0.588) (good solvent), and equals 1/2 (θ-solvent) for an ideal chain. The constant pre-factor of these equations is not universal, and depends on the detailed structure of the solution.

A.2 Polymer network and dynamics

Of specific importance to electrospinning is the distinction between the types of **polymer solutions**, as depicted in Figure A-7. In a dilute solution, the chains do not overlap, while in a semi-dilute solution they overlap and create a mesh, a network that is essential for fabrication of continuous fibers by electrospinning. A single cell in a network mesh is called the correlation volume, by definition not invaded by chains.

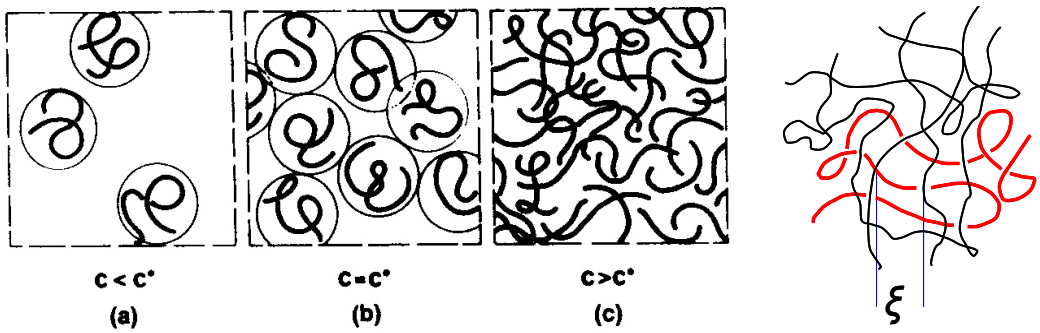

Figure A-7. Crossover between dilute and semi-dilute polymer solutions: (a) dilute, (b) onset of overlap (crossover concentration), and (c) semi-dilute,[20] and definition of the polymer network mesh size (correlation length) ξ.

As a result, semi-dilute polymer solutions are viscoelastic and exhibits both elastic behavior (resistance to static strain) and viscous behavior (resistance to strain rate) under deformation, and therefore their strain is time dependent. See more on this issue in Sections 2.1 and 2.2.

The crossover concentration c^* and the crossover volume fraction ϕ^* may be estimated as the monomers concentration inside a single coil of radius R (equal to R_0 for ideal chains or R_F for real chains)[20, 21]

$$c^* \cong N / R^3 \cong \frac{N^{1-3\nu}}{a^3} \quad \text{and} \quad \phi^* = c^* / \rho \cong N^{1-3\nu}, \tag{A.12}$$

where N is the number of monomers (chain elements, or the degree of polymerization of a linear chain), a is the monomer size, ν is the Flory scaling exponent, and $\rho \equiv a^{-3}$ the polymer density. The average mesh size ξ of the network (also called the correlation length) in a semi-dilute solution, or the distance between two topological interactions, is dependent on the coil radius R [mean-square end-to-end distance from Equation (A.10)] and the relative volume fraction ϕ / ϕ^*

$$\begin{aligned} \xi &= R\left(\frac{\phi}{\phi^*}\right)^m \cong aN^\nu\left(\frac{\phi}{N^{1-3\nu}}\right)^m \cong a\phi^{\nu/(1-3\nu)} \quad \text{or} \\ \xi &= R\left(\frac{\phi}{\phi^*}\right)^{\nu/(1-3\nu)} = R\left(\frac{c}{c^*}\right)^{\nu/(1-3\nu)}, \end{aligned} \tag{A.13}$$

where the exponent m is chosen so that R and ϕ^* are independent (their powers of N cancel, since above the crossover concentration the mesh size ξ does not depend on N but only on concentration); $m = \nu/(1-3\nu)$ has a value of -1 for ideal chains and -3/4 for real chains.

The dynamics of polymer chains in a solvent or a melt is also relevant to electrospinning. Its behavior and analysis are quite complex, especially for highly concentrated solutions. A single chain in a solvent returns to its equilibrium state within a **relaxation** time τ estimated by

$$\tau \cong \frac{\eta_s R^3}{k_B T} \approx \tau_0 N^{3\nu}, \quad \tau_0 \approx \frac{\eta_s a^3}{k_B T}, \tag{A.14}$$

where η_s is the solvent viscosity, R is either R_0 or R_F for ideal or real chains respectively, k_B is the Boltzmann constant, T is the temperature, and τ_0 is the

monomer's relaxation time. For R ~ 50 nm and η_s ~ 0.1 poise (0.01 Pa s), τ is of order 10^{-6} s.[20] The situation is, however, more complex for a polymer network, where the individual chain cannot relax freely, but rather reptates (crawls) slowly along a corridor formed by its neighboring chains. For real chains the reptation time is of order ~N^3, compared to a free chain relaxation time order of ~$N^{9/5}$, and it depends also on the concentration c. In the extreme case of a melt, the reptation time for a long chain of $N = 10^4$ is ~10 s.[20]

A.3 Coil stretch transition

De Gennes describes a model for deformation of a single chain in dilute solution (good solvent) under a strong **extensional flow** with constant velocity gradient s.[20, 81] Such conditions were created with the four-roll mill experiment by Crowley et al.[82] illustrated in Figure A-8, where chain elongation was detected by optical birefringence. This problem was also investigated by Feng et al., using numerical simulations of the flow of dilute polymer solutions.[83, 84]

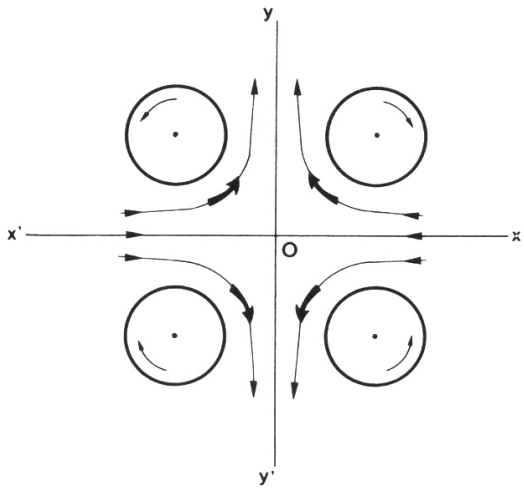

Figure A-8. Four roll mill used to create extensional flows with constant velocity gradient along the axis of exit y.[20]

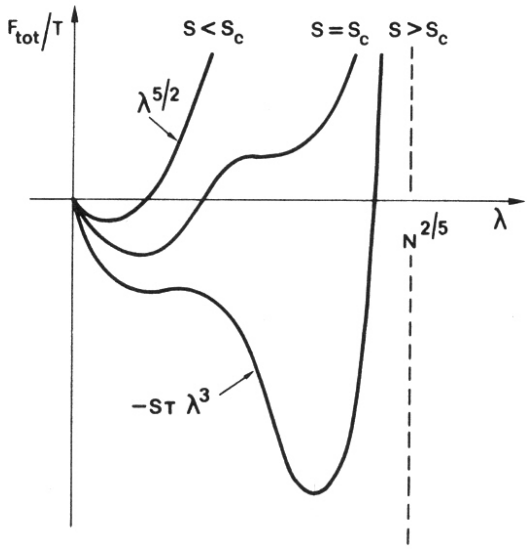

Figure A-9. Free energy versus relative elongation $\lambda \equiv r / R_F$ for a single polymer coil in a longitudinal extensional flow.[20]

For a given elongation r, the free energy F_{tot} of the chain consists of the coil elastic energy from Equation (A.19), the friction (hydrodynamic) energy $\sim \eta_s s r^3$, and the full-stretch elastic energy (at very high elongation). Using relative elongation $\lambda \equiv r / R_F$,

$$F_{tot} = F_{elastic(coil)} - F_{friction} + F_{elastic(full-stretch)}$$
$$\frac{F_{tot}}{k_B T} = \lambda^{5/2} - s\tau\lambda^3 + \frac{F(\lambda)_{elastic(full-stretch)}}{k_B T}, \quad \text{(A.15)}$$

where τ is used from Equation (A.14). When increasing the gradient s above $1/\tau$ (i.e., $s\tau > 1$), the friction energy dominates, until the relative elongation λ approaches full stretching, thereby increasing the elastic energy sharply.

The behavior of the chains under such conditions demonstrates two distinct energy equilibrium states, presented in Figure A-9: when the gradient is smaller than a critical value s_c, the chain is slightly stretched but remains in a conformation resembling a Gaussian coil; above the critical gradient, the chain goes to an almost fully stretched state; a phase transition (also called coil stretch transition) occurs at the critical gradient, with two energy minima separated by a huge energy barrier, corresponding to the coil shape and the stretched shape.

It should be noted that while stretching is effective, there is a balance between the hydrodynamic stretching force and the elastic contraction force of an entropic chain; there is no relaxation whatsoever, and the relaxation time τ in the expression $s\tau$ is only used for scaling convenience.

This analysis implies that substantial chain stretching can occur with high strain-rate extensional flows of concentrated (semi-dilute) polymer solutions, in which the polymer creates an entangled network, typical to electrospinning. Moreover, as shown in Section 2.1, during electrospinning the flow velocity gradient s is not constant, but rather rises linearly along the solution jet.

It is emphasized, however, that the coil stretch transition phenomenon is unique to a free chain in an extensional flow, in which the hydrodynamic force can exceed the opposing entropic elastic force, whereas in electrospinning the polymer forms an entangled network, in which the dominant forces rise from the elastic continuity of the network and are much higher than the local hydrodynamic force. The stretching dynamics of a network is developed in Section 5.1.[1] The difference between dilute and semi-dilute solutions, regarding chain stretching behavior in an extensional flow, is analyzed by random walk in Sections 4.1.4 and 4.1.5, respectively.

A.4 Polymer nanostructure and elasticity

Polymer chains are essentially one-dimensional macromolecules, with strong covalent bonds along the chain's backbone structure, and side groups bonded to that structure. Lateral cohesion between chains (intermolecular interaction) is affected by entanglement and cross-linking, and by secondary bonds such as van der Waals forces, hydrogen bonds and dipolar bonds, which are of lower order of magnitude than covalent bonds. These properties determine, for a given polymer type, its nanoscale and microscale matrix structure, and consequently its mechanical properties.

The main physical and mechanical properties of interest of polymers are their specific mass, hardness, electric conductivity, melting point, glass-transition point[85], elasticity, ultimate strength, and color. The following review is based mainly on the books by Arridge[17], Nielsen[18] and Ward[19]. Other books, such as those by Mallick[86] and Daniel[87], deal with polymer-matrix composite materials, and specifically with reinforced microfibers and their related design and application. Elastic theory is covered in the classic books by Landau[88] and Timoshenko[89].

Unlike metals and ceramics, which are composed of three-dimensional ordered structures of atoms, the physical and mechanical properties of polymers are the result of their chain conformation, cross-linking, crystallization and orientation. The polymer matrix structure consists of a network of entangled chains, with topological links preventing the crossing of chains (Figure A-10a).

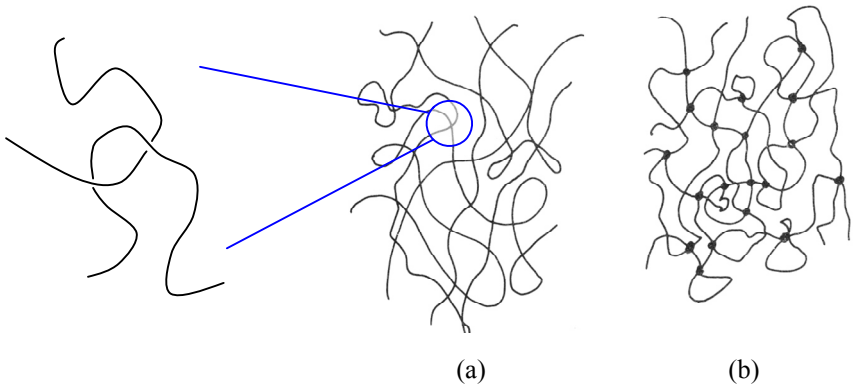

Figure A-10. Classes of polymer matrix structure: (a) topological links (entanglement), and (b) cross-linking with chemical bonds. Adapted from ref[17].

Thus, the polymer solid bulk behavior can be described as sliding of chains, with little interaction between distant atoms. Additionally, in polymers such as rubber, thermosets and resins, chemical bonds create strong cross-linking between chains (Figure A-10b).

Many polymers, such as polyethylene and nylon, tend to crystallize from a melt, forming small crystallic lamellae about 10 nm thick, which sometimes stack into ribbon-like or spherulites structures (Figure A-11).

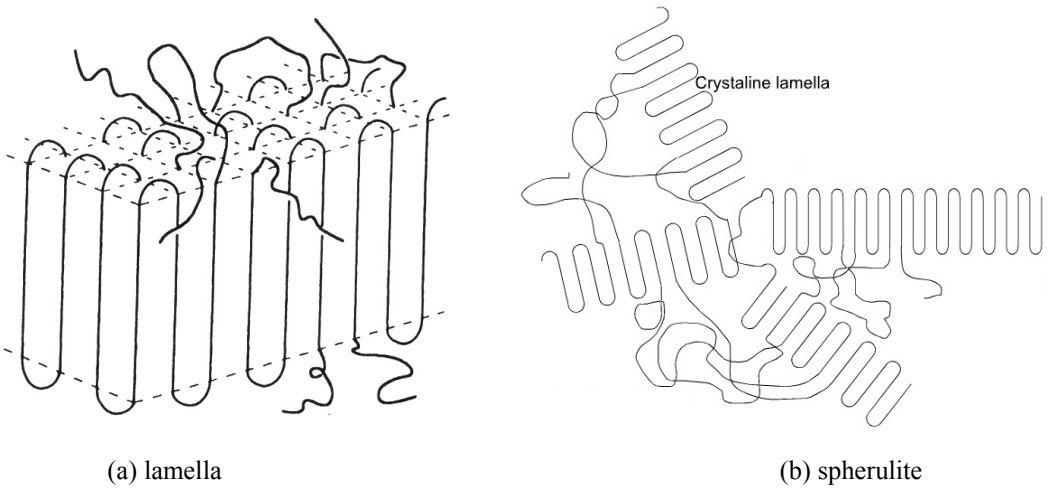

(a) lamella (b) spherulite

Figure A-11. Schematic illustrations of polymer crystalline structure: (a) chain folding in a crystallic lamella; note that the chains are oriented across the lamella surface[18], and (b) spherulite semi-crystalline region[90].

On a higher scale, the crystallites are dispersed within regions of amorphous material, creating a structure similar to composite materials. The degree of **crystallization** (crystallinity index) is defined as the volume fraction of crystallites in the polymer, and can range from 30% to 90% in semi-crystalline polymers.

When stretched, such as during electrospinning or cold drawing, the polymer matrix structure may possess a preferred **orientation** (alignment) of the amorphous and crystallic regions. Stretching may also enhance the degree of crystallization, as it drives chains into adequate side-by-side three-dimensional position. Arinstein et al.[10] observed these phenomena in electrospun nanofibers, and measured the orientation factors of both the amorphous and crystallic regions, and the crystallinity index, using X-rays diffraction tests.

Simple analytical models predict polymer **elasticity** for two cases: the random coil, and the fully extended chain. These cases represent two extremes – the amorphous structure (in the rubbery state, above glass transition temperature T_g), and

the crystalline structure, corresponding to complete disorder and complete order, respectively. These predictions are useful for determining the lower and upper bounds of polymer elasticity, and are therefore described ahead.

Random coil: The extension of a freely-jointed chain subjected to an external force is achieved by reorganization of its conformation (Figure 4-10). The Helmholtz free energy F of an ideal chain under extension can be derived from Equation (A.6), using the Boltzmann relation for the entropy S

$$\begin{aligned} S &= k_B \ln(\Omega) = const + k_B \ln[P(r)] \\ F &= U - TS = const + \frac{3k_B T r^2}{2R_0^2}, \end{aligned} \tag{A.16}$$

where $P(r)$ is the probability of the extension r, U is the chain constant internal energy, k_B is the Boltzmann constant, and T is the temperature. Ω is the number of possible coil configurations for a given extension vector r, and is proportional to the probability $P(r)$. The Helmholtz rather than Gibbs free energy is used, since all possible coils correspond to a constant chain length (analogous to constant volume condition). The internal energy U is independent of chain conformation because an ideal chain assumes no interaction energy between distant monomers. The corresponding extension force f is

$$f = \frac{\partial F}{\partial r} = \left(\frac{3k_B T}{R_0^2} \right) r \quad \text{where} \quad R_0^2 = a^2 N, \tag{A.17}$$

implying a linear relationship between the force f and the end-to-end distance r.[20-22] Thus, an ideal chain may be construed as an entropic spring, obeying Hooke's law for small elongations.

For large elongations, above one third of the fully extended length, more complex equations were derived (see for example Flory[17, 76]). Considering a freely-jointed chain subject to a constant elongation force f, and using the Gibbs free energy (the conditions are analogous to constant pressure), G_{ibbs}, the extension r is given by[21]

$$r = -\frac{\partial G_{ibbs}}{\partial f} = aN \left[\coth(f_N) - \frac{1}{f_N} \right] \quad \text{where} \quad f_N = \frac{fa}{k_B T}, \tag{A.18}$$

where the function in square brackets is called the Langevin function. At small relative elongations r/aN, the function converges to Hooke's law of Equation (A.17);

at large relative elongations, it deviates strongly from the linear behavior, and saturates at the maximal extension aN (see example in Figure 4-11).

Similarly, at small elongations, the free energy F of a real chain under extension in a good solvent can be derived [20], implying a non-linear dependence of the extension force f on the end-to-end distance r

$$F \approx k_B T \left(\frac{r}{R_F} \right)^{1/(1-\nu)} \approx k_B T \left(\frac{r}{R_F} \right)^{5/2} . \tag{A.19}$$

Consider a network with N_{sc} ideal subchains per unit volume, where a subchain is a chain section between two cross-links. The network strain energy U_ε per unit volume, for a small strain $\varepsilon = r / R_0$, can be scaled from Equation (A.16) using only the elastic energy component

$$U_\varepsilon = F N_{sc} = \frac{3 k_B T}{2 R_0^2} \varepsilon^2 R_0^2 N_{sc} = \frac{3 N_{sc} k_B T}{2} \varepsilon^2 . \tag{A.20}$$

This model assumes the same average deformation energy for all N_{sc} subchains in the network, and that the network is in the rubbery state so that intermolecular motions are possible (see more details in ref[19]). Using Hooke's law, the Young's modulus E is given by

$$E = \frac{\partial^2 U_\varepsilon}{\partial \varepsilon^2} = 3 N_{sc} k_B T , \tag{A.21}$$

and the shear modulus G for an incompressible material is

$$G \equiv \tfrac{1}{3} E = N_{sc} k_B T = \rho R_{gas} T / M_{sc} . \tag{A.22}$$

where ρ is the material density, R_{gas} is the gas constant, and M_{sc} is the molecular mass of the subchain. This model is called rubber elasticity, and is applicable for temperatures above the glass transition temperature T_g. For large elongations, other more complex rubber elasticity models exist – see reviews in ref[17, 19, 21] (see example in Figure A-12). For typical polymers, the value of E according to this model is of order 1 MPa.

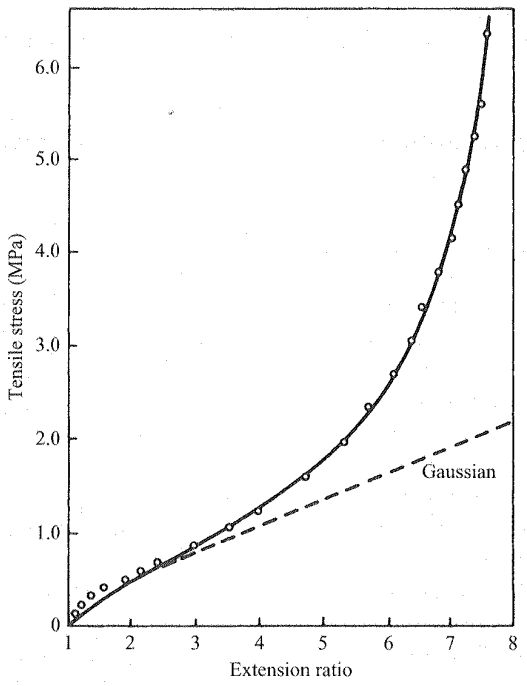

Figure A-12. Theoretical and experimental extension of rubber, with $N_{sc}k_BT = 0.27$ MPa.[19, 91]

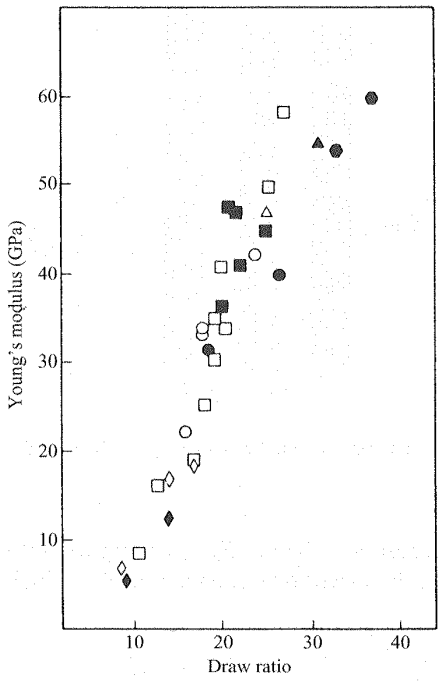

Figure A-13. Elastic modulus of mechanically drawn polyethylene.[19, 38]

Fully extended chain: This model was developed by Treloar[16] for various crystalline polymers, using molecular mechanics methods (additional molecular mechanics models are reviewed in the book by Rappé et al.[92]). A planar extended chain with bond size l is subjected to force f at both ends (Figure A-14). Each covalent bond has a tensile force constant k_l, and each vertex (the location of a carbon atom) has an angular force constant k_θ, both known from infrared data. The tetrahedral angle θ is the angle between the bond and the chain longitudinal axis. Intermolecular interaction forces can be ignored considering the ordered crystallic structure.

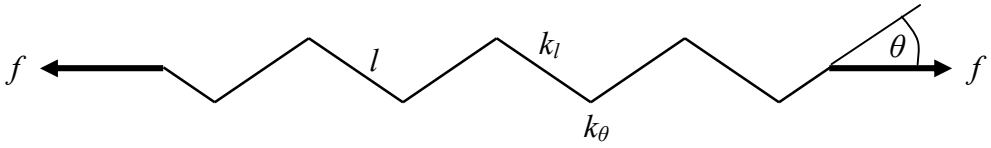

Figure A-14. Fully extended chain model, showing a segment of a straight planar chain.[16] The vertices designate carbon atoms.

The elastic tensile modulus (Young's modulus) $E = \sigma / \varepsilon$ (σ – stress, ε - strain) was calculated from the total deflection δL_s caused by the force f, where L_s is the overall segment length, and A is the chain cross-section estimated from measurements of intermolecular distances

$$E = \frac{f/A}{\delta L_s / L_s} \cong \frac{l}{A} \frac{\cos\theta}{\frac{\cos^2\theta}{k_l} + \frac{l^2 \sin^2\theta}{4k_\theta}} . \qquad \text{(A.23)}$$

This equation holds also for a crystallite containing many such extended chains, arranged in an ordered structure. The calculated values for Young's modulus for polyethylene and nylon 66 are 182 GPa and 197 GPa, respectively, agreeing with experimental results of highly crystallized samples.

The modulus estimations obtained by these two models, for amorphous rubber elasticity and for crystallites, range from 10^6 Pa to 10^{11} Pa, an enormous gap. Amorphous polymers in the glassy state (below T_g) are more rigid ($E \sim 10^9$ Pa), because of the more restrictive nature of their intermolecular interactions. The free volume theory is one of the interpretations for these differences, stating that the intermolecular free space consists of van der Waals radii and additional volume for vibrational motions. Up to T_g the free volume is fairly constant, while above T_g it starts growing with temperature, allowing the chains to move more freely.

The elasticity of semi-crystalline polymers has been estimated by models of aggregate crystallites, randomly oriented or with a preferred orientation, using methods similar to those used for composite material.[17, 19] For example, a crystalline fibril model was applied successfully in explaining the sharp increase in the elastic modulus of mechanically drawn polyethylene (Figure A-13)[38]. These methods can also be applied to amorphous polymers in the glassy state by assuming a certain degree of order (quasi-crystallites) in the matrix. Such methods may be useful for developing a model for nanofibers, explaining the effect of anisotropy on elasticity.

Appendix B. Review of nanofiber size-dependent elasticity

B.1 Experimental evidence

Substantial work has been reported on the elastic and strength properties of nanofibers, using both pure polymers and reinforced polymers.[93-96] A typical **stress-strain** behavior for Cl-PP (Figure B-1) and PVA (Figure B-2), at various volume fractions of carbon nanotubes (CNT) filler, illustrates the elastic and plastic strain regions, and the effect of the reinforcing filler fraction.

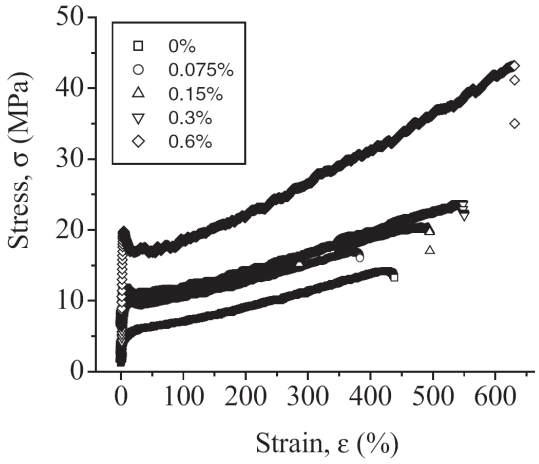

Figure B-1. Representative stress–strain curves for electrospun Cl-PP-based composites, for a range of nanotube volume fractions.[95]

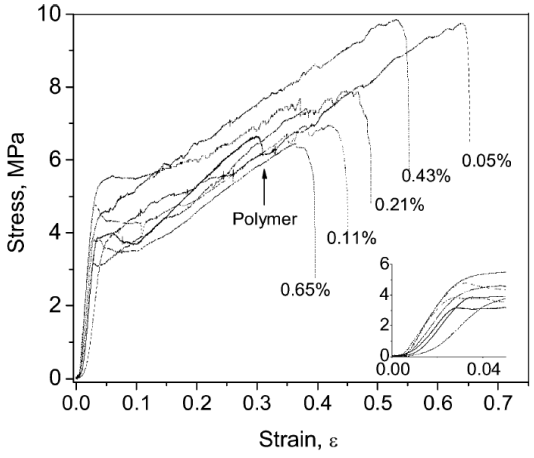

Figure B-2. Representative stress–strain curves for PVA electrospun membranes, as a function of nanotube volume fraction.[93] Inset: the low strain region.

For bulk isotropic materials, the elastic modulus is an intrinsic property, independent of size and shape. However, there is growing evidence for size effects on the elastic properties of nanofibers and nanofilms made of different types of materials. The following works provide experimental evidence.

Ji et al.[8] investigated the elasticity of electrospun polystyrene (PS) nanofibers, using the three-point bending test (Figure B-3), and observed a sharp increase in the tensile (Young's) modulus E with decreasing fiber diameter (Figure B-4). The modulus rose from 4 GPa at a large fiber radius (i.e. bulk material), up to 40 GPa at radius of 100 nm, a factor of 10. PS, an amorphous polymer, exhibits similar behavior when in pure state or reinforced with CNT, however, the **crossover diameter** at which the modulus rises is larger for the reinforced material.

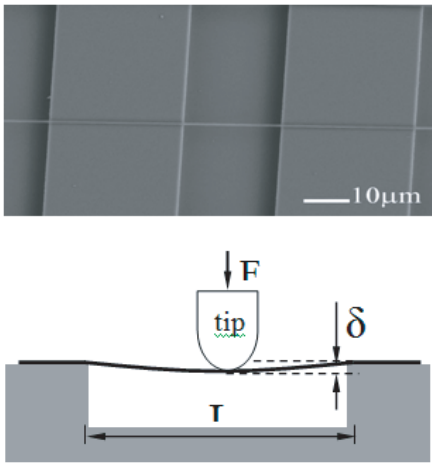

Figure B-3. Schematic of the three-point bending method: a rounded AFM tip presses on the suspended fiber (without indentation), displacing it to a distance δ.[8]

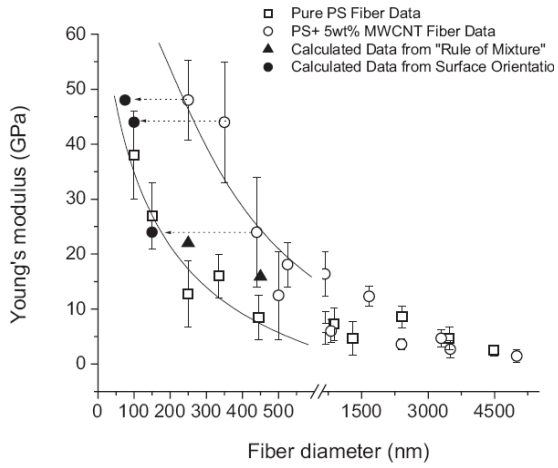

Figure B-4. Young's modulus of PS for fibers of different diameters, with and without reinforcement.[8]

Using shear modulation force microscopy (SMFM) (Figure B-5) to measure the shear modulus G, and scaling the fiber radius by the radius of gyration R_g of various PS molar masses, Ji et al. demonstrated a universal behavior (Figure B-6), common to both moduli, different molar masses, and both measurement methods, identifying the crossover of the moduli at fiber radius of ~30 R_g. These results clarify that the increase of the elastic modulus is a combined effect, dependent not only on the fiber radius but also on the size of the polymer macromolecules.

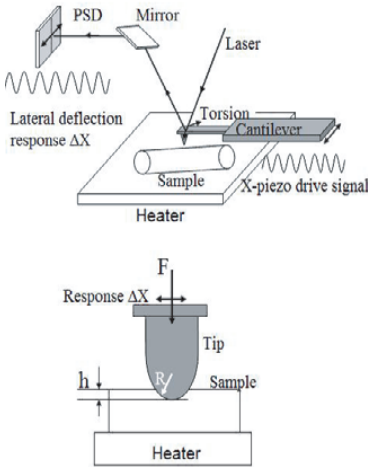

Figure B-5. Schematic of the SMFM method: the fibers are indented by the AFM tip, and the deflection amplitude of an applied modulation is measured.[8]

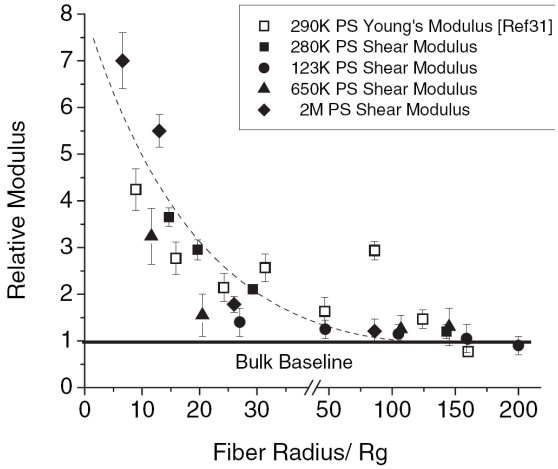

Figure B-6. Relative tensile and shear moduli (E/E_0 and G/G_0, respectively) of fibers, versus their radius, scaled by R_g.[8]

Similar phenomena was observed in tests conducted by Burman et al.[6, 9, 10] on nylon 66, a semi-crystalline polymer, using the single nanofiber tensile test and the free-flight pendulum test (Figure B-7). Young's modulus rose by a factor of more than 30 at fiber diameter of 200 nm, and the crossover diameter was around 500 nm.

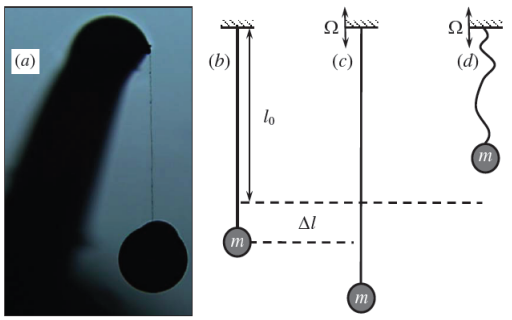

Figure B-7. The string pendulum test: a ball is glued to a nanofiber and suspended from a cantilever beam, attached to a piezoelectric-actuated base. The pendulum's vibration consists of downward and free-flight upward motions, with a resonant frequency that allows calculation of the Young's modulus.[9]

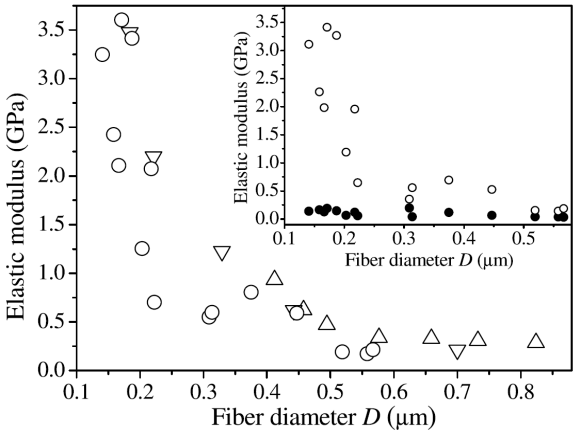

Figure B-8. Young's modulus E of nylon 66 versus nanofiber diameter D, obtained by tensile tests (Δ)[10], free-flight pendulum resonant vibration method (∇)[9], and 3-point bending method (○)[6]. The inset shows the contribution of surface area during bending (●) to the material's elastic modulus (○).[6]

Arinstein et al.[10] also measured the degrees of crystallization and orientation for the same fibers used in the tensile and pendulum tests (Figure B-9), and found that these parameters show only mild dependence on fiber diameter, without visible crossover. This observation implies that the modulus increase is associated with the existence of supramolecular structures in the fiber, whereas the influence of the molecular orientation is not dominant.

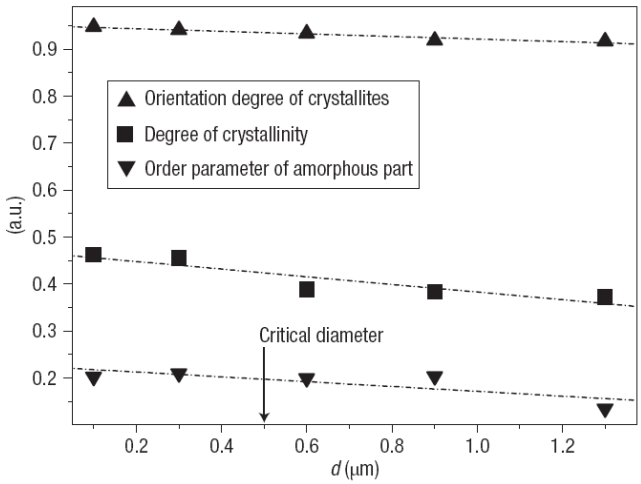

Figure B-9. X-rays diffraction tests of electrospun Nylon 66 nanofibers: orientation degree of crystallites along the fiber axis, degree of crystallinity, and order parameter of macromolecule orientation in the amorphous part, versus fiber diameter d.[10]

Measurements of the elastic modulus of poly-(ethylene-co-vinyl acetate) (PEVA260, a semicrystalline polymer) by Liu et al.[7], using both SMFM and AFAM (atomic force acoustic microscopy) methods, demonstrated similar behavior (Figure B-10). However, the onset of modulus rise occurred at a fiber diameter of 10 μm, an order of magnitude higher than previously reported, implying that the diameter itself is not the cause for the increase in modulus, but rather the fiber nanostructure associated with the electrospinning conditions that led to that diameter.

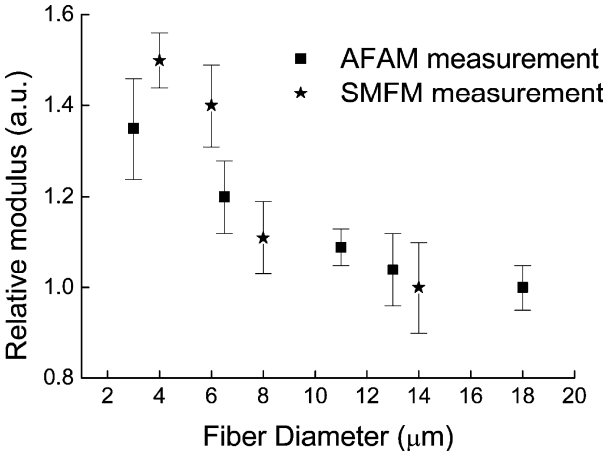

Figure B-10. Relative modulus of electrospun PEVA260 fibers measured by two different methods: AFAM and SMFM method.[7]

The effect of size on the tensile modulus was observed also on materials other than polymers, such as polypyrrole nanotubes (Figure B-11), Ag nanowires (Figure B-12) and Pb nanowires tested by Cuenot et al.[11, 13], and Ag, Au, ZnO and Si nanowires tested by Park[66]. These experiments suggest that the dependence of the modulus on fiber diameter at nanoscale is a universal phenomenon, however the mechanism is not necessarily the same as for macromolecules.

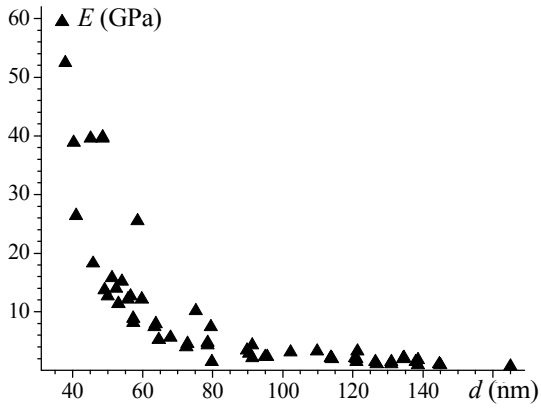

Figure B-11. Three-point bending tests of polypyrrole nanotubes using AFM: relative Young's modulus (E/E_0) versus diameter d.[11]

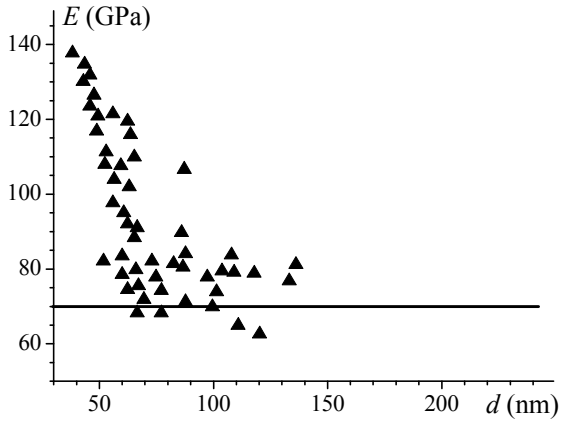

Figure B-12. Three-point bending tests of Ag nanowires using AFM: relative Young's modulus (E/E_0) versus diameter.[13]

Sui et al.[14, 15] showed on PMMA fibers that, in parallel to the rise in the Young's modulus at increasingly smaller fiber diameters, the fiber strength, strain at failure, and tensile toughness increase as well, particularly at diameters below 500 nm. Addition of NaCl or multi-walled CNTs also increases these properties, but, at the same time, retains a similar diameter-dependent behavior.

In addition to elastic moduli, the **glass transition** temperature T_g is also affected by nanoscale sizes, as reported by Ji et al.[8] for PS nanofibers filled with CNT. Addition of 5 wt% CNT filler increases T_g by 10°C, explained by a reduction in the free volume due to adsorption of polymer chains onto the CNT, leading to further increase in the modulus. Conversely, de Gennes[97] reported that for PS films of thickness < 20 nm, smaller than R_g, the T_g was reduced, explained by more chain loops extending to the surface region of the thin film where the mobility is larger.

B.2 Suggested physical mechanisms

The current literature provides three different theoretical explanations for the dependence of elasticity on nanoscale sizes:

- Surface tension – Cuenot et al.[11] and others[11, 13, 64-66]
- Molecular orientation at the fiber boundary – Ji et al.[8]
- Confinement of supramolecular structure - Arinstein et al.[10, 39, 40].

While surface tension only changes the apparent measured modulus, stretching and confinement cause anisotropy and change the material intrinsic modulus, as will be clarified further on.

Surface tension: Surface tension becomes a significant factor at nanoscale, since the ratio of surface area to volume is an inverse function of size. However, its effect depends on the mode of deformation and on geometry.

Under uniaxial stretching, the surface tension energy density U_{st} of a fiber is given by (assuming incompressible material)

$$U_{st} = \frac{\gamma \Delta S_f}{V_f + \Delta V_f} \approx \frac{2\pi R\gamma}{\pi R^2} \frac{\Delta L_f}{L_f} = \frac{2\gamma}{R}\varepsilon \,, \tag{B.1}$$

where L_f is the fiber length, S_f its surface area, V_f its volume, γ the surface tension, R the fiber radius, and ε the strain caused by surface tension; ΔL_f, ΔS_f and ΔV_f are the corresponding small changes due to surface tension. The surface tension energy is then proportional to the strain ε, unlike the elastic energy that is proportional to ε^2 [see, for example, Equation (A.20)].

The stress σ (compression) caused by surface tension is constant and does not depend on elongation, resulting in a constant compression strain ε of

$$\varepsilon = \frac{\sigma}{E} = \frac{1}{E}\frac{\partial U_{st}}{\partial \varepsilon} \approx \frac{2\gamma}{DE} = \frac{2 \cdot 0.05_{\mathrm{N/m}}}{10^{-7}{}_{\mathrm{m}} \cdot 2 \cdot 10^{9}{}_{\mathrm{N/m^2}}} = 0.05\% << \varepsilon_{\max}, \qquad \text{(B.2)}$$

where an estimate is given for fiber of diameter 100 nm and typical polymer properties, showing that the strain is quite negligible with respect to the maximal elastic strain ε_{max} (~2% for polymers in the glassy state – see for example Figure B-2). Thus, surface tension does not adequately explain the observed increase in the elastic modulus of nanofibers under uniaxial stretching.[10, 39, 40]

This, however, may not be the situation in three-point bending. According to Cuenot et al.[11], the apparent Young's modulus E_{app}, calculated after taking surface tension effects into consideration, is given by

$$E_{app} = E_0 + \frac{(1-\nu)\gamma L_f^2}{(5/8)D^3}, \qquad \text{(B.3)}$$

where E_0 is the material's bulk tensile modulus and ν the Poisson ratio, showing an added expression that strongly depends on the fiber diameter D, as well as on the geometry and fiber clamping boundary conditions. Hence, E_{app} can represent the change in the material intrinsic modulus only if the surface tension term is much lower than E_0. Indeed, Burman et al.[6] showed by the 3-point bending method that the surface tension effect was negligible in the case of Nylon 66 nanofibers of diameter smaller than 1 μm (Figure B-8).

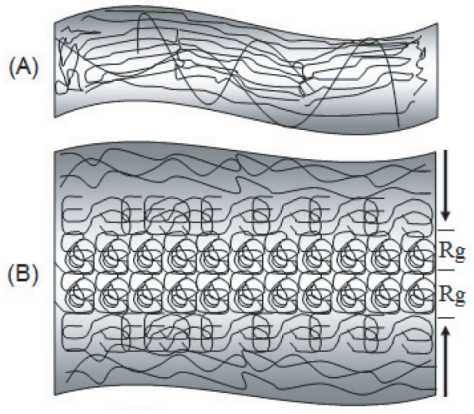

Figure B-13. Model of the molecular chain orientation: (a) thin fiber - polymer chains orient through the entire fiber; and (b) thick fiber - polymer chain orientation starts at the surface and propagates into the bulk.[8]

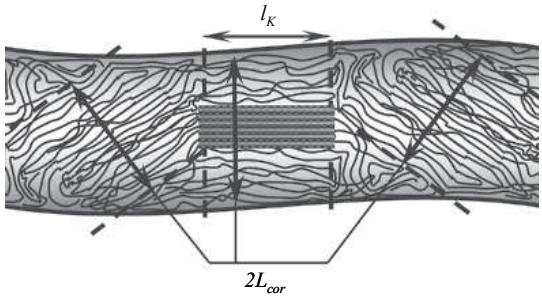

Figure B-14. Arrangement of crystallites and oriented amorphous matrix in a polymer nanofiber. L_{cor} is the orientation correlation length within the amorphous polymer portion, and l_k is the length of the Kuhn segment.[10]

Molecular orientation: The combination of the large shear imposed during electrospinning and the effect of surface tension orients the chains in the outermost regions of the fiber (Figure B-13). Chain orientation starts at the surface and propagates into the bulk, fading gradually as the distance from the surface grows. The degree of orientation is determined by the number of monomers in contact with the surface, which has been shown to scale with R / R_g of the polymer.[8]

Evidence presented in this thesis (Section 5.1 through 5.4) shows that, under high electrospinning strain rates, the situation is reversed, and the ordered aligned nanostructure forms at the fiber core rather than at the boundary, as a result of stretching and compacting of the polymer network.

Confinement: The size of regions consisting of orientation-correlated macromolecules is comparable to the nanofiber diameter, thereby resulting in confinement of the supramolecular structure (Figure B-14). Rigid segments of the chain [i.e. Kuhn segments – refer to Appendix A and Equations (A.2) and (A.3)] are aligned to corresponding rigid segments in adjacent chains, forming a stack of many such segments, of thickness defined as the correlation length. Arinstein et al.[10] estimated the correlation length L_{cor}, based on the modified Onsager rigid rods model corresponding to the case of densely-packed rods

$$d = 2L_{cor} \sim \frac{2l}{\sqrt{1-\vartheta}} \left(n_k \ln \vartheta\right)^2 \approx 300_{\text{nm}} \tag{B.4}$$

where d is the size of the ordered region, l the bond size (0.1 nm), ϑ the free volume (8 %), and n_k the number of C-C bonds in a Kuhn segment (15 bonds). The size of the ordered region is, according to this estimation, of the same order of the fiber diameter, thereby confining the supramolecular structure, and forcing alignment in the amorphous and crystallic regions. According to Ji et al.,[8] the addition of CNT filler enhances the effect of confinement due to the added CNT interface area.

Recent modeling by Arinstein,[40] showed, in good agreement with the experimental evidence,[6, 8-10] that during elastic stretching of a nanofiber, the rotation of partially oriented anisotropic regions is hindered by the fiber boundary, creating confinement and consequently increasing the effective elastic modulus.

References and notes

1. Greenfeld, I.; Arinstein, A.; Fezzaa, K.; Rafailovich, M. H.; Zussman, E. *Physical Review E* **2011,** 84, (4), 041806.
2. Greenfeld, I.; Fezzaa, K.; Rafailovich, M. H.; Zussman, E. *Macromolecules* **2012,** 45, (8), 3616-3626.
3. Camposeo, A.; Greenfeld, I.; Tantussi, F.; Pagliara, S.; Moffa, M.; Fuso, F.; Allegrini, M.; Zussman, E.; Pisignano, D. *Nano Letters* **2013,** 13, (11), 5056−5062.
4. Camposeo, A.; Greenfeld, I.; Tantussi, F.; Moffa, M.; Fuso, F.; Allegrini, M.; Zussman, E.; Pisignano, D. *Submitted for publication* **2013**.
5. Greenfeld, I.; Zussman, E. *Journal of Polymer Science Part B-Polymer Physics* **2013,** 51, (18), 1377–1391.
6. Burman, M.; Arinstein, A.; Zussman, E. *Europhys. Lett.* **2011,** 96, 16006.
7. Liu, Y.; Chen, S.; Zussman, E.; Korach, C. S.; Zhao, W.; Rafailovich, M. *Macromolecules* **2011,** 44, (11), 4439-4444.
8. Ji, Y.; Li, C.; Wang, G.; Koo, J.; Ge, S.; Li, B.; Jiang, J.; Herzberg, B.; Klein, T.; Chen, S.; Sokolov, J. C.; Rafailovich, M. H. *Epl* **2008,** 84, (5), 56002.
9. Burman, M.; Arinstein, A.; Zussman, E. *Applied Physics Letters* **2008,** 93, (19), 193118.
10. Arinstein, A.; Burman, M.; Gendelman, O.; Zussman, E. *Nature Nanotechnology* **2007,** 2, (1), 59-62.
11. Cuenot, S.; Fretigny, C.; Demoustier-Champagne, S.; Nysten, B. *Physical Review B* **2004,** 69, (16).
12. Schonherr, H.; Frank, C. W. *Macromolecules* **2003,** 36, (4), 1188-1198.
13. Cuenot, S.; Demoustier-Champagne, S.; Nysten, B. *Physical Review Letters* **2000,** 85, (8), 1690-1693.
14. Sui, X. M.; Wagner, H. D. *Nano Letters* **2009,** 9, (4), 1423-1426.
15. Sui, X. M.; Wiesel, E.; Wagner, H. D. *Journal of Nanoscience and Nanotechnology* **2011,** 11, (9), 7931-7936.
16. Treloar, L. R. G. *Polymer* **1960,** 1, (1), 95-103.
17. Arridge, R. G. C., *Mechanics of polymers*. Clarendon Press: Oxford [Eng.], 1975; p ix, 246 p.
18. Nielsen, L. E.; Landel, R. F., *Mechanical properties of polymers and composites*. 2nd ed.; M. Dekker: New York, 1994; p xiii, 557 p.
19. Ward, I. M.; Sweeney, J., *An introduction to the mechanical properties of solid polymers*. 2nd ed.; Wiley: Chichester, West Sussex, England, 2004; p x, 382 p.
20. de Gennes, P. G., *Scaling concepts in polymer physics*. Cornell University Press: Ithaca, N.Y., 1979; p 324 p.
21. Rubinstein, M.; Colby, R. H., *Polymer physics*. Oxford University Press: Oxford ; New York, 2003; p xi, 440 p.

22. Grosberg, A. I. U.; Khokhlov, A. R., *Statistical physics of macromolecules*. AIP Press: New York, 1994; p xxvii, 350 p.

23. Huang, Z. M.; Zhang, Y. Z.; Kotaki, M.; Ramakrishna, S. *Composites Science and Technology* **2003,** 63, (15), 2223-2253.

24. Andrady, A. L., *Science and technology of polymer nanofibers*. Wiley: Hoboken, N.J., 2008; p xix, 403 p.

25. Stanger, J.; Tucker, N.; Staiger, M. *Electrospinning*; 2005.

26. Gogotsi, I. U. G., *Nanotubes and nanofibers*. CRC Taylor & Francis: Boca Raton, FL, 2006; p 248 p.

27. Han, T.; Yarin, A. L.; Reneker, D. H. *Polymer* **2008,** 49, (6), 1651-1658.

28. Gupta, P.; Elkins, C.; Long, T. E.; Wilkes, G. L. *Polymer* **2005,** 46, (13), 4799-4810.

29. Reneker, D. H.; Yarin, A. L.; Zussman, E.; Xu, H. *Advances in Applied Mechanics* **2007,** 41, 43-195.

30. Reneker, D. H.; Yarin, A. L.; Fong, H.; Koombhongse, S. *Journal of Applied Physics* **2000,** 87, (9), 4531-4547.

31. Bellan, L. M.; Craighead, H. G.; Hinestroza, J. P. *Journal of Applied Physics* **2007,** 102, (9), 094308.

32. Hohman, M. M.; Shin, M.; Rutledge, G.; Brenner, M. P. *Physics of Fluids* **2001,** 13, (8), 2201-2220.

33. Shin, Y. M.; Hohman, M. M.; Brenner, M. P.; Rutledge, G. C. *Polymer* **2001,** 42, (25), 9955-9967.

34. Dayal, P.; Liu, J.; Kumar, S.; Kyu, T. *Macromolecules* **2007,** 40, (21), 7689-7694.

35. Casper, C. L.; Stephens, J. S.; Tassi, N. G.; Chase, D. B.; Rabolt, J. F. *Macromolecules* **2004,** 37, (2), 573-578.

36. Guenthner, A. J.; Khombhongse, S.; Liu, W. X.; Dayal, P.; Reneker, D. H.; Kyu, T. *Macromolecular Theory and Simulations* **2006,** 15, (1), 87-93.

37. Dayal, P.; Kyu, T. *Physics of Fluids* **2007,** 19, (10), 107106.

38. Capaccio, G.; Crompton, T. A.; Ward, I. M. *Journal of Polymer Science Part B-Polymer Physics* **1976,** 14, (9), 1641-1658.

39. Arinstein, A.; Zussman, E. *Journal of Polymer Science Part B-Polymer Physics* **2011,** 49, (10), 691-707.

40. Arinstein, A. *Journal of Polymer Science Part B-Polymer Physics* **2013,** 51, (9), 756-763.

41. Taylor, G. *Proceedings of the Royal Society of London Series a-Mathematical and Physical Sciences* **1969,** 313, (1515), 453.

42. Gatford, J., A diagram of the electrospinning process showing the onset of instability. In The New Zealand Institute for Plant and Food Research Ltd: 2008.

43. Landcuo A diagram of electrospinning process for polymer production.

44. Campbell, D.; Pethrick, R. A.; White, J. R., *Polymer characterization physical techniques*. 2000.

45. Roe, R. J., *Methods of X-ray*. Oxford University Press: New York, 2000; p xiv, 331 p.

46. Demir, M. M.; Yilgor, I.; Yilgor, E.; Erman, B. *Polymer* **2002,** 43, (11), 3303-3309.

47. Hsu, C. M.; Shivkumar, S. *Journal of Materials Science* **2004,** 39, (9), 3003-3013.

48. Fridrikh, S. V.; Yu, J. H.; Brenner, M. P.; Rutledge, G. C. *Physical Review Letters* **2003,** 90, (14), 144502.

49. Colby, R. H.; Fetters, L. J.; Funk, W. G.; Graessley, W. W. *Macromolecules* **1991,** 24, (13), 3873-3882.

50. McKee, M. G.; Wilkes, G. L.; Colby, R. H.; Long, T. E. *Macromolecules* **2004,** 37, (5), 1760-1767.

51. Gu, S. Y.; Ren, J. *Macromolecular Materials and Engineering* **2005,** 290, (11), 1097-1105.

52. Kedem, S.; Schmidt, J.; Paz, Y.; Cohen, Y. *Langmuir* **2005,** 21, (12), 5600-5604.

53. Kidoaki, S.; Kwon, K.; Matsuda, T. *Journal of Biomedical Materials Research Part B-Applied Biomaterials* **2006,** 76B, (1), 219-229.

54. Baker, S. C.; Atkin, N.; Gunning, P. A.; Granville, N.; Wilson, K.; Wilson, D.; Southgate, J. *Biomaterials* **2006,** 27, (16), 3136-3146.

55. Kirichenko, V. N.; Petrianovsokolov, I. V.; Suprun, N. N.; Shutov, A. A. *Doklady Akademii Nauk SSSR* **1986,** 289, (4), 817-820.

56. Spivak, A. F.; Dzenis, Y. A. *Applied Physics Letters* **1998,** 73, (21), 3067-3069.

57. Hohman, M. M.; Shin, M.; Rutledge, G.; Brenner, M. P. *Physics of Fluids* **2001,** 13, (8), 2221-2236.

58. Higuera, F. J. *Journal of Fluid Mechanics* **2006,** 558, 143-152.

59. Reznik, S. N.; Zussman, E. *Physical Review E* **2010,** 81, (2), 026313.

60. Reznik, S. N.; Zussman, E. *Stationary uniform and compound viscous jets of leaky dielectrics in a strong electric fields*; EM10338; Technion, internal report EM10338: 2007, 2007.

61. Yarin, A. L.; Koombhongse, S.; Reneker, D. H. *Journal of Applied Physics* **2001,** 89, (5), 3018-3026.

62. Arinstein, A.; Zussman, E. *Physical Review E* **2007,** 76, (5).

63. Core-shell is an electrospinning method, using two polymer solutions drawn through two coaxial capillaries, obtaining a jet with two concentric layers, core and shell, in which the outer layer (the shell) dries quickly, allowing investigation of the diffusion and evaporation of the inner layer (the core).

64. Dingreville, R.; Qu, J. M.; Cherkaoui, M. *Journal of the Mechanics and Physics of Solids* **2005,** 53, (8), 1827-1854.

65. Sharma, P.; Ganti, S.; Bhate, N. *Applied Physics Letters* **2003,** 82, (4), 535-537.

66. Park, H. S.; Cai, W.; Espinosa, H. D.; Huang, H. C. *MRS Bulletin* **2009,** 34, (4), 232-232.

67. Gersappe, D., Discussion at the Technion. In The question of connectivity was brought to our attention by Prof. Dilip Gersappe from State University of New York at Stony Brook, during his visit to the Technion on June 2009 ed.; 2009.

68. Kramers, H. A. *J. Chem. Phys.* **1946,** 14, 415-424.

69. Feynman, R. P., *Statistical mechanics; a set of lectures*. W. A. Benjamin: Reading, Mass.,, 1972; p xii, 354 p.

70. Greenfeld, I. Effect of polymer matrix structure on mechanical properties of electrospun nanofibers. PhD research proposal, Technion, Haifa, 2009.

71. Wang, Y. J.; Liu, X.; Im, K. S.; Lee, W. K.; Wang, J.; Fezzaa, K.; Hung, D. L. S.; Winkelman, J. R. *Nature Physics* **2008,** 4, (4), 305-309.

72. Im, K. S.; Fezzaa, K.; Wang, Y. J.; Liu, X.; Wang, J.; Lai, M. C. *Applied Physics Letters* **2007,** 90, (9), 091919.

73. Sasov, A. *European Conference for Non-Destructive Testing (ECNDT)* **2006,** We.1.5.4, 1-6.

74. Gullikson, E. X-Ray Interactions with Matter. http://henke.lbl.gov/optical_constants/

75. Roe, R. J., *Methods of X-ray and neutron scattering in polymer science*. Oxford University Press: New York, 2000; p xiv, 331 p.

76. Flory, P. J., *Statistical mechanics of chain molecules*. Interscience Publishers: New York,, 1969; p xix, 432 p.

77. Graessley, W. W., *Polymeric liquids & networks: dynamics and rheology*. 2008.

78. Askeland, D. R.; Phulé, P. P., *The science and engineering of materials*. 5th ed.; Thomson: Toronto, Ont., 2006; p xx, 863 p.

79. Flory, P. J. *Abstracts of Papers of the American Chemical Society* **1983,** 186, (Aug), 4-Acsc.

80. Kirste, R. G.; Kruse, W. A.; Ibel, K. *Polymer* **1975,** 16, (2), 120-124.

81. de Gennes, P. G. *Journal of Chemical Physics* **1974,** 60, (12), 5030-5042.

82. Crowley, D. G.; Frank, F. C.; Mackley, M. R.; Stephenson, R. G. *Journal of Polymer Science Part B-Polymer Physics* **1976,** 14, (6), 1111-1119.

83. Feng, J.; Leal, L. G. *Journal of Non-Newtonian Fluid Mechanics* **1997,** 72, (2-3), 187-218.

84. Feng, J.; Leal, L. G. *Journal of Non-Newtonian Fluid Mechanics* **2000,** 90, (1), 117-123.

85. The glass-transition point Tg is the temperature above which the polymer's thermal expansion coefficient increases abruptly, causing transition from glassy state to rubbery state. Tg is below the melting point Tm.

86. Mallick, P. K., *Fiber-reinforced composites : materials, manufacturing, and design*. 3rd ed.; CRC Press: Boca Raton, FL, 2008; p xvii, 619 p.

87. Daniel, I. M.; Ishai, O., *Engineering mechanics of composite materials*. 2nd ed.; Oxford University Press: New York, 2006; p xviii, 411 p.

88. Landau, L. D.; Lifshits, E. M.; Kosevich, A. d. M.; Pitaevskii, L. P., *Theory of elasticity*. 3rd English ed.; Pergamon Press: Oxford [Oxfordshire] ; New York, 1986; p viii, 187 p.

89. Timoshenko, S.; Goodier, J. N., *Theory of elasticity*. 3d ed.; McGraw-Hill: New York,, 1969; p xxiv, 567 p.

90. Gillis, J. A schematical sketch of a spherulite semi-crystalline region in a linear polymer.

91. Treloar, L. R. G. *Plastics and Rubber* **1976,** 1, (5), 209-211.

92. Rappé, A. K.; Casewit, C. J., *Molecular mechanics across chemistry*. University Science Books: Sausalito, Calif., 1997; p xii, 444 p.

93. Blond, D.; Walshe, W.; Young, K.; Blighe, F. M.; Khan, U.; Almecija, D.; Carpenter, L.; McCauley, J.; Blau, W. J.; Coleman, J. N. *Advanced Functional Materials* **2008,** 18, (17), 2618-2624.

94. Bokobza, L. *Polymer* **2007,** 48, (17), 4907-4920.

95. Coleman, J. N.; Cadek, M.; Blake, R.; Nicolosi, V.; Ryan, K. P.; Belton, C.; Fonseca, A.; Nagy, J. B.; Gun'ko, Y. K.; Blau, W. J. *Advanced Functional Materials* **2004,** 14, (8), 791-798.

96. Jordan, J.; Jacob, K. I.; Tannenbaum, R.; Sharaf, M. A.; Jasiuk, I. *Materials Science and Engineering a-Structural Materials Properties Microstructure and Processing* **2005,** 393, (1-2), 1-11.

97. de Gennes, P. G. *European Physical Journal E* **2000,** 2, (3), 201-203.

לקוטר הסיב בריבוע, לבין גידול במודול האלסטיות, בהתאמה לתצפיות ניסוייות, ויש בכך כדי לקרב אותנו למענה לשאלה כיצד הטוויה החשמלית משפיעה על האלסטיות של ננוסיבים.

יעדי המחקר ותכולתו מוצגים בפרק 3 (באנגלית), והשיטות התאורטיות והניסוייות שפותחו במסגרת המחקר מתוארות בפרק 4. התיאור המפורט של המחקר ותוצאותיו מוצגים במאמרים בפרק 5, ונידונים ומסוכמים בפרק 6. מתווה המחקר וממצאיו העיקריים מתוארים בציור 1-1.

קיטוב (polarization modulation) קרן הלייזר, נמדדה הכיווניות המועדפת של שרשרות הפולימר, ונמצא כי באזור מרכז הסיב יש עדיפות בכיוון אורך הסיב, בשעה שקרוב יותר לשפת הסיב יש כיווניות בניצב לסיב. מדידה זו אישרה שתצורת רשת הפולימר אכן נשארת לאחר ההתמצקות, בהתאמה לחיזוי.

במטרה לאפשר בקרה של משתני התהליך, המודל והסימולציה שפותחו עבור פולימרים בעלי שרשרות גמישות הוכללו לפולימרים גמישים-למחצה בעלי דרגת גמישות משתנה, והודגמו על ידי שינוי מבוקר של המשתנים. בקרה כזו מאפשרת להשיג תוצאות מורפולוגיות רצויות של הסיב, למשל שיפור הכיווניות המולקולרית במרכזו, ובכך הגדלת האורך האפקטיבי של הכרומופורים (קטעי שרשרת שבולעים או פולטים קרינת צבע) ושיפור המוליכות החשמלית והבליעה והקרינה האופטיות. הננומבנה שנצפה, עם הצפיפות והכיווניות הלא אחידים, יכול לשמש לבניית התקנים המשלבים הולכה חשמלית ואופטית עם תשתית מבנית חזקה וקשיחה.

אפקט חשוב נוסף בדינמיקה של רשת פולימר בתמיסה דלילה-למחצה הוא התרת הרשת כתוצאה של מתיחה חזקה. אפקט זה הודגם על ידי טוויה חשמלית של תמיסת פולימתיל מתהקרילט (PMMA) בקצב עיבור גבוה, בשילוב של ריכוז פולימר נמוך (אך עדיין דליל-למחצה) עם עוצמה גבוהה של השדה החשמלי. בתנאים אלה הסילון עובר פרגמנטציה לקטעי סילון קצרים, אשר יוצרים ננוסיבים קצרים באורכים הנעים בין מיקרונים בודדים לעשרות מיקרונים ויותר. השוואת ממדי הסיבים הקצרים לחיזוי תאורטי המבוסס על הדינמיקה של חילוץ שרשרות מתוך הרשת, אישרה את ההשערה שהסיבים הקצרים נובעים מהתרת הרשת במהלך הטוויה החשמלית. בקרה של התהליך על פי המודל יכולה לאפשר יצירת ננוסיבים רצופים בעלי קוטר וקשיחות רצויים לתנאים נתונים, כמו גם ננוסיבים קצרים בעלי מורפולוגיה לא אחידה בשני הכיוונים הניצבים, שיכולים לשמש להנדסת רקמות, שחרור מבוקר של תרופות, חומרים מרוכבים ועוד.

אף כי השאלה מדוע האלסטיות של ננוסיבים תלויה בגודלם אינה בתכולת המחקר, ניתן להציג אותה בפרספקטיבה כללית. פוטנציאלית, על ידי הגדלת קצב העיבור של הסילון והקטנת רמת הסביכות (entanglement) של הרשת באמצעות משתני התהליך (מסה מולרית, ריכוז התמיסה, שדה חשמלי, ספיקה, מרחק אלקטרודות וכו'), ניתן להקטין את קוטר הסיב בהדרגה עד מעט לפני פרגמנטציה של הסילון, ובכך להשיג קוטר סיב מינימלי לתנאים נתונים, ועל ידי כך קשיחות מקסימלית האפשרית לתנאים אלה. הגדלת הכיווניות של השרשרות כתוצאה מהמתיחה, אף כי היא מביאה להגדלת קשיחות הסיב, אינה יכולה כשלעצמה להסביר את התלות של האלסטיות במימדי הסיב ובמיוחד בקוטרו. הגישה המבוססת על ננומבנים, שנוצרים מקורלציה בין קטעי שרשרות סמוכים, אמנם מסבירה כיצד מודול האלסטיות יכול לגדול כתוצאה ממגבלות הנפח (confinement) סביב הננומבנה בקוטר סיב נתון, אך אינה רגישה לשאלה כיצד הושגו קוטר הסיב והמורפולוגיה הפנימית שלו.

ואמנם, ניתן להגיע לאותו קוטר סיב על ידי שילובים שונים של משתני התהליך, למשל על ידי הגדלת המסה המולרית תוך כדי הקטנת ריכוז התמיסה ו/או הגדלה של המרחק בין האלקטרודות. הננומבנה הנוצר במבנה המוצק בכל שילוב כזה הינו שונה, בין היתר באורך של קטעי שרשרת בין קשרים טופולוגיים, או לחילופין בצפיפותם הנפחית של הקשרים טופולוגיים. ניתן לקשור כמותית בין גידול באורך הקטעים האלה (לחילופין, קיטון בצפיפותם של הקשרים טופולוגיים), שהוא יחסי הפוך

לפיכך, המוטיבציה למחקר זה היא להגיע להבנה טובה יותר של הסיבות לתכונות הייחודיות של ננוסיבים בטוויה חשמלית, ידע בעל ערך רב לפיתוחים ויישומים עתידיים. שתי שאלות מחקר הקשורות זו בזו נשאלו: כיצד משפיעה טוויה חשמלית על המבנה הננומטרי של מטריצת הפולימר בתוך הסיב? וכיצד משפיע הננומבנה על התכונות המכניות של הסיב ובמיוחד האלסטיות? מפאת ההיקף הנרחב של תחומי המחקר הנסקרים בתזה זו - פיזיקה של פולימרים, טוויה חשמלית, ותכונות מכניות של פולימרים - המחקר מתמקד בשאלה הראשונה. באופן ספציפי, המחקר עוסק בהתנהגות הדינמית של רשת הפולימר בתוך הסילון שנוצר בטוויה חשמלית. למרות שהקשר בין הננומבנה של הסיב וקשיחותו (השאלה השנייה) אינו בתכולת המחקר, השפעותיו האפשריות על האלסטיות נידונות בהרחבה.

במסגרת המחקר נבנה מודל תאורטי של התצורה הדינמית של רשת סבוכה של פולימר בתוך סילון טוויה חשמלית, המדמה את הרשת כסריג של חרוזים המחוברים ביניהם בקפיצים בעלי אלסטיות אנטרופית, ומגדיר את הכוחות ההידרודינמיים באמצעות הראולוגיה הידועה של סילונים מונעים חשמלית. כמו כן, נכתבה ובוצעה סימולציית תנועה אקראית (random walk) של הרשת, שמדמה את שרשרת הפולימר כרצף של צעדים, כאשר ההסתברות לצעידה בכל כיוון אפשרי מחושבת מפוטנציאל אפקטיבי הנובע משדה הזרימה של הסילון ומהכוחות האלסטיים הפועלים בקצוות השרשרת על ידי השרשרות הקשורות אליה טופולוגית. תוצאות המודל והסימולציה חוזות מתיחה אורכית משמעותית של הרשת, מלווה בהתכווצות והידוק של הרשת בכיוון הרדיאלי של הסילון. טרנספורמציה זו של הרשת, ממצב שיווי משקל למצב כמעט מתוח לחלוטין, מתרחשת קרוב למוצא הסילון, פחות ממילימטר אחד מקצה המחט הקפילרית. הסימולציה, שפותחה במיוחד עבור מחקר זה ונעשה בה במסגרתו שימוש נרחב, הינה כלי גמיש ואפקטיבי המאפשר ניתוח והצגה חזותית של שרשרות בודדות ושל הרשת כולה, תחת תנאי זרימה שונים.

הדמיה של סילון טוויה חשמלית של פוליאתילן אוקסיד (PEO) מומס במים, באמצעות קרני רנטגן (X-ray) בקונטרסט גבוה ובזמן חשיפה קצר, אימתה את החיזוי התאורטי, והראתה שאכן יש גידול בריכוז הפולימר באזור מרכז הסילון, בקרבה למוצא הסילון. תצפית זו אף הדגימה את ההשפעות המנוגדות של המתיחה וההתאדות על תצורת רשת הפולימר: ההתאדות הופכת דומיננטית כאשר המתיחה חלשה, למשל כאשר עוצמת השדה החשמלי נמוכה או ספיקת התמיסה גבוהה, וגורמת להפחתת ההתכווצות של רשת הפולימר ולירידת ריכוז הפולימר במרכז הסילון. טכניקת ההדמיה של הסילון באמצעות קרני רנטגן, לרבות פיתוח האלגוריתמים והשיטות לעיבוד וניתוח התמונות, נתוני הבליעה של הקרן, ותנועת חלקיקים, פותחו במיוחד עבור מחקר זה. הם אפשרו לקבל מידע על שדה הזרימה בתוך הסילון ועל התפלגות ריכוז הפולימר לאורכו ולרוחבו, מידע שלא ניתן היה להשיג עד כה בשיטות מדידה אחרות בגלל אי היציבות האופיינית לסילון טוויה חשמלית.

שאלה חשובה היא האם התצורה המתוחה של הרשת נשארת לאחר התמצקות הסילון ויצירת הסיב. שאלה זו נבחנה בצילום אופטי בשדה קרוב (near field) של סיבי MEH-PPV, פולימר גמיש-למחצה בעל תכונות חשמליות ואופטיות אקטיביות, באמצעות סריקה מיקרוסקופית ברזולוציה ננומטרית. הבליעה החזקה של פולימר זה בתחום אורך הגל הנראה אפשרה מדידה של התפלגות צפיפות הפולימר בניצב לאורך הסיב, והראתה צפיפות גבוהה יותר של הפולימר במרכז הסיב. יתרה מכך, באמצעות אפנון

תקציר

זרימה מותחת של תמיסה דלילה-למחצה (semi-dilute) של פולימר, בתנאים של קצב עיבור גבוה, יכולה לגרום למתיחה ולהתרה (disentanglement) משמעותיות של רשת הפולימר. החקירה התאורטית והניסויית שבוצעה במחקר זה משתמשת בטכניקת הטוויה החשמלית (electrospinning), המתאפיינת בזרימה עם קצב עיבור גבוה והתאדות מהירה, לצורך לימוד ההשפעות של זרימה עם מתיחה חזקה על רשת הפולימר המומסת, וכתוצאה מכך על הננומבנה והתכונות המכניות של הסיבים הנוצרים.

מבנים ננומטריים, בסדר גודל של מיליונית המילימטר (1 ננומטר), מגלים תכונות מכניות, חשמליות ואופטיות ייחודיות התלויות בממדיהם, מכיוון שגודלם הוא מאותו סדר גודל של האטומים והמולקולות המרכיבים אותם. בפולימרים, שהמולקולות שלהם גדולות וגמישות, התלות בממדים מובחנת אף בגדלים גבוהים יותר.

פולימרים בנויים ממולקולות מאוד ארוכות (מקרומולקולות או שרשרות), שהשלד שלהן מורכב מרצף ארוך של קשרי פחמן-פחמן כימיים. כאשר שרשרות הפולימר מתוחות ומיושרות האחת ביחס לשנייה, החוזק והקשיחות של הפולימר יכולים להגיע באופן תאורטי לשני סדרי גודל יותר מאשר בחומרים פלסטיים מסחריים נפוצים, ובכך מסמנים את הפוטנציאל המיטבי של פולימרים כחומרים הנדסיים. יחד עם זאת, הגמישות של מקרומולקולות כתוצאה מפיתול הקשרים הכימיים גורם להן, כאשר הן מומסות על ידי ממס, להתכווץ למבנה של סליל כדורי בעל תצורות אקראיות, וליצירת רשתות סבוכות (entangled), והתוצאה היא ירידה בחוזק ובקשיחות לאחר התמצקות התמיסה.

אחת השיטות היותר נגישות ליצירת ננומבנים היא טוויה חשמלית, שמשכה אליה תשומת לב רבה של הקהילייה המדעית וההנדסית בחמש עשרה השנים האחרונות. לטוויה חשמלית נמצאו שימושים חדשים וחזויים רבים בתחומי מדעי החיים, הנדסת רקמות, סינון, קוסמטיקה, ביגוד, חיישנים זעירים ועוד. בטוויה חשמלית נוצר סילון נוזלי על ידי משיכה אלקטרוסטטית של תמיסת פולימר מתוך מחט קפילרית, באמצעות שדה חשמלי בעוצמה גבוהה. הממס מתאדה ברובו תוך כדי המעוף החופשי של הסילון, והסיבים הנוצרים – ננוסיבים בקטרים אופייניים בין 50 ל-1000 ננומטר - נאספים על מצע. קצב המתיחה הגבוה של רשת הפולימר במהלך הטוויה החשמלית, וההתאדות המאוד מהירה של הממס מהסילון, הם שני הגורמים הדומיננטיים המשפיעים על המורפולוגיה והננומבנה של סיבים בטוויה חשמלית.

ניסויים שבוצעו לאחרונה מצאו, שהחוזק והגמישות של ננוסיבים בטוויה חשמלית תלויים מאוד בקוטרם ובאורך שרשרות הפולימר (כלומר, המסה המולרית). ככל שקוטר הננוסיבים קטן יותר, כך חוזקם וקשיחותם עולים. ידוע זה מכבר כי ניתן לשפר את החוזק והקשיחות של סיבי פולימר בעלי ממדים מיקרוניים על ידי בתר-תהליך של משיכה או ערגול מכניים של הסיבים המוצקים. התופעה דומה בשני המקרים, הן בתהליך הננו והן בתהליך המיקרו הסלילים האקראיים של שרשרות הפולימר נמתחים בכיוון ציר האורך של הסיב, ובכך מושגת רמה גבוהה של התיישרות ושיפור רב בתכונות המכניות. יחד עם זאת, בננוסיבים המבנים הללו נוצרים כחלק מהתהליך ולא בבתר-תהליך, וגורמים נוספים משפיעים כתוצאה מהיווצרות מבנים סופרמולקולריים שממדיהם מאותו סדר גודל של קוטר הסיב.

תודות, פרסומים והצגות

המחקר נעשה בהנחיית פרופ' איל זוסמן בפקולטה להנדסת מכונות, עם דר' ארקדי ארינשטיין כיועץ.

אני אסיר תודה לפרופ' זוסמן על שנתן בי אמון מתחילת הדרך, על הנחייתו המקצועית והמסורה ומעל לכל החברית, ועל פתיחת עולמו, עולם הדברים הזעירים, בפני. אני מודה לדר' ארינשטיין על השעות הרבות והמהנות בהן הכניס אותי לסודות הפיזיקה של הפולימרים, ועל העבודה המשותפת בפיתוח המודל והסימולציות.

אני מודה לטכניון, הקרן הדו-לאומית למדע ארה"ב-ישראל, מכון הננו-טכנולוגיה ע"ש ראסל ברי בטכניון, והקרן הלאומית למדע על התמיכה הכספית הנדיבה בהשתלמותי.

המחקר בוצע בשיתוף פעולה עם פרופ' מרים רפאלוביץ' מאוניברסיטת סטוני ברוק בארה"ב, דר' קמאל פצה מהמעבדה הלאומית ארגון בארה"ב, פרופ' דריו פיזיניינו ודר' אנדראה קמפוסאו מאוניברסיטת סלנטו באיטליה, ודר' אולריקה וונגנהיים ופרופ' רוברט שוסטר מהמכון לטכנולוגיית גומי בגרמניה. אני בעל חוב להם על שיתוף הפעולה הפורה ועל התמיכה במחקר.

המחקר סוכם בחמישה מאמרים, והוצג על ידי הכותב פעמים אחדות בהרצאות בטכניון ובאוניברסיטת סטוני ברוק בארה"ב, וכן בשלושה כנסים שנתיים של האגודה האמריקאית לפיזיקה בארה"ב. רשימת פרסומים והצגות מופיעה בפרק באנגלית.

למשפחתי

דינמיקת רשת פולימר בטוויה חשמלית
והשפעתה על הננומבנה של הסיבים

מודלים, סימולציה וניסויים

חיבור על מחקר

לשם מילוי חלקי של הדרישות לקבלת התואר
דוקטור לפילוסופיה

ישראל גרינפלד

הוגש לסנט הטכניון - מכון טכנולוגי לישראל

תשרי תשע"ד, חיפה, ספטמבר 2013

דינמיקת רשת פולימר בטוויה חשמלית
והשפעתה על הננומבנה של הסיבים

מודלים, סימולציה וניסויים

ישראל גרינפלד